



**HAL**  
open science

# Toxoplasma gondii, a super fast runner and cell invader. Studying motion and forces

Georgios Pavlou

► **To cite this version:**

Georgios Pavlou. Toxoplasma gondii, a super fast runner and cell invader. Studying motion and forces. Chemical Physics [physics.chem-ph]. Université Grenoble Alpes [2020-..], 2020. English. NNT : 2020GRALV023 . tel-03153264

**HAL Id: tel-03153264**

**<https://theses.hal.science/tel-03153264>**

Submitted on 26 Feb 2021

**HAL** is a multi-disciplinary open access archive for the deposit and dissemination of scientific research documents, whether they are published or not. The documents may come from teaching and research institutions in France or abroad, or from public or private research centers.

L'archive ouverte pluridisciplinaire **HAL**, est destinée au dépôt et à la diffusion de documents scientifiques de niveau recherche, publiés ou non, émanant des établissements d'enseignement et de recherche français ou étrangers, des laboratoires publics ou privés.

## THÈSE

Pour obtenir le grade de

### **DOCTEUR DE LA COMMUNAUTE UNIVERSITE GRENOBLE ALPES**

Spécialité : **Chimie Physique Moléculaire et Structurale**

Arrêté ministériel : 25 mai 2016

Présentée par

**Georgios PAVLOU**

Thèse dirigée par **Isabelle TARDIEUX, Directeur de Recherche,  
Institute for Advanced Biosciences, Grenoble**

dans l'École Doctorale Chimie et Sciences du Vivant

***Toxoplasma gondii*, un champion de course et  
un redoutable envahisseur. Etude des forces  
motrices et invasives**

***Toxoplasma gondii*, a super fast runner and cell  
invader. Studying motion and forces**

Thèse soutenue publiquement le «**22 June 2020**»,  
devant le jury composé de :

**Isabelle, TARDIEUX**

Directeur de Recherche, Institute for Advanced Biosciences, Directeur de  
thèse

**Mohamed-ali, HAKIMI**

Directeur de Recherche, Institute for Advanced Biosciences, Président

**Ana-Maria, LENNON-DUMENIL**

Directeur de Recherche, Institute Curie, Examineur

**Friedrich, FRISCHKNECHT**

Professeur, Center for Infectious Diseases Heidelberg University Medical  
School, Rapporteur

**Serge, MOSTOWY**

Professeur, Department of Infection Biology London School of Hygiene &  
Tropical Medicine, Rapporteur

**Geneviève, MILON**

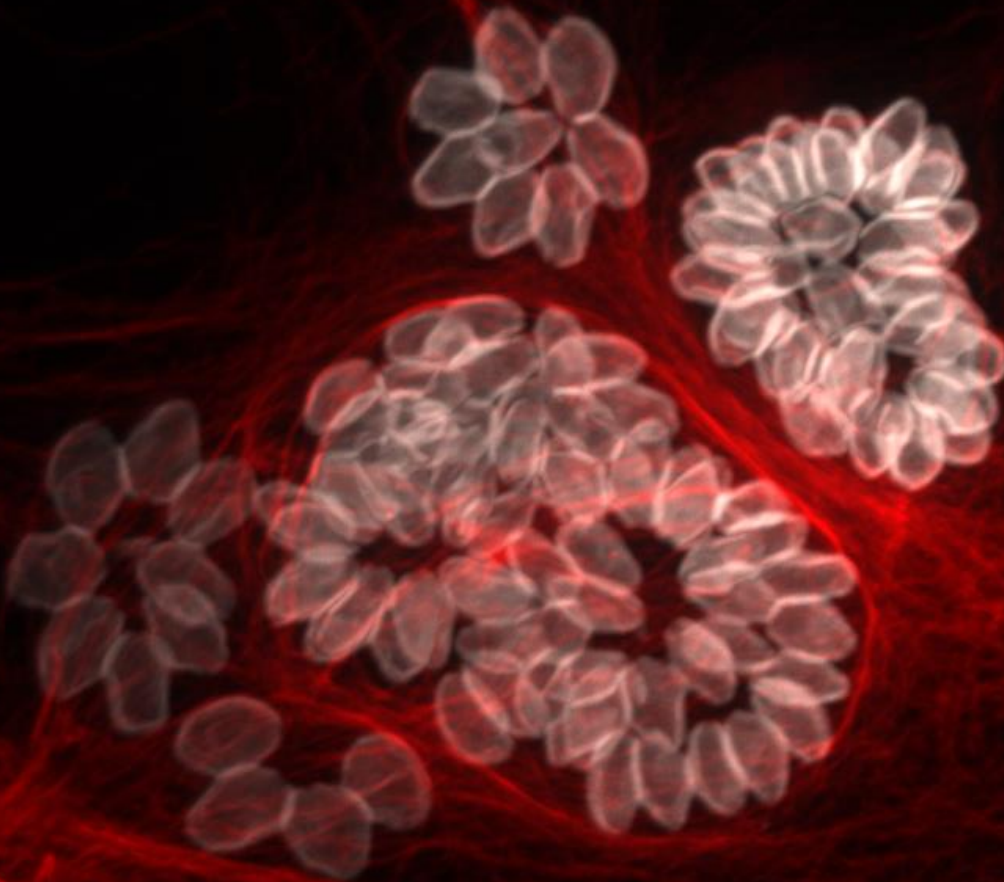
Directeur de Recherche Emérite, Institute Pasteur, Examineur



***Toxoplasma gondii*, a super fast runner and cell invader**

**Studying Motion and Forces**

**PhD Thesis Georgios Pavlou**



*Toxoplasma* from Greek τόξον (toxon, "arc, bow") and πλάσμα (plasma, "shape, form")

**Under supervision of Dr Isabelle Tardieux  
Institute for Advanced Biosciences  
Grenoble, France**

# ***Toxoplasma gondii*, a super fast runner and cell invader**

## **Studying motion and forces**

**PhD Thesis Georgios Pavlou**

This document begins with a short introduction describing major biological features of the protozoan microbe named *Toxoplasma gondii*/*T. gondii* with special reference to (1) its main structural attributes, (2) its life cycle as a parasite of warm-blooded metazoans including with the diseases it can cause to the hosts, and (3) its fast replicating developmental stage called tachyzoite, with a focus on the importance of motile behaviors along its life. We will then consider in more details the mechanisms evolved by the *T. gondii* tachyzoite to efficiently navigate within extracellular matrices or in between cells and then invade host cells, two steps that determine the success of the *T. gondii* parasitic lifestyle and which we have successively investigated during the PhD period. To this end, we will provide a brief context and question presentation before recapitulating the main highlights of the work and insisting on the techniques we implemented while the corresponding research article under evaluation or recently published will follow. To further flesh out the discussion chapter of these manuscripts, major issues emerging from this work will be listed and analyzed in an additional section with respect to the concepts, tools and techniques we could design for better knowledge in the future. Finally, we briefly conclude with a perspective mentioning different aspects of application the PhD work may lead to including in fields beyond parasitology, thereby strengthening the importance of cross feeding between fields and expertise for optimal chance of innovation and promising end-product delivery to the society.

# Contents

## List of abbreviations

## 1. Introduction

- 1.1. The Apicomplexa *Toxoplasma gondii*, a member of the Alveolata group is the causative agent of toxoplasmosis.....2
- 1.2. *T. gondii* life cycle.....4
- 1.3. The *T. gondii* tachyzoite stage.....6
- 1.4. The *T. gondii* tachyzoite motile behaviors.....7
- 1.5. The *T. gondii* tachyzoite invasive behavior.....10
- 1.6. The *T. gondii* tachyzoite forms progeny, which eventually displays an egress behavior.....12

## 2. Chapters

- 2.1. Chapter 1 - Exploring mechanistically the complex choreography of *T. gondii* tachyzoite movement.....17
  - 2.1.1. Context and questions.....17
  - 2.1.2. Implementing methods to study the movement of *T. gondii* tachyzoite.....23
  - 2.1.3. Main highlights of the study.....31
  - 2.1.4. Publications.....31
  - 2.1.5. Discussion and perspectives.....51
- 2.2. Chapter 2 – Investigating host cell invasion by the *T. gondii* tachyzoite with a focus on the late steps of the process.....54
  - 2.2.1. Context and questions.....54
  - 2.2.2. Implementing methods to study the cell invasion by *T. gondii* tachyzoite.....60
  - 2.2.3. Main highlights of the study.....63
  - 2.2.4. Publications.....64
  - 2.2.5. Discussion and perspectives.....113

## 3. Conclusion.....116

## 4. Other publications.....118

## 5. Acknowledgements.....161

## 6. References.....163

## Abbreviations

|               |  |
|---------------|--|
| ALIX          | ALG-2-interacting protein X                                |
| AMA           | Apical membrane antigen                                    |
| CIN           | Cbl-interacting  |
| DAG           | Diacylglycerol   |
| DALYs         | Disability adjusted life years                             |
| DC            | Dendritic cell   |
| DG            | Dense granules   |
| DNM           | Dynamin  |
| ECM           | Extracellular matrix                                       |
| EDC           | 1-ethyl-3- [3-dimethylaminopropyl] carbodiimide            |
| ELC           | Essential light chain                                      |
| ESCRT         | Endosomal sorting complex required for transport           |
| FCS           | Fetal calf serum   |
| HA            | Hyaluronan   |
| HAART         | Highly active antiretroviral therapy                       |
| IMC           | Inner membrane complex                                     |
| IFN- $\gamma$ | Interferon gamma   |
| IP3           | Inositol triphosphate                                      |
| F-actin       | Filamentous actin  |
| GAC           | Glideosome-associated connector                            |
| GAP           | Gliding-associated protein                                 |
| GAPM          | Glideosome-associated protein with multiple-membrane spans |
| GED           | GTPase effector domain                                     |
| mC            | mCherry  |
| MD            | Middle domain  |
| MEF           | Mice embryonic fibroblasts                                 |
| MIC           | Microneme protein  |
| MIP           | Maximum intensity projection                               |
| MLC           | Myosin light chain   |
| MTOC          | Microtubule organizing center                              |
| Myo           | Myosin   |
| NK            | Natural killer   |
| PAA           | Polyacrylamide   |
| PEG           | poly(ethylene glycol)                                      |
| PKA           | Protein kinase A   |
| PKG           | Protein kinase G   |
| PHD           | Pleckstrin homology domain                                 |
| PLL-g-PEG     | poly(L-lysine)-graft-poly(ethylene glycol)                 |
| PM            | Plasma membrane  |
| PRD           | Proline-rich domain  |
| PV            | Parasitophorous vacuole                                    |

|      |   |
|------|---|
| PVM  | Parasitophorous vacuole membrane            |
| qFSM | Quantitative fluorescent speckle microscopy |
| RB   | Residual body                               |
| RICM | Reflection Interference Contrast Microscopy |
| ROM  | Rhomboid protease                           |
| RON  | RhOpry Neck Protein                         |
| TIRF | Total internal reflection fluorescence      |
| TFM  | Traction force microscopy                   |
| Tg   | <i>Toxoplasma gondii</i>                    |
| ZCJ  | Zoite cell junction                         |

# Introduction

## 1. Introduction

### 1.1 The Apicomplexa *Toxoplasma gondii*, a member of the Alveolata group is the causative agent of toxoplasmosis

*Toxoplasma gondii* is a single-celled eukaryote and one of the thousands members of the Apicomplexa phylum. This large and diverse phylum is part of a higher order group of protozoans known as Alveolata, which is also composed of the ciliates, a set of micropredators and the marine phytoplankton Dinoflagellates. Alveolata are characterized by flattened vesicle-like structures lying beneath the plasma membrane defined as cortical alveoli and in the case of Apicomplexa are termed Inner Membrane Complex/IMC (see Figure 2 in the next section 1.3).

The Apicomplexa name stems from a unique complex localized at the apical pole that typifies the motile stages, also called **zoites**, of these protozoans (Levine 1970). Another unifying trait across the Apicomplexan species is the parasitic lifestyle they have evolved since they strictly rely on hosting cells to produce progeny (Dubey, 1998). Among the Apicomplexa members already identified, *T. gondii* is often seen as one of the most successful because of an impressive ability to parasitize virtually all warm-blooded wild and domestic animals, and this in all terrestrial ecosystems. In addition to be quite cosmopolitan and to accommodate a broad range of hosts, *T. gondii* multiplies in a vast repertoire of cells from different lineages *in vivo* and parasitizes all nucleated cells under *in vitro* conditions. In line with these features and according to serological surveys, about a third of the human population has been exposed to *T. gondii* (Halonen & Weiss, 2013) and the prevalence rate is even higher in areas of Europe and South America. The serological markers used in the surveys inform on the proportion of people that have been in contact with the fast replicating **tachyzoite** stage during the acute but subsequently controlled expansion of the *T. gondii* population. However, they are also considered as fair indicators for the presence of the slow replicating, hence a long-term persisting parasite population, which takes over the acute phase. The persistent population is represented by the *T. gondii* developmental stage called **bradyzoite** that settle in tissue cells away from the initial intestinal site of colonization, especially in cells from the nervous central and peripheral systems, but also in skeletal and cardiac muscles.

At the clinical level, the acute phase of infection remains subclinical and the long-term infection, often referred as to the chronic phase, is perceived as clinically *quasi* silent with little or no direct harmful impact in healthy humans. Of note, severe cases of toxoplasmosis in immunocompetent persons were reported from South America and were assigned to several *T. gondii* atypical strains (Carme *et al*, 2002). Of higher clinical concern are the transient or prolonged dysfunctions of the immune system that can cause life-threatening or life-debilitating toxoplasmosis-related diseases. As examples, when patients are under

immunosuppressive anti-cancer chemotherapy, anti-auto-immune therapy or anti-graft rejection protocols post organ transplantation, the “silent” bradyzoites can revert back to non-silent tachyzoites through a differentiation process termed “parasite reactivation”. The massive replication of newly converted tachyzoites can induce irreversible damages in sites of parasite persistence and lead to lethal disseminated infection unless pharmacologically controlled (Dubey, 1996). Of note, the reverse bradyzoite-tachyzoite conversion and its consequences were a leading cause of the AIDS-related encephalitis in HIV infected immunocompromised people (Luft & Remington, 1992) prior to the development of Highly Active AntiRetroviral Therapy (HAART) but it still remains after HAART a common cause of cerebral focal lesion in AIDS patients, and the third most frequent AIDS-defining condition in developing countries (Colombo *et al*, 2005). In the same line, recent metadata analysis based on 74 studies that has scanned in total 25 989 HIV-infected people from 34 countries, highlighted the high prevalence of *Toxoplasma*-HIV co-infection (25 to 60%) especially in North Africa and the Middle East (Wang *et al*, 2017).

Aside from pathology- or therapy-induced immunosuppressive situations, pregnancy is another case in which the immune balance is shifted towards an immunosuppressive state, compatible with the establishment of fetomaternal tolerance, and thus development of the fetus in the uterus while the mother’s immune system remains functional. While the fetus can be naturally protected from harmful microbes thanks to the transfer of maternal antibodies across the placenta throughout the umbilical cord, the same route can also promote fetus colonization by microbes including *T. gondii* tachyzoites. Interestingly, the first known photographic images of *T. gondii* were published in 1923 by Josef Janku taken from the retina of an infant suffering from congenital toxoplasmosis (McGovern & Wilson, 2013). In the last years, the global annual incidence of congenital toxoplasmosis was estimated about 200.000 cases which corresponds to a burden of 1.20 million Disability Adjusted Life Years (DALYs) with the highest values seen in South America and some Middle Eastern and low-income countries (Torgerson & Mastroiacovo, 2013). DALYs represent the total number of years lost to illness, disability, or premature death within a given population (Murray *et al*, 2012).

In this context, primo-infection with *T. gondii* during the early stages of pregnancy is associated with (i) a low probability of fetus contamination because of the restricted size of maternal-fetal placenta interface but (ii) severe consequences including abortion and stillbirth or severe neurological defects. In contrast when primo-infection occurs at later stages of pregnancy, the risk of congenital toxoplasmosis for the fetus increases but the contamination leads to less severe outcomes in particular chorioretinitis and uveitis (reviewed in Weiss & Dubey, 2009). In addition, in the case of early infection (during the first trimester of infection), the focal proliferation of tachyzoites was reported to

continue specifically in the fetal brain over time thus creating lethal damages even when the maternal immune anti-*Toxoplasma* response has started to take place and the maternal IgGs have crossed the placenta and reach the fetus (Ferguson *et al*, 2013).

## 1.2 *T. gondii* life cycle

*T. gondii*, like many other Apicomplexa parasites, has a complex life cycle that involves both asexually reproducing forms and sexual stages. Because these stages are timely formed through unique differentiation processes - as already mentioned for the tachyzoite and bradyzoite asexual stages during bi-directional conversion- that occur in different host species, the *T. gondii* life cycle is described as heteroxenous (Figure 1). By definition, the hosts in which parasitic organisms can sexually reproduce are classified as **definitive hosts** and those supporting only asexual reproduction are the **intermediate hosts**. *T. gondii* can sexually reproduce only in felids (i.e. the definitive *T. gondii* hosts) while all the other warm-blooded animals are intermediate hosts. Of note many intermediate hosts including birds, rodents and other mammals are typical preys for the felids and contribute to the *T. gondii* genetic diversity potentially generated in the felids.

Aside from the tachyzoite and bradyzoite stages mentioned above, the **sporozoite** is the third infectious stage of *T. gondii*. This stage is formed in the protecting **oocyst** which itself derives from the fertilization of female gamete and the resulting zygote in the felid intestine. After fertilization, the zygote evolves in an oocyst, which is released from the host enterocyte into the intestine lumen and further shed in the environment. Upon appropriate aeration and temperature conditions, the unsporulated oocyst converts into a sporulated oocyst, which consists of two sporocysts and each of these contains four sporozoites (Dubey *et al*, 1970).

Once a potential host (definitive or intermediate) ingests *T. gondii* oocysts together with unwashed raw vegetable or contaminated water, the sporozoite is next released from the oocyst following mechanical and enzymatic disruption of the envelope, a process, which mainly takes place in the host stomach. Ending its journey in the host intestinal tractus, the sporozoites invade enterocytes of the ileum (small intestine) and differentiate into the tachyzoite stage that rapidly amplifies the parasite population in cells from the gut mucosa. In this multi-component mucosa, resident immune cells, in particular the CD8 $\alpha^+$ dendritic cells (DCs) together with chemotactically recruited monocytes and neutrophils are highly permissive to tachyzoite multiplication (Mowat & Agace, 2014). Importantly some of these leucocytes are early sources of interleukin 12, a cytokine that elicits among other cells, natural killer (NK) and CD4 $^+$  and CD8 $^+$ T

cells to produce interferon gamma (IFN- $\gamma$ ) which orchestrates the host resistance to *T. gondii* in hematopoietic and non-hematopoietic cells through the activation of toxoplasmacidal activities (Hunter & Sibley, 2012). Remarkably, this “vigorous innate immune response” ensures significant control of the replicating parasite population. However, it concomitantly promotes the survival of a subpopulation that exits from the inflamed site and reaches distant sites to further reside in tissue cells protected from a too harsh immune surveillance, in particular the brain and muscles. In these distant tissues, the tachyzoite undergoes bradygenesis, which drives the formation of a cyst enclosing bradyzoites that accounts for the long-term parasitism phase and was first described in 1908 by Splendore (McGovern & Wilson, 2013). In a close scenario, once a potential carnivorous host (definitive or intermediate) ingests food contaminated with *T. gondii* cysts, and following cyst wall disruption in the stomach, the bradyzoites colonize cells from the host small intestine and differentiate into tachyzoites. The tachyzoite population expansion and its reduction concomitant to the formation bradyzoite cysts parallels the scheme described for the sporozoite-mediated gut infection. In conclusion, the relatively recent discoveries of the oral mode of transmission by two distinct parasite stages, each protected by a cyst wall, were achieved separately in the 1955 to 1970 years and can explain the wide geographical distribution of *T. gondii* (Ferguson, 2009).

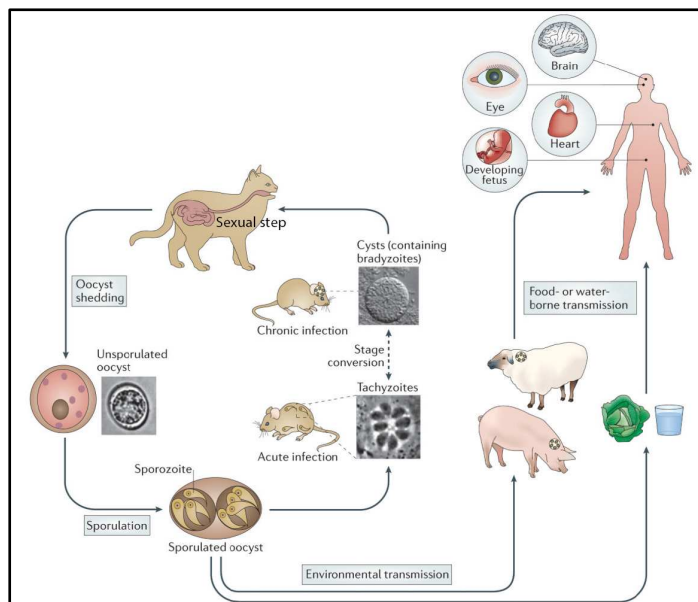


**Figure 1. Schematic representation of the *T. gondii* life cycle.**

Warm-blooded metazoans ingest either encysted-bradyzoites or sporozoites of *T. gondii*. The two parasite developmental stages are released out of their respective cyst envelope in the host stomach and infect the epithelial cells from the ileum part of the intestine. They rapidly transform into highly replicative

tachyzoites in the intestinal mucosa. The innate immune system further controls the expansion of the tachyzoite population but also promotes the colonization of intestine-distant tissues. In these tissues, tachyzoites differentiate as slow replicating bradyzoites in long lasting cysts, which are taken up by new hosts through carnivorism and the same

cycle repeats. However, in felids that feed upon contaminated preys, gametes are formed in the intestine through a complicated set of developmental stages and they produce zygotes that evolve as oocysts, which are released in the environment with the felid feces. There they sporulate and can be taken by herbivores while feeding or by both carnivores and herbivores while drinking oocyst-contaminated water. Adapted from Hunter & Sibley, 2012.

### 1.3 The *T. gondii* tachyzoite stage

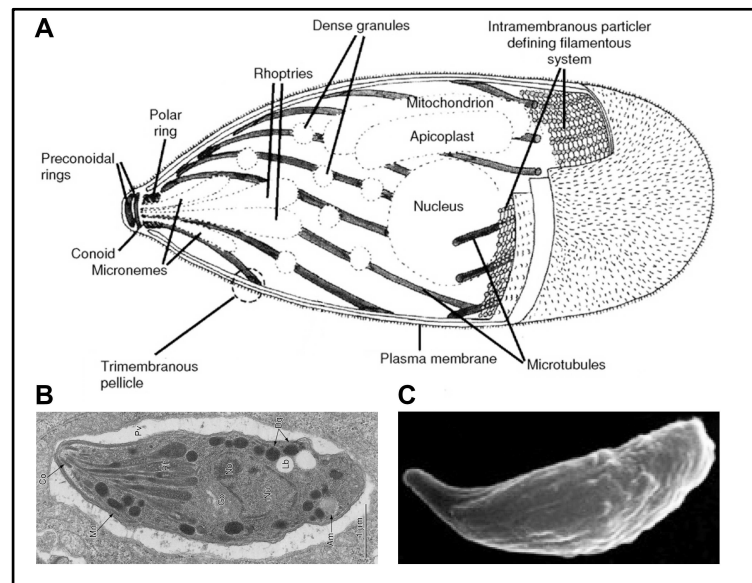


**Figure 2. The *T. gondii* tachyzoite.** (A) Schematic representation showing the main structural elements and organelles from left to right the conoid and the polar ring from which emerge the cortical twisted microtubules, the microneme and the rhoptry secretory vesicles, the dense granules scattered within the cytoplasm, the mitochondrion nearby the apicoplast and the nucleus. The three layers of membrane that form the pellicle and the intramembrane particles connecting the formers are indicated. (B) Electron micrograph showing an intracellular tachyzoite. (C) Scanning electron micrograph of an extracellular tachyzoite with an extruded conoid. Adapted from Carmen *et al*, 2016. The three parasites are oriented with the apical pole on the left side. (A) and (B) adapted from Heintzelman, 2006.

*T. gondii* took its name from the Greek Toxo (τόξο = bow) and plasma (πλάσμα = body) since it was initially described by Nicolle and Manceaux in 1908 who observed in the rodent named “gundii”, extracellular and intracellular unicellular organisms with a bow shape and measuring about 5-8  $\mu\text{m}$  in length and 2-3  $\mu\text{m}$  in width. This description corresponds to the developmental stage called tachyzoite years later in 1973 by Frenkel based on the rapid (tachos = ταχός, fast in Greek), the biology of which has been since decades heavily studied. A major characteristic of the tachyzoite lies in the robust polar architecture organized around a distinct apical pole that houses a unique microtubule-made appendage

called conoid and two sets of secretory organelles named rhoptries, and micronemes, respectively (Figure 2). A wealth of these products has already been identified and a repertoire found involved to promote cell movement and host cell invasion (Frénal *et al*, 2017). As such they will be highlighted in the “context and question section” opening each result chapter of this document. Central to the apical complex and connected to the conoid is the so-called apical polar ring that serves as an atypical MicroTubule Organizing Center (MTOC) for the nucleation of 22 unusually stable subpellicular MicroTubules (MTs) which elongate as spirals until about two third of the parasite length. The MTs tightly subtend the alveoli/IMC that lines most of the plasma membrane (Liu *et al*, 2016). The IMC is made of flattened vesicles aligned in longitudinal rows and joined in a patchwork fashion by sutures.

Briefly, other secretory vesicles called Dense Granules (DGs) populate the whole cell cytoplasm together with the nucleus, the single mitochondria, the Golgi apparatus and the Apicomplexa-restricted organelle called the apicoplast. The apicoplast term was coined from APICOMplexan PLASTid since it was recognized as a vestigial non-photosynthetic plastid homologous to the chloroplasts of algae and plants acquired through endosymbiosis (McFadden & Yeh, 2017).

Importantly the shape and “rigidity” characterizing the extra-cellular tachyzoite is primarily determined by the apical complex together with the juxtaposed IMC and the cortical MTs as revealed by the production of parasites expressing tubulin or IMC mutants (Ma *et al*, 2007)(Barkhuff *et al*, 2011). Reinforcing this conclusion is the recent identification of IMC integral proteins that typically carry multiple membrane spans (the so-called GAPM) and which significantly contribute to the MT stable curved shape (Harding *et al*, 2019).

#### **1.4 The *T. gondii* tachyzoite motile behaviors**

Motility is critical for *T. gondii* survival since once the tachyzoite stage emerges in the intestinal cells through differentiation of the bradyzoite or the sporozoite stages, it further rapidly expands its population in the intestinal mucosa prior to spread in the draining lymph node likely *via* the lymphatic system but also distant tissues. Therefore the tachyzoite needs to (i) navigate in the extracellular matrices composing tissues to access a growth permissive host cell, (ii) invade a host cell where to form progeny and (iii) egress from host cells, as schematized below (Figure 3).

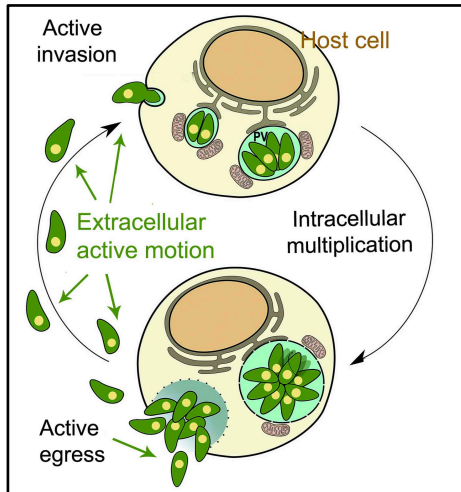


**Figure 3. The intracellular-extracellular life cycle of the *T. gondii* tachyzoite.**  
Adapted from Hortua Triana *et al*, 2018.

To initiate and sustain a motile behavior, the tachyzoite utilizes a very unique actomyosin motor, which despite the notorious difficulties in visualizing the short actin filaments, has been located within the 20- to 30-nm space between the IMC and PM. Together with actin, the divergent class XIV of myosins that typifies the Apicomplexa zoites but also specific scaffolding and regulatory molecules define functional units called **glideosomes** (Soldati *et al*, 2004). Since these units are known to govern force generation underpinning the tachyzoite motile and invasive skills (Frénil *et al*, 2017), they will be more detailed in the specific chapter introducing the study on motile forces.

Pioneer video-microscopic and kinematic studies using 2D conditions revealed three main types of tachyzoite motile behaviors, all requiring attachment to a substrate and all typically associated with body rotation along the long axis of the cell (Frixione *et al*, 1996)(Håkansson *et al*, 1999). While the counterclockwise **helical** and clockwise **circular** types of gliding are considered as productive since they ensure forward cell migration, the third complex set of clockwise motions grouped as **twirling** defines a non productive -i.e. stationary- motion. In contrast to what has been initially proposed, helical motility is not the only behavior that allows subsequent cell invasion. Actually, our team analyzed the preinvasive behavior of several hundreds of tachyzoites and found that most frequently, the tachyzoite executes only a short motion, referred to as “minimal impulse” that associates with extrusion of conoid and concomitant body extension prior to invade the cell (Bichet *et al*, 2014). At about the same time, two elegant settings were designed by the G. Ward’ laboratory enabling for the first time to monitor how tachyzoites move in 3D first *in vitro* using the matrigel, a reconstituted extracellular matrix derived from a mouse sarcoma line and second, *ex vivo* in a mouse earflat imaged by two-photon laser scanning microscopy (Leung *et al*, 2014). These live imaging studies demonstrate that under 3D conditions, the tachyzoite moves only by making irregular corkscrew-like trajectories, which closely recapitulate the 2D helical gliding (Figure 4).

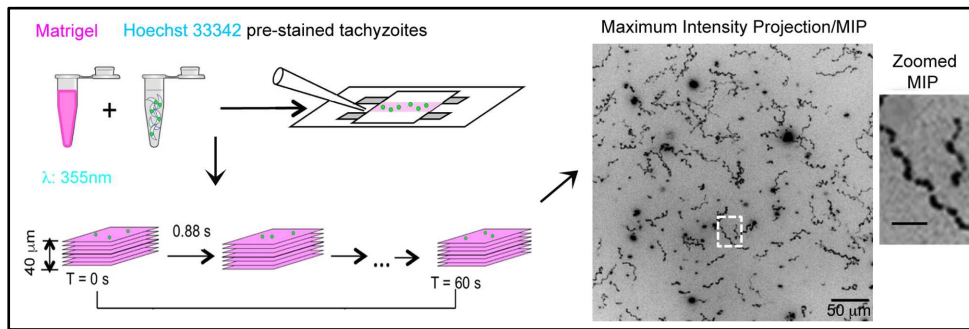


**Figure 4. *T. gondii* tachyzoite motility assay in 3 dimensions.** Preparation of matrigel and tachyzoites stained for nucleus with Hoechst 33342 inside the so-called “Pitta” chambers. Maximum intensity projection (MIP) from the tracking of the nucleus overtime illustrates the corkscrew-like movement of the tachyzoites. Adapted from Leung *et al*, 2014.

Interestingly, a wealth of studies related to cell motility has been conducted in the phylogenetically related Apicomplexa *Plasmodium spp*, the causative agents of the devastating malaria in subtropical and tropical geographical areas. The sporozoite is the developmental stage that is formed in the mosquito host, stored in the insect salivary gland and eventually inoculated into the skin mammalian host along with a blood feeding bite. The sporozoite has the ability to locomote in a fairly similar way as the *T. gondii* tachyzoite and hence it shows fairly conserved glideosome machinery which power gliding motility. However the major sporozoite motile behavior on 2D substrates *in vitro* follows a circular pattern whereas in the dermis, this motion is transformed to a complex non-linear path (Amino *et al*, 2006)(Hellmann *et al*, 2011) which, over time shifts to continuous circular pattern (Hopp *et al*, 2015). In contrast to the tachyzoite case, no typical helical trajectory has been reported (Figure 5).

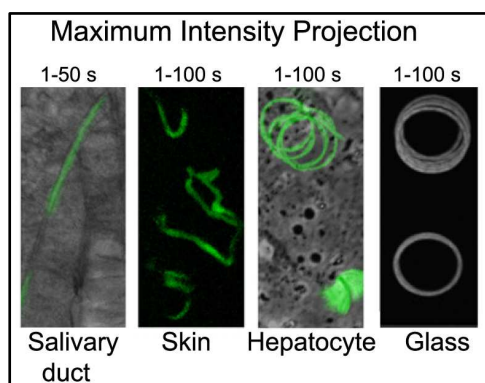


**Figure 5. *Plasmodium* sporozoite gliding pattern *in vivo* and *in vitro*.** Sporozoite motility within a time period was monitored in salivary duct, skin, hepatocyte and glass by reconstituting the trajectory of the parasite. Adapted from Münter *et al*, 2009.

## 1.5 The *T. gondii* tachyzoite invasive behavior

In line with the intracellular lifestyle, *T. gondii* has evolved strategies to invade a host cell from which to steal the nutritive resources required to produce a progeny within a growth permissive intracellular niche. Therefore, by securing the offspring production, the invasion process appears as a crucial event.

To achieve active invasion of a metazoan cell in a minimal time frame, that does not exceed a few tens of seconds, with a maximum chance of success, the parasite relies on a tetrameric molecular complex of proteins pre-stored in the duct of the rhoptry secretory organelles that abuts the conoid tip. The members of this complex identified in 2009 are named RhOpry Neck Protein (RON2,4,5,8) among which RON2 is the one that displays a trans-membrane domain (Besteiro *et al*, 2009). The other RON members face the host cell cytoplasm and possibly directly interact with components of the underlying cortical actin cytoskeleton thereby promoting stabilization of the RON complex in site. As instances, RON8 was proposed to bind to the host F-actin cortical cytoskeleton and to provide the necessary strength to anchor the invading tachyzoite because RON8-deficient parasites do not seem to form stable grip and eventually fail to complete the invasion process (Straub *et al*, 2011). The contribution of the host cortical actin dynamics in the anchoring of the ring-shaped RON structure was supported by the observation that *de novo* formation of actin polymerization through the activation of the actin nucleating ARP2/3 complex is required for invasion to proceed properly (Gonzalez *et al*, 2009).

In this scheme, the availability of G-actin monomers is an important parameter. To fuel the local and transient actin polymerization reaction, it was proposed that the rhoptry bulb-resident toxofilin protein a tiny pool of which is concomitantly released with the RON complex indeed drives the production of free actin monomers. As first evidence, the parasites genetically lacking toxofilin are impaired in their ability to promote disassembly of the host cell cortical actin when compared to those secreting toxofilin. These differences were noticed when fixed samples of invading tachyzoites were analyzed by correlative light and electron microscopy combined with electron tomography, followed by 3D analysis (Delorme-Walker *et al*, 2012). The  $\Delta$  toxofilin mutants show difficulties to pass through the RON made ring, and frequent abortive invasion was observed by live imaging. Finally, when recombinant toxofilin and fluorescent G-actin were successively microinjected in cells prior to perform quantitative Fluorescent Speckle Microscopy (qFSM), toxofilin was shown to enhance the dynamics of actin at the leading edge by promoting the dissociation and the turnover of actin filaments. Therefore toxofilin, which has the right function and is timely secreted, is a primary candidate to drive the host cell remodeling that optimizes anchoring of the RON complex to the host cell cortex at the site of entry.

Apart from RON8, the RON4 member was shown to bind to ALIX (ALG-2-interacting protein X) an accessory member of the endosomal sorting complex

required for transport (ESCRT), and the adaptor protein CIN85 (Cbl-interacting protein of 85kDa) which acts as a scaffold for a variety of endocytic accessory proteins, including ALIX (Guérin *et al*, 2017). Guérin and collaborators propose that CIN85 might also assist the actin cytoskeleton for cortical anchoring of the nanodevice through the ability to bind cortactin, an activator of the ARP2/3 actin nucleator complex, but these interesting possibilities await confirmation.

Importantly, the ring-shaped complex and the host cell potential partners already mentioned, together defines the so-called **junction** between the two cells, which we will hereafter refer to as **Zoite-Cell Junction/ZCJ**. The ZCJ serves not only as a door of entry, but studies from our team have demonstrated that the ZCJ acts as a strong anchor withstanding transmission of the invasive force (Bichet *et al*, 2014) and will be discussed in the chapter introducing the work on invasion. Force transmission during cell invasion implies the transient formation of a bridge between the RON-made ZCJ and the force generating apparatus of the tachyzoite. Upon the release of the RON complex, the RON2 core partner not only inserts into the plasma membrane of the host cell but also exposes a C-terminal region to the outside. This short region of RON is highly structured and can be captured into a high-affinity interaction with the micronemal protein called AMA1 (Apical membrane antigen 1). AMA1 is a calcium-induced secreted protein, which like other microneme proteins, is proteolytically cleaved after apical secretion onto the parasite surface by the rhomboid class of proteases, thereby releasing its ectodomain. It is also shed posteriorly from the surface of invading parasites (Parussini *et al*, 2012). At the onset of invasion, binding of the RON2 C-terminal peptide to the AMA1 groove induces AMA1 conformation change that strengthens the interaction. The co-structure of the AMA1-RON2 peptide has been solved for both *Plasmodium* and *Toxoplasma* zoites and strongly supports a key function in the force transmission process (Tonkin *et al*, 2011). The structural organization of the ZCJ and the contribution of toxofilin are depicted in the following schematic and composite representation whereas more mechanistic insights will be provided in the appropriate chapter (Figure 6).

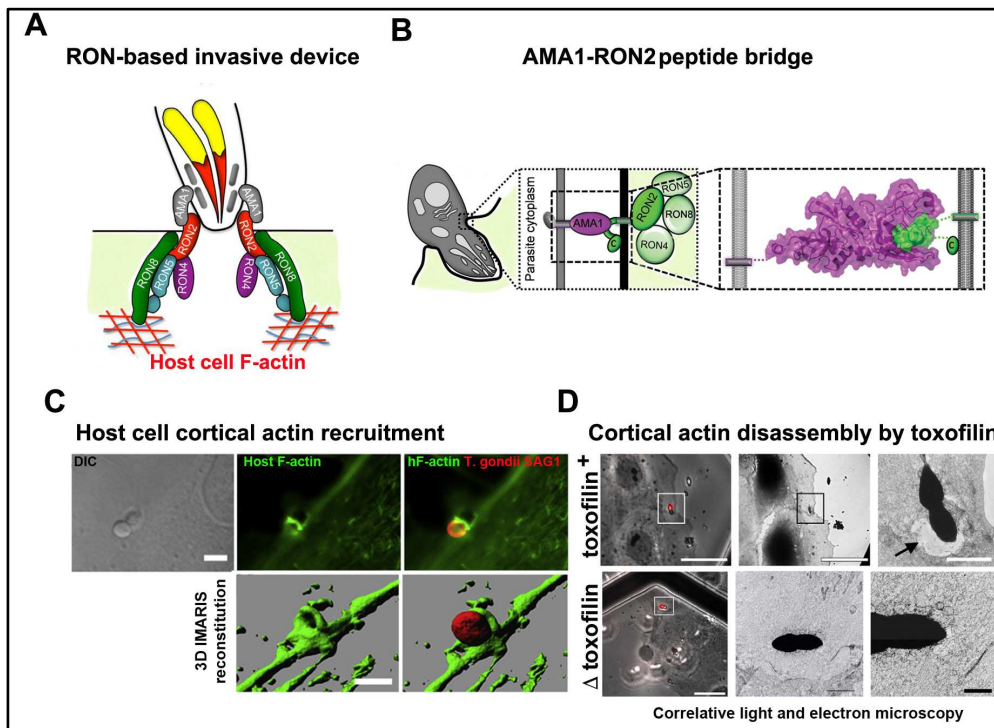


**Figure 6. Presentation of the tachyzoite invasive nanodevice as a key element for successful entry.** (A) Schematic representation of the multi subunit complex forming the invasive nanodevice once released into the host cell plasma membrane and underlying cortex. Adapted from Straub *et al*, 2011. (B) Representation of the RON2-AMA1 complex that connects the tachyzoite and the host cell during invasion. Adapted from Tonkin *et al*, 2011. (C) Confocal images (top) and 3D images (bottom) of host cell F-actin during invasion of *T. gondii* tachyzoite. Adapted from Gonzalez *et al*, 2009. (D) Correlative light and electron microscopy images of *T. gondii* tachyzoites with or without toxofilin protein and the effect of them in the host cell plasma membrane respectively. Tachyzoites genetically devoid of toxofilin in the process of cell invasion are not associated with a sparse host cortical actin network whereas the wild type toxofilin + tachyzoites induce the early dissolution of the actin network at the site of entry. Adapted from Delorme-Walker *et al*, 2012.

### 1.6 The *T. gondii* tachyzoite forms progeny, which eventually displays an egress behavior

Following invasion, the tachyzoite is enclosed in a sub-cellular compartment that it dynamically remodels in large part by secreting products from the rhoptry and the cytoplasmic DGs that inserts in the Parasitophorous Vacuole Membrane (PVM) or assembles a tubular network connecting the parasite with the PVM. In this intracellular niche, the tachyzoite starts to replicate by a process called endodyogeny in which two daughter cells progressively bud within the mother cell without loss of maternal cell shape and apical polarity. The daughter cell assembly starts by the building of two nascent IMC scaffolds that each underlies

newly assembled cortical microtubules and encompasses the Golgi and apicoplast, which have already divided. Meanwhile the nucleus profoundly deforms showing a typical horseshoe-shaped bifurcation but the nuclear membrane remains intact throughout the division cycle. The daughter IMC complexes continue to grow and the two mature daughter cells acquire their plasma membrane while budding from the mother and adopting her membrane, therefore being ready for another round of endodyogeny replication cycle (Figure 7, 8).

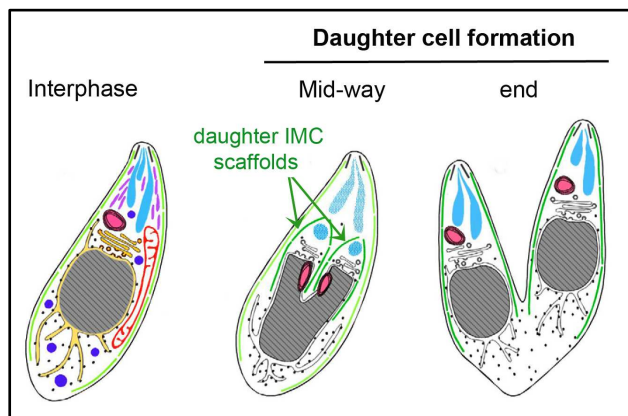


**Figure 7. Endodyogeny of *T. gondii* tachyzoites.** Subcellular structures include, the conoid (blacklines), IMC (light green lines), rhoptries (turquoise), micronemes (lavender), dense granules (blue), apicoplast (pink), mitochondrion (red), Golgi (gold) and nucleus (grey), bordered by endoplasmic reticulum (yellow). Mid-way through daughter cell formation steps show the developing daughter IMC scaffolds (dark green). Adapted from Nishi *et al*, 2008.

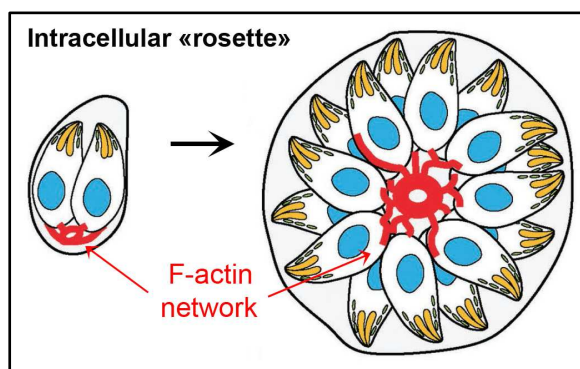


**Figure 8. F-actin during production of the tachyzoite progeny.** F-actin forms a ring at the RB that remains while the actin network spreads between the tachyzoites. Adapted from Periz *et al*, 2017.

It is noteworthy that during the breakdown of the maternal material subsequently recycled for the daughter cell needs, pieces of such material collapse at the posterior end of the cells and organize as the Residual Body (RB). This RB maintains the two offspring connected, thereby directing the similar polar organization of the progeny, a feature that leads to the so-called rosettes of

tachyzoite progeny with aligned centripetal apical poles. The recent production of a tachyzoite cell line that expresses a fluorescently tagged actin chromobody by the M. Meissner laboratory has allowed for the first time to monitor F-actin dynamics in live. These observations have highlighted that a F-actin network assembles at the posterior pole of mature daughter cells and concentrated at the RB where it builds a thick ring structure. When the progeny continues to expand within the parasitophorous vacuole (PV), there are extensive actin networks that likely bundle and connect the daughter cells with each other but spread as well within the PV space (Periz *et al*, 2017). Periz and collaborators propose that molecules are transported from one parasite to the neighbor *via* the actin-based filamentous network (Figure 9).

After five to six cycles of endodyogeny multiplication which at 37°C in the laboratory condition takes about approximately 42 hours, the vacuole containing the mature progeny fills most of the hosting cell. The actin filaments between the parasites and the ring break in a calcium dependent manner just prior to egress. The network then collapses and when the tachyzoites eventually bud from the mother and egress from the parasitophorous vacuole, they leave behind an accumulation of actin patches in the RB. Mechanisms and signaling pathways that drive tachyzoite egress have been dissected. While a timely calcium-dependent secretion from micronemes, and accordingly the release of pore-forming proteins, has been shown to be key to compromise the integrity of the PV and host cell membrane, thereby enabling egress, multiple external stimuli have also been identified upstream secretion to trigger microneme release in *in vitro* cultures. Without going into details on the complex signaling recently dissected in particular by the group of D. Soldati, these include a drop in external  $K^+$  (Moudy *et al*, 2001) or pH (Roiko *et al*, 2014), and serum albumin (Brown *et al*, 2016). A recent scheme accounting for egress induced by intracellular acidification involves a complex cross talk between parasite cAMP-dependent Protein Kinase A1 (PKA1) and the cGMP-dependent Protein Kinase G (PKG). PKG stimulates  $Ca^{2+}$  mobilisation from tachyzoite intracellular stores (reticulum endoplasmic, acidocalcisome, mitochondrion...) and the phospholipase C activity which lead to the production of the second messengers Inositol-1,4,5-triPhosphate (IP3) and DiAcylGlycerol (DAG). These products induce microneme secretion and eventually support the gliding behavior that is required for parasite egress (Jia *et al*, 2017). Once released, the free tachyzoites continue to glide until they successfully invade host cells to ensure amplification and dissemination of the *T. gondii* tachyzoite population. The sequence of molecular events leading to microneme secretion and the breakage of the F-actin connecting network are depicted in a simplified schematic representation (Figure 9).

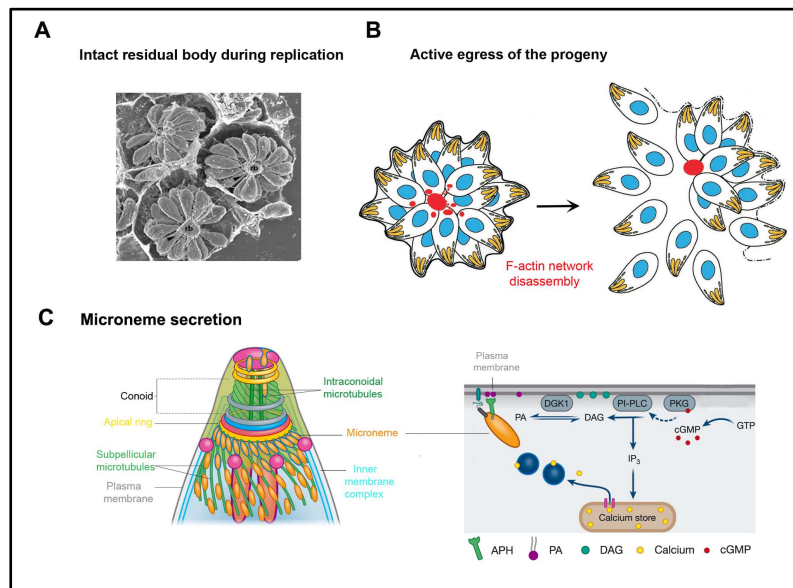


**Figure 9. Egress process and microneme secretion.** (A) Scanning electron micrograph showing intracellular vacuoles that each contains the progeny of a single tachyzoite. Note the rosette organization of the progeny. Adapted from Caldas & de Souza, 2018. (B) Schematic representation of replicating tachyzoites that are connected by F-actin bundles at the RB position. Egress from the host cell occurs concomitantly with the disruption of the F-actin network. Adapted from Periz *et al*, 2017. (C) Schematic representation of the tachyzoite apical part that shows the distribution of micronemes on the MTs and the putative secretion of micronemal proteins at the apical tip (left), and the signaling cascade upstream the release of micronemal proteins that activates the egress behavior of the tachyzoite progeny (right). Adapted from Dubois & Soldati-Favre, 2019.

# Chapter 1

## 2. Chapters

### 2.1 Chapter 1 - Exploring mechanistically the complex choreography of *T. gondii* tachyzoite movement

#### 2.1.1 Context and questions

##### **Cell movement: a panel of strategies dictated by chemical and physical cues**

While the Dutch scientist van Leeuwenhoek is universally acknowledged as the father of microbiology, having discovered the world of protists and bacteria with pioneering work in microscopy, he was also the first to observe cell movement in 1675, and describe the crawling behavior of cells across his microscope slide. Yet, the molecular mechanisms behind cell movement have started to be investigated and molecularly understood only in the past decades with decisive advances achieved in fluorescence microscopy, molecular biology and biochemistry. These experimental techniques have allowed identifying a wealth of proteins primarily required for cell movement, and remarkably conserved across different cell and organism systems, but it is the introduction of biophysical studies to this framework that informed on (i) where forces and force-generating elements are dynamically localized in cells as well as (ii) the amplitude and contractile or non-contractile nature of these forces. Furthermore, the theoretical studies and computational modeling have significantly helped quantify how the forces generated at a molecular level are integrated to produce whole cell movement.

Over this period, researchers have analyzed in details how their favorite single cell or even group of cells move in space and time including under *in vitro*, *ex* and *in vivo* conditions, hence they documented the key role of single cell and “collective cell” migratory behaviors in promoting and maintaining cell and tissue homeostasis in metazoans. As a matter of fact, motility dysfunctions were shown to impair the fundamental and diverse functions of immune cells over processes ranging from embryogenesis, cell/tissue renewal, or progress/resolution of microbe-induced inflammatory responses among others. In addition, a hyper migratory phenotype characterizes tumor cells that undergo metastasis, hence they move out from the initial tumor site, enter the vascular compartments and eventually colonize a distant site.

Most of the initial studies on motility of non-swimming cells were performed *in vitro* in two dimensions (2D) where cells were plated on glass coverslips, coated or not with any flat substrate. Under these conditions, the cells commonly adopt the so-called “crawling” mode of migration. Also referred to as mesenchymal type, this migratory mode requires the formation of a thin lamellipodial front protrusion known to be driven by actin polymerization in conjunction with cell–

matrix adhesion and cytoskeletal contractility (Abercrombie *et al*, 1970a)(Abercrombie *et al*, 1970b). However, in *in vitro* 3D reconstituted extracellular matrices, cells elicit more than one crawling strategy, and grouped under the term amoeboid, these motion patterns share a constant change in cell shape, which is mediated by the rapid protrusion and retraction of extensions called pseudopods or ‘false feet’ (Lämmermann & Sixt, 2009)(Petrie & Yamada, 2012). A significant advance in our understanding of cell motility has come with the demonstration that the physical properties of the extracellular matrix, the degree of extracellular proteolysis and specific soluble signaling factors were key parameters to dictate the “choice” of a cell to undergo a given 3D migratory mode (Gupta *et al*, 2016). These observations imply that cells can shift from one to the other modes while encountering in native ECM microenvironments a variety of physical and chemical cues. Among main cues have been identified, the adhesive ligands, the substrate degradability but also the stiffness, viscosity, geometry and porosity (Yamada & Sixt, 2019).

In 2D but also 3D collagen rich environments, cells commonly migrate following the mesenchymal pattern, a pattern which involves the coordinated assembly of multi-molecular adhesion platforms that once mature are defined as focal adhesions. These platforms are organized around pairs of integrins that physically bridge the outside world, i.e. ECM ligands or cell surface-exposed ligands, to the internal cytoskeleton, thereby providing anchorage to the substrate but also enabling traction force transmission to the ECM while they can ideally convey bi-directional signaling (Ridley *et al*, 2003).

In contrast, the different amoeboid motion types which are classified based on the type of protrusions formed at the leading edge are generally characterized by weak adhesions, low traction forces, high contractility as well as marked cell body deformations which can be driven by actin protrusions or hydrostatic membrane blebs (Yamada & Sixt, 2019) (Paluch & Raz, 2013). Using this combination of actions, these cells can go significantly faster as they do not have the same need to disassemble and detach from organized adhesion platforms than cells undergoing crawling. Indeed leukocytes such as neutrophils and monocytes can move respectively at speeds up to 18  $\mu\text{m}/\text{min}$  and  $5 \pm 7 \mu\text{m}/\text{min}$  under microfluidic devices and chemotactism (Butler *et al*, 2010). Although we mentioned the gain in speed of cells using the amoeboid movement style, it is worth noting the case of the wound-healing cells in the fish skin, which are called keratocytes. Keratocytes require polymerization of actin and contraction of actin stress fibers to expand a leading edge and retract the rear, hence they belong more to the mesenchymal type, yet they reach speeds of 10-50  $\mu\text{m}/\text{min}$ . This fast speed feature together with the persistence of their elongated, half moonshape while they move smoothly along a fairly straight track let to describe them as gliders. Interestingly, 3D high-speed video-recording revealed that the stress fibers in keratocytes, which typically surround the cytoplasm and organize perpendicularly

to the migration-direction, thereby connecting the left and right focal adhesions, rotate like a wheel during the peculiar crawling-gliding mode of migration these cells adopt (Okimura *et al*, 2018).

If we now enter the world of protozoan non-swimming motility, we can consider *T. gondii* as one top leader in the class of fast motile cells, which surpass the gliding keratocytes since tachyzoites reach speeds of approximately 3-5  $\mu\text{m/s}$  (Frixione *et al*, 1996). They also preserve their shape during motion and display unidirectional but no persistent migration and indeed belong to the glider descriptive category. In addition the gliding tachyzoite exclusively follows left-handed corkscrew-like tracks in 3D conditions (Leung *et al*, 2014). It is worth noticing that helical gliding is a descriptive trait of several bacteria devoid of propulsive organelles on their surface, that move on substrates covered with only a thin aqueous film. Using this smooth gliding, *Myxococcus Xanthus* bacteria, which reach speeds of 4 to 5  $\mu\text{m/min}$ .

Why would a tachyzoite gain to go faster than almost any cells? Let's mention that the tachyzoite must avoid spending too much time within the ECM where immune cells endowed with high killing capacity, are also navigating. Furthermore, a number of enzymes including proteases, lipases, DNase are released by tissue-resident cells in the surrounding ECM and could thus harm the tachyzoite. In this context, it is expected that the motile skills of the tachyzoite constituted a trait under selection, hence determine to which extent the microbe population expands and locally disseminate prior to be controlled by the immune system.

### **The tachyzoite peculiar motor machinery**

To ensure rapid movement during navigation through tissues, host cell invasion and egress, the tachyzoite relies on the interaction of short actin filaments (F-actin) and the type XIV myosin TgMyoA housed in the parasite pellicle between the PM and IMC. As already mentioned in the Introduction, the composite IMC lies on the alveolin network and the underlying basket of cortical microtubules (Figure 10). The TgMyoA was the founding member of the class XIV non conventional myosins. They are typified by a single head myosin that carries the actin binding motor domain, a neck domain containing ID motifs that interact with light chains but lack the canonical C terminal tail domain, which is usually implicated in interactions with partners that dictate the localization.

The TgMyoA is found tightly associated with the IMC in a hetero-oligomeric complex that was then called glideosome (Opitz & Soldati, 2002). In addition to TgMyoA, a myosin light chain (TgMLC1), two essential light chains (ELC1 and ELC2) and three additional partners, TgGAP40, TgGAP45 and TgGAP50

compose the glideosome (Gaskins *et al*, 2004)(Fréchal *et al*, 2014). A similar complex has also been described in *Plasmodium* (Bosch *et al*, 2006). For net gliding movement to occur, the glideosome must be immobilized within the plane of the IMC membrane, an anchoring provided by the integral membrane GAP50 protein while being assisted by the GAP45 that spans the entire space between the PM and IMC (reviewed in Heintzelman, 2015) (Figure 10).

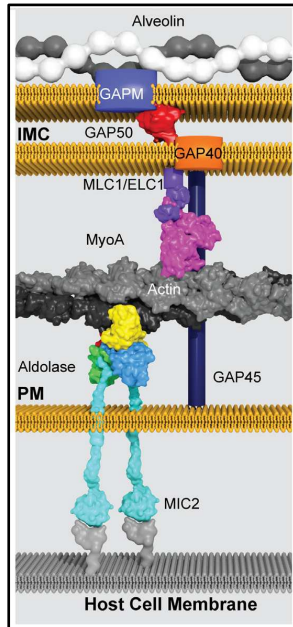


**Figure 10. Schematic representation of the MyoA glideosome.** Starting from the bottom with the host cell membrane (or gliding permissive substrate) to the top with the Alveolin that is connected to the microtubule network. In between the PM and the IMC, the MyoA glideosome is presented with all the identified partners of this machinery. Adapted from Boucher & Bosch, 2015.

In addition, *T. gondii* possesses two orthologs of GAP45; GAP70 interacts with the MyoA glideosome at the apical cap, while GAP80 is located at the basal pole of the parasite along with another myosin motor (MyoC), and IMC-associated protein. Overall, it is tempting to consider three glideosomes machineries organized around three distinct myosins (Figure 11). The myosinH function is restricted at the apical part of the parasite and more specifically in the conoid. Upon initiation of movement and conoid extrusion, the myosinH which is thought to interact with the tubulin fibers of the conoid, takes action until the apical polar ring where it is relayed by the MyoA which connects to the IMC that emerges to the vicinity of the polar ring (Jacot *et al*, 2016).

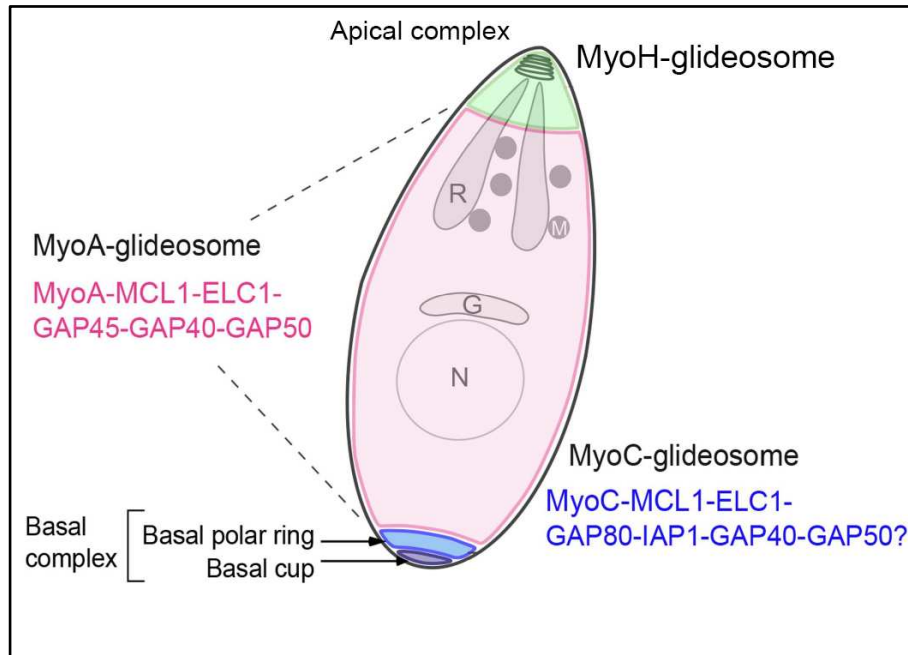


**Figure 11. Schematic representation of the 3 identified *T. gondii* glideosomes.** Starting from the basal complex occupied by the MyoC glideosome, then the MyoA glideosome along most of the body length, and at the apical pole, the MyoH glideosome. Adapted from Fréna1 *et al*, 2014.

The Tg myosins are mechanoenzymes that use the free-energy change associated with the binding and hydrolysis of ATP of its motor domains to generate force and displacement along filamentous actin, as do the dimeric myosins II expressed in most eukaryotes but Apicomplexa. Despite that MyoA belongs to the class of much smaller myosins than myosin II, it is a fast motor, and its kinetics and mechanical properties are close to the fast skeletal muscle myosin. MyosinA has been shown to reach a speed around 3  $\mu\text{m/s}$  *in vitro* on mammalian actin, but interestingly, this speed corresponds to the tachyzoite gliding speed (Herm-Gotz, 2002). Of note TgActin as well as other Apicomplexan actins are also notoriously divergent from canonical actins and have proven to be difficult to visualize *in vivo*. There were indeed until recently no reliable reagents or tools for labeling and visualizing the unconventional apicomplexan actin, whereas long filaments have been visualized in *Theileria* (Kühni-Boghenbor *et al*, 2012). This limitation was thought related to the high monomer:filament ratio and the short length, transient nature and rapid turnover of the filaments (Schmitz *et al*, 2005)(Sahoo *et al*, 2006)(Schmitz *et al*, 2010) but the recent introduction of a chromobody actin in *T. gondii* allowed to ascertain an unexpected F-actin subpopulation in the tachyzoite (Periz *et al*, 2017) as well as in the *Plasmodium* merozoite (Stortz *et al*, 2019). In addition, while F-actin assembly in eukaryotes usually relies on a set of actin nucleating factors, in the case of *T. gondii*, only the formin class is expressed with three members. Actin polymerization is facilitated by the formins,

and specifically formin 1 is essential since can not be compensated by either formin 2 or 3, and appears exclusively dedicated to promote the required elongation of actin filaments during gliding motility. In contrast, formin 2 has been shown to participate in apicoplast division whereas formin 3 was reported to localize to the RB and contribute to a peculiar network of F-actin involved in cell-cell communication (Tosetti *et al*, 2019).

Overall, the glideosomes, at least the glideosome A and H which are better known, are strongly attached to the parasite internal membranes and cytoskeleton(s) and they need to interact with extracellular host cell receptors or adhesive substrates in order to proceed forward for invasion and motility, respectively. The interaction occurs with the help of adhesive proteins named micronemal proteins such as MIC2, and apical membrane antigen 1(AMA1) proteins that are released at the tachyzoite PM upon exocytosis of micronemes. Other MIC proteins are also released with the same way. The bridging between the adhesins and the glideosome is performed by the glideosome-associated connector (GAC), which connects F-actin and MIC2 protein. In order to disengage the adhesion points, cleavage of the adhesins is needed and ensured by the intramembrane serine proteases of the subtilisins and the rhomboid-like proteases in particular ROM4.

Inspired by what has been achieved in the large field of metazoan cell migration but also with the *T. gondii* brother model, namely the *Plasmodium* sporozoite by the team of F. Frischknecht (Münter *et al*, 2009)(Quadt *et al*, 2016), we decided to bring biophysical quantitative approaches with Force Microscopy and Reflection Interference Contrast Microscopy in order to decode the migratory strategy evolved by the tachyzoite to efficiently cope with complex extracellular microenvironments, en route for their hosting cells. As briefly mentioned earlier, the tachyzoite is the developmental motile stage that establishes in the intestinal mucosa and locally disseminates but also reaches intestine-distant tissues to settle into intracellular niches in which it transforms into the persistent bradyzoite stage. While significant advances in the identification of specific glideosomes that drive tachyzoite high-speed helical gliding -in 2D and 3D settings- have been achieved (Frénal *et al*, 2017), two knowledge gaps remain as listed below.

- The mechanisms of force generation and the spatiotemporal coordination of force and adhesion to the substrate that account for successful forward helical propelling,
- The integration of biochemical and biomechanical cues provided by the surrounding extracellular composite material (i.e. ECM) sensed by the free tachyzoite and that control gliding.

In the next section, we will develop in more details than in the publication (see below) the techniques and assays we have introduced in this study.

### **2.1.2 Implementing methods to study the movement of *T. gondii* tachyzoite**

#### **- Reflection Interference Contrast Microscopy (RICM)**

We have already highlighted the crucial need of dynamic interactions between the tachyzoite and the substrate during gliding. Therefore, we decided to accurately quantify the adhesion pattern of a tachyzoite when it undergoes an helical cycle by measuring the distance between the latter and a flat substrate. To this end we applied quantitative Reflection Interference Contrast Microscopy (qRICM).

RICM provides a way to measure the distance between an object and its substrate under water with nanometric precision and milliseconds time resolution. In the beginning, Interference Reflection Microscopy (IRM) was established as a method to study interactions between surfaces by simply using the interference of the light but only from a qualitative point of view. As the optics of surfaces improved, several upgrades in this system made it possible for quantitative measurement of the inter-surface distances using an improved contrast (qRICM). The technique has been used in various scientific fields and it has major applications in live Science since it allows comparing adhesion strength, dynamics and spreading, as well as cell membrane fluctuations, reconstruction of cell membrane conformations and others. A major improvement in the robustness and accuracy of the technique came with the dual wave RICM where two wavelengths are used instead of the single used before to provide accurate measurement of the height between inter-surfaces. The general principle of this technique is that a monochromatic incident ray  $I_0$  (Figure 12) is reflected at the glass surface to obtain the  $I_1$  and it reflects further to reach the surface of the object-cell to give the  $I_2$ . Then using these intensity values, the height ( $h$ ) can be accurately measured if image processing and analysis were carefully performed to reduce the probability of errors. Among main sources of errors are the heterogeneity of the background and the reference intensity or the movement of organelles inside cells. Overall, RICM provides quantification of adhesion patterns and dynamics without the need of labeling the cells. It requires fast imaging but can be combined with other microscopy techniques.

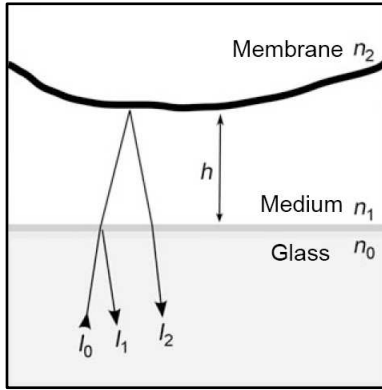


**Figure 12. Representation of light interferences in the case of glass-membrane contact and calculation formula.** A monochromatic incident ray  $I_0$  is first reflected at the glass/medium interface to create the ray  $I_1$ , the transmitted ray is reflected further at the surface of the membrane and gives rise to ray  $I_2$ .  $I_1$  and  $I_2$  interfere and will result the creation of the intensity  $I$ . Adapted from Limozin & Sengupta, 2009.

$$I = I_1 + I_2 + 2\sqrt{I_1 I_2} \cos[2kh(x, y) + \phi]$$

The combination of RICM with Total Internal Reflection Fluorescence (TIRF) microscopy is quite promising since it allows cross-validation of the current models in membrane shape reconstruction and can provide time-lapse recording of the membrane and related proteins during a variety of cell processes. New improvements in the RICM signal have already started to be applied by using anti-reflecting substrates that are easily reproducible in optical properties. One current challenge in the RICM field is its application on the examination of cell functions that occur in a micro and nano resolution scale on non-flat substrates.

RICM was recently coupled to microfluidic devices in order to get insights on the interactions between thick glycocalyx-mimetics and cells/cell-mimetics under flow (Davies *et al*, 2019) (Figure 13). Indeed in addition to distinguish the distance between an object and a surface with nanometer precision, the RICM is sensitive enough to detect in flow assays the arrests of particles interacting with a surface by observation of particle height with respect to the surface, compared to measurement of velocity alone. These achievements are of great interest to better understand how a variety of cells, including leucocytes such as T lymphocytes or neutrophils, but also stem or cancer cells can be “captured” by the endothelial cells before they eventually cross the endothelium. These migrating cells engage thanks to their surface-exposed CD44 molecule a critical interaction with the polysaccharide hyaluronan (HA), a major component of the glycocalix that lines the luminal side and protrudes in the lumen of blood vessels. A combined RICM-microfluidic setting appears particularly well suited for integrating key dynamics and biomechanical features of the HA-enriched glycocalix as the CD44<sup>+</sup> cells are captured and further roll on the surface under flow.

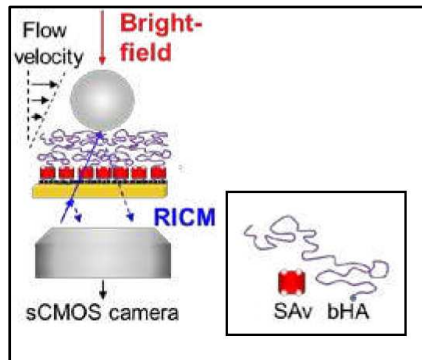


**Figure 13. Coupling RICM with a microfluidic device.** Mounting of the assembled flow chamber - allowing laminar tuneable flow rates- on a multi-modal inverted microscope with RICM capability provides a method to examine bead height with respect to HA films, in addition to velocity under flow. HA chains were grafted through a biotin functionality at their reducing end to the Lipid SA monolayer. Adapted from Davies *et al*, 2019.

### - Traction Force Microscopy (TFM)

While the combination of high-speed videorecording and RICM allowed unveiling a typical apical deformation of the tachyzoite at the onset of the helical cycle, the next challenge was to get insights on the location and amplitude of forces that are applied by the parasite during helical movement, and to thus verify whether traction forces could be generated at the site of adhesion. Traction Force Microscopy (TFM) had never been used for analyzing forces during *T. gondii* movement but has been in contrast successfully developed and applied to the slender *Plasmodium* sporozoite in the course of circular gliding (Münter *et al*, 2009).

Cellular traction was first demonstrated using compliant silicon-rubber substrate, on which adherent non-muscle cells could produce wrinkling patterns. Quantitative techniques were then developed, based on the principle that traction forces can be extrapolated from substrate deformations and they commonly use polyacrylamide (PAA) elastic gels and micropillars. The one using PAA gels is conventionally called Traction Force Microscopy (TFM). TFM requires fluorescent beads that are evenly embedded into the PAA gel (Figure 14) to be used as fiduciary markers whereas cells of interest are plated on top of the gel and both the beads and the cells are recorded overtime. In the end of the assay, exposing the cells to the enzymatic activity of trypsin will give the opportunity to obtain the relaxed position of the beads when the cells are no longer attached and these bead positions serve for force calibration. Knowing the relaxed position of the beads and tracking the beads overtime allows producing a displacement map for the substrate, which is then used to solve the ‘inverse’ problem using the Boussinesq’s formulation: an equation for the displacement data in infinite half-space is derived into a convolution integral using Green’s tensor, discretized and then inverted to determine traction forces (Gupta *et al*, 2016) (Figure 14). Critically, the substrate stiffness value and stability are essential parameters to allow proper calculations (Martiel *et al*, 2015).

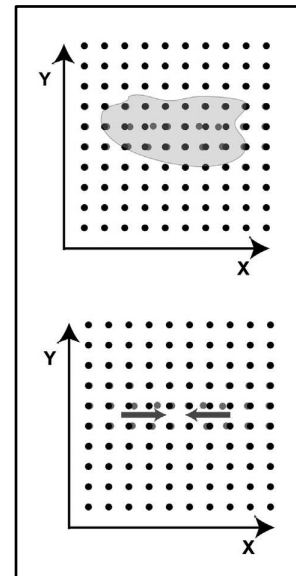
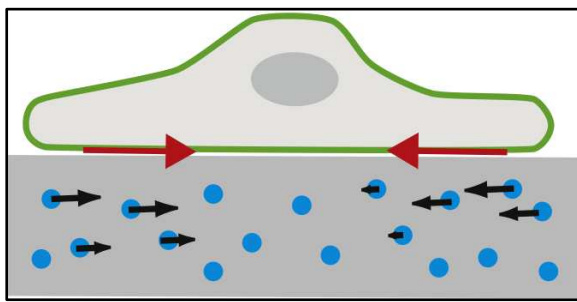


**Figure 14. Schematic representation of cell lying on top of PAA gel embedded with beads and displacement-force calculation approach.** Left panel: A cell creates focal adhesions and pulls the substrate in x-y direction. Right panel: Calculation of the beads displacement overtime ( $t_0$ =black color,  $t_1$ =grey color). Knowing the displacement, force value can be also computed. In this approach it is considered that the beads displacement in the z direction is zero or close to zero. Left panel adapted from Schwarz & Soiné, 2015. Right panel adapted from Martiel *et al*, 2015.

Challenges and parameters to optimize for *T. gondii* motility:

- PAA gels coated with fibronectin
  - Concentration of fibronectin
    - Trying two extreme conditions where we put much higher concentration of fibronectin than the one that is commonly used, didn't affect the gliding proprieties.
  - Stiffness of PAA gel
    - Starting with 5 kPa Young's modulus stiffness PAA gels coated with fibronectin, parasites could nicely glide in these conditions but although beads displacement could be observed, it was not enough convincing, as the displacement length was very small. Testing different stiffness we found out that 2 kPa was enough to have gliding and bead displacement. The problem was that reducing the stiffness, parasite motility percentage and travel distance length were both decreased.
  - TFM bead size and concentration
    - The concentration of beads used during the preparation of the PAA gels (0.4  $\mu$ l / 164  $\mu$ l of PAA), was not good enough to have separate beads that could cover all the area underneath the parasite while it was moving. Increasing

this to approximately 0.8  $\mu\text{l}$  / 164  $\mu\text{l}$  of PAA, we managed to have ideal conditions of bead displacement without lots of aggregates and overlapping of beads. One other suggestion that we had, was to use two different color beads in order to cover the gaps but because we used streaming option for recording (see after), we could not use more than two channels overall (we need brightfield and one fluorescence).

- Microscopy
  - Recording timing
    - Fast recording – less quality
      - 1 frame/second was not good enough to catch the displacement of the beads for longer time. For this reason, we utilize the streaming option of the microscope with the help of the management software MetaMorph in order to record at around 6 frames/second. Limitation of this was that you decrease the exposure time and the number of lasers that you can use during the acquisition.
    - Streaming option-only two laser channels
  - No focus outside of the beads height (for example for cytoskeleton proteins as researchers use with mammalian cells, they can observe proteins' behavior at the same time with the forces dynamics).

By performing control experiments, we found out that reducing the stiffness significantly affects the tachyzoite motile behavior which translated in a decreased number of moving parasites for a given time and in the same line, a reduction in the duration of the gliding behavior. Increasing the concentration of TFM beads inside the gel two times more than the initial one and performing a well-controlled sonication step to avoid aggregates of beads, have helped in increasing the probability of having a visible bead displacement event. The more uniform distribution of single (not clustered) beads provides the most accurate detection bead displacement by the software during image analysis.

The next level of TFM approaches is to implement the  $z$  dimension in order to have a more physiologically relevance with the *in vivo* situation. Some of them (Legant *et al*, 2010) have been described but the limitations of a closely related to the *in vivo* substrate is still missing. This is because the extracellular matrices are a mix of different proteins that complicates the establishment of a “real” elastic substrate with a stable relaxed position. To counteract this problem, hydrogels which provide uniform and complete crosslinked networks have been used. Although collagen (fibrillar) and matrigel gels work very nicely, it is impossible to get stable stiffness value overtime, thus you cannot get force estimation.

## - PRIMO micropatterning

Micropatterning techniques are widely used in the field of cell biology and mechanobiology in order to interrogate for example how cells interact with each other or, how tissue-like layers behave, how cells attach to a given substrate and develop stress fibers, how these forces act during cell division or cell migration, or phagocytosis (Senger *et al*, 2019). At the subcellular level, these approaches have been applied to investigate how organelles or proteins deal with the micropattern-driven constraint. In some cases, high precision in the designing process is needed like in this study since we wanted to create a pattern where there is a clear separation of the fibronectin coated area (gliding area) and the PEG area (non gliding area). When we tried to make micropatterns manually (without the use of PRIMO) we found out that there were always a few pieces of fibronectin around the main design, therefore in a area supposed to remain non adherent (Figure 15).

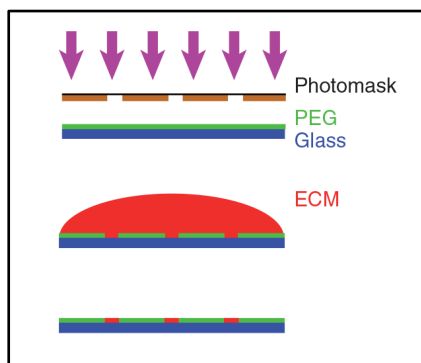


**Figure 15. Schematic representation of the micropatterning principle.** UV light exposure to PEG coated glass coverslip, through a photomask with the specific pattern. Patterns will be created in the PEG layer and then ECM (fibronectin in our case) protein will cover the patterns space. Making these patterns by hands, we saw that some protein (red in last step) stays next to the pattern position and it is not visible enough to know the exact fibronectin region of the pattern. Adapted from Thery, 2010.

This could not ensure the clear separation of the two substrates, which was something very crucial for our experiment knowing that the size of the parasite is 5-7  $\mu\text{m}$ . Therefore, we worked with the Alveole company ([www.alveolelab.com](http://www.alveolelab.com)) that has been able to design using the PRIMO device (Figure 16) the design we chose with a high precision. The design we needed includes a sharp demarcation between permissive (fibronectin) and non permissive (PEG) gliding substrates so we could examine how the tachyzoite behaves when the apical part of the parasite body was “touching” the non permissive area while the posterior part was “touching” the permissive fibronectin area.

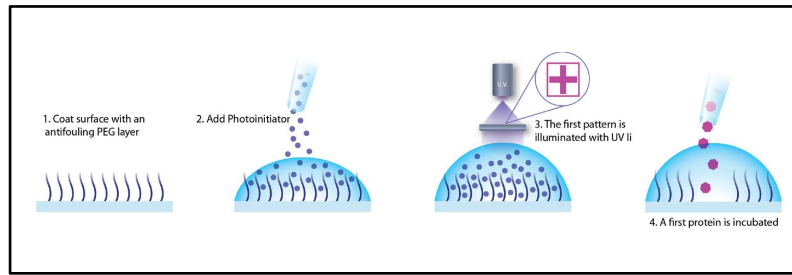


**Figure 16. Schematic representation of the micropatterning principle using PRIMO.** Solution of PLL-g-PEG is deposited on an air-plasma-activated glass coverslip. After rinsing, photoinitiator is added and UV light is projected onto the surface through a pattern mask. The UV activated photoinitiator molecules locally cleave the PEG chains. Then the substrate becomes adhesive and at the last step, we have the protein coating. Adapted from Strale *et al*, 2016.

In addition, micropatterning can be combined with other techniques such as Traction Force Microscopy and Atomic Force Microscopy where researchers are interested in the forces that are applied by a single cell, few cells or even whole tissues.

**- Nano/microtools to design innovative assays: Immobilizing the parasite on a substrate by forcing adhesion of the posterior pole**

Once cellular forces have been mapped during motion, the logical next step is to attempt to locally interfere with the force application in order to bring definitive conclusions on how these forces control the movement under study. To this end, we have used the permissive-non permissive micropattern as explained above to interfere with tachyzoite front adhesion with the substrate. However, we also wanted to see the outcome of mechanically holding the parasite, the time that it was ready to move. Immobilizing posteriorly the tachyzoite but keeping it alive and potentially active was the main goal of this experiment. To this end we incubated the parasite with sub-micrometer beads under conditions that would statistically allow some parasites to be tightly bound to the bead at their posterior while the bead itself would be trapped in interaction with the substrate made of fibronectin layer. As the result the parasite would be indirectly but firmly attached to the substrate so a “normal” front traction force would remain inefficient at disengaging the posterior pole from the adhesion with the substrate.

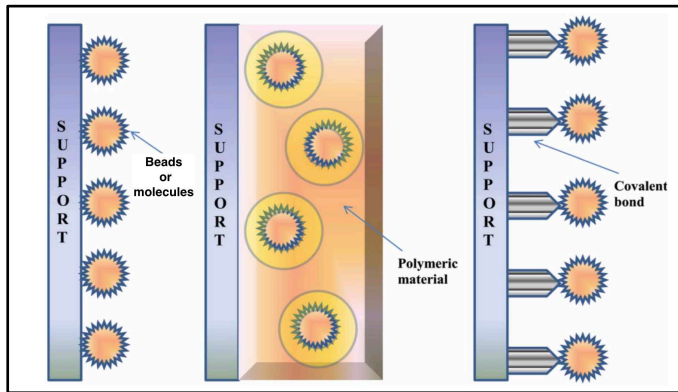


**Figure 17. Schematic of immobilization techniques.** From left to right: physical adsorption, entrapment and covalent attachment. Adapted from Mohamad *et al*, 2015.

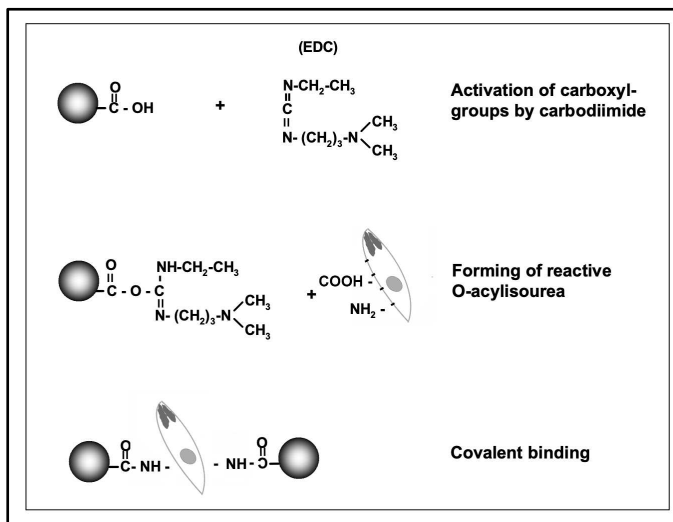


**Figure 18. Schematic representation of beads activation with EDC.** Activation of the carboxyl groups by EDC which then forms reactive O-acylisourea to account for covalent binding between the beads and the *T. gondii* membrane proteins.

There are different techniques of molecule immobilization (Figure 17) such as (i) physical adsorption (ii) embedding inside gels or (ii) covalently binding. We chose commercially available carboxylated beads that were subsequently activated using the manufacturer protocol to promote covalent binding of the beads surface to the parasite surface-exposed proteins (Figure 18). Activation of the carboxyl groups on the beads surface was achieved with water-soluble 1-ethyl-3-[3-dimethylaminopropyl] carbodiimide (EDC) and led to the formation of an active intermediate (O-acylisourea). The latter quickly reacted with primary amines (nucleophile) to form a stable amide bond. Given that tachyzoite PM is covered by large amount of glycoproteins and proteins, it was expected that by chemically activating beads, the latter would engage covalent interaction with the amine of the surface-exposed tachyzoite molecules. At the same time, we hoped that because active parasites would theoretically engage the surface-bound bead in an antero-posterior capping process, the beads would end at the posterior pole and there engage new interactions with the fibronectin substrate. As the result, we expected that the parasite would be trapped by the posteriorly positioned beads and incapable of disengaging from the substrate. To succeed in setting the optimal experimental protocol, we had to readjust the protocol by reducing the Fetal Calf Serum (FCS) concentration since this parameter was crucial to lower the probability the parasite manages to escape from the posteriorly capped beads.

### 2.1.3 Main highlights of the study

Combining these approaches, we were able to explore the mechanisms of force generation required for successful forward helical propelling of the tachyzoite. While the results of a serie of assays are presented in the published article below, the main highlights are summarized as follows:

- The tachyzoite establishes an apical strong adhesion with the substrate.
- The tachyzoite applies traction forces accounting for kink formation while the kink release coincides with maximal forward helical acceleration.
- Apical and posterior attachment-detachment need to be coordinated for successful engagement of the traction forces.
- Microtubule bending during the kink should account for energy storage upon loading by the traction force.

### 2.1.4 Publications

Pavlou G, Touquet B, Vigetti L, Renesto P, Bougdour A, Debarre D, Balland M and Tardieux I. (2020) Coupling Polar Adhesion with Traction, Spring, and Torque Forces Allows High-Speed Helical Migration of the Protozoan Parasite *Toxoplasma*. *ACS Nano* acsnano.0c01893. <https://pubs.acs.org/doi/10.1021/acsnano.0c01893>

# Coupling Polar Adhesion with Traction, Spring, and Torque Forces Allows High-Speed Helical Migration of the Protozoan Parasite *Toxoplasma*

Georgios Pavlou, Bastien Touquet, Luis Vigetti, Patricia Renesto, Alexandre Bougdour, Delphine Debarre, Martial Balland, and Isabelle Tardieux\*

Cite This: <https://dx.doi.org/10.1021/acsnano.0c01893>

Read Online

ACCESS |

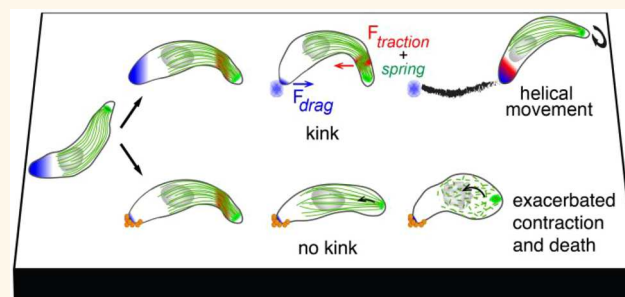
Metrics & More

Article Recommendations

Supporting Information

**ABSTRACT:** Among the eukaryotic cells that navigate through fully developed metazoan tissues, protozoans from the Apicomplexa phylum have evolved motile developmental stages that move much faster than the fastest crawling cells owing to a peculiar substrate-dependent type of motility, known as gliding. Best-studied models are the *Plasmodium* sporozoite and the *Toxoplasma* tachyzoite polarized cells for which motility is vital to achieve their developmental programs in the metazoan hosts. The gliding machinery is shared between the two parasites and is largely characterized. Localized beneath the cell surface, it includes actin filaments, unconventional myosin motors housed within a multimember glideosome unit, and apically secreted transmembrane adhesins. In contrast, less is known about the force mechanisms powering cell movement. Pioneered biophysical studies on the sporozoite and phenotypic analysis of tachyzoite actin-related mutants have added complexity to the general view that force production for parasite forward movement directly results from the myosin-driven rearward motion of the actin-coupled adhesion sites. Here, we have interrogated how forces and substrate adhesion–de-adhesion cycles operate and coordinate to allow the typical left-handed helical gliding mode of the tachyzoite. By combining quantitative traction force and reflection interference microscopy with micropatterning and expansion microscopy, we unveil at the millisecond and nanometer scales the integration of a critical apical anchoring adhesion with specific traction and spring-like forces. We propose that the acto-myosin motor directs the traction force which allows transient energy storage by the microtubule cytoskeleton and therefore sets the thrust force required for *T. gondii* tachyzoite vital helical gliding capacity.

**KEYWORDS:** cell migration, cell focal contact, 3D collagen, *Toxoplasma*, traction force microscopy, reflection interference contrast microscopy, expansion microscopy



Across eukaryotic phyla, cell migration is an evolutionary conserved function which appears vital for both free living protozoans and metazoans.<sup>1</sup> In metazoans, cells such as fibroblasts and leukocytes use a wide spectrum of adhesion-dependent motility modes conjointly defined as crawling and primarily driven by the dynamics of the cell actin–myosin cytoskeleton.<sup>2,3</sup> These cells crawl with the help of dynamic actin-powered membrane protrusions that fold at the leading edge as a flat lamellipodium or as a variety of pseudopodia-like membrane projections. Firmly attached to the substrate upon coordinated assembly of integrin-driven adhesive platforms, the lamellipodium is a hallmark of the mesenchymal cell migration mode in 2D and 3D micro-

environments. These anchoring multimolecular platforms allow the development of actomyosin bundles that tune contractile forces between the front and trailing margins and eventually lead to the release of trailing adhesions, hence allowing cell forward translocation.<sup>4,5</sup> Likewise, metazoan cells—as well as large free-living protozoans—can display a

Received: March 4, 2020

Accepted: May 20, 2020

Published: May 20, 2020

more versatile motility mode and cope with heterogeneous 3D microenvironments. In addition to the lamellipodium style, they can adopt diversified pseudopodia mechanisms that, combined with a range of relative cell-matrix adhesion and actomyosin contractility, account for the rapid amoeboid type of motility ( $\sim 10$  to  $20 \mu\text{m}/\text{min}$  versus less than  $1 \mu\text{m}/\text{min}$  for the lamellipodia mode).<sup>6</sup> Alternatively, fibroblasts can utilize an amoeboid–mesenchymal hybrid type of 3D migration called lobopodial during which a pressure-driven bleb-like membrane protrusion stems at the leading margin from the piston-like forward movement of the nucleus itself driven by the cortical actomyosin contractility.<sup>7</sup> Biophysical studies have proved instrumental in mapping and measuring the development of forces in cells, and they brought insights on how cells differentially regulate the adhesion–contractile balance to spatiotemporally control the adhesion assembly/deassembly cycle and achieve productive forward movement in different contexts.<sup>8</sup>

Intriguingly, unicellular eukaryotic parasites from the ancient phylum of Apicomplexa have evolved an adhesion- and actin-dependent motility mode that differs from the mesenchymal, amoeboid, lobopodial repertoire and enables the microbes to glide within host tissues and across barriers to follow their complex stepwise developmental program. The several thousand members of the Apicomplexa phylum include among the world's most pre-eminent mammal-invasive protozoan parasites. In humans, *Plasmodium* spp. are inoculated in the vascularized dermis extracellular matrix (ECM) by a blood-feeding mosquito which hosts parasites in salivary glands. *Plasmodium* displays a prolonged asexual developmental phase in red blood cells, which results in a range of clinical outcomes known as malaria, impacting human populations in tropical and subtropical regions of the Earth. Its relative *Toxoplasma gondii* is present in a large assortment of endotherm metazoans worldwide. Being ingested with contaminated food and water, *T. gondii* is hosted quasi-silently by possibly up to a third of the human population in tissues such as the brain, retina, and heart and skeletal muscles. However, in case of immune dysfunction, *T. gondii* can re-emerge from these tissues and proliferate, causing life-threatening or debilitating complications.<sup>9</sup>

Throughout their life cycle in their respective hosts, both *Plasmodium* and *T. gondii* ensure their perpetuation by undergoing multiple cell differentiation events that give rise to specific developmental stages with sizes of several microns, harboring a crescent shape and endowed with high motility skills.<sup>10</sup> Best studied are the *Plasmodium* slender mature sporozoite inoculated in the host skin and the *T. gondii* bulky highly replicative tachyzoite stages that glide 10 times faster than the amoeboid cells without folding any of the crawling-associated protrusions.<sup>10–12</sup> Instead, they share a robust longitudinal apico-basal polarity which persists during the generally unidirectional motile activity with the apex leading.<sup>13</sup> Whereas the *Plasmodium* sporozoite moves on a circular path in either counterclockwise (CCW) or clockwise (CW) directions with an irregular stop and go kinetics,<sup>13</sup> it can also occasionally adopt a random motion or a corkscrew-like pattern *in vivo*.<sup>14,15</sup> Instead a left-handed helix characterizes the path the mosquito-restricted ookinete *Plasmodium* stage used to move in Matrigel-based 3D matrices.<sup>16</sup> The *Toxoplasma* tachyzoite can similarly glide CCW on a circular path under 2D *in vitro* settings but often uses a CCW helical trajectory or a succession of the two mechanisms over the same gliding

sequence.<sup>11,17</sup> Another intermittent 2D movement termed twirling accounts for the stationary CW rotation executed by the upright-positioned tachyzoite around its posterior end.<sup>18</sup> The corkscrew-like mode of gliding, which is the obligate mechanism in 3D reconstituted or *in vivo* environments was proposed to relate to the 2D helical mode of gliding.<sup>19</sup> The latter typically starts with a CW short motion, follows with a  $180^\circ$  twist; meanwhile, the body flattens on the substrate before twisting up and flipping on the side, which allows starting another helical cycle.<sup>11,18</sup>

To initiate and sustain all types of gliding activity, both the sporozoite and tachyzoite rely on the regulated secretion of adhesive protein oligomers at the cell surface<sup>20,21</sup> that, once delivered at the apical tip, can coengage with ECM proteins and short cortical actin filaments organized beneath the plasma membrane. Force production driving parasite movement has long been considered to directly translate from the apico-basal translocation of the ECM-bound adhesins coupled to the flowing actin filaments and their enzymatic-mediated release of these adhesins at the trailing edge.<sup>22,23</sup> It is the Apicomplexa specific, fast, nonprocessive, single-headed motor myosin A (MyoA) that was assigned an essential powering role in pulling backward the apically initiated actin filaments and the captured adhesins.<sup>24,25</sup> Upstream from MyoA however, the *T. gondii* tachyzoite additionally requires myosin H (MyoH) to propel actin filaments from the parasite apical tip formed by the conoid,<sup>26</sup> a retractile appendage missing in *Plasmodium*. Both MyoA and MyoH molecules function within a multisubunit complex identified as glideosome<sup>22</sup> that also comprises several regulatory subunits and scaffolding partners.<sup>27–29</sup> Specifically for MyoA, the glideosome associated proteins (GAPs) anchor the motor machinery to the plasma membrane and the lining internal bilayered membrane complex (IMC) which underside is tethered to a cytoplasmic array of cortical microtubules (cMTs), the number and arrangement of which typify each Apicomplexa species and developmental stage.<sup>27,30</sup>

However, the recent introduction of force microscopy, reflection interference contrast microscopy (RICM) and optical tweezers in conjunction with molecular genetics in the *Plasmodium* field has added more complexity to the prevalent force production model.<sup>31</sup> A key observation is the discrepancy between the speed of the retrograde flow of optically trapped microbeads on the apical surface of the sporozoite and the speed achieved during typical circular gliding, the former being up to 50% faster than the latter.<sup>31</sup> In addition, several distinct areas of contact between the moving sporozoite and the substrate were uncovered at the apex, base, and center over the circular path and were shown to display specific on–off dynamics,<sup>13</sup> whereas the genetic loss of a surface-exposed adhesin reported to function during motility was found to trigger a speed increase in the retrograde flow and a concomitant decrease in force production.<sup>31</sup> Collectively, these studies bring compelling evidence for the assembly of distinct force-generating adhesive structures which differentially control production of the force required for migration.

By contrast, how forces and dynamic adhesions coordinate in space and time and integrate with the impressive high-speed helical path that features the *T. gondii* tachyzoite gliding mechanism has been much less investigated. Intriguingly, the rearward capping of nanobeads bound to the tachyzoite surface was shown not to require an intact actomyosin system but rather a polarized secretory–endocytic cycle that would locally drive membrane tension.<sup>32</sup> On the other hand, qualitative

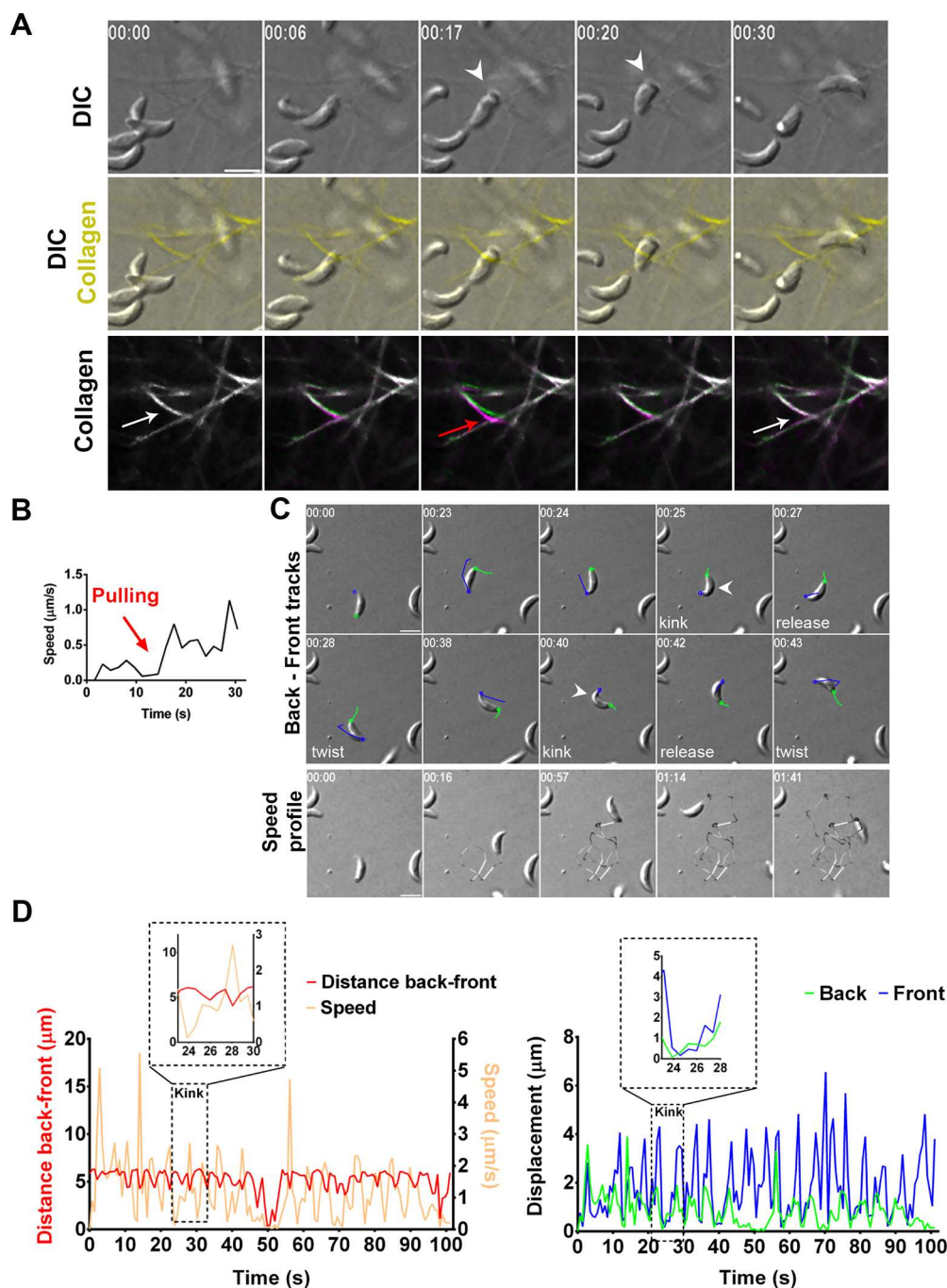


**Figure 1.** Tachyzoite pulls on the collagen fibers prior to helical acceleration. (A) Successive images from a time lapse of a tachyzoite navigating within a 3D-meshwork of rat collagen1 fibers pre-labeled with the CNA35-GFP collagen chimeric probe. Panels show images of (top) DIC, (middle) DIC-GFP over, giving yellow-colored fibers, (bottom) the fiber initial ( $t_0$ , green) and over time ( $t_x$ , magenta) positions when encountered by the moving tachyzoite. The overimposition of the green and magenta signals comes as white (white arrows) when the fiber maintains the  $t_0$  position, whereas the separation between the green ( $t_0$ ) and magenta ( $t_x$ ) signals attests two distinct positions overtime. The backward displacement indicates the parasite pulls on the fiber (red arrow), whereas the graph (B) documents that this pulling coincides with the parasite low speed. Next the acceleration step coincides with the merge back of the green and magenta signals that signs for the release of fiber tension post motion. (C) Successive DIC images from a time lapse of a tachyzoite undergoing helical gliding on fibronectin-coated glass. (Top) back (green) and front (blue) tracks over three last frames ( $t_{x-2}$  to  $t_x$ ) are shown, (bottom) speed profile is shown from black to white scaling with increasing speeds. All white arrowheads point to the kink, all scale bars:  $5 \mu\text{m}$ , time is in minutes/seconds. (D) Graph (left) plots the tachyzoite back–front distance (red line) and the speed based on the back tracking (light orange); note that the value close to zero corresponds to the time the tachyzoite twirls, hence the apex is out of focus and the back–front distance not measurable (right) the  $xy$  displacement for both the back (green) and front (blue) sites over the helical sequence. Zoomed of a typical kink step for both graphs shown as inlays.

RICM allowed identifying an early tachyzoite contact with the substrate at the cell front and its rearward translocation which

was assumed to directly power the force-producing parasite movement.<sup>33</sup> In this study, we revisited the mechanisms

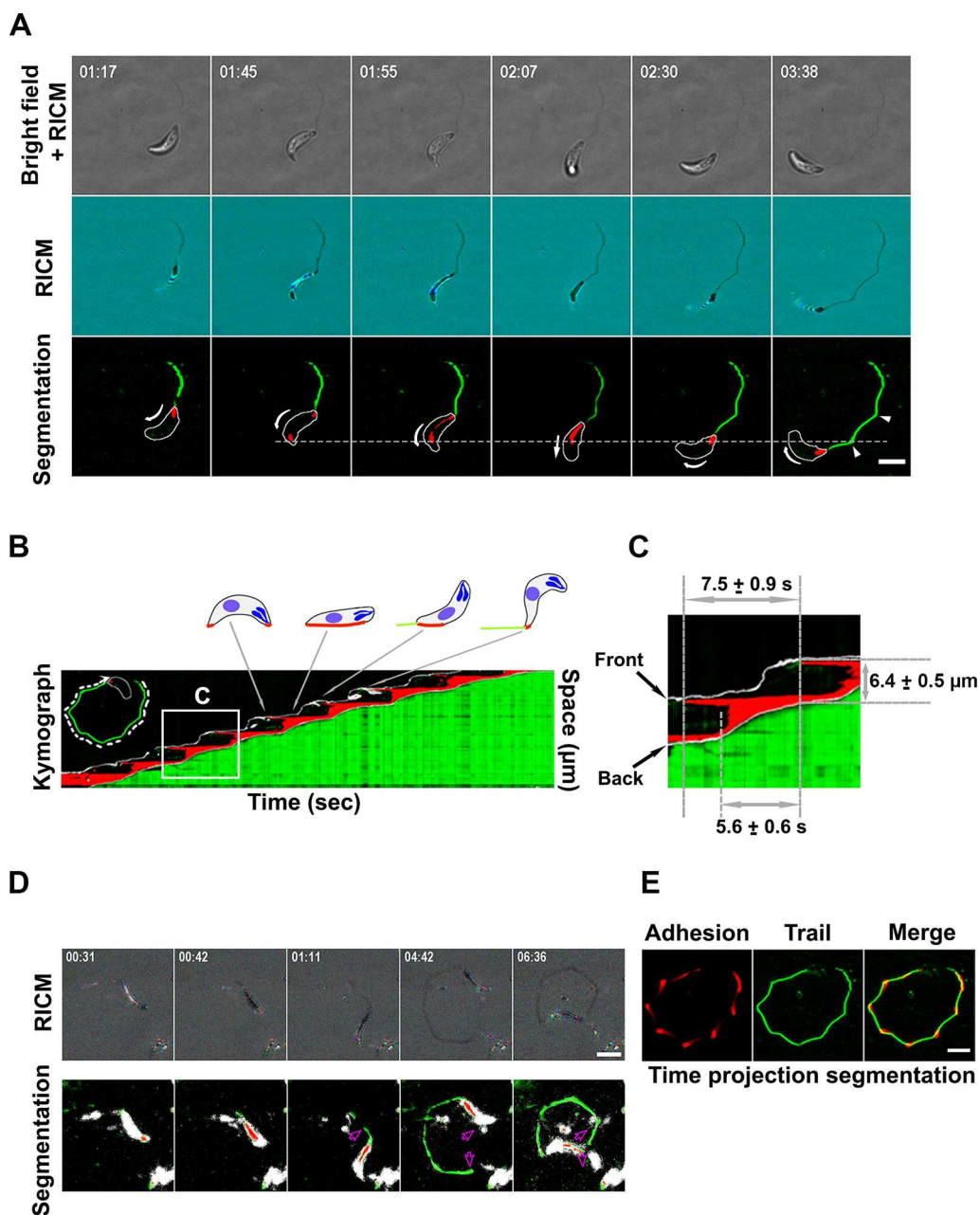


**Figure 2.** Helical cycle starts with an apical site of adhesion that constraints sliding of both the parasite and the parasite posteriorly shed trail. (A) Successive RICM images from a time lapse of a tachyzoite undergoing helical motion on a glass coverslip. Panels show (top) simultaneous bright-field (BF) and RICM images, (middle) blue and green RICM images superimposed and displayed as RGB, (bottom) segmentation of BF and RICM images showing the parasite outline (white), areas of close contact between the glass and the moving parasite (red), and material shed behind as trail (green). White arrows indicate the direction of the parasite movement. The dotted line marks the position of the initial contact over one helical cycle and delineates the trajectory angular point. (B,C) Kymograph of the whole gliding sequence from (A) and for a single zoomed helical cycle (C) shows the evolution of the close contact area along the trajectory over time. (D) Successive three-color RICM images (shown as RGB) from a time lapse of a tachyzoite undergoing helical motion on a poly-L-lysine-coated glass coverslip (top) and corresponding segmentation with the Weka FIJI plugin (bottom). The pink arrows indicate that over time the tachyzoite pulls on the trail that slides without breaking but follows the polygonal trajectory imposed by the initial anchoring sites. (E) Time projection of the segmented close contact areas over the gliding sequence on which (left) the longest-lived attachment points are brightest, (middle) the trails are green, and (right) adhesion and trails are overimposed. Note that angles in the polygonal path coincide with both the long-lived close contacts and the kinks. All scale bars: 5  $\mu\text{m}$ ; time is in minutes/seconds.

underpinning the helical gliding of *T. gondii* by combining quantitative live imaging with traction force microscopy, quantitative RICM, micropatterning and expansion microscopy. We provided evidence for a spatiotemporal coordination of an actoMyoA-based traction force produced at a stable apical adhesion site and a spring-like force which, driven by the

left-handed cMT spiral orientation, directs straightening and helical propelling of the *T. gondii* tachyzoite.

## RESULTS/DISCUSSION

### Tachyzoite Pulls on the Collagen Fibers in a 3D Meshwork Prior to Accelerating with a Helical Motion.

Pioneering work on *T. gondii* 3D *in vitro* motility has relied on Matrigel-based matrices under rather elastic and homogeneous conditions.<sup>19</sup> However, *in vivo*, most ECM microenvironments are enriched in a nonlinear, anisotropic, and dynamic fibril-rich meshwork. Because collagens are dominant ECM components that form multiscale fibrils withstanding tensile forces,<sup>34</sup> we analyzed how the *T. gondii* tachyzoite moves within a confined collagen fibril-based matrix. Whereas the tachyzoite squeezed its body to pass through the meshwork, it first paused and bent, showing an apical deviation as it next accelerated, possibly with a rotation around its main axis, to escape from the collagen fibrils (Figure 1A,B and Supporting Information Figure S1, Movie 1, and Movie 2). Using a fluorescent probe selectively associated with collagen fibrils,<sup>35</sup> we applied a temporal color-code (green and magenta) and identified fibers encountered by the motile tachyzoite that shifted backward before returning to initial position as the parasite propelled forward (Figure 1A, Supporting Information Movie 1). This fiber backward displacement was seen in all cases of moving tachyzoites encountering a fiber ( $n = 10$ ), and qualitatively indicated that the parasite exerted pulling forces on the surrounding fibers.

To get more mechanistic insights on the front-rear spatiotemporal coordination over the helical gliding cycle, we further analyzed the changes in the tachyzoite shape with high spatiotemporal acuity using a 2D setting. We observed a yet undefined apical inward bending immediately post the initial clockwise arc motion and concomitant with the parasite pause (Figure 1C). Indeed, tracking the front and back revealed a shortening of the parasite that coincided with an apical flexure and thus an increased curvature, resembling the observation made within the fibrous 3D matrix, and which we defined as the kink step. Associating with the apical pole arrest we detected the contraction of the cell body and retraction of the posterior pole. Next the apex re-extended and lifted up, a phase defined as the kink release, while the tachyzoite straightened and slid to further twisted in the typical CCW motion (Figure 1C, Supporting Information Movie 3a and Movie 3b, slow motion). Accordingly, not only the instantaneous speed was about null during the kink step and reached maximal value as the latter relaxed back (Figure 1D), resulting in the characteristic periodic speed fluctuations documented under 3D conditions.<sup>19</sup> No such pattern was detected when the parasite performed the 2D-restricted CCW circular trajectory (Supporting Information Figure S1B,C and Movie 4). Of note, high temporal resolution live imaging of *Plasmodium* sporozoites also reveals alternating periods of rapid movement in which they travel up to one body length and periods of slow movement in which they more firmly adhere to the substrate, thereby indicating that distinct adhesion types operate during motility.<sup>13</sup> Although such kinetics was associated with the sporozoite body stretching upon firm adhesion of its polar and center regions to the substrate and the subsequent thrust in speed,<sup>13</sup> no peculiar apical deformation that could resemble a kink has been observed to initiate movement. We proposed that the kink deformation and the subsequent body extension might reflect the tension built in the tachyzoite cytoskeleton to achieve the thrust force required for the helical twisting motion.

**Apical Focal Adhesion Behaves as a Firm Long-Lived Anchor That Constrains Sliding of the Parasite Body.** Because the apical kink suggests the assembly of a specific contact between the parasite front and the substrate, which

would be appropriate for building up tension in the *T. gondii* cytoskeleton, we first used qRICM to monitor the parasite-substrate distance. In contrast to a recent study,<sup>33</sup> we used high-speed (30 frames/s), multicolor RICM with simultaneous transmitted-light imaging coupled with machine-learning-based image processing to achieve a precise segmentation of close contact regions between the parasite and the substrate at high temporal resolution (33 ms) over thousands of frames (Figure 2 and Supporting Information Movie 5 and Movie 6). In addition to the low-distance patches detected between the parasite basal pole and the substrate even in absence of movement, we found that at the onset of a helical cycle, the membrane of the tachyzoite apex came in contact with the glass surface. Because these RICM-detected signals coexisted with motion, we assumed they accounted for two polar parasite-substrate adhesive areas in agreement with Tosetti and collaborators<sup>33</sup> and similarly to what was found for the *Plasmodium* sporozoite.<sup>13</sup> Crucially, the apical contact remained static over the full length of the helical cycle ( $7.5 \pm 0.9$  s), and the posterior contact progressively expanded to account for  $\sim 80\%$  of the tachyzoite length along its major axis (Figure 2A–C, see kymographs, Supporting Information Movie 5). Upon release of the kink, the parasite propelled forward and shifted orientation before it started a new front attachment. For each helical cycle, the kink step could be *a posteriori* inferred through the mix of parasite-derived membrane hydrophobic droplets and surface-exposed proteins/glycoproteins left as a complex trail behind the cell edge onto the substrate, a common feature of Apicomplexa motile stages (Figure 2A,D,E).<sup>11,36</sup> Quantitative modeling of the RICM signal provides transverse dimensions for these trails of  $\sim 70$  nm (isotropic) or 100 nm (width) and 40–60 nm (height). By comonitoring the parasite helical motion and the trail assembly in real time, we were able to uncover that the tachyzoite not only slid on the adhesive tracks it built itself but could also pull these, an observation that has not been reported for the RICM data collected on *Plasmodium*.<sup>13</sup> These observations suggest a continuous nature of the shed material that remained close but not firmly fixed on the substrate (Figure 2D and Supporting Information Movie 6), which would agree with membrane components including lipids as previously deduced from the analysis of fixed samples.<sup>11</sup> Importantly, the sliding trajectories of the shed material once pulled by the moving tachyzoite appeared constraint by the periodically distributed firm anchors, which could occasionally be stripped off from the substrate (Supporting Information Movie 6). In further support of these periodic stable anchors, the time projection of the trail trajectory postimage segmentation allowed positioning the longest-lived parasite-substrate contacts at each angular point of the trajectory, matching the initial apical anchoring sites (Figure 2E). The relative homogeneity in the trail observed at our RICM resolution cannot inform on a specific distribution or arrangement in proteins and lipids upon specific secretory events or/and due to local physical constraints that would compose the periodic anchors. The microneme-stored MIC2 is seen as the adhesion prototype that bridges the parasite motor system and ECM ligands during motility. Indeed partial or full silencing of the *mic2* expression significantly impairs both the helical and twirling motions.<sup>37,38</sup> This double default argues more for a MIC2 contribution to the posterior adhesion force,<sup>37</sup> hence *mic2* KO parasites show a reduced capacity to bind to host cells and collagen-coated surfaces.<sup>38</sup> Consistently,

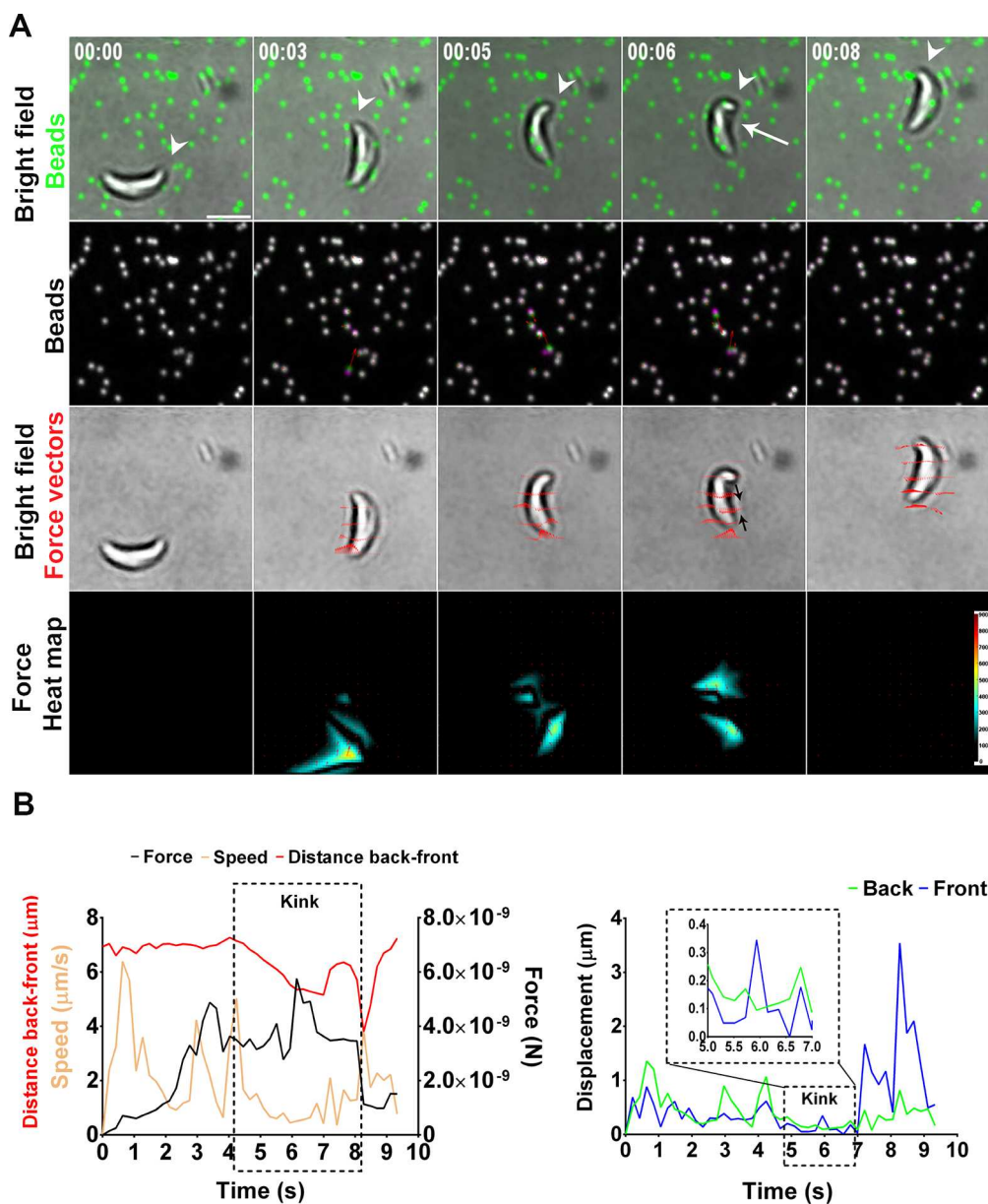


**Figure 3.** Helical motion includes the development of apical traction at the kink site and basal dragging forces. (A) Traction force microscopy (TFM) images were taken at the time a parasite glides on a 2 kPa PAA gel in which fluorescent TFM beads are embedded underneath the gel surface itself coated with fibronectin (20  $\mu\text{g}/\text{mL}$ ). Panels show (top) bright-field (BF) and TFM beads composite images; white arrowheads indicate the apex of the tachyzoite, and white arrow marks the kink, (second row) BF with force vectors computed by the MATLAB TFM code. Red arrows indicate the force direction and value; black arrows have been manually added to ease visualization of the two longitudinal forces and their orientation, (bottom) force heat map computed MATLAB TFM code. Scale bar: 5  $\mu\text{m}$ , time is in minutes/seconds; au for force heat map. (B) (Left) Speed (light orange line), the back to front body distance (red line) and the traction force applied by the parasite over time (black line) are shown with a zoomed inlay (black dotted line) at the kink step time, and (right) the back and front displacement (green and blue trajectories, respectively) are shown with a zoomed inlay (black dotted line) at the kink time.

when the *T. gondii* tachyzoite expresses only residual levels of the rhomboid protease (ROM4) in charge of cleaving the surface-exposed MIC2, MIC2 molecules accumulate at the surface of the parasite that can no longer glide forward but instead shows enhanced twirling motility.<sup>39</sup> Similarly, when *Plasmodium berghei* sporozoites express a mutant version of the MIC2 homologue TRAP that cannot be processed by the rhomboid protease, the parasite can no longer disengage its posterior pole from the substrate and move forward.<sup>36</sup> Whereas we detected both SAG1 and MIC2 proteins in patches over successive segments of the helical trails

postfixation and immunolabeling, we did not find MIC2-specific enrichment at the angular adhesion regions that were accurately identified using the RICM live sequences as recognition pattern (Supporting Information Figure S2). Therefore, it is possible that another unknown adhesin(s), which would not integrate the retrograde flow, might modulate force production at the parasite apex in line with the turnover-specific adhesion sites built by the *Plasmodium* sporozoite during circular gliding.<sup>13</sup> In addition, monitoring the apico-basal flow of optically trapped beads pinned out that specific adhesions do not integrate the apico-basal capping process, yet

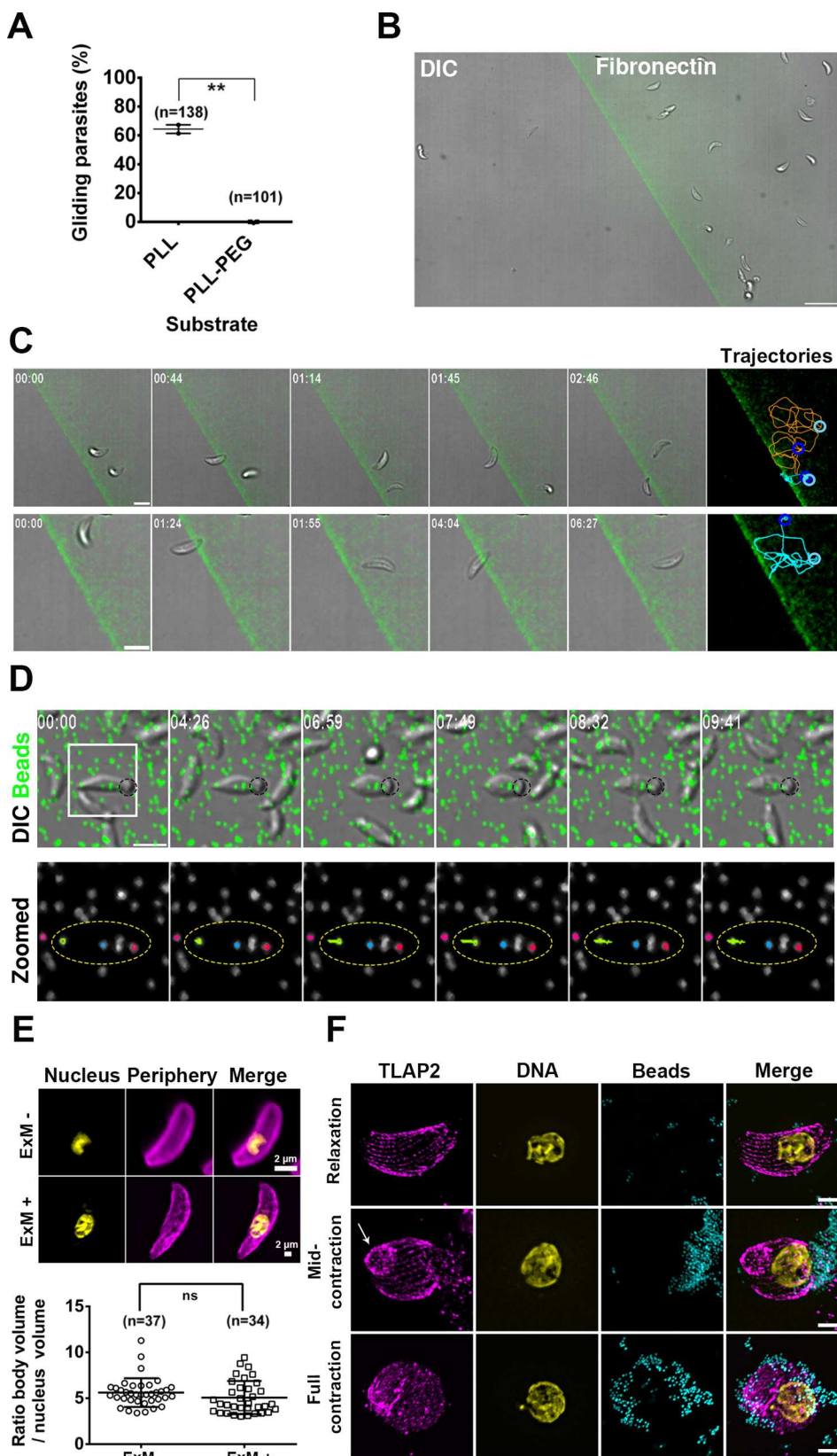


Figure 4. Front adhesion to and back disengagement from the substrate are both required for kink formation and traction force development. (A) Percentage of tachyzoites that moved by at least one body length displacement over a 20 min period post contact with poly-L-lysine (PLL) or poly(ethylene glycol) (PEG) chains grafted on PLL coating, unpaired *t* test,  $**p = 0.021$ . (B) Large view of the poly-L-lysine PEG–fibronectin composite micropattern shows that tachyzoites are selectively retained in the fibronectin area, which is fluorescently labeled by fibrinogen-Alexa647, scale bar: 15  $\mu\text{m}$ . (C) Images from a sequence of two (top) or one (bottom) representative gliding tachyzoite(s) that fail to pass over the fibronectin–PLL–PEG demarcation line being incapable of interacting apically with PEG. Instead they elicit twirling around their posterior end bound to fibronectin and regain helical motion once apically sensing fibronectin. Blue and

Figure 4. continued

cyan circles in the trajectories window indicate the initial and the final position of the tachyzoite over the several-minute gliding sequence. Trajectories were reconstituted by tracking the tachyzoite base, which unlike the apex stays in focus even during twisting and twirling motions. (D) TFM on a tachyzoite posteriorly immobilized on fibronectin through carboxylated microbeads (black circle). (Top) Selective inward displacement of TFM beads (green) beneath the apex of the immobilized parasite occurs during sustained contraction, whereas the beads relax back to initial position upon parasite relaxation, (bottom) zoomed white square from top, showing the colored trajectories; note the large yellow trajectory that attests significant bead inward displacement, the yellow dotted ellipsoid delineates the tachyzoite. (E) Confocal images showing a representative tachyzoite immunolabeled for the GAP45 protein (pink) that delineates the parasite periphery and PI stained for DNA (yellow) prior ExM (ExM<sup>-</sup>) and after ExM (ExM<sup>+</sup>), maximal projection intensity are presented, compare the scale bars that attests the physical magnification of the ExM specimen. The graph shows the ratio of the body and nucleus volumes after 3D reconstruction prior (ExM<sup>-</sup>) and after ExM (ExM<sup>+</sup>), Kruskal–Wallis test, NS,  $p = 0.17$ . (F) ExM on tachyzoites posteriorly immobilized on beads (cyan) and immunolabeled for the cortical MT-associated TLAP2 protein (pink) and PI stained for DNA (yellow), (top) no contraction has yet started, (middle) contraction has started, note the apical humpy deformation in the cMT cytoskeleton indicated with a white arrow, (bottom) cMT disruption at a latest time of tachyzoite sustained contraction. Scale bars: 5  $\mu\text{m}$  unless indicated, time is in minutes/seconds. The ExM allowed reaching about a 70 nm  $xy$  resolution thanks to a  $\sim 3$ – $5$ -fold increase in the biological sample size.

they can optimize force production. Accordingly, the trap-like protein (TLP) was proposed to promote firmer adhesion to the substrate by enabling specific actin remodeling underneath the plasma membrane. Such function would explain why TLP causes specific slowdown of the actin-dependent flow.<sup>31</sup> With these in mind, we next interrogated whether the firm stable apical anchor formed by the moving tachyzoite and localized at the kink could indeed serve as a platform for force transmission by using traction force microscopy (TFM). These assays also allowed testing whether the kink-induced cell shortening could be associated with tension stored in the parasite that would be released to promote the thrust required for productive helical movement.

**Traction force Spatiotemporally Associates with the Kink and Coincides with Body Dragging.** To design the TFM assay, we first identified a substrate in which the stiffness was sufficient to allow helical gliding while being elastic enough to measure substrate deformations *via* a displacement field analysis performed using fluorescent beads embedded into the polyacrylamide (PAA) hydrogel. Particle image velocity (PIV) combined with single-particle tracking allowed analyzing substrate deformation with a spatial resolution in the range of tenth of nanometers. Tracking in space and time the tachyzoite posterior pole and scoring as motile those that performed at least one body length displacement, we found that stiffer substrates such as glass ( $n = 73$ ) and 40 kPa PAA ( $n = 55$ ) correlated with optimal gliding skills, whereas lowering stiffness gradually decreased the frequency and duration of the motile behavior. Yet, the tachyzoites retained a short-lasting ability to perform helical motion on the soft 2 kPa PAA substrate ( $n = 103$ ) (Supporting Information Figure S3). Applying TFM<sup>40</sup> to parasites gliding on 2 kPa fibronectin–PAA substrate, we obtained a traction vector map and identified an early inward-oriented traction force stemming at the cell front and exerted longitudinally in line with the backward displacement of the in-gel beads (*i.e.*, TFM beads) underneath the apical part of the parasite (Figure 3A and Supporting Information Movie 7a and Movie 7b, slow motion). As the force progressively increased, concomitant dragging of the parasite body occurred and accounted for the TFM bead's displacement underneath the posterior pole in the direction of the parasite motion, in line with the previous detection of trails being pulled by the tachyzoite (Supporting Information Movie 6). Relaxation of the TFM beads back to their initial position was recorded immediately after the kink release and the parasite forward acceleration (Figure 3A,B). Pioneering TFM on the *Plasmodium* sporozoite has allowed

uncovering two longitudinal forces applied at each pole during circular gliding, alike what we found for the *T. gondii* tachyzoite undergoing helical gliding. A large force localized at the posterior adhesion site peaked just prior sporozoite de-adhesion, whereas a lower pulling traction force at the apex pointed toward the center. In contrast to what we detected for the tachyzoite, large forces were also found to point orthogonally toward the sporozoite center,<sup>13</sup> where they promote body stretching and thus favor close contact of the whole cell with the substrate—an obligate requirement for circular gliding—without contributing to force production.<sup>41</sup> Therefore, although both the tachyzoite and sporozoite likely use a stalling force at the back, which upon rupture of the adhesive contact contributes to a thrust force, the spatiotemporal distribution and intensity of the forces during their specific gliding cycle (*i.e.*, helical *versus* circular) likely differ. Accordingly, the overall force during the helical cycle was computed to a few nanoNewtons ( $\sim 1$  to 4 nN,  $n = 10$ ) with an increment over the kink step, therefore significantly higher than the 100–200 pN range inferred for cortical forces using laser trap on nongliding *T. gondii* tachyzoites<sup>42</sup> or gliding *Plasmodium* sporozoites.<sup>31</sup> By comparison, the nanoNewton range characterize forces applied by both bacteria and mammalian cells on their surroundings.<sup>43</sup>

**Toxoplasma Apical Focal Adhesion Is Essential to Switch from Nonproductive Twirling to Productive Helical Motion.** To demonstrate the functional contribution of the apical body adhesion to the subsequent helical gliding, we sought interfering with the parasite adhesive step at the apical traction force site. First, we screened for substrates not permissive to parasite adhesion using several chemicals of distinct charge and wettability properties. We found that tachyzoites were unable to stabilize and glide on the densely packed polymeric poly(ethylene glycol) (PEG) brushes grafted on poly-L-lysine (PLL) (Figure 4A) similarly to what was reported for *Plasmodium* sporozoites.<sup>44</sup> Therefore, composite substrate was photopatterned: the parasites underwent energetic gliding on the fibronectin-coated area when approaching the demarcation line between the fibronectin and PLL–PEG-juxtaposed areas. The tachyzoites stopped when facing PEG, sometimes sliding on it prior to stepping back in a reverse motion while still posteriorly bound to fibronectin (Figure 4B,C and Supporting Information Movie 8 and Movie 9). They responded to the exclusive basal attachment by spinning around the main axis in a typical twirling nonproductive motion<sup>18</sup> until the front region was eventually caught again in an interaction with fibronectin,

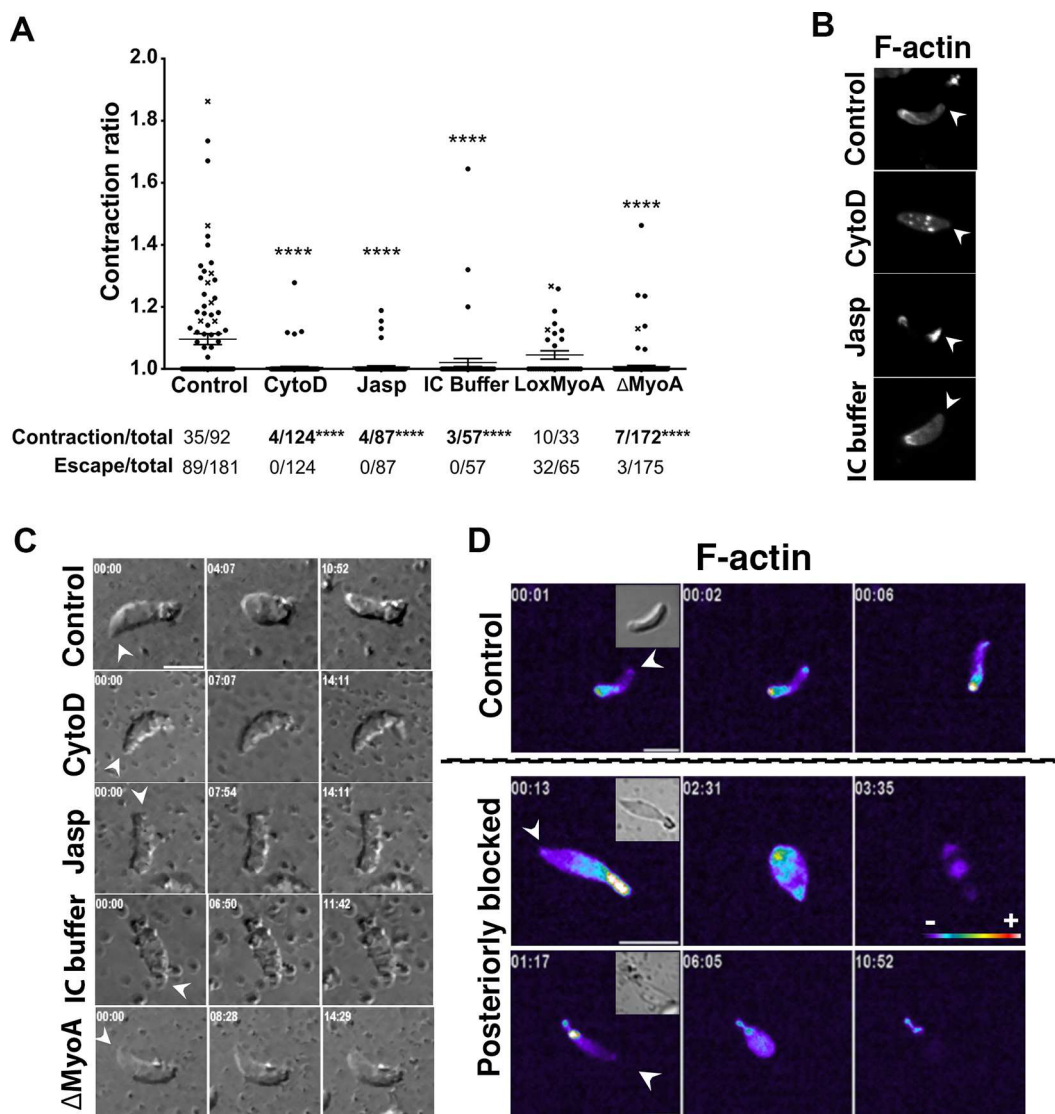


**Figure 5.** Prolonged and exacerbated tachyzoite contraction relies on intact actin filaments and MyoA motor. (A) Graph shows the contraction ratio after posterior immobilization on beads over a 20 min period for (i) wild-type control tachyzoites expressing the F-actin chromobody-Emerald (Acb-E) and incubated in EC buffer supplemented or not with 1  $\mu$ M cytochalasin D or 1  $\mu$ M jasplakinolide actin poisons or in IC buffer, and (ii) for tachyzoites before (LoxMyoA) and after ( $\Delta$ MyoA) Cre-mediated excision of the *myoA* gene. Kruskal–Wallis test, \*\*\*\* $p < 0.001$  Dunn’s multiple comparisons with the control genotype. Table below the graph shows (i) proportions of number of parasites contracted over the total and (ii) proportions of number of parasites that escape over the total. For both, chi square test, \*\*\*\* $p < 0.001$  Fisher’s exact test with the control. (B) Confocal images of tachyzoites showing F-actin prior to record the contractile behavior. Maximal projection intensities are presented. (C) Representative DIC images of tachyzoites posteriorly immobilized to monitor both contractile behavior and bead-capping ability under each setting over a 20 min period ( $57 > n > 181$  depending on the actin poison used and  $65 > n > 165$  for *myoA* KO, 3 independent assays). (D) Representative fluorescent images of F-actin dynamics in tachyzoites expressing the Ach-E undergoing helical gliding (top panel) or sustained contraction upon posterior immobilization (middle and bottom panels); DIC images are presented as inlays for each sample. Heat map intensity is presented in arbitrary units.

hence restoring the tachyzoite ability to perform helical trajectory. These data reinforce the view that the tachyzoite builds an apical stable adhesion site with the substrate that is compatible with the development of traction force. As we showed that both adhesion and force spatiotemporally coincide with the kink-like deformation, we expected then that the thrust productive force would be at least partly driven by the relaxation of the kink, which drives the slight lift of the parasite apex. Of note, this thrust force might also require some contribution from the parasite basal contact which loosens when traction operates allowing both dragging and retraction of the body. Given that tachyzoites must overcome

the resistance of the 3D—nonlinear—meshwork to navigate in physiological microenvironments, the acceleration induced upon the kink release should provide the right thrust to pass through the meshwork of fibers they pulled on. Accordingly, we next addressed how the contact and dragging force at the cell back identified by, respectively, RICM and TFM contribute to the helical gliding mode of the tachyzoite.

**Adhesion–De-adhesion Coupling at Both Poles Drives the *Toxoplasma* Apical Kink and Its Release, in Turn Promoting the Helical Thrust Force.** We designed another TFM assay in which the tachyzoite would be unable to disengage its posterior pole from the substrate using submicron

sticky beads. As already reported in the context of membrane flow or cortical forces studies,<sup>32,42</sup> the beads deposited on the tachyzoite surface underwent apico-basal translocation. However, because in our setting the bead's surface engaged covalent interactions not only with the parasite but also with the fibronectin layer in a configuration that forced the former to stay posteriorly immobilized on the latter, the cell forward progression could be hindered (Figure 4D). Such posteriorly constrained tachyzoites never formed the apical kink ( $n = 0/92$ ) and, instead, underwent a directional, minute time scale and repetitive inward-oriented contraction visualized by the whole body rounding (Figure 4D and Supporting Information Movie 10). The TFM captured the displacement of in-gel beads suitably positioned underneath the apex of the immobilized parasite consistent with a sustained apical traction force, and therefore a sustained adhesion between the parasite front and the substrate (Figure 4D, zoomed panel, yellow bead and trajectory). The prolonged force application induced pronounced shrinkage of the cell body along the longitudinal axis and eventually led to membrane damages to the extent the tachyzoite was likely wounded beyond repair. Meanwhile, we observed that the in-gel beads shifted back to almost the initial position, which we assumed to relate to the sudden relaxation of the cell "ghost" when internal tension fell (Figure 4D and Supporting Information Movie 10). Strong evidence for the rupture of the plasma membrane upon excessive contraction of the YFP-expressing tachyzoite was provided by the acute loss of fluorescence that occurred immediately after maximal cell rounding and concomitantly with the relaxation of the cell (Supporting Information Figure S4). The relaxed tachyzoite cell looked mis-shapen for the rest of the recording time as expected for a cell ghost, therefore attesting that the exacerbated and sustained contraction induced cell death. To next visualize the deleterious effect of the long-lasting contraction on internal cytoskeletal structures at the nanoscale resolution, we applied the expansion microscopy technique (ExM)<sup>45</sup> and first validated the isotropic expansion of the specimen with the 3D co-reconstruction of the tachyzoite body and nucleus prior and after expansion (Figure 4E). We then analyzed a tachyzoite line engineered to express a fluorescent version of TLAP2, a protein aligned with the 22 cMTs,<sup>30</sup> and confirmed that during the prolonged contraction period, the capped beads accumulated posteriorly while the spiral cMTs deformed. We first observed an apical hump in the cMT network (Figure 4F, middle panel), and eventually, the latter fell apart while the capped beads were redistributed over the damaged surface (Figure 4F, bottom panel). Overall, these data support that the kink rose from the interplay between the apical adhesion/base de-adhesion and the forces generated at both poles rather than from the apical traction force only. They also highlight that creating unbalance between the front and back responses can result in a contractile force that imposes a mechanical compression to the cMT network to which it cannot resist. The need for a balanced myosin-A-based contractile activity that stems at the tachyzoite apex and promotes disengagement of the posterior pole can explain why the genetically myosinA-deficient tachyzoites, which retain only residual motility, do not any longer undergo helical gliding.<sup>37,32</sup>

**Tachyzoite Apico-Basal Contraction Requires Intact Actin Filaments and Myosin A Motor and Correlates Only Partially with the Requirements for Rearward Membrane Flow.** Apart from the prolonged contraction and

fatal outcome described earlier, we also observed that the tachyzoites, which were posteriorly immobilized, could either rotate on the beads, slightly contract, and move forward, hence those escaped (Supporting Information Movie 11) or remain inactive, hence those showed no contraction and stayed attached. To verify whether actin dynamics and MyoA motor the function of which are required for motility<sup>25,46</sup> would also contribute to the apically driven exacerbated contraction, we first defined a quantitative readout for measuring the contraction extend over time. Using the ratio between the resting body length (*i.e.*, no contraction) and the minimal body length (*i.e.*, maximum contraction) as a contraction indicator, we found that nearly half of the wild-type (WT) control parasites were able to escape from the immobilization setting, therefore attesting to the energetically active status of the specimens under study. Approximately 40% of the second half ( $n = 35/92$ ) contracted over a wide range of amplitude, whereas 20% of this contracting population actually showed signs of irreversible damages ( $n = 7/35$ ) (Figure 5A). Blocking actin dynamics with cytochalasin D (0.5 and 1  $\mu\text{M}$ ) or jasplakinolide (1  $\mu\text{M}$ ) that work through different mechanisms<sup>47,48</sup> almost abolished both the escape (*i.e.*, motile) and contractile behaviors. Of note, the few (less than 5%) tachyzoites that displayed contraction never reached the stage of high and sustained body compression, hence none of them died (Figure 5A). We confirmed the cytochalasin and jasplakinolide potency on tachyzoite actin as parasites expressing the fluorescent chromobody actin-Emerald (Acb-E)<sup>49</sup> displayed the typical drug-induced redistribution of actin filaments as, respectively, cytoplasmic aggregates and apical acrosome-like.<sup>50</sup> With the same readout, we also compared the contractile behavior of parasites following or not *MyoA* gene silencing using the well-characterized DiCre Lox *MyoA* strains.<sup>24</sup> We observed that loss of *MyoA* ( $\Delta\text{MyoA}$ ) significantly altered the contractile capability of tachyzoites immobilized on their base when compared to the *MyoA*-expressing parental line (Lox*MyoA*) ( $\Delta\text{MyoA} = 175$ ,  $p < 0.001$ ) (Figure 5A). Finally, we checked if the contractile activity was specific for tachyzoites metabolically ready for initiating motility by measuring the contraction of WT control tachyzoites kept in the Endo buffer which mimics the intracellular buffer (hereafter referred to as IC buffer) and is known to drastically decrease microneme secretion (*i.e.*, adhesin delivery on the tachyzoite surface) and consequently motility.<sup>20</sup> Those tachyzoites showed the typical actin posterior network of intracellular tachyzoites<sup>51</sup> and were significantly inefficient at contracting under the posterior microbead setting ( $n\text{IC} = 57$ ,  $p < 0.001$ ) (Figure 5A–C and Supporting Information Movie 12). Finally, we monitored actin filaments in real time in Acb-E-expressing tachyzoites undergoing either helical gliding or forced contraction during the immobilization phase. The F-actin apical focus detected at the onset of the helical cycle remained discrete and rapidly resolved into the large stable basal F-actin pool, as reported<sup>33,51</sup> and in line with our force mapping assays. In contrast, an increasing F-actin signal was detected within the whole body, in particular, in the cell front upon prolonged contraction of the immobilized and rounding tachyzoites (Figure 5D and Supporting Information Movie 13). Eventually, the F-actin signal vanished, which fits with the loss of fluorescence observed with YFP-expressing tachyzoite artificially immobilized on the substrate through their basal pole (Supporting Information Figure S4), thereby confirming that the membrane had ruptured upon excessive

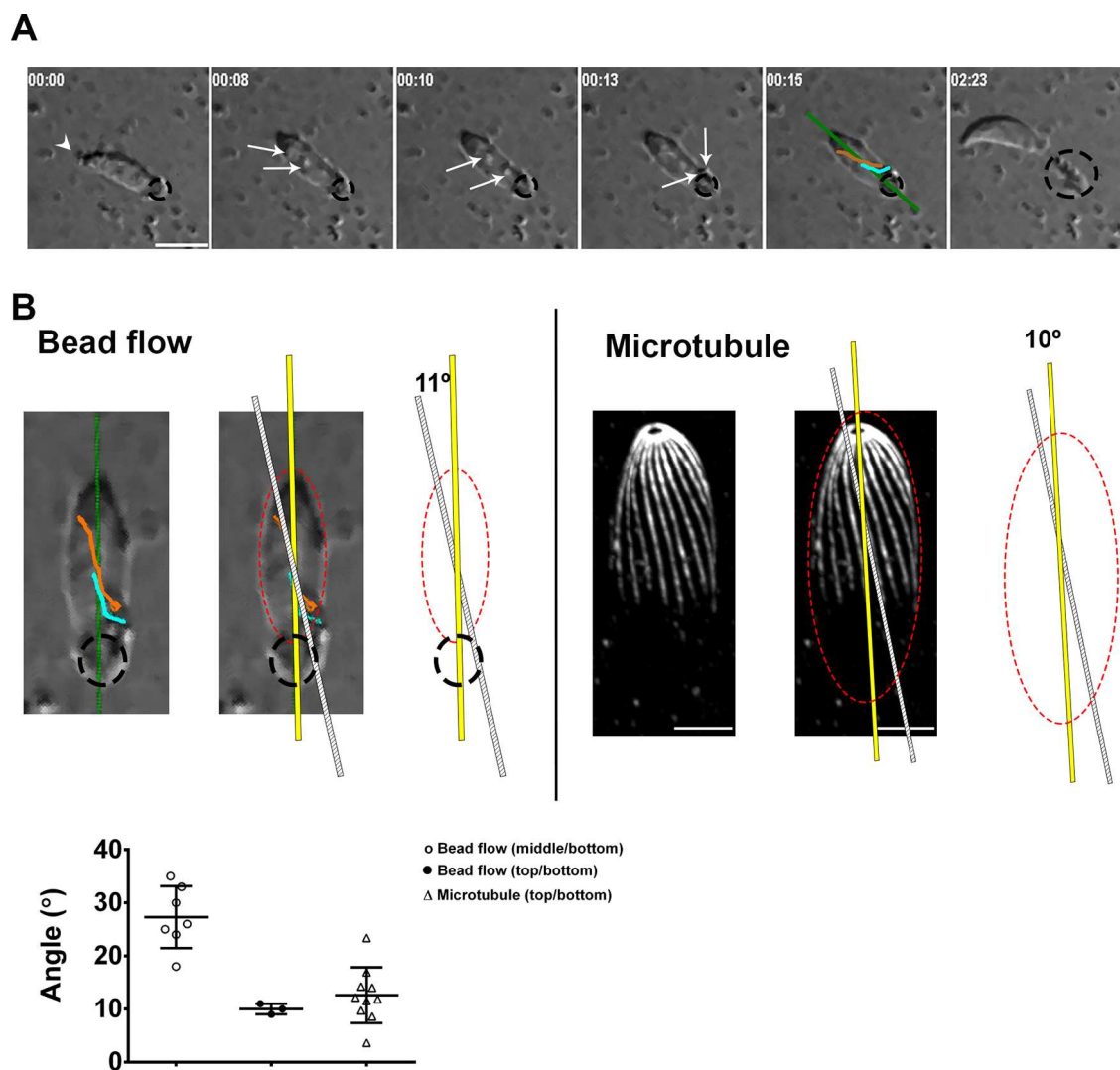


**Figure 6.** Apico-basal translocation of surface-bound microbeads follows a helical path that approximates the spiral direction of the tachyzoite cMTs. (A) Representative images of apico-basal bead capping monitored in real time for tachyzoites posteriorly immobilized on beads encircled with the dotted black line. The two surface-bound beads are indicated with white arrows, and their trajectory depicted in orange and cyan lines is shown on the fifth panel, before active escape of the tachyzoite from the immobilizing setting. In all panels, white arrowheads mark the tachyzoite apex; all scale bars:  $5\ \mu\text{m}$ , time is in minutes/seconds. (B) Zoomed panels show images and schematics for (left) trajectory of two beads over the capping time taken from the sequence shown in A, which deviates from the body main axis (yellow line) of about a  $11^\circ$  angle, while (right) the spiral cMTs visualized on an extracellular tachyzoite treated for U-ExM and stained with antipolyglutamylated tubulin show about a  $10^\circ$  angle orientation. (Bottom) Plot of the different angles calculated for the cMTs; the mean with SD is shown for each group ( $n = 10$  tachyzoites, mean of 4 cMTs per tachyzoite) and for the capping bead flow ( $n = 9$  tachyzoites). Please note the larger variability shown by the bead angles, which depends on the bead position at the initial time of capture and tracking.

contractile activity, leaving a tachyzoite ghost, the apex of which no longer attached to the substrate.

As the retrograde membrane flow process has been shown to operate in *T. gondii* tachyzoites in absence of the actomyosin system,<sup>32</sup> we analyzed how this process would operate for tachyzoites artificially immobilized on their base. Unlike previously,<sup>32</sup> we monitored in real time the bead-capping process and found that the loss of contractility driven by actin poisons and IC conditions did correlate with the inhibition of the rearward bead capping along the parasite surface ( $57 > n > 181$  depending on the condition) (Figure 5C and Figure 6A and Supporting Information Movie 14), thus recapitulating the phenotype of formin 1 (FRM1)-deficient tachyzoites<sup>33</sup> and consistent with the need of apically initiated actin filaments. However, on loss of myosinA,<sup>46</sup> whereas the tachyzoites showed almost no ability to contract (Figure 5A), they

intriguingly maintained a bead-capping activity almost as efficient as tachyzoites from the parental line ( $65 > n > 165$ ) (Figure 5C and Supporting Information Movie 12), in agreement with a MyoA contribution to force transmission rather than production.<sup>32</sup> Furthermore, along with these bead-translocation assays we observed in WT tachyzoites that the bead-capping process could precede productive helical movement (Figure 6A and Supporting Information Movie 14), and that the bead apico-basal motion could follow the cMT helical trajectory. To confirm this observation, we applied ExM with a recently refined near-native expansion microscopy (U-ExM) protocol,<sup>52</sup> and labeled the  $\alpha,\beta$ -tubulin dimer that forms the cMT polymers taking advantage of the polyglutamylation post-translational modification of these isoforms.<sup>53</sup> With this level of resolution, we could measure the angle with the longitudinal axis made by the cMTs when they emanate at the apical polar

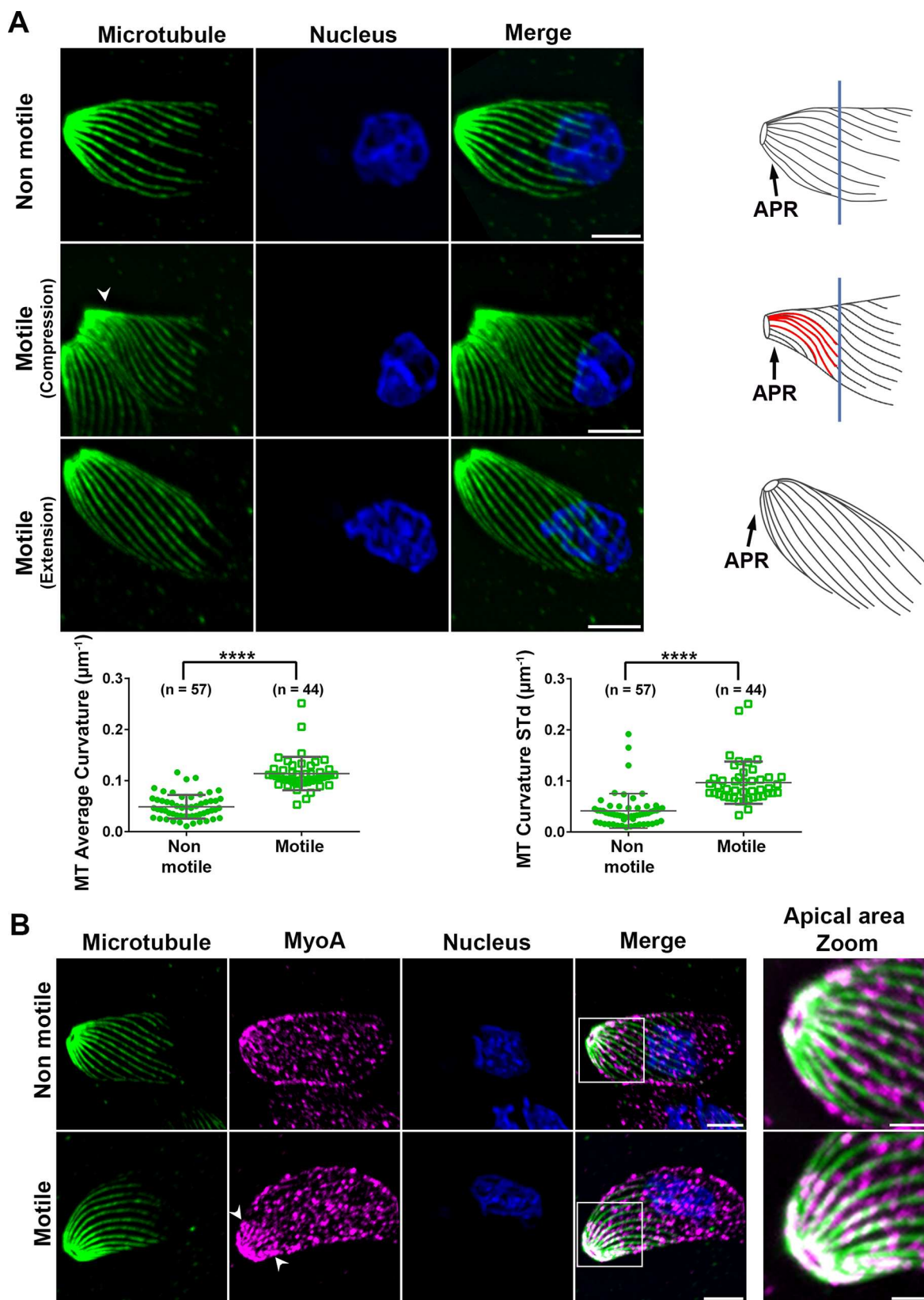


Figure 7. Curvature of cortical microtubules changes during helical gliding suggesting a spring-like mechanism apically driven by myosin-based contractile forces. (A,B) Confocal images representative of extracellular tachyzoites following U-ExM and immunofluorescence co-staining of (A) tachyzoite cMTs using antipolyglutamylated tubulin antibodies (green) and nucleus (blue). Maximal projection intensities of the cMTs from the tachyzoite ventral side are shown for (top) a nonmotile tachyzoite, (middle and bottom) two motile tachyzoites. Note the pronounced torsion and compression (white arrowhead, middle panel) and the extension (white arrowhead, bottom panel) that likely account for the spring like force underlying helical gliding. Right: Schematics of the cMTs for each stage show the highly curved cMTs at the apical region of the motile tachyzoites, drawn in red. (Bottom) Graph on the left shows a significant increase in mean curvature of the cMTs

Figure 7. continued

for the motile tachyzoites in torsion, unpaired  $t$  test,  $***p < 0.0001$   $n = 44$ , when compared to the nonmotile ( $n = 57$ ); graph on the right shows enhanced curvature amplitude over the length of single cMT for motile tachyzoites during the compression step ( $n = 47$ ) when compared to nonmotile ( $n = 57$ ) tachyzoites, unpaired  $t$  test,  $***p < 0.0001$ . (B) Co-staining of the cMTs (green) and MyoA-HA tagged using anti-HA antibodies (purple) and the nucleus (blue). (Top) Nonmotile tachyzoite, (bottom) motile tachyzoite are shown. Note the clear MyoA signal enrichment at the apex of the motile parasite indicated with white arrowheads, which co-aligns with the MT signal. The right frames show zoomed areas delineated in the merge frames with a white square. All scale bars:  $5 \mu\text{m}$  except for the B zoomed frames:  $2 \mu\text{m}$ . The U-ExM protocol gave a 3–5-fold increase of the tachyzoite size and provided a  $\sim 70 \text{ nM}$   $xy$  resolution. APR: Apical polar ring.

ring while approximating the angle made by the microbeads monitored over the capping process (Figure 6B and Supporting Information Movie 14). Although we observed for some beads that the angles were off the range of those made by the well-resolved cMTs, it is worth noting that these gaps mainly correspond to situations where the microbeads were tracked while they had already reached the minor axis plane of the ellipsoid tachyzoite. While traveling toward the posterior pole, the beads approached an area devoid of cMTs and often collided with the substrate before reaching the posterior pole, an observation already reported when monitoring the apico-basal trajectory of  $0.6 \mu\text{m}$  beads delivered by laser trap to the surface of resting (*i.e.*, nonmotile) tachyzoites.<sup>42</sup> Collectively, these data indicate that the actomyosin system mobilized during the rearward bead translocation process has aligned with the longitudinal cMT network, this independently of the apical adhesion and thus before the apical traction force operates.

**Curvature of Cortical Microtubules Significantly Changes during Helical Gliding, Suggesting a Spring-like Mechanism Apically Driven by Myosin-Based Contractile Forces.** Triggered upon relaxation of the apical kink, the extension of the tachyzoite body coincided with the thrust force while the parasite rotated with an orientation dictated by the MTs' helical architecture (Figure 1C and Figure 3A and Supporting Information Movie 3a). In metazoans, the general ability of MTs to bear compressive loads imposed by contractile forces translates into a coordinated bending of MTs and to drive a spring-like force mechanism as exemplified with the rhythmically contracting cardiac myocytes.<sup>54</sup> To interrogate whether the cMTs could transiently store energy upon actomyosin activation and acts as a torsional spring to promote the required thrust for helical propelling, we analyzed the behavior of cMTs during helical motion. Whereas the U-ExM allows nanoscale resolution, it does not permit to affirm that the tachyzoites under observation were actually caught in motion. As under progliding conditions, the tachyzoites displayed a statistically significant elongation of the nucleus as compared to the samples of either extracellular tachyzoites left in IC buffer or tachyzoites which had just invaded host cells ( $n > 75$  for each condition, Supporting Information Figure S5A), we used the nucleus sphericity as first criterion. We next selected for tachyzoites associated with helical trails using the surface-exposed glycoprotein SAG1 known as robust trail marker,<sup>11</sup> which also bore an elongated nucleus ( $p < 0.0001$ ,  $n = 12$  motile helical and  $n = 15$  intracellular) (Supporting Information Figure S5B). To analyze whether individual cMTs could display a specific compression, relaxation and torsion behavior in motile tachyzoites, we applied U-ExM and used both antiacetylated  $\alpha$ -tubulin and antipolyglutamylated  $\alpha$ , $\beta$ -tubulin antibodies which have been widely used for labeling *T. gondii* cMTs.<sup>53</sup> When quantifying the curvature of the cMTs

in nonmotile extracellular (Figure 7A, top panel) or nonmotile intracellular (Supporting Information Figure S5C, top panel) and motile parasites (Figure 7A, middle panel; Supporting Information Figure S5C, bottom panel), we observed for the motile specimens, a highly significant increase in the mean curvature of the MTs as compared to the nonmotile ones (Figure 7A, polyglutamylated tubulin,  $p < 0.0001$ ,  $n = 57$  nonmotile and  $n = 44$  motile parasites) (Supporting Information Figure S5B,C, acetylated tubulin,  $p < 0.0001$ ,  $n = 24$  nonmotile and  $n = 22$  motile tachyzoites). Importantly, the curvature amplitude over the length of a single MT was also significantly enhanced in gliding when compared to intracellular parasites as assessed by the standard deviation values of the curvature profile over the full length MTs (Figure 7A, polyglutamylated tubulin,  $p < 0.0001$ , Supporting Information Figure S5B,C, acetylated tubulin,  $p < 0.0001$ ). The decreased interdistance between single cMT nearby the apical ring (APR) from where they emanate together with the observed nonuniform bending over the cMT length strongly argue for a specific compression occurring at the tachyzoite apex during cell movement. In addition, situations where the cMTs straightened at the apical region likely corresponded to the time of the thrust force occurring upon kink release (Figure 7A, bottom panel; see also schematics on the right). To further test the hypothesis of cooperation between the actoMyoA-based and the cMT-based cytoskeletons could contribute to force production at the kink, we performed U-ExM imaging of MyoA and cMTs simultaneously on either motile or nonmotile tachyzoites. To this end, we used a tachyzoite line that expresses a chimeric MyoA-HA protein under the endogenous promoter and anti-HA antibodies. A clear co-alignment of the MyoA and the cMTs was detected in the apical region of motile tachyzoites together with a local enrichment in MyoA when compared to nonmotile parasites (Figure 7B). Although it is not possible to ascertain that this situation reflects the kink step, the alignment between the MyoA and the cMTs makes plausible an indirect connection and thus argue for an energy transfer between the two cytoskeletons. In addition, this co-alignment is consistent with the helical path taken by the beads undergoing actin-based rearward capping. In metazoans cells, it was found that the MTs were embedded in a viscoelastic material provided by the surrounding medium and MT-associated proteins—in particular, kinesin motors<sup>55</sup>—that influence the MT ability to buckle and bear energy load.<sup>54</sup> Therefore, it would be worth investigating whether some MT or/and IMC protein partners - including the APR-associated kinesin,<sup>56</sup> proteins that coat the cMT length and alveolins—positioned at the apical flexure site could behave as pro-elastic elements and thus optimize a cMT driven spring-like reaction. Of note the intrinsic stable left-handed curvature of «resting» cMTs already sign for their ability to withstand large forces within the cytoplasm in agreement with their contribution to shape maintenance.<sup>30,57</sup> As the activation of

the actomyosin system translates into force-powering motility, it is plausible that the significant local increase in cMT curvature of motile tachyzoites accounts for higher compressive loads on the cMTs in response to the increased contractility. Indeed, when the tachyzoite underwent exacerbated actomyosin-driven contraction (Figure 4F) in a failed attempt to disengage its base from the adhesion site, the cMT cytoskeleton overcame its bending capacity and eventually broke up.

## CONCLUSIONS

In this study, by combining surface sensitive biophysical techniques with high resolution-high speed 2D and 3D live imaging and expansion microscopy, we provided insights on how the *T. gondii* parasite couples cycles of adhesion–de-adhesion to the substrate with traction and spring-like force generation to achieve helical gliding, a function which is required for perpetuating *T. gondii* populations in the homeothermic hosts. Owing to its persistent structural polarity over the intracellular/extracellular cycles, the tachyzoite bypasses the canonical symmetry break most eukaryotic cells must undergo to start migrating.<sup>58</sup> In addition, although lacking the typical actomyosin II motor commonly used to generate traction in eukaryotes, *Toxoplasma* has evolved an Apicomplexa-restricted unconventional myosinA motor that, immobilized within the glideosome unit and between the membrane layers forming the pellicle at the cell surface, works on noncanonical actin filaments to activate motility.<sup>29</sup> The pellicle and the subtending twisted 22 microtubules provide the tachyzoite with a peculiar crescent shape and flexibility, which has proposed to act as the primary driver of the helical motion. We now demonstrate that the *T. gondii* tachyzoite must engage its apical region in a specific stable adhesion with the substrate that is compatible with the development of a balanced traction force and drives, in turn, the loosening of the posterior contact point, allowing retraction of the parasite base and dragging force. Therefore, similarly to what was found for the *Plasmodium* motile sporozoite, real time analysis of adhesion dynamics and force mapping supported by recently refined high spatiotemporal resolution imaging approaches and biophysics characterization applied to the *Toxoplasma* motile tachyzoite have challenged the classic model of Apicomplexa gliding motility. In addition to the backward capping of adhesion proteins at the cell surface, both parasite rely on a distinct class of adhesive contact that do not enter the rearward flow but directly contribute to build tension in the parasite cytoskeleton and produce force by strengthening anchors points with a specific on–off dynamics, hence regulating the motile process. Although these studies confirm the need to shift paradigm for a comprehensive mechanistic understanding of Apicomplexa gliding motility, they raised key questions on the nanoscale architecture of the singular adhesive platforms including the adhesin ligand identities on the extracellular side, the actin filament organization on the cytoplasmic side, but also how they would transmit tensional forces from the cytoskeleton to the ECM with the yet to clarify contribution of the MyoA motor, and eventually, it would be worth investigating their putative contribution for mechanotransduction. Providing indication of a spatiotemporally regulated cooperation between the tachyzoite actomyoA-based contractile activity and the helical flexible cMT ability to build tension, this study gives credit to pioneered kinematic analysis.<sup>18</sup> These results also highlight the necessity to delve deeper into the

compressive, torsional, and tensile strengths of *Toxoplasma* tachyzoite and also *Plasmodium* sporozoite cMTs as some differences between the two stages could in part account for their specific motile behavior.

## METHODS/EXPERIMENTAL

**Parasite Strain Maintenance and Preparation for All Motility Live Assays.** All media and products used for cell culture were from Gibco-Life Technologies (St Aubin, France) unless specified. *T. gondii* strains were propagated on *Mycoplasma*-free human foreskin fibroblast monolayers (HFFs) and grown in Dulbecco's modified Eagle medium (DMEM) supplemented with glutamax, 10% heat-inactivated fetal calf serum (FCS), penicillin (100 U/mL), and streptomycin (100 µg/mL) at 37 °C and 5% CO<sub>2</sub>. The laboratory type 1 RH strain was used as well as the YFP-expressing RH<sup>17</sup> and the mutant deleted for the KU80 protein<sup>59</sup> (gift from V. Carruthers, Michigan University, USA; see [Molecular Cloning](#) section). The RH Δku80: DiCre/lox MyoA, RH Δku80: DiCre/ΔMyoA,<sup>60</sup> and the RH cbactinEmFP<sup>49</sup> expressing strains were given by M. Meissner (MLU Munich University, Germany) and hereafter designated LoxMyoA, ΔMyoA, or Ach-E, respectively. For most motility assays, tachyzoites were collected within a few hours following spontaneous egress from the HFF monolayers, and ~10<sup>5</sup> cells were centrifuged in HBSS<sup>++</sup> supplemented with 0.2% FCS (0.2% HBSS). The pellet containing parasites was resuspended in 150 µL of 1% FCS HBSS (1% HBSS) and adjusted at 1.6 mM of CaCl<sub>2</sub> (1% HBSS-Ca<sup>2+</sup>). Typically, when using the 18 mm diameter glass coverslip fitting chamber, 50 µL of the tachyzoite suspension was added to 100 µL of 1% FCS HBSS-Ca<sup>2+</sup> covering the coverslip. The amounts of FCS, CaCl<sub>2</sub>, and pharmacological reagents were adjusted upon need as described in each appropriate section.

**Molecular Cloning.** A mCherry (mC) tag was fused in frame with the C-terminus of TLAP2 gene ([ToxoDb.org](#), TGGT1\_232130) in the ΔKu80 strain using the ligation independent cloning strategy.<sup>59</sup> A 1.5 kb fragment corresponding to the 3' end of the TLAP2 excluding the stop codon was amplified by PCR with the forward primer 5'-GCGCCCTCCTTCAGTGTTCCTC-3' and reverse primer 5'-TGCACCTGCGGCACCGGCAG-3'. The PCR fragment and vector p-LIC-mCherry-HXG were digested with T4 DNA polymerase and annealed, yielding plasmid pTLAP2mCherry-LIC-DHFR. Freshly egressed Δku80 tachyzoites from a 1/2 T25 flask were transfected with 15 µg of the EcoRV-linearized plasmid. After one cycle without drug, ΔKu80/TLAP2-mC transformants were selected with 2 µg/mL pyrimethamine and single-cell cloned by limiting dilution.

Endogenous tagging of MyoA with HA-tag was achieved using the pLIC-MyoA-HA-HXGPRT vector. To construct this plasmid the coding sequence of MyoA was amplified using primers 5'-TACTTCCAATCCAATTTAGCAAAGCAGCAAATGCCCCA-GCGAAG-3' and 5'-TCCTCCACTTCCAATTTTAGC-GAACCCTGCGGTGAACAGTCGCGGG-3' and RH Δku80 genomic DNA as template. The PCR product was cloned to pLIC-mAID-HA-HXGPRT vector using the LIC cloning method as described above.<sup>61</sup> RHku80 OsTir1-(Ty)3 parasites were electroporated with BstBI-linearized plasmid, and recombinant parasites were selected with mycophenolic acid (25 µg/mL) and xanthine (50 µg/mL). Stable transgenic parasites were single-cell cloned by limiting dilution.

**Video Microscopy.** Time-lapse video microscopy was conducted in Chamli chambers (LCI Corp., Seoul, Korea) accommodating 18 mm diameter coverslips or 35 mm MatTek glass bottom dishes (Matek corporation) installed on an Eclipse Ti inverted confocal microscope (Nikon France Instruments, Champigny sur Marne, France) set up with a temperature and CO<sub>2</sub>-controlled stage and chamber (LCI Corp., Seoul, Korea). The microscope was equipped with the sCMOS prime camera (Photometrics), a 60× objective, and a CSU X1 spinning disk (Yokogawa, Roper Scientific, Lisses, France). MetaMorph software was used for controlling the microscope (Universal Imaging Corporation, Roper Scientific, Lisses, France). All live microscopy was performed at 37 °C and 5% CO<sub>2</sub>.

**Image Processing.** For image processing, we combined the use of ImageJ, Icy, MATLAB, ChimeraX, and Amira-Avizo (Thermo-Fisher) software. Details of image processing are included in the appropriate protocol sections. Slow motion videos were created using Adobe Premiere with the optical flow module.

**Motility Assays in Collagen1 Fibrous Matrices.** Collagen gels were made using rat tail type I collagen (CellSystems). Nine parts of collagen dissolved in acidic medium were mixed with 1 part of neutralization solution to reach the concentration of 4 mg/mL and promote matrix formation. All solutions were kept in 4 °C during preparation. Then dilution of the gel at a concentration of 2 mg/mL in HBSS<sup>++</sup> supplemented with 1% FCS was rapidly spread in the middle of a MatTek glass bottom dish and incubated for 30 min at 37 °C and 5% CO<sub>2</sub>. Labeling of the collagen fibers was achieved with the recombinant CNA35-EGFP produced in *Escherichia coli* (BL21-DE3 strain) used at 2 μM final concentration according to the protocol.<sup>35</sup> A 50 μL volume of the tachyzoite suspension prepared in 1% FCS HBSS-Ca<sup>2+</sup> was deposited on top of the gel prior to being transferred in the microscopy stage for video microscopy. Once tachyzoites had penetrated within the mesh, images were captured at 1 frame/s. For tracking the fibers during parasite navigation, we used Icy and visualized with green the initial position of the fibers at  $t = 0$  s while we duplicated this frame as many times as the number of the time-lapse frames. Then we merged this “time zero” stack with the original time lapse in which the fibers were colored in magenta. The whitish color accounts for the green and magenta overlay and indicates no displacement, whereas the detection of the green and magenta reveals the fiber displacement during the sequence.

**Tachyzoite 2D Gliding Assays.** Parasites were prepared as described above, and assays were carried on 18 mm plasma-activated glass coverslips coated with either fibronectin (20–50 μg/mL in phosphate-buffered saline (PBS)) or poly-L-lysine (150–300 kDa PLL, 50 μg/mL in PBS). Image analysis included tracking the tachyzoite back and front parts over the gliding time by using Icy as described.<sup>62</sup> “Manual tracking” and “Motion profiler” plugins were used to extract the  $x$ - $y$  position of the back and front spots over time. Having tracked the  $x$ - $y$  positions over time, we used the “Distance profiler” plugin to calculate the distance between the two positions (back and front) over time.

**Reflection Interference Contrast Microscopy.** RICM images were acquired on an inverted microscope (IX71, Olympus) on which a white-light source (HPLS 345, Thorlabs) was coupled using a home-built illumination arm incorporating a diaphragm (SM1D12C, Thorlabs) controlling the illumination numerical aperture (NA = 0.46 in all experiments shown here) and a triple-band spectral filter (FF01-457/530/628-25, Semrock) as described.<sup>63</sup> The usual fluorescence cube in the microscope turret was replaced by polarization optics, allowing separation of the incoming and reflected light (polarizer WP25M-VIS, Thorlabs), polarizing beamsplitter cube (PBS251, Thorlabs), and achromatic imaging flat quarter waveplate (QWP; custom-made, Fichou, France). The sample was imaged with an oil-immersion objective (60XO UPLSApo, Olympus, Japan) onto a sCMOS camera (Orca Flash 4 v2, Hamamatsu) after passing through an autofocus device (CRISP system, ASI imaging, USA) and a home-built image-splitting setup incorporating a variable slit (VA100/M, Thorlabs), achromatic relay lenses (ITL200, Thorlabs), imaging flat dichroic mirrors (FF484-FDi01-25X36 and FF560-FDi01-25X36, Semrock) gently held through curable silicon paste (Sugru, Form-Form, UK), silver mirrors (PFSQ10-03-P01, Thorlabs) and dichroic filters (blue: Semrock FF01-452/45-25; green: FF01-531/46-25; red: FF01-629/56-25, Semrock). In addition, for bright-field (BF) imaging, a red colored glass filter (FGL610S, Thorlabs) was used to filter the light for the microscope illumination arm that was subsequently focused by a long-distance 0.3 NA condenser (all Olympus, Japan). BF and RICM images were acquired simultaneously, in the red channel, and thus show a dim RICM image superimposed. Finally, a custom-built thermostated box (Digital Pixel, UK) enclosing most of the microscope was used to control the temperature at the sample. Image processing was done using ImageJ. Blue, green, and red stacks of images were first manually registered.

RICM images were subsequently filtered using the “FFT band-pass filter” plugin (1–100 pixels) to remove high-frequency noise and uneven illumination background. The two (in the case of simultaneous BF/RICM imaging) or three (in the case of only RICM imaging) RICM images were then superimposed and converted into a RGB image. BF images and RGB RICM images were then segmented using the “trainable Weka segmentation” plugin.<sup>64</sup> For BF images, the classifier was trained to segment the whole parasite, and the outline of the resulting binary image was extracted subsequently. For RICM images, the algorithm was used to separate the “close contact” area defined by the first dark RICM fringe on the parasite surface, the trail (when relevant), the rest of the RICM signal coming from the parasite (when no BF image was present), and the rest of the image. Because the classifier could detect the second dark RICM fringe manual correction of the segmented images was performed afterward to remove incorrect areas classified as “close contact”. A binary image was obtained for the “close contact” area, whereas an 8-bit probability image was extracted for the trail. Analysis of the processed images was also performed using ImageJ. The kymograph was obtained using the plugin “KymoResliceWide”. For measuring the speed of the parasite back end, the corresponding white line on the kymograph was isolated and the positions of the pixels were exported to Origin. After smoothing, the position curve was derived to obtain the velocity of the back end over time.

**Traction Force Microscopy.** TFM setting was adapted from ref 65. The 2 kPa PAA gels were made and mixed with TFM beads (FluoSpheres carboxylate-modified microspheres, ThermoFisher Scientific, 0.2 μm dark red fluorescent,  $\lambda$ : 660/680, 2% solid). The gel was top-coated with fibronectin (20 μg/mL, 30 min, 23 °C) diluted in sodium bicarbonate pH 8.3 (100 mM). Typical samples were made from stocks of 0.7 μL beads mixed in 165 μL of gel supplemented with 1 μL of both tetramethylethylenediamine (TEMED) and ammonium persulfate (APS) 10% using 20 μL of bead-gel suspension for an 18 mm diameter silanized glass coverslip. A 50 μL volume of the tachyzoite suspension prepared in 1% HBSS-Ca<sup>2+</sup> (see above) was deposited on top of the fibronectin-coated PAA gel already filled with 100 μL of 1% HBSS-Ca<sup>2+</sup> in the appropriate chamber and video recording started upon tachyzoite contact with the substrate. MetaMorph streaming option was used for fast recording (<1 frame/s) in both the DIC and far-red channels. Analysis of the TFM beads displacement for extracting the force values carried out using MATLAB. The TFM bead displacement was assessed using as a reference bead position, the frame with a gel area free of parasite (*i.e.*, relaxed position of the gel). Then using the frames taken over time, the bead's displacement was tracked from their initial relaxed position. To check the tachyzoite gliding behavior on a substrate of different stiffness, gels of different PAA concentration and coated with a layer of fibronectin were made using the same protocol, omitting the bead addition step, and the stiffness was controlled by atomic force microscopy.

**Micropatterned Devices.** Micropatterned PEG-fibronectin composite coverslips were engineered by Alveole using the PRIMO patterning with specific area coated with a mix of fibronectin (100 μg/mL) and AlexaFluor647-coupled fibrinogen (10 μg/mL) and other coated with PLL-PEG. Fifty microliters of the tachyzoite suspension prepared in 1% HBSS-Ca<sup>2+</sup> was deposited on top of the fibronectin-coated glass coverslip placed in the chamber and prefilled with 100 μL of buffer prior to video microscopy.

**Rear-Blocked Parasite Assay.** The 0.2 μm diameter beads (FluoSpheres carboxylate-modified microspheres, ThermoFisher Scientific F8807,  $\lambda$ : 660/680, 2% solid) were activated using the microsphere coupling—two-step EDC/Sulfo NHS covalent coupling procedure for Estapor carboxyl-modified dyed microspheres protocol (MerckMillipore). Fifty microliters of the stock-activated bead solution was diluted in 150 μL of MES buffer (50 mM, pH 6.0). Then 30 μL of the bead solution was added to 120 μL of the tachyzoite suspension in 0.15% FCS HBSS<sup>++</sup> (0.15% HBSS). Fifty microliters of the parasite suspension (from either the RHΔKu80, ΔMyoA, RHΔKu80Acb-E, or YFP tachyzoite lines) was deposited on the (50 μg/mL) fibronectin-coated glass coverslips in the microscopy

chamber, which was already filled with 200  $\mu\text{L}$  of 0.15% HBSS<sup>++</sup>. In some experiments, parasites were preincubated for 10 min with 0.5 or 1  $\mu\text{M}$  of either jaspalakinolide or cytochalasin D (Sigma) and video-recorded in the presence of the compounds. For the intracellular mimicking conditions, tachyzoites collected by centrifugation in 0.15% HBSS<sup>++</sup> were rinsed in ENDO buffer referred to here as IC buffer (145 mM KCl; 5 mM NaCl; 1 mM MgCl<sub>2</sub>; 15 mM MES; 15 mM HEPES; pH 8.3)<sup>66</sup> before use, and the activated beads were prepared in IC buffer. The mixture prepared as mentioned above was deposited on the microscopy chamber, which was prefilled with 200  $\mu\text{L}$  of IC buffer. Images were acquired at 1 s intervals for 20 min. To describe the contractile potential of tachyzoites under each experimental condition, we calculated the contraction ratio by measuring two times the length of the parasite body starting from the back until its farther apical point but excluding the conoid to avoid false measurements in case of fluctuating extrusion. The first measure corresponded to the relax position and the second to the maximal contraction. Division of the relaxed *versus* the contracted length provided the contraction ratio. When needed, both DIC and fluorescence channels were recorded at  $\sim 1$  frame/s.

**Bead Flow Assays.** The assay was performed similarly to the rear blocked parasite assay. For tracking the beads, visualizing their tracks and extracting their speed, “Spot detector” and “Track manager” plugins (Icy) were used.

**Expansion Microscopy.** To analyze gliding tachyzoites, we collected the parasites in either in prewarmed 1% FCS HBSS-Ca<sup>2+</sup> or IC buffer, which were centrifuged at low speed to synchronize their sedimentation and left to glide for 10 min on PLL (50  $\mu\text{g}/\text{mL}$ )-coated plasma-activated glass coverslips (37 °C, 5% CO<sub>2</sub>). Gliding was stopped by addition of paraformaldehyde (PFA, 3.2%, 15 min). The tachyzoite surface and trails were immunolabeled with anti-TgPSAG1 antibodies (mAb, clone TP3), and the chimeric TLAP2 protein was detected using the rabbit anti-mCherry antibodies (Institut Curie, TAb-IP Paris, France) directed against the mC tag after cell permeabilization with TritonX-100 (0.1% in PBS, 5 min). The samples were next incubated with appropriate secondary highly cross-adsorbed antibodies (4  $\mu\text{g}/\text{mL}$ , 2h). The ExM protocol was adapted from ref 45. Briefly Acryloyl-X was used at 0.1 mg/mL PBS for 2 h at 23 °C prior to the gelation step, which was performed by placing the gelation solution (80  $\mu\text{L}$ ) on parafilm and the coverslip with the cell sample face down on top of it. Gelation was allowed to proceed at 37 °C for 1 h followed by the digestion step (0.5% Triton X-100, 8 units/mL Proteinase K) carried out overnight at 23 °C. A 4 mm diameter gel core sample was collected with a puncher and immersed in 5 mL of ddH<sub>2</sub>O in a 50 mm diameter Petri dish to promote expansion, while PI staining was concomitantly performed (2.5  $\mu\text{M}$  in PBS). H<sub>2</sub>O was exchanged every 20 min until maximal expansion. The piece of gel was next gently transferred onto a PLL-coated glass coverslip in the minimal liquid volume to avoid gel drift. The 0.2  $\mu\text{m}$  Z-image stacks of parasites in stages were captured using a spinning disk confocal Eclipse-ti Nikon microscope.

**Ultrastructure Expansion Microscopy.** Gliding assays were performed with RH $\Delta$ Ku80MyoA-HA similarly to that for ExM. Additionally, for the invasion assay, HFF cells were plated on a poly-L-lysine-coated glass coverslip to obtain 80% cell confluence on the following day. Parasites were settled on top of the cells by gentle centrifugation (2 min, 250g) and left to invade for 1 h (37 °C, 5% CO<sub>2</sub>). For U-ExM, we followed the protocol developed by the Guichard laboratory,<sup>52</sup> but to optimally preserve both free and intracellular tachyzoite shapes, we found it better to fix the samples before expansion in a solution made of 0.7% formaldehyde and 1% acrylamide in PBS (4–5 h, 37 °C). Next, similar to the ExM protocol, gelation was carried out for 1 h (37 °C). Coverslips with gels were then transferred into  $\sim 2$  mL of the denaturation buffer in a 6-well plate for 15 min (23 °C). Gels were removed from the coverslips with tweezers and transferred to a 35 mm diameter glass Petri dish filled with fresh denaturation buffer for a 60 min incubation at 95 °C. After denaturation, gels were placed in a 150 mm diameter glass Petri dish filled with ddH<sub>2</sub>O for the first expansion. Water was exchanged at least twice every 30 min at room temperature, and gels were

incubated overnight in ddH<sub>2</sub>O. After limited shrinkage in PBS, several 4 mm diameter pieces of gel were collected and deposited on 24-well plates. Gels were then incubated for 3 h at 37 °C under shaking in primary antibodies (antiacetylated  $\alpha$ -tubulin, mAb, clone 6-11B-1) or rabbit  $\alpha$ -polyglutamylated (mAb, clone GT335) and rat anti-HA antibodies (mAb, clone 3F10). Gels were washed in PBS-Tween 0.1% prior to incubation with appropriate secondary highly cross-adsorbed antibodies (4  $\mu\text{g}/\text{mL}$ ) for 150 min at 37 °C and washed again in PBS-Tween 0.1%. Expansion was achieved by controlled immersion in ddH<sub>2</sub>O. The PI staining, final ddH<sub>2</sub>O wash, and gel mounting steps were all performed as mentioned for ExM.

**ExM and U-ExM Image Processing.** 3D reconstruction was achieved with the UCSF ChimeraX software from the raw data (*i.e.*, xyz files) processed with ImageJ to first crop the region of interest and then to apply the “Iterative Deconvolve 3D” plugin for each channel. We used the ImageJ “3D Object counter” plugin to check for the isotropic physical expansion of the specimen by comparing the ratio of the parasite (SAG1 staining) and the nucleus (PI staining) volumes in controlled and expanded extracellular tachyzoite samples. The nucleus sphericity index of motile, nonmotile, and intracellular tachyzoites was compared by thresholding each image object to create 3D binary images, whereas the “3D Object counter” plugin was next used to segment Z-stack binary images and retrieve the volume and surface of the 3D objects (*i.e.*, parasite nucleus and whole body). The sphericity index was calculated using the formula where  $V$  is the volume and  $S$  the surface:

$$\text{sphericity } \Psi = \frac{(36\pi V^2)^{1/3}}{S}$$

The nucleus roundness was obtained by thresholding a Z-Max projection from the Z-stack images and using the “Particle analysis” plugin.

For the tubulin curvature analysis in expanded specimens, we used the “Kappa” plugin in Fiji on the Z-Max projection from Z-stack images of the tachyzoite ventral cMTs (*i.e.*, facing the substrate), which allowed tracing each MT shape and retrieving the mean curvature of each cMT as well as the curvature amplitude over the cMT length (standard deviation).

**MIC2 and SAG1 Analysis in Helical Trail.** Extracellular tachyzoites were let to glide for 15 min prior to be fixed with PFA as described in the ExM section. A double immunolabeling was performed sequentially using the anti-TgSAG1 protein (clone TP3, 30 min, 23 °C) and the anti-TgMIC2 (clone 6D10, overnight, 4 °C) as primary antibodies, each followed by incubation with appropriate secondary highly cross-adsorbed antibodies (4  $\mu\text{g}/\text{mL}$ , 2 h). Images were acquired on the Axio Imager Z1 Zeiss microscope using the Zeiss imaging software ZEN before being processed using Fiji software.

To determine the size and position of the adhesion point formed at the early step of the helical cycle (*i.e.*, coinciding with the kink) on the MIC2/SAG1 immunolabeled trails, we used the machine-learning-based segmentation of the real-time RICM sequence as a template. The region of interest for the trail trajectory, the angular area, and the parasite apical adhesion area were defined manually with Fiji: the distance between the center of adhesion point and the angle point was measured for six angles over a sequence of successive helical cycles, which allowed positioning the apical adhesion at about +0.170  $\mu\text{m}$  downstream the angle point, and the size of the adhesion point was estimated around 0.5  $\mu\text{m}$ . Applying these values on the MIC2/SAG1 labeled trails, it was possible to accurately identify the adhesion and angle area over the profiles of fluorescence intensity measured for the whole trails trajectories that in total defined 40 helical cycles performed by eight tachyzoites. The fluorescence intensity is given as a ratio by normalizing on the mean intensity value.

**Quantification and Statistical Analysis.** Data were statistically analyzed, and plots were made using GraphPad Prism 6.0 software for Windows (La Jolla, CA, USA). Data are presented as mean  $\pm$  standard error of mean if not indicated otherwise. Figure legends include the statistical test and resulting comparison when appropriate.

For Figure 4A, Figure 7A, and Figures S3A and S5B,C, an unpaired *t* test was used with significance being represented as a *p* value <0.05, and the *n* indicated represents the parasite sample size or the number of individual microtubules analyzed. For Figure 4E, Figure 5A, and Figure S5A, an unpaired Kruskal–Wallis test was performed, and the *n* indicates the sample size. For the table in Figure 5A, a chi-square test followed by Fisher's exact test was used, with the *n* showing the proportions analyzed.

## ASSOCIATED CONTENT

### Supporting Information

The Supporting Information is available free of charge at <https://pubs.acs.org/doi/10.1021/acsnano.0c01893>.

Helical and circular gliding by *T. gondii* tachyzoites; tachyzoite apical adhesion site is not enriched in MIC2 and SAG1 proteins; frequency and duration of *T. gondii* tachyzoite gliding behavior depends on the substrate stiffness; prolonged and exacerbated contraction induced upon tachyzoite posterior immobilization leads to membrane leakage; expansion microscopy allows uncovering cMT local selective compression and torsion in gliding tachyzoites (PDF)

Movie 1: Parasite moving in 3D collagen fibers1 (AVI)

Movie 2: Parasite moving 3D collagen fibers2 (AVI)

Movie 3a: Parasite helical gliding in 2D (AVI)

Movie 3b: Slow motion but same as movie 3a (AVI)

Movie 4: Parasite circular gliding in 2D (AVI)

Movie 5: RICM analysis of parasite helical gliding (AVI)

Movie 6: RICM-pulling on or breaking the trail (AVI)

Movie 7a: TFM analysis of parasite helical gliding (AVI)

Movie 7b: Slow motion but same as movie 7a (AVI)

Movie 8: Parasite helical gliding on micropattern Alveole1 (AVI)

Movie 9: Parasite helical gliding micropattern Alveole2 (AVI)

Movie 10: Parasite base blocked by microbeads (AVI)

Movie 11: Bead release from the base of a moving parasite (AVI)

Movie 12: Parasite contraction in the presence of drugs (AVI)

Movie 13: Actin dynamics in gliding or immobilized parasites (AVI)

Movie 14: Bead flow and bead release in tachyzoites (AVI)

## AUTHOR INFORMATION

### Corresponding Author

**Isabelle Tardieux** – *Institute for Advanced Biosciences (IAB), Team Membrane Dynamics of Parasite–Host Cell Interactions, CNRS UMR5309, INSERM U1209, Université Grenoble Alpes, 38700 Grenoble, France*; [orcid.org/0000-0002-5677-7463](https://orcid.org/0000-0002-5677-7463); Email: [isabelle.tardieux@inserm.fr](mailto:isabelle.tardieux@inserm.fr)

### Authors

**Georgios Pavlou** – *Institute for Advanced Biosciences (IAB), Team Membrane Dynamics of Parasite–Host Cell Interactions, CNRS UMR5309, INSERM U1209, Université Grenoble Alpes, 38700 Grenoble, France*

**Bastien Touquet** – *Institute for Advanced Biosciences (IAB), Team Membrane Dynamics of Parasite–Host Cell Interactions, CNRS UMR5309, INSERM U1209, Université Grenoble Alpes, 38700 Grenoble, France*

**Luis Vigetti** – *Institute for Advanced Biosciences (IAB), Team Membrane Dynamics of Parasite–Host Cell Interactions, CNRS UMR5309, INSERM U1209, Université Grenoble Alpes, 38700 Grenoble, France*

**Patricia Renesto** – *Institute for Advanced Biosciences (IAB), Team Membrane Dynamics of Parasite–Host Cell Interactions, CNRS UMR5309, INSERM U1209, Université Grenoble Alpes, 38700 Grenoble, France; TIMC-IMAG UMR 5525 - UGA CNRS, 38700 Grenoble, France*

**Alexandre Bougdour** – *Institute for Advanced Biosciences (IAB), Team Host–Pathogen Interactions & Immunity to Infections, CNRS UMR5309, INSERM U1209, Université Grenoble Alpes, 38700 Grenoble, France*

**Delphine Debarre** – *Laboratoire Interdisciplinaire de Physique, UMR CNRS, 5588, Université Grenoble Alpes, Grenoble 38402, France*

**Martial Balland** – *Laboratoire Interdisciplinaire de Physique, UMR CNRS, 5588, Université Grenoble Alpes, Grenoble 38402, France*

Complete contact information is available at: <https://pubs.acs.org/10.1021/acsnano.0c01893>

### Author Contributions

Conceptualization, I.T., M.B., G.P.; Software, M.B., D.D., G.P.; Formal Analysis, G.P., B.T., D.D., L.V.; Funding acquisition, I.T.; Investigation, G.P., B.T., I.T., V.L., D.D., P.R., A.B.; Methodology, I.T., G.P., B.T., A.B.; Project administration, I.T.; Supervision, I.T., M.B., P.R.; Validation, I.T., G.P., M.B., D.D.; Visualization, G.P., B.T., L.V.; Writing—original draft, I.T. Writing—review and editing, I.T., G.P., P.R., A.B., M.B., D.D.

### Funding

This work has been funded by the IAB department “Prevention and Therapy of Chronic Diseases (Grenoble, France) with an internal grant. The University Grenoble-Alpes and the Fondation pour la Recherche Médicale (FRM FDT201904008408) awarded to G.P. with a 3 year Ph.D. fellowship and 6 month Ph.D. extension fellowship, respectively.

### Notes

The authors declare no competing financial interest.

### ACKNOWLEDGMENTS

We thank T. Boudou for help with the collagen gels, T. Andersen, V. Petrolli, and A. Ruppel for help in setting and analyzing the TFM assays. They all belong to the Laboratoire Interdisciplinaire de Physique, UMR CNRS, 5588, Université Grenoble Alpes, France. We thank C. Guilluy for the AFM assays to probe gels, M. Bogeda for help in micropatterning (IAB, Grenoble), and the Alveole team for providing the composite micropatterns. We thank the therapeutic antibodies (Tab-IP) and recombinant antibodies platform from the Curie Institute, Paris, France for providing the anti-mCherry antibodies.

### REFERENCES

- (1) Scarpa, E.; Mayor, R. Collective Cell Migration in Development. *J. Cell Biol.* **2016**, *212*, 143–155.
- (2) Friedl, P.; Weigelin, B. Interstitial Leukocyte Migration and Immune Function. *Nat. Immunol.* **2008**, *9*, 960–969.
- (3) Tschumperlin, D. J. Fibroblasts and the Ground They Walk On. *Physiology* **2013**, *28*, 380–390.

- (4) Raftopoulou, M.; Hall, A. Cell Migration: Rho GTPases Lead the Way. *Dev. Biol.* **2004**, *265*, 23–32.
- (5) Gardel, M. L.; Schneider, I. C.; Aratyn-Schaus, Y.; Waterman, C. M. Mechanical Integration of Actin and Adhesion Dynamics in Cell Migration. *Annu. Rev. Cell Dev. Biol.* **2010**, *26*, 315–333.
- (6) Yamada, K. M.; Sixt, M. Mechanisms of 3D Cell Migration. *Nat. Rev. Mol. Cell Biol.* **2019**, *20*, 738–752.
- (7) Petrie, R. J.; Koo, H.; Yamada, K. M. Generation of Compartmentalized Pressure by a Nuclear Piston Governs Cell Motility in a 3D Matrix. *Science* **2014**, *345*, 1062–1065.
- (8) Copos, C. A.; Walcott, S.; del Álamo, J. C.; Bastounis, E.; Mogilner, A.; Guy, R. D. Mechanosensitive Adhesion Explains Stepping Motility in Amoeboid Cells. *Biophys. J.* **2017**, *112*, 2672–2682.
- (9) Robert-Gangneux, F.; Darde, M.-L. Epidemiology of and Diagnostic Strategies for Toxoplasmosis. *Clin. Microbiol. Rev.* **2012**, *25*, 264–296.
- (10) Tardieux, I.; Baum, J. Reassessing the Mechanics of Parasite Motility and Host-Cell Invasion. *J. Cell Biol.* **2016**, *214*, 507–515.
- (11) Håkansson, S.; Morisaki, H.; Heuser, J.; Sibley, L. D. Time-Lapse Video Microscopy of Gliding Motility in *Toxoplasma Gondii* Reveals a Novel, Biphasic Mechanism of Cell Locomotion. *Mol. Biol. Cell* **1999**, *10*, 3539–3547.
- (12) Amino, R.; Thiberge, S.; Martin, B.; Celli, S.; Shorte, S.; Frischknecht, F.; Ménard, R. Quantitative Imaging of *Plasmodium* Transmission from Mosquito to Mammal. *Nat. Med.* **2006**, *12*, 220–224.
- (13) Münter, S.; Sabass, B.; Selhuber-Unkel, C.; Kudryashev, M.; Hegge, S.; Engel, U.; Spatz, J. P.; Matuschewski, K.; Schwarz, U. S.; Frischknecht, F. *Plasmodium* Sporozoite Motility Is Modulated by the Turnover of Discrete Adhesion Sites. *Cell Host Microbe* **2009**, *6*, 551–562.
- (14) Frischknecht, F.; Matuschewski, K. *Plasmodium* Sporozoite Biology. *Cold Spring Harbor Perspect. Med.* **2017**, *7*, a025478.
- (15) Amino, R.; Giovannini, D.; Thiberge, S.; Gueirard, P.; Boisson, B.; Dubremetz, J.-F.; Prévost, M.-C.; Ishino, T.; Yuda, M.; Ménard, R. Host Cell Traversal Is Important for Progression of the Malaria Parasite through the Dermis to the Liver. *Cell Host Microbe* **2008**, *3*, 88–96.
- (16) Kan, A.; Tan, Y.-H.; Angrisano, F.; Hanssen, E.; Rogers, K. L.; Whitehead, L.; Mollard, V. P.; Cozijnsen, A.; Delves, M. J.; Crawford, S.; Sinden, R. E.; McFadden, G. I.; Leckie, C.; Bailey, J.; Baum, J. Quantitative Analysis of *Plasmodium* Ookinete Motion in Three Dimensions Suggests a Critical Role for Cell Shape in the Biomechanics of Malaria Parasite Gliding Motility. *Cell. Microbiol.* **2014**, *16*, 734–750.
- (17) Bichet, M.; Joly, C.; Hadj Henni, A.; Guilbert, T.; Xemard, M.; Tafani, V.; Lagal, V.; Charras, G.; Tardieux, I. The *Toxoplasma*-Host Cell Junction Is Anchored to the Cell Cortex to Sustain Parasite Invasive Force. *BMC Biol.* **2014**, *12*, 773.
- (18) Frixione, E.; Mondragón, R.; Meza, I. Kinematic Analysis of *Toxoplasma Gondii* Motility. *Cell Motil. Cytoskeleton* **1996**, *34*, 152–163.
- (19) Leung, J. M.; Rould, M. A.; Konradt, C.; Hunter, C. A.; Ward, G. E. Disruption of TgPHIL1 Alters Specific Parameters of *Toxoplasma Gondii* Motility Measured in a Quantitative, Three-Dimensional Live Motility Assay. *PLoS One* **2014**, *9*, No. e85763.
- (20) Carruthers, V. B.; Tomley, F. M. Receptor-Ligand Interaction and Invasion: Microneme Proteins in Apicomplexans. *Subcell Biochem* **2008**, *47*, 33–45.
- (21) Lagal, V.; Binder, E. M.; Huynh, M.-H.; Kafsack, B. F. C.; Harris, P. K.; Diez, R.; Chen, D.; Cole, R. N.; Carruthers, V. B.; Kim, K. *Toxoplasma Gondii* Protease TgSUB1 Is Required for Cell Surface Processing of Micronemal Adhesive Complexes and Efficient Adhesion of Tachyzoites: TgSUB1 Microneme Protein Processing. *Cell. Microbiol.* **2010**, *12*, 1792–1808.
- (22) Opitz, C.; Soldati, D. The Glideosome: A Dynamic Complex Powering Gliding Motion and Host Cell Invasion by *Toxoplasma Gondii*. *Mol. Microbiol.* **2002**, *45*, 597–604.
- (23) Fréchal, K.; Dubremetz, J.-F.; Lebrun, M.; Soldati-Favre, D. Gliding Motility Powers Invasion and Egress in Apicomplexa. *Nat. Rev. Microbiol.* **2017**, *15*, 645–660.
- (24) Andenmatten, N.; Egarter, S.; Jackson, A. J.; Jullien, N.; Herman, J.-P.; Meissner, M. Conditional Genome Engineering in *Toxoplasma Gondii* Uncovers Alternative Invasion Mechanisms. *Nat. Methods* **2013**, *10*, 125–127.
- (25) Bichet, M.; Touquet, B.; Gonzalez, V.; Florent, I.; Meissner, M.; Tardieux, I. Genetic Impairment of Parasite Myosin Motors Uncovers the Contribution of Host Cell Membrane Dynamics to *Toxoplasma* Invasion Forces. *BMC Biol.* **2016**, *14*, 97.
- (26) Graindorge, A.; Fréchal, K.; Jacot, D.; Salamun, J.; Marq, J. B.; Soldati-Favre, D. The Conoid Associated Motor MyoH Is Indispensable for *Toxoplasma Gondii* Entry and Exit from Host Cells. *PLoS Pathog.* **2016**, *12*, No. e1005388.
- (27) Morrissette, N. S.; Sibley, L. D. Cytoskeleton of Apicomplexan Parasites. *Microbiol. Mol. Biol. Rev.* **2002**, *66*, 21–38.
- (28) Fréchal, K.; Polonais, V.; Marq, J.-B.; Stratmann, R.; Limenitakis, J.; Soldati-Favre, D. Functional Dissection of the Apicomplexan Glideosome Molecular Architecture. *Cell Host Microbe* **2010**, *8*, 343–357.
- (29) Mueller, C.; Graindorge, A.; Soldati-Favre, D. Functions of Myosin Motors Tailored for Parasitism. *Curr. Opin. Microbiol.* **2017**, *40*, 113–122.
- (30) Liu, J.; He, Y.; Benmerzouga, I.; Sullivan, W. J.; Morrissette, N. S.; Murray, J. M.; Hu, K. An Ensemble of Specifically Targeted Proteins Stabilizes Cortical Microtubules in the Human Parasite *Toxoplasma Gondii*. *Mol. Biol. Cell* **2016**, *27*, 549–571.
- (31) Quadt, K. A.; Streichfuss, M.; Moreau, C. A.; Spatz, J. P.; Frischknecht, F. Coupling of Retrograde Flow to Force Production During Malaria Parasite Migration. *ACS Nano* **2016**, *10*, 2091–2102.
- (32) Whitelaw, J. A.; Latorre-Barragan, F.; Gras, S.; Pall, G. S.; Leung, J. M.; Heaslip, A.; Egarter, S.; Andenmatten, N.; Nelson, S. R.; Warsaw, D. M.; Ward, G. E.; Meissner, M. Surface Attachment, Promoted by the Actomyosin System of *Toxoplasma Gondii* Is Important for Efficient Gliding Motility and Invasion. *BMC Biol.* **2017**, *15*, 1.
- (33) Tosetti, N.; Dos Santos Pacheco, N.; Soldati-Favre, D.; Jacot, D. Three F-Actin Assembly Centers Regulate Organelle Inheritance, Cell-Cell Communication and Motility in *Toxoplasma gondii*. *eLife* **2019**, *8*, e42669.
- (34) Mouw, J. K.; Ou, G.; Weaver, V. M. Extracellular Matrix Assembly: A Multiscale Deconstruction. *Nat. Rev. Mol. Cell Biol.* **2014**, *15*, 771–785.
- (35) Aper, S. J. A.; van Spreuwel, A. C. C.; van Turnhout, M. C.; van der Linden, A. J.; Pieters, P. A.; van der Zon, N. L. L.; de la Rambelje, S. L.; Bouten, C. V. C.; Merckx, M. Colorful Protein-Based Fluorescent Probes for Collagen Imaging. *PLoS One* **2014**, *9*, No. e114983.
- (36) Ejigiri, I.; Ragheb, D. R. T.; Pino, P.; Coppi, A.; Bennett, B. L.; Soldati-Favre, D.; Sinnis, P. Shedding of TRAP by a Rhomboid Protease from the Malaria Sporozoite Surface Is Essential for Gliding Motility and Sporozoite Infectivity. *PLoS Pathog.* **2012**, *8*, No. e1002725.
- (37) Huynh, M.-H.; Carruthers, V. B. *Toxoplasma* MIC2 Is a Major Determinant of Invasion and Virulence. *PLoS Pathog.* **2006**, *2*, No. e84.
- (38) Gras, S.; Jackson, A.; Woods, S.; Pall, G.; Whitelaw, J.; Leung, J. M.; Ward, G. E.; Roberts, C. W.; Meissner, M. Parasites Lacking the Micronemal Protein MIC2 Are Deficient in Surface Attachment and Host Cell Egress, but Remain Virulent *In Vivo*. *Wellcome Open Res.* **2017**, *2*, 32.
- (39) Buguliskis, J. S.; Brossier, F.; Shuman, J.; Sibley, L. D. Rhomboid 4 (ROM4) Affects the Processing of Surface Adhesins and Facilitates Host Cell Invasion by *Toxoplasma Gondii*. *PLoS Pathog.* **2010**, *6*, No. e1000858.
- (40) Martiel, J.-L.; Leal, A.; Kurzawa, L.; Balland, M.; Wang, I.; Vignaud, T.; Tseng, Q.; Théry, M. Measurement of Cell Traction Forces with ImageJ. *Methods Cell Biol.* **2015**, *125*, 269–287.

- (41) Hegge, S.; Uhrig, K.; Streichfuss, M.; Kynast-Wolf, G.; Matuschewski, K.; Spatz, J. P.; Frischknecht, F. Direct Manipulation of Malaria Parasites with Optical Tweezers Reveals Distinct Functions of *Plasmodium* Surface Proteins. *ACS Nano* **2012**, *6*, 4648–4662.
- (42) Stadler, R. V.; White, L. A.; Hu, K.; Helmke, B. P.; Guilford, W. H. Direct Measurement of Cortical Force Generation and Polarization in a Living Parasite. *Mol. Biol. Cell* **2017**, *28*, 1912–1923.
- (43) Biais, N.; Higashi, D. L.; Bruijic, J.; So, M.; Sheetz, M. P. Force-Dependent Polymorphism in Type IV Pili Reveals Hidden Epitopes. *Proc. Natl. Acad. Sci. U. S. A.* **2010**, *107*, 11358–11363.
- (44) Perschmann, N.; Hellmann, J. K.; Frischknecht, F.; Spatz, J. P. Induction of Malaria Parasite Migration by Synthetically Tunable Microenvironments. *Nano Lett.* **2011**, *11*, 4468–4474.
- (45) Asano, S. M.; Gao, R.; Wassie, A. T.; Tillberg, P. W.; Chen, F.; Boyden, E. S. Expansion Microscopy: Protocols for Imaging Proteins and RNA in Cells and Tissues. *Curr. Protoc. Cell Biol.* **2018**, *80*, No. e56.
- (46) Egarter, S.; Andenmatten, N.; Jackson, A. J.; Whitelaw, J. A.; Pall, G.; Black, J. A.; Ferguson, D. J. P.; Tardieux, I.; Mogilner, A.; Meissner, M. The *Toxoplasma* Acto-MyoA Motor Complex Is Important but Not Essential for Gliding Motility and Host Cell Invasion. *PLoS One* **2014**, *9*, No. e91819.
- (47) Bubb, M. R.; Spector, L.; Beyer, B. B.; Fosen, K. M. Effects of Jasplakinolide on the Kinetics of Actin Polymerization. An Explanation for Certain *In Vivo* Observations. *J. Biol. Chem.* **2000**, *275*, S163–S170.
- (48) Sampath, P.; Pollard, T. D. Effects of Cytochalasin, Phalloidin, and PH on the Elongation of Actin Filaments. *Biochemistry* **1991**, *30*, 1973–1980.
- (49) Periz, J.; Whitelaw, J.; Harding, C.; Gras, S.; Del Rosario Minina, M. I.; Latorre-Barragan, F.; Lemgruber, L.; Reimer, M. A.; Insall, R.; Heaslip, A.; Meissner, M. *Toxoplasma Gondii* F-Actin Forms an Extensive Filamentous Network Required for Material Exchange and Parasite Maturation. *eLife* **2017**, *6*, e24119.
- (50) Shaw, M. K.; Tilney, L. G. Induction of an Acrosomal Process in *Toxoplasma Gondii*: Visualization of Actin Filaments in a Protozoan Parasite. *Proc. Natl. Acad. Sci. U. S. A.* **1999**, *96*, 9095–9099.
- (51) Del Rosario, M.; Periz, J.; Pavlou, G.; Lyth, O.; Latorre-Barragan, F.; Das, S.; Pall, G. S.; Stortz, J. F.; Lemgruber, L.; Whitelaw, J. A.; Baum, J.; Tardieux, I.; Meissner, M. Apicomplexan F-Actin Is Required for Efficient Nuclear Entry during Host Cell Invasion. *EMBO Rep.* **2019**, *20*, e48896.
- (52) Gambarotto, D.; Zwettler, F. U.; Le Guennec, M.; Schmidt-Cernohorska, M.; Fortun, D.; Borgers, S.; Heine, J.; Schloetel, J.-G.; Reuss, M.; Unser, M.; Boyden, E. S.; Sauer, M.; Hamel, V.; Guichard, P. Imaging Cellular Ultrastructures Using Expansion Microscopy (U-ExM). *Nat. Methods* **2019**, *16*, 71–74.
- (53) Plessmann, U.; Reiter-Owona, I.; Lechtreck, K.-F. Posttranslational Modifications of  $\alpha$ -Tubulin of *Toxoplasma Gondii*. *Parasitol. Res.* **2004**, *94*, 386–389.
- (54) Brangwynne, C. P.; MacKintosh, F. C.; Kumar, S.; Geisse, N. A.; Talbot, J.; Mahadevan, L.; Parker, K. K.; Ingber, D. E.; Weitz, D. A. Microtubules Can Bear Enhanced Compressive Loads in Living Cells Because of Lateral Reinforcement. *J. Cell Biol.* **2006**, *173*, 733–741.
- (55) Kabir, A. Md. R.; Inoue, D.; Afrin, T.; Mayama, H.; Sada, K.; Kakugo, A. Buckling of Microtubules on a 2D Elastic Medium. *Sci. Rep.* **2015**, *5*, 17222.
- (56) Leung, J. M.; He, Y.; Zhang, F.; Hwang, Y.-C.; Nagayasu, E.; Liu, J.; Murray, J. M.; Hu, K. Stability and Function of a Putative Microtubule-Organizing Center in the Human Parasite *Toxoplasma Gondii*. *Mol. Biol. Cell* **2017**, *28*, 1361–1378.
- (57) Harding, C. R.; Gow, M.; Kang, J. H.; Shortt, E.; Manalis, S. R.; Meissner, M.; Lourido, S. Alveolar Proteins Stabilize Cortical Microtubules in *Toxoplasma Gondii*. *Nat. Commun.* **2019**, *10*, 401.
- (58) Cramer, L. P. Forming the Cell Rear First: Breaking Cell Symmetry to Trigger Directed Cell Migration. *Nat. Cell Biol.* **2010**, *12*, 628–632.
- (59) Huynh, M.-H.; Carruthers, V. B. Tagging of Endogenous Genes in a *Toxoplasma Gondii* Strain Lacking Ku80. *Eukaryotic Cell* **2009**, *8*, 530–539.
- (60) Andenmatten, N.; Egarter, S.; Jackson, A. J.; Jullien, N.; Herman, J.-P.; Meissner, M. Conditional Genome Engineering in *Toxoplasma Gondii* Uncovers Alternative Invasion Mechanisms. *Nat. Methods* **2013**, *10*, 125–127.
- (61) Farhat, D. C.; Swale, C.; Dard, C.; Cannella, D.; Ortet, P.; Barakat, M.; Sindikubwabo, F.; Belmudes, L.; De Bock, P.-J.; Couté, Y.; Bougdour, A.; Hakimi, M.-A. A MORC-Driven Transcriptional Switch Controls *Toxoplasma* Developmental Trajectories and Sexual Commitment. *Nat. Microbiol.* **2020**, *5*, 570–583.
- (62) Pavlou, G.; Tardieux, I. Phenotyping *Toxoplasma* Invasive Skills by Fast Live Cell Imaging. *Methods Mol. Biol.* **2020**, *2071*, 209–220.
- (63) Davies, H. S.; Baranova, N. S.; El Amri, N.; Coche-Guérente, L.; Verdier, C.; Bureau, L.; Richter, R. P.; Débarre, D. An Integrated Assay to Probe Endothelial Glycocalyx-Blood Cell Interactions under Flow in Mechanically and Biochemically Well-Defined Environments. *Matrix Biol.* **2019**, *78–79*, 47–59.
- (64) Arganda-Carreras, I.; Kaynig, V.; Rueden, C.; Eliceiri, K. W.; Schindelin, J.; Cardona, A.; Sebastian Seung, H. Trainable Weka Segmentation: A Machine Learning Tool for Microscopy Pixel Classification. *Bioinformatics* **2017**, *33*, 2424–2426.
- (65) Martiel, J.-L.; Leal, A.; Kurzawa, L.; Bolland, M.; Wang, I.; Vignaud, T.; Tseng, Q.; Théry, M. Measurement of Cell Traction Forces with ImageJ. *Methods Cell Biol.* **2015**, *125*, 269–287.
- (66) Moudy, R.; Manning, T. J.; Beckers, C. J. The Loss of Cytoplasmic Potassium upon Host Cell Breakdown Triggers Egress of *Toxoplasma Gondii*. *J. Biol. Chem.* **2001**, *276*, 41492–41501.

### 2.1.5 Discussion and perspectives

In this study, we report for the first time on the actomyosin-based traction forces the tachyzoite needs to apply against the substrate to propel forward. We eventually propose that the chemical energy generated by the functional actomyosin could be loaded on the stable, but not necessarily rigid cortical microtubules. Indeed while early after the parasite starts to move, it bents inward its apex, which leads to an increase in the body curvature and coincides with a pause in the motile pattern before the parasite extends again, a step associated with the typical phase of acceleration. As a result, the tachyzoite performs a helical trajectory and finds its way to navigate inside fibrous and heterogeneous matrices that it likely encounters before to reach host cells. We brought evidence that the parasite made contact with the fiber and pulls on it whereas in 2D it also builds an early contact with the substrate which can be further described as a stable adhesion, a prerequisite for the properly coordinated front and back attachment-detachment that, overall looks like a fine-tuned choreography. This study, especially owing to the panel of biophysical approaches it uses, opens a new window for further investigation in particular for identifying the components and the nano-architecture of the front adhesion and for getting a comprehensive understanding of how parasite material is deposited to build tracks underneath. The preliminary quantitative modeling of the track would agree with a cylinder that would be loosely glued to the surface and coupled to periodic firm anchors but this warrants confirmation with high resolution imaging and would deserve to be studied under 3D settings. It is well known that microneme secretion is crucially required for triggering the gliding motile behavior: proteins that are secreted are ideal candidates to be screened for their role in this strong early adhesion. It would be very exciting if we could identify proteins specifically positioned at these elusive adhesion platforms and then dissect how some of these interact with varying surfaces while others connect to the actomyosin machinery. It would also be exciting to follow their spatiotemporal assembly/disassembly over the helical cycle and the molecular mechanisms of their force-transmitting properties. A second investigation axis would be to decipher the bending properties and flexural behavior of the cortical microtubules and their physical connection with the actomyosin system at least if one considers that energy can be transferred to the microtubule cytoskeleton during helical motility. It is quite remarkable that these cortical microtubules keep their shape and show no cycle of assembly-disassembly in free non-dividing, hence potentially motile parasites. However this long-standing statement should be addressed in more details in the future since recent work on *Plasmodium* shows that cytoplasmic microtubules undergo some level of shrinkage and growth, although on the time scale of hours to days rather than the seconds time scale observed in mammalian cells. Furthermore, the same study points that sporozoites engineered to assemble microtubules of reduced length and numbers show changes in their body

curvature that affects sporozoite gliding potential and in turn infectivity (Spreng *et al.*, 2019). Recently, researchers highlighted the connection of alveolar integral proteins with the microtubule cortical network, which similarly to several microtubule-associated proteins, have been shown to secure the stability of these microtubules. Thus, the bending capacity of the network might be in part driven by the alveoli structural organization. The interplay between the actomyosin and the microtubules during the motile behavior is nicely evidenced by the bead antero-posterior trajectory just prior and during movement, a trajectory that follows the helical path of the cortical microtubules. Finally, an important issue that we would like to address is the presence of a motor other than MyoA, which may serve as a rear wheel to assist the twisting thrust during helical propelling.

Live imaging and image analysis speaking, this study could be used as an example guide for tracking very fast cells, therefore implying the collection of large and high-content image dataset and one perspective would be to bring artificial intelligence software in the image analysis task. The migration and cell invasion processes of *T. gondii* tachyzoites, which are small and rapid cells compared to most metazoan cells, not only need fast recording but also accurate monitoring of a single or several specific fluorescent reporters. Therefore the live imaging assays often require capturing images using more than one laser channel, a condition that results in a huge number of signals to analyze. For example we needed the brightfield and a parasite fluorescent marker that was stable enough so to reliably track the speed of the parasite during gliding or to follow the behavior and fate of the zoite-cell junction during cell invasion. In some instances, applying machine learning to dynamically detect specific shape and transient shape changes could ease the tracking of a parasite, even in complex 3D contexts and would even avoid the need for using a fluorescent marker. On other circumstances, the segmentation of fluorescent signal over hundreds of images can also greatly benefit from machine learning as we have showed in the RICM-based sequence analysis.

In conclusion, this work only starts to give light to some biomechanical properties of the *T. gondii* tachyzoite. However, it already proves that a number of “old” but refined or recent imaging in conjunction with force microscopy techniques can be applied to this small and rapid cell to get the desired information at the millisecond and nanometer scales, thereby providing a new framework to understand the complex and unique way evolved by this parasite to move.

# Chapter 2

## 2.2 Chapter 2 - Investigating host cell invasion by the *T. gondii* tachyzoite with a focus on the late steps of the process

### 2.2.1 Context and questions

#### A variety of strategies to sculpt the plasma membrane of the hosting cell as an entry vesicle and eventually a parasitophorous vacuole

Intracellular protozoans utilize diverse tactics to overcome the challenge of invading cells from a range of metazoan hosts and to further shape a protective and feeding membrane-bound niche in order to sustain transient to prolonged-time intracellular residency (Pavlou *et al*, 2019). After contacting the surface of the target cell, they indeed are able to divert and sculpt a piece of the plasma membrane to reach the intracellular milieu and initiate the folding of a microbe-enclosing compartment. This membrane subversion often proceeds *via* the formation of outward protrusions of various architecture including large ruffles or thinner pseudopods, which all grow driven by local actin polymerization, and progressively enwrap the microbes in a nascent vacuole. In other situations, the subversion of plasma membrane occurs *via* inward budding through processes grouped as endocytosis, for which actin polymerization also helps in pulling or/and pushing the membrane bud inside the cell (Figure 19). Some protozoans have also evolved strategies to co-hijack the plasma membrane *via* the endocytosis machinery, and intracellular pools of membrane through the exocytosis pathway as in the case of lysosomes that are recruited at and then fuse with the PM at the site of entry. This is exemplified with the trypomastigote developmental stage of *Trypanosoma cruzi* or the metacyclic promastigote stage of *Leishmania* (Tardieux *et al*, 1992)(Pavlou *et al*, 2019).

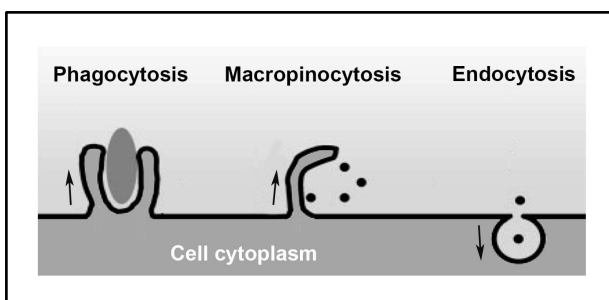


**Figure 19. Schematic representation of typical subversion of the host cell PM properties by protozoans to access the intracellular environment.** In phagocytosis, actin assembly causes membrane extensions in the outward direction and progressively engulf the

particle. In the same outward topology, macropinocytosis works with F-actin driven protrusions which internalize the particle within macropinosomes. In the inward opposite direction as during endocytosis, particles are taken up within PM local invaginations with the help of F-actin and are internalized when the pits (coated or not) separate from the PM. The arrows indicate the outward and inward directions the PM folds during each of these processes. Adapted from Khalil *et al*, 2006.

*T. gondii* performs differently since in contrast to the aforementioned cases, it is the parasite itself that provides the force that eventually directs the budding of the PM, and thereby the folding of an **entry vesicle**. As mentioned in the Introduction, the *T. gondii* tachyzoite reproduces asexually by giving birth to usually two offsprings but this process depends from nutrients that can only be supplied by the hosting cell. In this context, the free tachyzoite displays an impressive ability to **actively** invade virtually any type of nucleated cell and this action mobilizes mainly two distinct machineries. The first one is made by the RON protein complex and can be qualified as an **invasive nanodevice** since it is delivered by the tachyzoite just before any attempt of active invasion, and the second is the **actomyosin motor system** organized in the narrow space between the PM and the IMC within the trilayer pellicle (Introduction 1.3). The secretion of the nanodevice from the rhoptry is a tightly regulated event with still many unknowns, in particular as regard to the upstream signal(s) required for secretion. However, this event remains so far the first that can be visualized and thus reliably informs on the on-going invasion attempt even before changes due to the bud formation can be detected in the host cell surface. The two machineries tightly work together during the invasion event since the invasive nanodevice shapes a **circular bridge** between the two cells, namely the **Zoite Cell Junction (ZCJ)**, which our lab shows to act as a force anchor point to transmit the driving force that propels the tachyzoite inside the cell. To briefly describe the invasion sequence according to the prevailing model, let's consider the succession of five steps that are all directed by the invasive nanodevice. This sequence includes (i) the release of the invasive nanodevice from the rhoptry to the tip of the conoid in contact with the target cell surface, (ii) the insertion of the invasive nanodevice into the target cell PM and underlying cortex, (iii) the pulling force applied by the parasite on the static but somehow elastic invasive nanodevice, (iv) the closure of the invasive nanodevice once the budding entry vesicle encloses the whole tachyzoite body, and (v) the pinching off of the budding entry vesicle from the plasma membrane to release a separate membrane bound compartment enclosing the parasite and defined as the PV.

To collect dynamic insights possibly for these five steps, our lab has engineered a tachyzoite in which the RON2 protein was replaced by a fluorescent RON2 chimeric protein using tagging at the C terminal part and which proved fully functional (Huynh & Carruthers, 2009). As shown in Figure 6, the C terminal region of RON2 remains exposed to the outside and contains a loop region that fits in the cleft designed by the AMA1 protein but also accommodates the addition of the fluorescent tag at the Cterminal end. The invasive behavior of RON2-mCherry (RON2-mC) tachyzoites was then monitored by fast and high resolution live imaging allowing to demonstrate that once the RON2-mC positive nanodevice is delivered into the recipient PM, the parasite tracts itself in the tight PM bud it directs (Bichet *et al*, 2014). Interestingly, it was possible for the first

time to follow the “one-shot” release of the RON2-mC material, which clearly signs for the release of a fully functional complex and then its delivery into the PM to further delineate the ZCJ.

When I arrived in the lab, the transgenic fluorescent RON2-mC parasite line and a number of human and murine cell lines expressing a variety of fluorescent reporters for the cell PM or cortex were available. I was given the charge to develop quantitative live imaging for accurately monitoring and analyzing the RON-invasive nanodevice behavior in conjunction with the local PM remodeling that accounts for the budding entry vesicle in the target cell. One particular issue left *quasi* untouched in the recent years concerns the mechanisms by which the invasion event ends, namely the processes covering both the closure of the ring-shaped RON-nanodevice and the separation of the PM-derived bud that contains the invading parasite from the host cell PM.

### **A missing piece of the invasion puzzle: how does invasion give birth to a tachyzoite-loaded intracellular parasitophorous vacuole?**

As early as 1996, a pioneer patch-clamp study performed by G. Ward and collaborators has provided definitive evidence that the parasite induces the target cell PM to invaginate as the primary source of the membrane material needed to fold the budding entry vesicle (Suss-Toby *et al*, 1996). Therefore, unlike previously stated, the products released from the secretory organelles of the parasite had only a minor if any contribution to this early step. This study also provided the first timing of the PV birth upon bud pinch off and subsequent PV release in the host cell cytoplasm. Performing electrophysiological studies on the simian fibroblast-like cell (COS-1 cell line) into which the tachyzoite was entering, the authors measured in time the capacitance electrical parameter as a direct way to assess the net membrane surface area and thus they could detect any change over the invasion event (Figure 20). They concluded on the absence of significant increase in surface area during bud formation, invalidating a significant role of parasite secreted material in this step. In contrast, they monitored a drop in capacitance consistent with the reduction of surface area that corresponded to the amount of membrane needed to enwrap the tachyzoite and concomitant with the pinch off of the entry vesicle. Furthermore, the assay allowed the detection of the tachyzoite-induced fission pore. A fission pore is the small aqueous connection between a forming endocytic vacuole and the extracellular medium that forms and constricts to closure during the final stages of vacuole pinch off. The electrical parameter measured during the tachyzoite-induced fission pore argues for (i) a process possibly related to the endocytic fission and (ii) the maintenance of cell membrane integrity during pinch off.

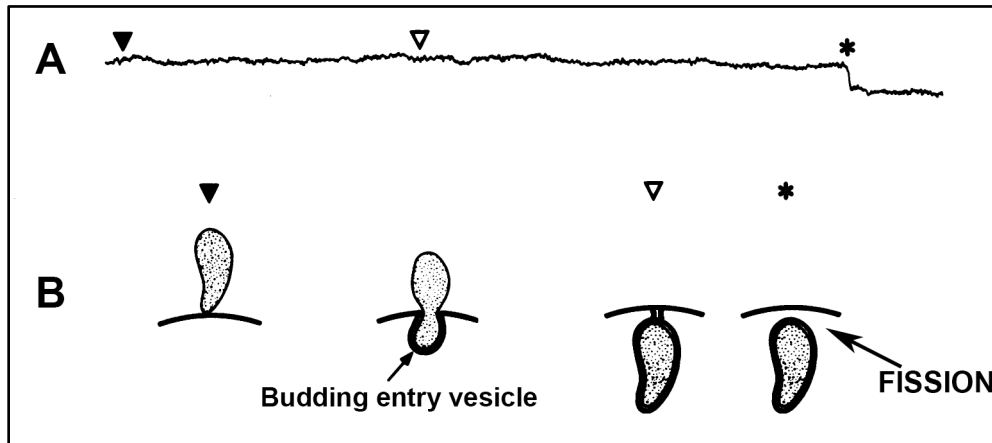


**Figure 20. Measurement of host cell membrane capacitance during *T. gondii* invasion using patch clamping.** (A) Host cell capacitance measurement during invasion. Black inverse triangle indicates the time frame when the tachyzoite is in contact with the host cell membrane, white inverse triangle indicates the time when the tachyzoite has finished entering the cell and asterisk represents the time that fission from host cell PM has occurred. Drop in the signal signifies that part of membrane has been lost being internalized along with the PV compartment enclosing the tachyzoite. (B) Schematic representation of the invasion process with the symbols that indicate the specific time points from A. Adapted from Suss-Toby *et al*, 1996.

Pinching off of a budding vesicle from PM commonly proceeds with the bending of the latter, a process whereby a neck region forms bridging the PM and the nascent vesicle and where two pieces of membrane face each other. Next the neck breaks as a result of both a local strong constriction and a membrane fission event and leads to the birth of two different membrane-bound compartments. It is in the context of the endosome release from the cell PM and of the synaptic vesicle transport that the family of dynamins were identified as main players of the PM fission event (Ferguson & De Camilli, 2012). Since then, a wealth of studies have been performed under *in vitro* conditions with purified components and synthetic lipids to reconstitute membrane tubulation and fission but also *in situ* using cells expressing wild type or non functional dynamin mutants or even lacking dynamin. Dynamin is a 100-kDa protein macromolecule, belonging to the superfamily of GTPases. Widely present in eukaryotes the dynamin family includes dynamin 1 (DNM1), dynamin 2 (DNM2), and dynamin 3 (DNM3), which are known as classic dynamins and share about 80% of homology but differ in their expression pattern. While neurons express high levels of DNM1, DNM2 is expressed ubiquitously and DNM3 is mainly restricted in the brain, testes, and lungs. Most studies have focused on the function of DNM1 and DNM2. Each dynamin displays the five characteristic domains listed as: A large N-terminal GTPase domain; a middle domain (MD); a pleckstrin homology domain (PHD); a GTPase effector domain (GED); and a proline-rich domain (PRD).

Several models have been proposed with the main view that dynamin assembles into contractile helical polymers that wrap around the neck of the budding vesicle to direct fusion of the PM leading to hemifission and upon supercontraction, to fission. As a result, the PM bud transforms into a membrane-bound intracellular vesicle that can further move by passive or active transport within the cell cytoplasm.

It is well established that the catalyzing membrane fission activity of dynamins emerges from main properties (see also Figure 21). First, dynamins oligomerize into lock-washer-like rings or cylindrical helices. This oligomerization reaction explains the membrane tubulation activity and was proposed to promote membrane curvature at the neck of budding vesicles such as endocytic pits. Secondly dynamin oligomers constrict membrane in the presence of GTP. Finally, the GTP hydrolysis of dynamin promotes “super” constriction and oligomer disassembly that eventually cause the subunit release from the PM. The Figure 21 depicts schematically the sequential activity of the dynamin oligomers.

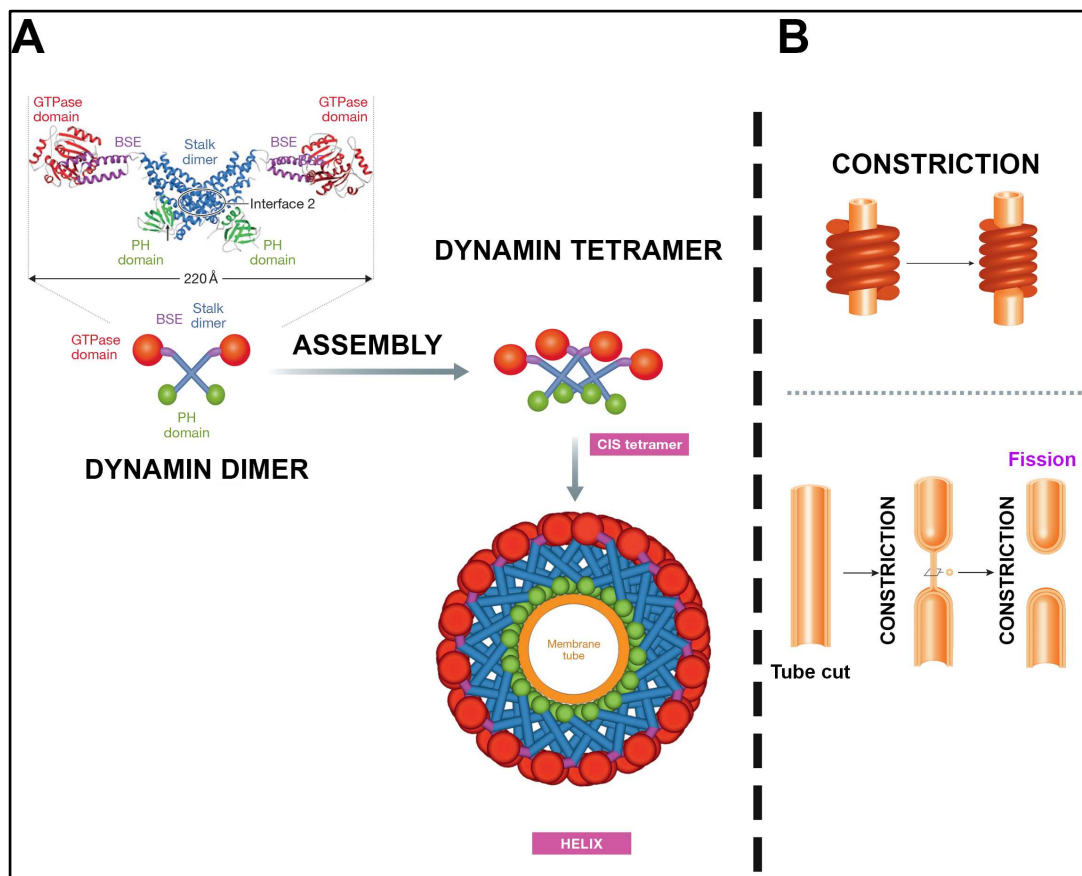


**Figure 21. Structure and assembly of dynamin in a membrane tube to mediate fission.** (A) Crystal-based structure of the dimer and assembly into tetramers that surround the membrane tube in a helix formation. (B) Dynamin constricts the membrane tube in a helical way. According to the original constriction model for dynamin-mediated membrane fission, dynamin will first constrict the membrane tube to bring the bilayers close enough (hemifission) and then more constriction occurs to account for fission. Adapted from Antonny *et al*, 2016.

In the context of tachyzoite PV birth, it was proposed that the host cell dynamins could be involved during pinching off of the nascent PV. These conclusions were drawn based on the effect of dynasore, a widely used pharmacological inhibitor of dynamins, which in the case of *T. gondii* was reported to significantly decrease the rate of invasion (Caldas *et al*, 2009). The same authors reported that when cells and parasites were exposed to dynasore, the tachyzoites could not complete invasion and instead remained blocked at the periphery. However, recent advances in molecular genetics allowed obtaining cells which were simultaneously conditionally silenced for the three genes encoding dynamins. Using these cells, dynasore was then shown to have several off target effects in particular related to cholesterol changes in the cell membrane (Park *et al*, 2013). Therefore these findings called into question the specificity of the dynasore effect during cell invasion by tachyzoites. We chose to interrogate the mechanisms of PV birth by addressing the following points.

- Could the nanodevice impose specific requirements for the sealing of the budding entry vesicle and its release in the host cell cytoplasm?
- What could be the nanodevice contribution to the PV birth event?
- Could the host cell dynamins contribute to the process?
- Could the fission event serve as signal for down stream remodeling of the PV?

## **2.2.2 Implementing methods to study the cell invasion of *T. gondii* tachyzoite**

### **- Video microscopy with two fluorescent markers**

We already referred to the importance of video microscopy for studying the process of invasion by *T. gondii* tachyzoites. One of the main challenges is to collect enough details over the whole process that lasts around 30 seconds, and this implies to have a camera with fast imaging capabilities. Fast live imaging using more than one laser is not obvious if one needs to apply longer time exposure in order to optimize the signal to noise ratio of the fluorescent reporter. We upgraded our original confocal spinning disk microscopy platform by shifting to a camera with higher resolution imaging, sensitivity and image acquisition time and we established protocols where we could acquire images from brightfield and 1-3 lasers (green, red, dark red) within 1 to 2 seconds depending on the goal of the experiment. For most of our experiments, we needed the red channel open to record the behavior of the RON2-mC protein within the invasive nanodevice, while at the same time we were interested in monitoring the formation of the budding entry vesicle and its development until it separates from the host cell PM. This necessitated the use of the green channel to capture the fluorescence associated with the PM reporter we chose. In other cases, we had dyes (variety of fluorescent colors) in the medium, as instances to verify the viability of the tachyzoite in particular when the process of invasion was artificially slowed down or impaired. To interfere with the process of invasion, we design assays for which fluorescent microbeads (dark red for instances) were used. So overall, at least two lasers had to be active simultaneously and we did not have a dual view system where two cameras allow simultaneous recording of two emission channels. Therefore, we optimized the laser exposure time and power to our needs for the best informative image. Last but not least, we rationalized the best upgrading we could afford, in particular with the installation of a piezo objective that offers great focus adjustment and high-speed Z-stack acquisition.

### **- Image processing to develop quantitative analysis**

As we described before, we applied fast live imaging where acquisition of at least three images per second was performed for two to three channels. This generated large amount of images. Thus powerful computers were needed for the analysis of these data. I would like to highlight the particle tracking techniques (using Icy software) that were used for this study since they helped for describing the twisting motion in an informative way. Using a variety of plugins and tools, we managed not only to quantify parameters of motion characteristics of the twist but also to clarify the visualization of the results (i.e. the parasite rotation). This image analysis protocol has been included as a book chapter in the *Toxoplasma gondii* book (Pavlou & Tardieux, 2020). Generally, image processing was

performed with ImageJ, Metamorph, ChimeraX and MATLAB software that are widely used. I would like to separately refer to Icy software as I performed most of the image analysis needed for this manuscript. It is an open source user-friendly software that through all the years of my PhD, was my main software for image analysis and I can admit that I am more than satisfied with the environment and the tools that it offers for analyzing any data from microscopy experiment. One other strong point of this software is the interactive forum that supports the users and turned quite helpful when problems arose during my analyzing experiments.

### **- Blocking invasion using nanotools/microbeads**

We used the same method as explained in chapter 2.1.2 for immobilizing the parasite in a substrate. In this case, we had the addition of the host cells in our experiments because we wanted to block the tachyzoite while it tries to invade a host cell using the capping behavior of microbeads pre-bound to the parasite surface. The idea was that if we manage to keep the beads capped at the tachyzoite posterior end, we could test the consequences of failed closure of the invasive nanodevice. In some cases, the beads detached from the tachyzoite body as explained in chapter 1 but in most cases, the beads stayed attached to the posterior and therefore they did interfere with the torus closure. In control, we confirmed that the host cells were not affected by the presence of the microbeads by performing live imaging of host cells alone with microbeads.

### **- Utilization of /Engineering of mammalian cell lines expressing genetically encoded markers**

There was a need for engineering mammalian cell lines that express different PM to monitor in live the membrane budding and fission. Stable cell lines with different PM reporters engineered as described in Pavlou *et al*, 2018 because we needed stable expression and 100% positive cells since invasion is not an event that is easy to record. First, we needed to make sure that we produced healthy active parasites and that we kept all the conditions to maintain their invasiveness over the recording period. Then we wanted to ensure the stable protein expression of all the potential host cells. Thus, colleagues in the lab used plasmids encoding fluorescent markers of interest to transfect a variety of mammalian cell lines and carried antibiotic resistance selection before isolating clones by limiting dilution. For testing the importance of host cell dynamins during the fission process, we were given by P. de Camilli a line of Mice Embryonic Fibroblasts (MEF) derived from a tamoxifen-inducible triple conditional KO mouse ( $Dnm1^{loxP/loxP}$ ;  $Dnm2^{loxP/loxP}$ ;  $Dnm3^{loxP/loxP}$ ; Cre-ER<sup>+/0</sup>). Using tamoxifen, we could silence the expression of the three genes encoding dynamins as described in Park

*et al*, 2013 and the effectiveness of the treatment was controlled by visualizing the block in endocytosis. When we tested the contribution of ALIX during tachyzoite entry in MEFs, we benefited from MEFs derived from a *Alix* knock-out mouse generated in the lab of colleagues at Grenoble (Laporte *et al*, 2017). We needed however to compare with a MEF KO line genetically complemented with a wild type copy of the ALIX encoding gene. To this end, the lab generated a MEF line expressing a chimeric version of ALIX that carries the GFP protein at the N terminal position, which we selected with puromycine and isolated by limiting dilution.

Overall, we have been successful in providing highly informative image datasets on the mechanisms by the *T. gondii* tachyzoite ends entry into the host cell because we used (i) well-controlled and stable lines for both the tachyzoite and the host (human/mouse) cells, but also (ii) we carefully chose the fluorescent markers of interest, and finally (ii) we applied image processing for accurate spatio-temporal signal visualization coupled with quantitative analysis.

### 2.2.3 Main highlights of the study

- *T. gondii* RhOptry Neck protein complex forms a torus-shaped invasive device in the membrane of the target cell that stretches and shrinks to accommodate the passage of the ellipsoid tachyzoite.
- *T. gondii* tachyzoite rotational twisting motion completes host invasion in 2D but also 3D (spheroids) conditions and it works independently of host cell dynamins.
- The budding entry vesicle pinches off of the host cell PM to give birth to a parasitophorous vacuole through a fission process upstream the position of the RON-nanodevice. The time of fission varied between parasites with two distinct motion sequences of specific kinematical parameters.
- The first remodeling of the tachyzoite-loaded budding vacuole can be detected immediately post-twist and reveals the assembly of specific microdomains in the membrane of the parasitophorous vacuole.
- Artificially induced failure of torus closure impedes proper sealing of the budding entry vesicle, promotes influx of extracellular  $\text{Na}^+$  ions inside the unclosed bud which eventually leads to osmotic driven swelling and subsequent parasite death.

## 2.2.4 Publications

Pavlou G, Biesaga M, Touquet B, Lagal V, Balland M, Dufour A, Hakimi M & Tardieux I (2018) *Toxoplasma* Parasite Twisting Motion Mechanically Induces Host Cell Membrane Fission to Complete Invasion within a Protective Vacuole. *Cell Host & Microbe* **24**: 81-96.e5  
<https://linkinghub.elsevier.com/retrieve/pii/S1931312818303159>

Pavlou G, Tardieux I (2018) The *Toxoplasma* Tour de Force to Unfold its Intravacuolar Developmental Program. *J Infectiology*. 1(3): 13-18  
<https://www.infectiologyjournal.com/articles/the-toxoplasma-tour-de-force-to-unfold-its-intravacuolar-developmental-program.pdf>

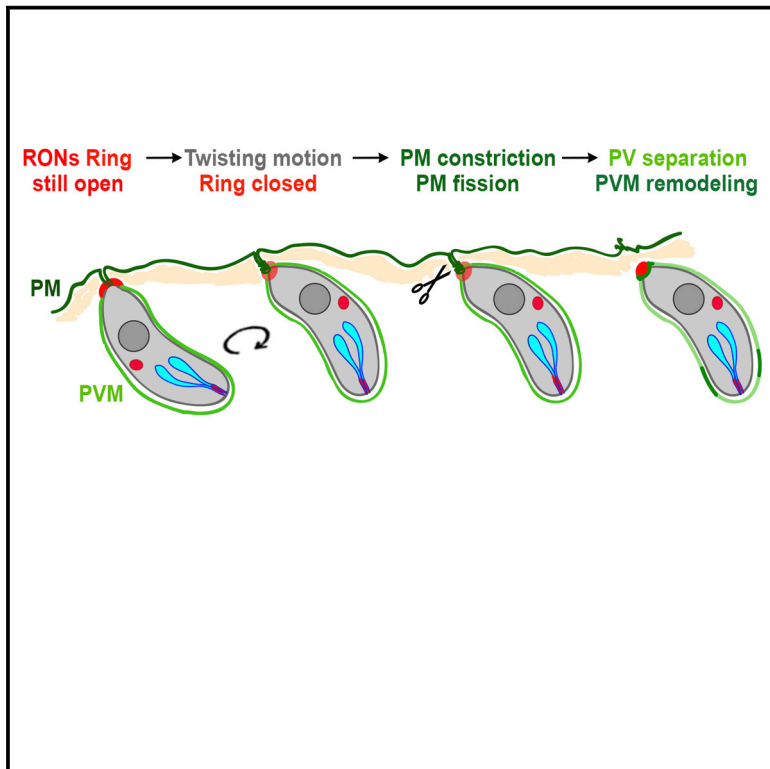
Pavlou G, Milon G & Tardieux I (2019) Intracellular protozoan parasites: living probes of the host cell surface molecular repertoire. *Current Opinion in Microbiology* **52**: 116–123  
<https://linkinghub.elsevier.com/retrieve/pii/S1369527419300256>

Pavlou G & Tardieux I (2020) Phenotyping *Toxoplasma* Invasive Skills by Fast Live Cell Imaging. In *Toxoplasma gondii*, Tonkin CJ (ed) pp 209–220. New York, NY: Springer US [http://link.springer.com/10.1007/978-1-4939-9857-9\\_12](http://link.springer.com/10.1007/978-1-4939-9857-9_12)

# Cell Host & Microbe

## *Toxoplasma* Parasite Twisting Motion Mechanically Induces Host Cell Membrane Fission to Complete Invasion within a Protective Vacuole

### Graphical Abstract



### Authors

Georgios Pavlou, Mateusz Biesaga, Bastien Touquet, ..., Alexandre Dufour, Mohamed-ali Hakimi, Isabelle Tardieux

### Correspondence

isabelle.tardieux@inserm.fr

### In Brief

During host cell invasion, the protozoan parasite *Toxoplasma gondii* injects a parasite-derived complex, or nanodevice, that consists of the RhOptry Neck proteins. This nanodevice opens the host cell membrane and directs budding of the parasitophorous vesicle. Pavlou et al. uncover a parasite-directed rotation that drives vesicle closure and release.

### Highlights

- *T. gondii*/Tg RhOptry Neck protein complex forms an invasive device in target membrane
- Tg rotational twisting motion completes host invasion, independent of host cell dynamins
- First remodeling of the Tg parasitophorous vacuole occurs post-twist
- Failure to seal the vacuole prior to detachment promotes swelling and parasite death

# *Toxoplasma* Parasite Twisting Motion Mechanically Induces Host Cell Membrane Fission to Complete Invasion within a Protective Vacuole

Georgios Pavlou,<sup>1</sup> Mateusz Biesaga,<sup>1</sup> Bastien Touquet,<sup>1</sup> Vanessa Lagal,<sup>2</sup> Martial Balland,<sup>3</sup> Alexandre Dufour,<sup>4</sup> Mohamed-ali Hakimi,<sup>5</sup> and Isabelle Tardieux<sup>1,6,\*</sup>

<sup>1</sup>Institute for Advanced Biosciences (IAB), Team Membrane Dynamics of Parasite-Host Cell Interactions, CNRS UMR5309, INSERM U1209, Université Grenoble Alpes, Grenoble 38700, France

<sup>2</sup>Unit of Malaria Infection and Immunity, Department of Parasites and Insect Vectors, Institut Pasteur, Paris 75015, France

<sup>3</sup>Laboratoire Interdisciplinaire de Physique, UMR CNRS, 5588, Université Grenoble Alpes, Grenoble 38402, France

<sup>4</sup>Institut Pasteur, Bioimage Analysis Unit, CNRS UMR3691, Paris 75015, France

<sup>5</sup>Institute for Advanced Biosciences (IAB), Team Host-Pathogen Interactions & Immunity to Infection, INSERM U1209, CNRS UMR5309, Université Grenoble Alpes, Grenoble 38700, France

<sup>6</sup>Lead Contact

\*Correspondence: [isabelle.tardieux@inserm.fr](mailto:isabelle.tardieux@inserm.fr)

<https://doi.org/10.1016/j.chom.2018.06.003>

## SUMMARY

To invade cells, the parasite *Toxoplasma gondii* injects a multi-unit nanodevice into the target cell plasma membrane (PM). The core nanodevice, which is composed of the RhOptry Neck (RON) protein complex, connects *Toxoplasma* and host cell through a circular tight junction (TJ). We now report that this RON nanodevice mechanically promotes membrane scission at the TJ-PM interface, directing a physical rotation driven by the parasite twisting motion that enables the budding parasitophorous vacuole (PV) to seal and separate from the host cell PM as a bona fide subcellular *Toxoplasma*-loaded PV. Mechanically impairing the process induces swelling of the budding PV and death of the parasite but not host cell. Moreover, this study reveals that the parasite nanodevice functions as a molecular trigger to promote PV membrane remodeling and rapid onset of *T. gondii* to intracellular lifestyle.

## INTRODUCTION

The several-micron-sized and ellipsoid-shaped protozoan *Toxoplasma gondii* is an obligate intracellular parasite of warm-blooded metazoan nucleated cells. The *T. gondii* replicative stage, called tachyzoite, gains cellular entry within a membrane-bound vesicle by subverting a piece of the cell plasma membrane (PM). In contrast to those intracellular microbes that hijack endocytic vesicles to enter host cells (Kumari et al., 2010; Cossart and Helenius, 2014), the tachyzoite directs the selection of PM components that flow into the budding entry vesicle (Mordue et al., 1999). When the zoite entry is about complete, the adjacent bilayer regions that connect the budding vesicle to the PM merge and are severed, thus accounting for the release in the host cell cytoplasm of a sealed vesicle, the

so-called parasitophorous vacuole (PV) that houses the parasite and thereafter its progeny (Morisaki et al., 1995; Suss-Toby et al., 1996). How the PM-derived bud seals and pinches off a PV remains largely elusive.

To form a functional PV, the parasite secretes a multi-molecular complex that is pre-stored in its apical organelles called rhoptries (Besteiro et al., 2009; Straub et al., 2011; Bichet et al., 2014). The four-member complex consists of RhOptry Neck RON 2, 4, 5, 8 proteins and represents an invasive nanodevice as it provides, in combination with other parasite-derived products (Besteiro et al., 2009; Sidik et al., 2016), transient coupling of the two cells by building a tight circular interface, also called Tight Junction (TJ). The TJ serves several functions: (1) promoting delivery of the earliest parasite effectors into the host cell cytoplasm, in particular toxofilin (Poupel et al., 2000; Lodoen et al., 2010), which loosens the cortical actin meshwork and facilitates PM invagination (Delorme-Walker et al., 2012), (2) defining an entry door on which the tachyzoite applies invasive force (Bichet et al., 2014), and (3) acting as a gatekeeper for the metazoan cell PM proteins composing the budding entry vesicle (Mordue et al., 1999; Charron and Sibley, 2004).

A pioneer patch-clamp study has highlighted similarities between *T. gondii* PV pinch-off and endocytic fusion pores, albeit of slower kinetics (Suss-Toby et al., 1996). It then has been proposed that the parasitophorous vacuole membrane (PVM) fuses at the parasite rear to separate from the host cell PM (Charron and Sibley, 2004) while the TJ-associated RONS were immuno-localized in young PVs (Besteiro et al., 2009), suggesting that fission occurs at the PM. Moreover, the mechanoenzymes dynamins, which drive vesicle scission during Clathrin-Mediated (CME) or clathrin-independent endocytosis (Antonny et al., 2016), were implicated during *T. gondii* PV release, based on the effect of the pharmacological inhibitor dynasore (Caldas et al., 2009). However, recent data challenged these conclusions by reporting unspecific additional effects of dynasore on membrane homeostasis (Park et al., 2013; Preta et al., 2015; Persaud et al., 2018). Finally, among other drivers of PM fission is the ESCRT (Endosomal Sorting Complex Required for Transport) machinery whose cofactor Alix (ALG-2 Interacting protein X)

was detected at the *T. gondii* TJ where it interacted with the cytoplasmically exposed TJ member RON4 (Guérin et al., 2017). Yet, Alix contribution to cell invasion was not directly assessed and was proposed by the authors to be ESCRT-independent.

We raised the hypothesis that the RON nanodevice imposes unique requirements for vesicle sealing and scission from the host cell PM. In this study, we analyzed in depth the process that gives birth to the unique *T. gondii* PV using high-speed quantitative live fluorescence imaging in conjunction with kinematic modeling.

## RESULTS

### Genetic Ablation of Either the Mechanoenzymes Dynamins or the ESCRT Cofactor Alix in Host Cells Does Not Affect *T. gondii* Tachyzoite Invasiveness and PV Birth

Pharmacological inhibition of host cell dynamins was reported to drastically impair *T. gondii* tachyzoite invasiveness but also to retain tachyzoites that achieved invasion at the cell periphery (Caldas et al., 2009). This description resembles what is observed for endocytic vesicles when dynamin-mediated vesicle scission no longer operates (Ferguson and De Camilli, 2012). Using mouse embryonic fibroblasts (MEFs) derived from mice harboring floxed alleles of all dynamin 1, 2, and 3 genes (triple knockout [TKO]) and transgenic for 4-hydroxytamoxifen (OHT)-inducible Cre recombinase (Park et al., 2013), we re-examined the contribution of host cell dynamins during tachyzoite entry. We confirmed that dynamin expression in TKO MEF cells treated with OHT was quasi-undetectable using antibodies recognizing all three dynamin isoforms (Figure 1A, left panel). Indeed, consistent with the endocytosis defect caused by the lack of dynamins (Ferguson et al., 2009), the Arp2/3 complex, visualized by Arp2 immunostaining, significantly accumulated beneath the PM of the OHT-treated cells where it is expected to decorate the neck of endocytic vesicles (Figure 1B). Next, using automatic image capture and processing to measure the differential fluorescence of intracellular and extracellular parasites, we quantified RON2-mCherry (RON2-mC) tachyzoite invasiveness in wild-type (WT) and TKO MEF cells, as well as in either WT U2OS or U2OS cells ectopically expressing low to high amounts of a functional GFP-dynamin1 fusion protein (Persaud et al., 2018) (Figure 1A). Using clathrin light chain (CLC)-monomeric red fluorescent protein (mRFP) to detect CME, we observed a significant number of CLC-positive vesicles apposed to GFP-dynamin1 dot-like structures at the PM of these cells (Figure S1A), consistent with a functional GFP-dynamin1. In large-scale invasion assays, we found no significant differences in tachyzoite invasive capacities in MEFs or U2OS regardless of dynamin expression as indicated by the relative invasion rate on three independent assays (Figure 1C). In addition, we did not observe any retention of newly formed PVs at the cell periphery (data not shown). Next, since Alix, which assists the ESCRT machinery during membrane fission, was documented to team with TJ RON4 (Guérin et al., 2017), we used MEFs derived from Alix homozygous knockout (KO) mice (KO *Alix*) (Mercier et al., 2016). Alix rescued KO (KO *Alix* GFP-Alix) as well as U2OS overexpressing GFP-Alix cell lines were also generated to assess the functional contribution of Alix during

pinch-off of the entry vesicle. We confirmed that no signal was detected in the KO *Alix* cells by specific anti-Alix antibodies (Mercier et al., 2016), whereas these unambiguously recognized both the GFP-Alix fusion protein and the endogenous Alix in the relevant MEF and U2OS cell lines, respectively (Figure 1D). In addition, GFP fluorescence was detected in all KO *Alix* GFP-Alix cells (Figure 1E). We then compared invasion between Alix-deficient and Alix rescued MEF cells, and found no statistical differences in tachyzoite invasiveness (Figure 1F). Importantly, the detection of GFP-Alix at the Ron2-mC-positive TJ site mostly at the end of the invasion process (Figure S1B) confirmed the construct functionality (Mercier et al., 2016) and the TJ-associated Alix localization (Guérin et al., 2017). Finally, we observed that newly formed PVs were not retained at the cell periphery (data not shown). Collectively, these data indicate that neither dynamins nor Alix from the host cells are required for *T. gondii* tachyzoite optimal entry into a functional PV.

### Closure of the Toroidal TJ Is Concomitant with a Tachyzoite Anticlockwise Twisting Motion

Since we established that both dynamin and Alix were dispensable for pinch-off of tachyzoite-loaded budding vesicles, we hypothesized that tachyzoites use their own mechanical properties to drive the biogenesis of a functional PV. To investigate this possibility, we analyzed the dynamics of the invasion sequence using high-speed confocal microscopy. We first engineered a set of transgenic human U2OS cell lines ectopically expressing PM markers fused to GFP and benefited from the previously characterized transgenic tachyzoite line expressing the rhoptry RON2-mC (Bichet et al., 2014). In U2OS cells expressing a chimeric glycosylphosphatidylinositol (GPI) protein (i.e., GFP-GPI), we visualized a discrete reorganization of the cell PM at the site of contact with the parasite apex shortly prior to the discharge of the RON2-mC complex into the recipient PM. Insertion of RON2-mC within the PM coincided with the formation of a highly curved PM invagination (Figure 2A; see also Video S1). A significant stretch of the RON2-mC ring-shaped surface that in 3D geometrically defines a torus (or anchor ring) and coinciding with the TJ could then be tracked while it accommodated the passage of the ellipsoid-shaped tachyzoite into the unfolding PM (Figure 2A). When the tachyzoite had entered the cell half way, the torus started to shrink and was eventually detected as a thick dot behind the tachyzoite (Figure 2A; see also Video S1). Using Icy software (de Chaumont et al., 2012) to automatically track the different pools of RON2-mC, namely the (1) apical rhoptries, (2) posteriorly positioned TJ, both delineated by blue circles, and (3) internal spherical RON2-mC compartments marked by green circles, allowed to define approximately a  $\sim 90^\circ$ – $540^\circ$  anticlockwise twist rotation of the tachyzoite around its long axis which imposed a twisting motion on its basal end (Figures 2B and 2C; see also Videos S2 and S3). When the signal intensity of the tracked object was analyzed over the rotation time, the profile showed periodic fluctuations as only expected for a continuous  $360^\circ$  rotation of the parasite. Indeed, the weaker signals that followed the first bright spots detected corresponded to the rotation times for which the tracked object was slightly out of focus. Importantly the signal intensity came back to the initial level of intensity when the object returned to the initial in focus positions (Figure 2C). These datasets allow

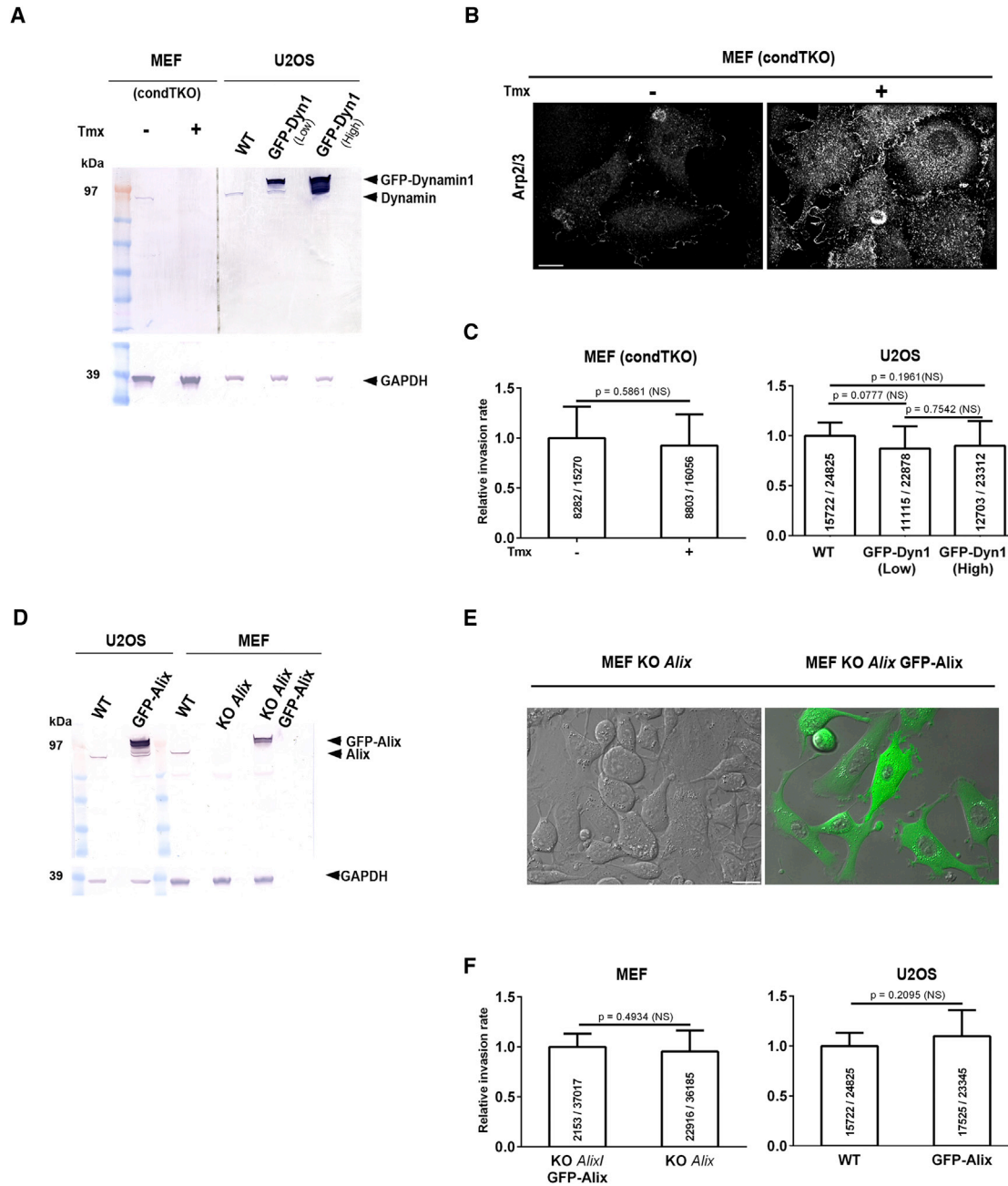


**Figure 1. The Host Cell Membrane Fission Mechanoenzymes Dynamins and ESCRT Cofactor Alix Are Not Required for Tachyzoite Entry**

(A) Western blotting on WT MEFs, MEFs conditionally silenced for the three dynamin encoding genes (TKO), WT U2OS, and U2OS ectopically expressing low to high number of dynamins.

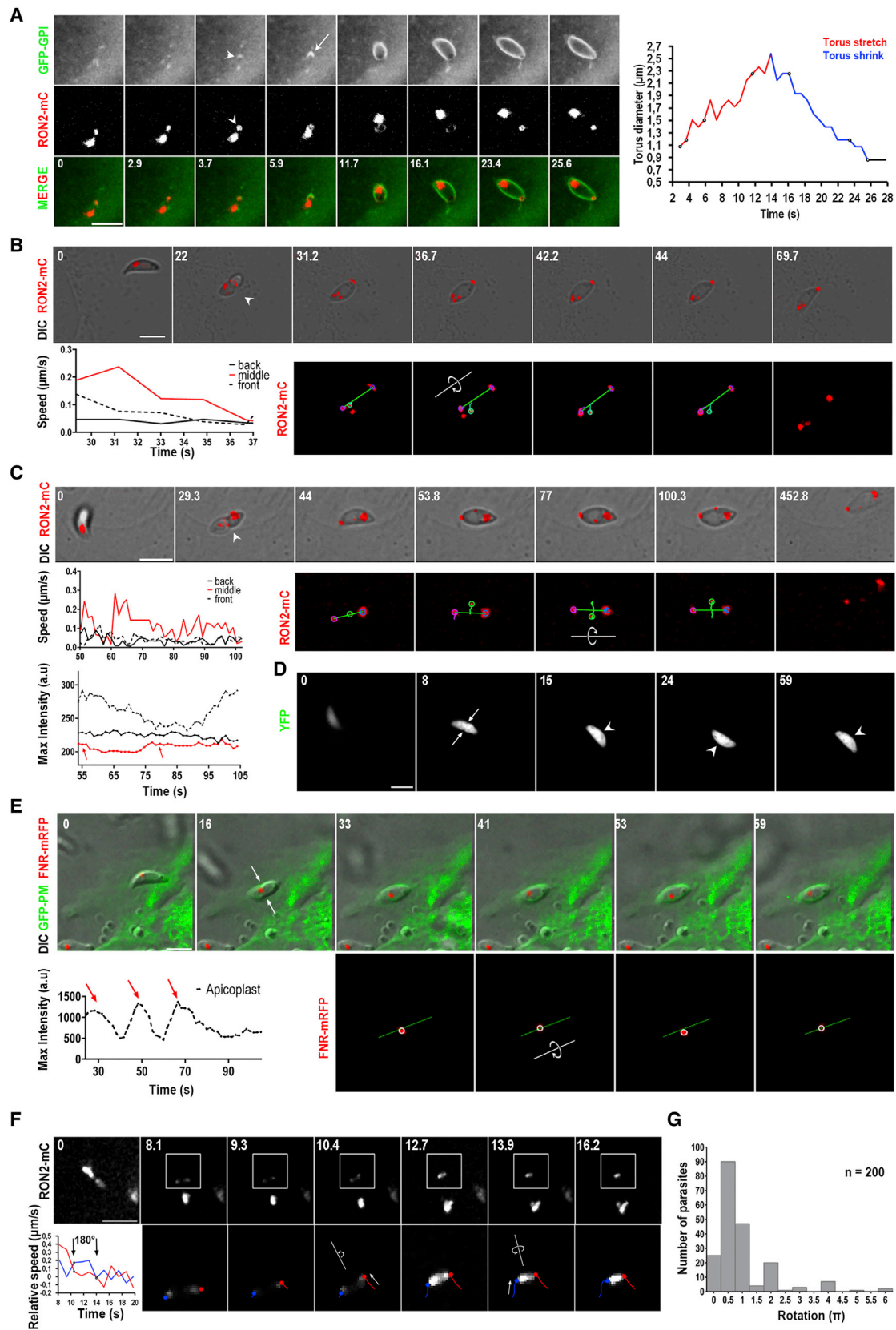
(B) *In situ* detection of the MEF Arp2/3 complex before and after tamoxifen (Tmx) treatment. Scale bar, 20  $\mu$ m.

(C) Quantitative large-scale invasion assays. Results show the relative invasion rate as mean  $\pm$  SEM for three independent assays, each performed three (MEF) or four (U2OS) times. The total number of intracellular tachyzoites and total number of human cells can be read in each column.

(D) Western blotting following SDS-PAGE separation of protein extracts from KO MEFs *Alix* and KO MEFs *Alix* GFP-Alix (rescued), WT U2OS and U2OS ectopically expressing GFP-Alix.

(E) Confocal images of DIC-GFP channel overlays of KO MEF *Alix* and KO MEF *Alix* GFP-Alix (“rescued”) cells. Scale bar, 20  $\mu$ m.

(F) Quantitative large-scale invasion assays with similar MOI for each host cell type. Results show the relative invasion rate when the rescued cells served as reference as mean  $\pm$  SEM for three independent assays, each performed in quadruplicate. (C and F) Raw data and p values (t test) are indicated. NS, nonsignificant.



(legend on next page)

not only arguing for a continuous rotation but also controlling for the absence of fluorescence bleaching over time. To confirm the twisting motion, we also tracked the slightly eccentric apicoplast using a fluorescent version of the Ferredoxin NADP<sup>+</sup> oxidoreductase (FNR-mRFP) (Amiar et al., 2016). By analyzing both particle motion and fluorescence intensity, we unambiguously assessed the ongoing 360° rotation over several revolutions prior to PV release (Figure 2E; see also Figure S2D and Video S4 as well as Movie S1 on Mendeley Data: <https://doi.org/10.17632/fmhnprp66j.1>). Finally, since a parasite 180° twist should lead to an opposite position of its convex curvature, we analyzed tachyzoites that expressed GFP in the cytoplasm as a reliable marker of cell shape and confirmed that a twisting motion of the parasite preceded PV release (Figure 2D; see also Mendeley Movie S2).

To next better characterize the kinematic parameters of the toroidal TJ at the time of closure and gain mechanistic insights, we applied image processing methods along with kinematic and mathematical modeling using MATLAB software. In 2D live imaging of the invasion, two informative settings were distinguished: either (1) the invasion of a.U2OS expressing the fluorescent chimeric transmembrane domain of the PDGF receptor (i.e., GFP-TM PDGFR) occurred on the plane of the toroid section or (2) the zoite entered an MEF cell in parallel to the recording plane, which resulted in the appearance of the TJ as a cross-section ring. In the first case, we carefully selected sequences in which the tachyzoite did not reorient during the entry event by checking that the apical tip of the rhoptry was not changing plane (Figure 2F; see also Figure S2B and Mendeley Movie S3). The displacements of two extreme points of the toroid were tracked using MATLAB and revealed alternated motion with one edge moving first (red trajectory) and the other edge following (blue trajectory) (Figure 2F bottom panel; see also Mendeley Movie S3) within the exact time of the tachyzoite twist that could be determined by the apical “rhoptry” motion. While the first track (red) could also signify the reorientation of the zoite resulting in the apparent faster displacement of one of the TJ edges, the subsequent track (blue) confirmed that the edges were symmetrically displaced but with a different time delay, which resulted in observed alternating motion (Figure 2F). Moreover, the

speeds of the ring edge motion in relation to first detected position were calculated (Figure 2F). In the second plane described, we attempted to mathematically model the toroid-shaped TJ by fitting an ellipse (Figure S2C; see also Mendeley Movie S4). Although tracking of the ellipse evolution in time was limited by the image resolution, it revealed an irregular type of closure. Interestingly, while the TJ has a symmetric toroid shape and could be expected to close as a result of a symmetric distribution of inward-directed forces, the irregularity of the tracking of the torus and the kinematic modeling possibly suggest asymmetric distribution of forces applied during the twist motion. Finally, it is worth mentioning that while the majority of tachyzoites executed a quarter to half turn, we saw rare instances of multiple rotations (Figure 2G; see also Figure S2A and Mendeley Movie S5). Interestingly we found this multi-rotation characteristic to invasion of host cells in metaphase ( $n = 15/15$  analyzed cells) (Figure S2E; see also Mendeley Movie S6). Remarkably, when the sister chromatids started separating as anaphase proceeded, the tachyzoite stopped rotating. Therefore, since cell surface tension of the mitotic cell is reported dramatically and transiently increased during metaphase (Fischer-Friedrich et al., 2014), the two determinants of surface tension, i.e., membrane in plane tension and cortex contractibility, might control successful membrane fission and PV pinch-off.

### The Disconnection of Exogenous Material Attached to the Tachyzoite Temporally Coincides with the Twisting Motion Ending Invasion

Since we expected release of exogenous material loosely retained at the posterior pole when the torus has closed, we analyzed the final twisting motion of invading parasites that carried posteriorly bound products. First, when host cell PM components were attached to the rear of a tachyzoite, they were pulled as filopodium-like projections by the moving parasite that eventually invaded a cell. We observed that the host cell filopodium detached from the parasite rear concomitantly with the twisting motion and retracted quickly as tension dropped (Figure 3A; see also Figure S3A, Video S5 and Mendeley Movie S7). We next designed an assay where microbeads would be similarly positioned at the posterior end of an invading

### Figure 2. RON2-mC Is Delivered into the Host Cell PM as a Torus that Stretches and Shrinks Along with Tachyzoite Entry into the Budding Vesicle

(A–G) The tachyzoite performs an anticlockwise twist that coincides with torus closure.

(A) Time lapse shows a RON2-mC tachyzoite (red) invading a.U2OS cell that expresses a GFP-GPI PM marker (green). The RON2-mC torus assembles (arrowhead) within the host cell PM that locally remodels (arrowhead), further stretches and shrinks while the parasite penetrates in the highly curved PM-derived budding vesicle (arrow). Tracking of the torus diameter during stretch (red line) and shrinkage (blue line) is shown on the graph.

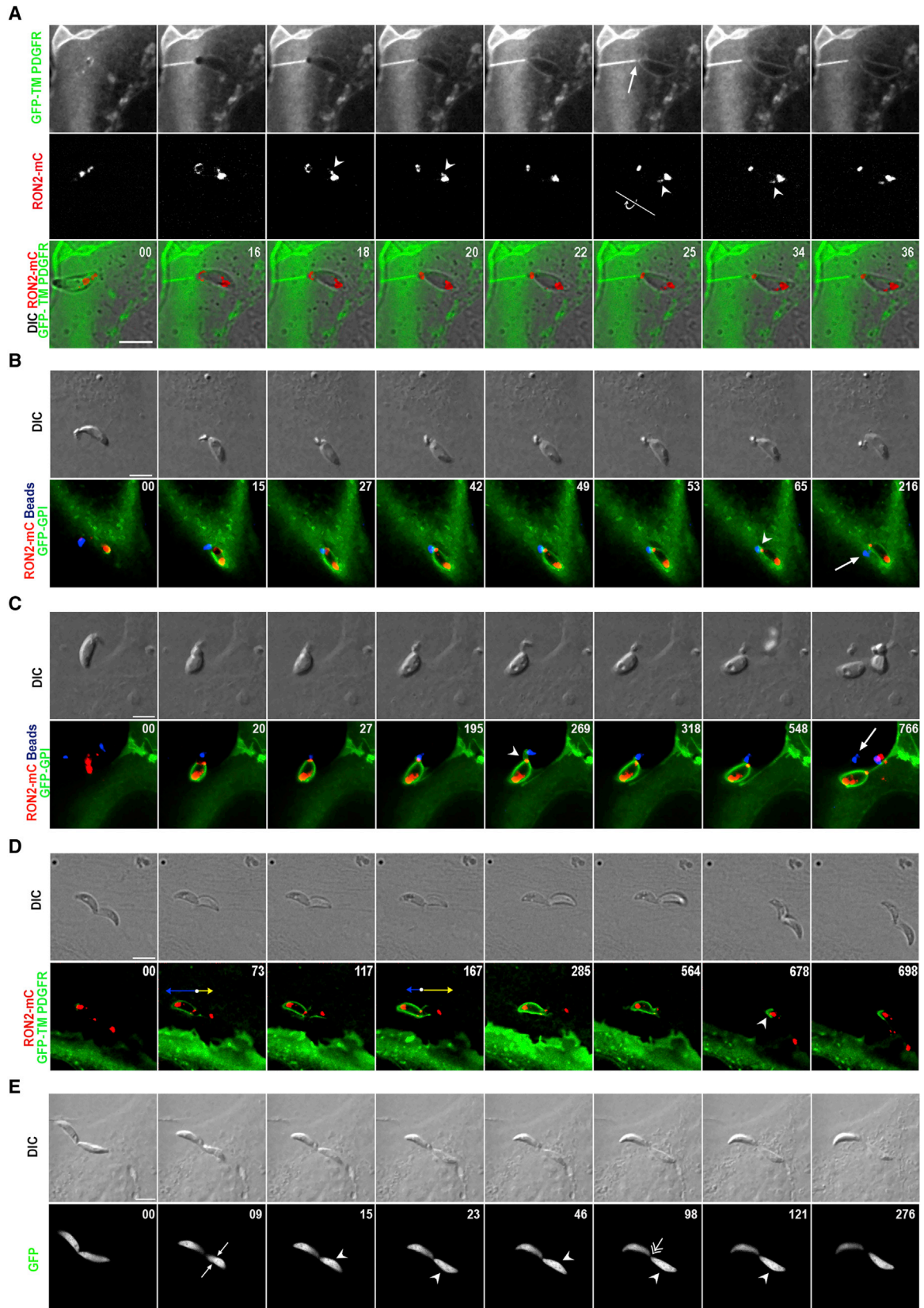
(B and C) Time lapses of DIC (top) and fluorescent channel overlays (bottom) show the parasites prior to RON2-mC release and halfway inside a.U2OS-expressing GFP-TM PDGFR (B) or an MEF (C) cell (see the torus marked by arrowheads). Upon torus closure, automatic tracking of the RON2-mC pools at the parasite poles is reported by blue circles and short blue trajectories, while the cytoplasmic RON2-mC circular object (middle, green circle) tracking identifies the twisting motion (~180° for B, ~540° for C) of the parasite along its main axis (green bar between the two poles, see the circular arrows). Graphs (B, top C) indicate the speed of the three objects tracked and (top C) the signal intensity profile of the tracked objects. Note (1) the higher speed of the internal reference and (2) the periodic fluctuations in signal intensity that correlates with the position with regard to focal point (full focus is indicated by red arrows).

(D) Time lapse shows a yellow fluorescent protein (YFP)-tachyzoite invading an a.U2OS cell. The TJ site is delineated with arrows while arrowheads show the position of the parasite convex side that alternates during the twisting motion.

(E) Time lapse shows DIC and fluorescent merged channels of an FNR-mRFP tachyzoite invading a GFP-PM U2OS cell (top). At the end of invasion, automatic tracking of the FNR-mRFP object (white circle) identifies the twisting motion (~2 turns) and white arrows indicate the TJ site. Note in the graph the periodic fluctuations in signal intensity that correlate with the position with regard to in-focus point (red arrows).

(F) Kinematic modeling of the RON2-mC toroid section during closure. Edge pixel is tracked in respect to its initial position and speed of the motion is represented on the graph. Note in enlargement of selected frames, the alternating motion of right edge (red track) that moves first and left edge (blue track) that follows.

(G) Histogram shows the distribution of the twist amplitude measured by the angle for  $n = 200$  parasites. All scale bars, 5 μm; time is indicated in seconds.



(legend on next page)

tachyzoite and expected to detach when the torus closes. We indeed observed that the twisting motion of the tachyzoites coincided with bead release from the zoite rear. A repetitive feature of these sequences was the emergence of membrane ruffles or tube-like projections emanating from the torus site and that engulfed the beads prior to and often during separation (Figures 3B and 3C; see also Figure S3B, Videos S6 and S7 and Mendeley Movie S8), in line with the concept of host cell membrane dynamics operating at the TJ (Bichet et al., 2016). Of note, because the beads stayed in place at the cell surface, they marked the site of entry enabling to follow the displacement of the PV post-twist. Finally, we took advantage of the fact that the daughter tachyzoite cells formed within the PV remain linked at their rear ends through a maternal Residual Body (RB), until they actively exit the host cell. In some occasions, pairs of posteriorly conjoined daughter cells can be released in the extracellular medium. We observed that when one of the paired tachyzoites actively entered the cell, it could be pulled back through the torus by the motile partner provided the former has not yet performed the final twist (Figure 3D; see also Mendeley Movie S9). Instead, if a paired tachyzoite has achieved twisting motion, the active conjoined partner could free itself from the joint by executing a twirling motion, which did not impact the intracellular parasite (Figure 3E; see also Mendeley Movies S10 and S11). Together, these data indicate that the final twisting motion likely reports on the closed status of the torus, a step that defines the “point of no return” for invasion.

### A Twisting Motion of the Tachyzoite Ends Entry into Cells under 3D Spatial Constraints

The *in vivo* environment provides cells with a different dimensionality as they experience neighboring cells on all sides and extracellular matrix that all supply mechanical constraints in addition to biochemical agonists. Accordingly, the PM lipid and protein composition was found to differ between 2D and 3D culture systems, thus conferring distinct mechanophysical properties, in particular membrane and cortex elasticity (Cesarz and Tamama, 2016), which likely influences membrane-associated interface processes. We thus determined whether the invasive behavior of tachyzoites, in particular the twist motion prior to PV birth, was retained in a more physiological tissue-related arrangement. To this end, we adjusted a protocol for 3D culture of breast cancer cells (Lee et al., 2007), such as human foreskin fibroblast (HFF) cells, each containing one to a few RON2-mC ta-

chyzoites, that were mixed with uninfected GFP-GPI expressing U2OS cells in a Matrigel-based matrix and deposited onto a Matrigel layer. By monitoring the 3D culture over 4 days, we observed, between 20 and 40 hr post embedding, mixed multicellular spheroid aggregates that were composed of a majority of round uninfected U2OS cells and of few round fibroblasts filled by growing tachyzoite rosettes (Figure 4A). With time, the tachyzoite-providing HFF cells were lost, whereas U2OS spheroids grew in size and most of their constituent cells hosted tachyzoites, providing evidence for the viability of both parasites and human cells over this period (Figure 4A; see also Mendeley Movie S12). We observed that tachyzoites injected the RON device in the cell PM that locally remodeled and moved through a static torus until the latter closed, a step concurring with a typical twisting motion of the parasites (Figures 4B and 4C; see also Mendeley Movies S13 and S14). Collectively, these data validated the view of the twisting as the mechanical mechanism accounting for torus closure and subsequent PV birth in a more physiologically relevant context.

### Sustained Mechanical Impairment of the Torus Closure Induces Impressive Osmotic Swelling of the Entry Vesicle with Concomitant Tachyzoite Death

To clarify how closure of the torus contributes to the release of a functional PV, we analyzed what would happen when invading tachyzoites were arrested at the exact step prior to this event. Therefore, we generated tachyzoites that carry microbeads covalently bound to their rear end and imaged invasion in U2OS cells expressing different PM markers. While the torus formed and shrank normally, the tachyzoite could not perform the typical final twist and instead stayed connected to the PM at the TJ site. Meanwhile, the dark-red fluorescent beads remained extracellularly positioned, juxtaposed to the torus and surrounded by host cell membrane ruffles. Under this configuration, the budding membrane invagination dilated but kept a similar fluorescence intensity, indicating that the PM components continued to selectively flow, hence preserving the usual lipid enrichment of the nascent PVM over the PM (Figures 5A and 5B; see also Video S8 and Mendeley Movie S15). The swelling bud then frequently retracted and could then expand as intracellular balloons that filled most of the cell cytoplasm. Intriguingly, the growing balloons eventually separated from the budding point and underwent massive vesiculation (Figure 5B). The addition of two cell impermeable RNA/DNA

**Figure 3. Exogenous Material Attached to the Tachyzoite Rear End Is Released Concomitantly to the Twist Motion upon RON2-mC Torus Closure**

(A) A RON2-mC (red) tachyzoite invades an a.U2OS cell expressing GFP-TM PDGFR (green) while carrying on its back a PM-derived filopodium that elongates along with forward movement. Note that the filopodium disconnects from the parasite (arrow) when the latter executes the anticlockwise twist (circular arrow and arrowheads).

(B and C) Microbead clusters (blue) bound to the rear of invading tachyzoites are released (arrows) when they rotate to close the RON2-mC torus prior to PV (green) birth. (C) Note also PM projections that form around the beads (arrowheads) shaped as a pedestal.

(D) An invading tachyzoite (blue arrow) is pulled backward by a posteriorly conjoined partner (yellow arrow) thus passing back through the RON2-mC torus. The direction and length of arrows describes the successive motile activity of each partner. Note, the simultaneous retraction of the budding entry vesicle membrane and the parasite (arrowhead).

(E) One partner of conjoined YFP-tachyzoites enters a.U2OS cell (white arrows show the constriction) and performs the final twisting motion as attested by the alternate flips of the convex side marked with white arrowheads. Note that the extracellular bound partner actively detached (double white arrow) without affecting the invaded partner.

Time lapses show DIC (C–F, top) and fluorescent channels (A, separate and merged channels; B–F, overlays) of entry sequences. All scale bars, 5  $\mu$ m; time is indicated in seconds.

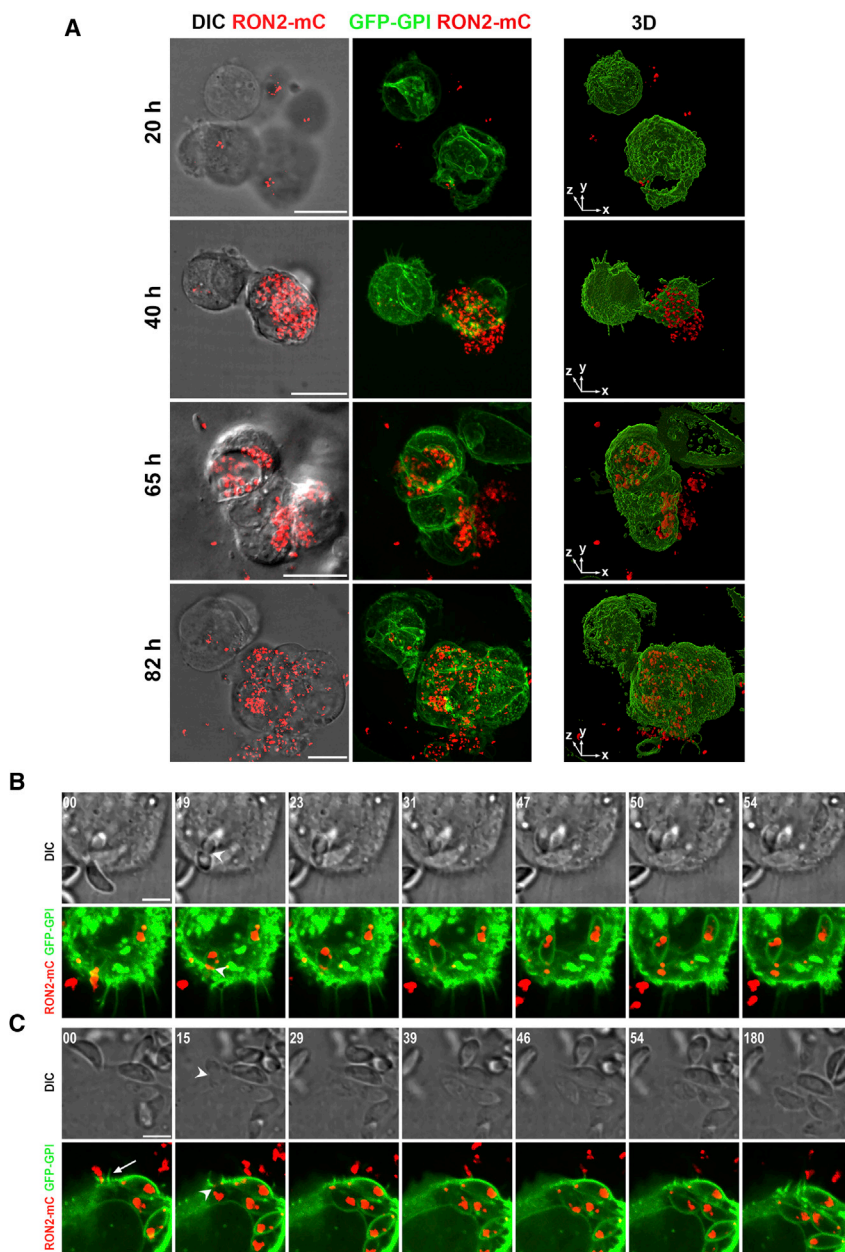


**Figure 4. A Twist Motion of the Tachyzoite Ends Entry into Matrigel-Embedded U2OS Spheroids**

(A) HFF infected with a few RON2-mC tachyzoites are co-cultivated with uninfected GFP-GPI expressing U2OS cells in Matrigel, and imaged at 20, 40, 65, and 82 hr post embedding. A single 0.5- $\mu$ m plane of DIC-mC image overlays are shown (left column); maximal intensity projections of 50–100 images of z planes for GFP-mC channel overlays are presented following image deconvolution (medium column), the deconvolved images are used for 3D representation (right column). Note that RON2-mC tachyzoites multiply in HFFs and the progeny expands in the spheroids. Scale bars, 20  $\mu$ m.

(B and C) Time lapses show DIC (top) and fluorescent merged (bottom) sequences of tachyzoite entry in two different orientations. Note the PM projections that form upon RON2-mC delivery (arrow), the typical static torus through which the tachyzoites squeeze (arrowheads), and the parasite twist that accompanies torus closure. Scale bars, 5  $\mu$ m; time is indicated in seconds.

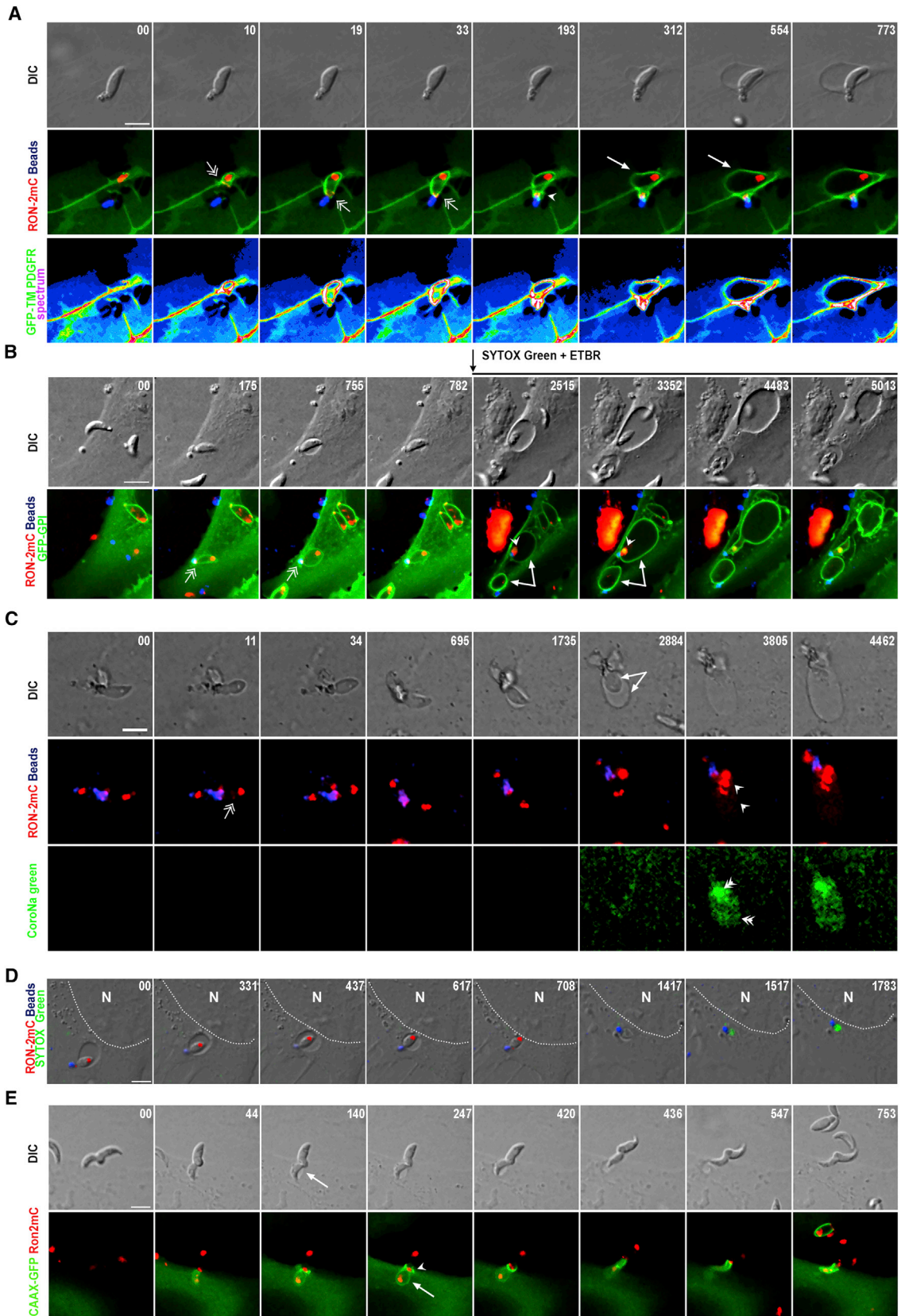
balloon and not in tight-fitting PVs (Figure 5C; see also Mendeley Movies S16 and S17) combined with the SYTOX staining of the parasite and not the host cell nucleus confirmed (1) TJ leakiness during unfinished invasion and (2) causal relation between balloon formation and parasite death (Figure 5D; see also Mendeley Movie S18). Finally, 2D and 3D imaging showed sustained opening of the torus during bead-induced vesicle swelling (Figure S4) while beads alone did not trigger any balloon at the site of contact with the host cell nor did they cause nuclear accumulation of the SYTOX dye (Mendeley Movie S19). Interestingly failure in torus closure and subsequent bulges of the entry vesicle were also observed under less artificial conditions with conjoined parasite pairs that remained trapped onto the maternal RB. The latter when in contact

intercalating agents of different spectral properties, i.e., SYTOX Green (SG) and ethidium bromide (ETBR), into the extracellular medium brought evidence for the tachyzoite death with first cytoplasmic and then nuclear dye accumulation (Figure 5B). Differential interference contrast (DIC) microscopy allowed visualization of the concomitant contraction of the parasite body together with membrane blebs. Importantly, while these processes occurred in other cell types (data not shown), none were detected when the microbeads detached from the parasites and stayed at the host cell PM while the latter were enclosed within PVs (Figure 5B). Next, to assess whether an inflow of  $\text{Na}^+$  ions into the bud through a leaky torus/TJ could cause swelling, we used the cell impermeant sodium indicator CoroNa-Green. The selective accumulation of  $\text{Na}^+$  ions in the

with the host cell PM was surrounded by PM protrusions, therefore recapitulating what was observed with the microbead setting. Importantly, the partner was able to pull both the arrested parasite and its entry vesicle out of the cell, without causing apparent damage to the host cell (Figure 5E; see also Video S9). Overall, these assays allowed demonstrating that proper closure of the toroidal TJ is essential for the biogenesis of a functional intracellular PV.

**Two Distinct Motion Sequences of Specific Kinematical Parameters Allow Establishing that Torus Closure Is Essential for the Biogenesis of the Functional PV**

The release of the PV compartment into the host cell cytoplasm is commonly described as occurring within a few minutes



(legend on next page)

post-closure, hence contrasting with the tens of seconds sufficient for TJ assembly and tachyzoite entry into the budding entry vesicle. Given the lack of PM and PVM markers, and the intrinsic limitations of the patch-clamping approaches, the kinetics of membrane severing and PV release have not been yet captured in real time. We collected data on the time interval between the closure, defined by a decrease of the parasite speed to a negligible value, and the first PV movement ( $n = 214$ ). We next used MATLAB software to determine which distribution model fit the dataset best, and found a bimodal shape, suggesting a dual nature of the observed processes (i.e., two different unimodal distributions) (Figure 6A). The first distribution should account for the process of PV birth per se and was achieved around 78.5 s (SD = 70.4 s) post-TJ closure for the majority of events (Figure 6A, dash line). Indeed, when we tracked both the apical rhoptries and the closed torus, we could observe a small displacement of the posterior end of the PV (i.e., RON2-mC torus tracking, green trajectory) but not of the anterior part (i.e., RON2-mC rhoptry tracking, blue trajectory), a scheme compatible with a moderate reorientation of the PV when fission was achieved (Figure 6C, green trajectory). Within the following 6–10 min, both the rhoptries and torus were seen to move in tandem over a longer distance (Figure 6C, overlapping blue and green trajectories), consistent with a cytoplasmic PV movement defining the second distribution component, which was centered at 263.6 s (SD = 112.9 s) post-torus closure (Figure 6A, dotted line). In other situations, the delay between the reorientation and the capture was negligible and the tracking could not discriminate between them (Figure 6D) or just one type of movement was distinguished (Figure 6E). Interestingly, we next analyzed the speed and the acceleration of the newly born PV ( $n = 32$ ) and defined the first type of motion as “slow” with an average speed around 100 nm/s and an acceleration below 10 nm/s<sup>2</sup> (mean = 5 nm/s<sup>2</sup>; SD = 2 nm/s<sup>2</sup>) (Figure 6B, red points) while the later motion had a comparatively higher average speed around 300 nm/s and higher acceleration (mean = 28 nm/s<sup>2</sup>; SD = 22 nm/s<sup>2</sup>) (Figure 6B, blue points). Collectively, these data fit with the view of (1) the first motion resulting from the actual separation of the entry vesicle from the PM and the consecutive readjustment of the PV position, and of (2) the second and “faster”-defined motion of broader kinetics and features but most typically nucleus-

directed. Indeed, 4D reconstruction provided an accurate description of the disconnection between the PM and the newly born PV within less than a minute, revealing a faster timescale than previously estimated (Figure 6F; see also Mendeley Movie S20). In addition, this analysis also unambiguously identified the site of membrane fusion/fission at the PM, since the RON2-mC torus continued to be detected as a “torus scar” in the PVM when the PV traveled toward the cell nucleus.

### The Rapid Transition Toward the Tachyzoite Intracellular Lifestyle Reflects PV Membrane Remodeling Starting upon Torus Closure

The current model of PVM biogenesis around an invading tachyzoite acknowledges the predominant contribution of the host cell PM while also positing that a minority of components could derive from parasite lipid/protein-released products (Suss-Toby et al., 1996) despite no parasite product delivery has ever been monitored in real time. To examine whether changes in the membrane of the entry vesicle could be associated with torus closure, we used U2OS cell lines expressing the GFP protein in fusion with four different PM targeting/anchoring motifs and for which the GFP reporter was incorporated into the membrane of the budding entry vesicle. The TM of the PDGFR, and GPI motifs drove GFP at the cell surface while the MyrPalm and CAAX motifs promoted the localization of the GFP at the inner leaflet of the host cell PM (Figure 7I). Given the resolution of imaging, they were all detected as a quasi-uniform fluorescent signal throughout the development of the nascent PV in line with no significant addition of non-PM-related material during the process. In contrast, immediately or shortly after torus closure, we observed either a redistribution of fluorescence within the PVM that generated GFP-enriched microdomains (Figures 7A and 7C) or GFP signal dissolution (Figures 7E and 7G). For instance, the GFP-TM PDGFR signal pattern shifted from uniform to transient dot-like sparkles as soon as the torus had closed and typically evolved with sustained enrichment of two symmetrical patches positioned at the anterior part of the PVM (Figure 7A; see also Video S10). In the case of the GFP-GPI membrane reporter, the pattern change was less prominent but characterized by a bright dot that overlapped with the TJ-associated RON2-mC pool in the membrane of the newly born PV (Figure 7C;

### Figure 5. Sustained Mechanical Impairment of the Torus Closure Induces TJ Leakage Assessed by the Inflow of Na<sup>+</sup> Ions and Swelling of the Budding Entry Vesicle within Which the Tachyzoite Dies

(A–D) Time lapses show DIC (top) and fluorescent channel overlays (lower). Tachyzoites attached to microbeads (blue) (A and B), to both a bead and a partner (C), to a partner through abnormal RB (D), enter a U2OS cell expressing GFP-TM PDGFR (A), GFP-GPI (B), CAAX-GFP (E), or a U2OS WT cell (C) but are arrested prior to TJ closure. The double-headed arrows point to the RON2-mC torus (A–C), whereas the swelling budding vesicles are marked with arrows (A–D).

(A) The bead and the torus remain juxtaposed with PM ruffles surrounding them (arrowhead), while bulging of the vesicle starts a few minutes post-block. Note that the fluorescence of the PM reporter does not decrease during bud swelling, consistent with a continuous PM component inflow in the bud membrane (pseudo-colored bottom panel).

(B) At about 40 min post-block, SG and ETBR added to the extracellular milieu (as indicated with an arrow above the frame) are readily incorporated in the cell debris in the medium and are detected in the tachyzoite nucleus, indicating loss of membrane integrity (arrowheads). Note that the extracellular beads are surrounded by PM protrusions and with time the huge balloon (arrows) can separate from the parasite to undergo vesiculation.

(C) At about 45–60 min post-block, ETBR (arrowheads) and CoroNa-Green reagents (double arrowheads) are detected in the PV and the parasite, attesting torus leakiness and subsequent tachyzoite death.

(D) SG specifically accumulates in the parasite posteriorly attached to a bead and within a developing balloon; note that the nucleus (dotted lines) of the host cell is not stained attesting from the leakiness of the torus.

(E) The physical constraint imposed by the RB and the conjoined partner impedes torus closure and triggers a moderate osmotic response (arrow), which reverts upon opposite pulling from the partner. Note the PM projections at the torus site (arrowhead).

All scale bars, 5  $\mu$ m; time is indicated in seconds.

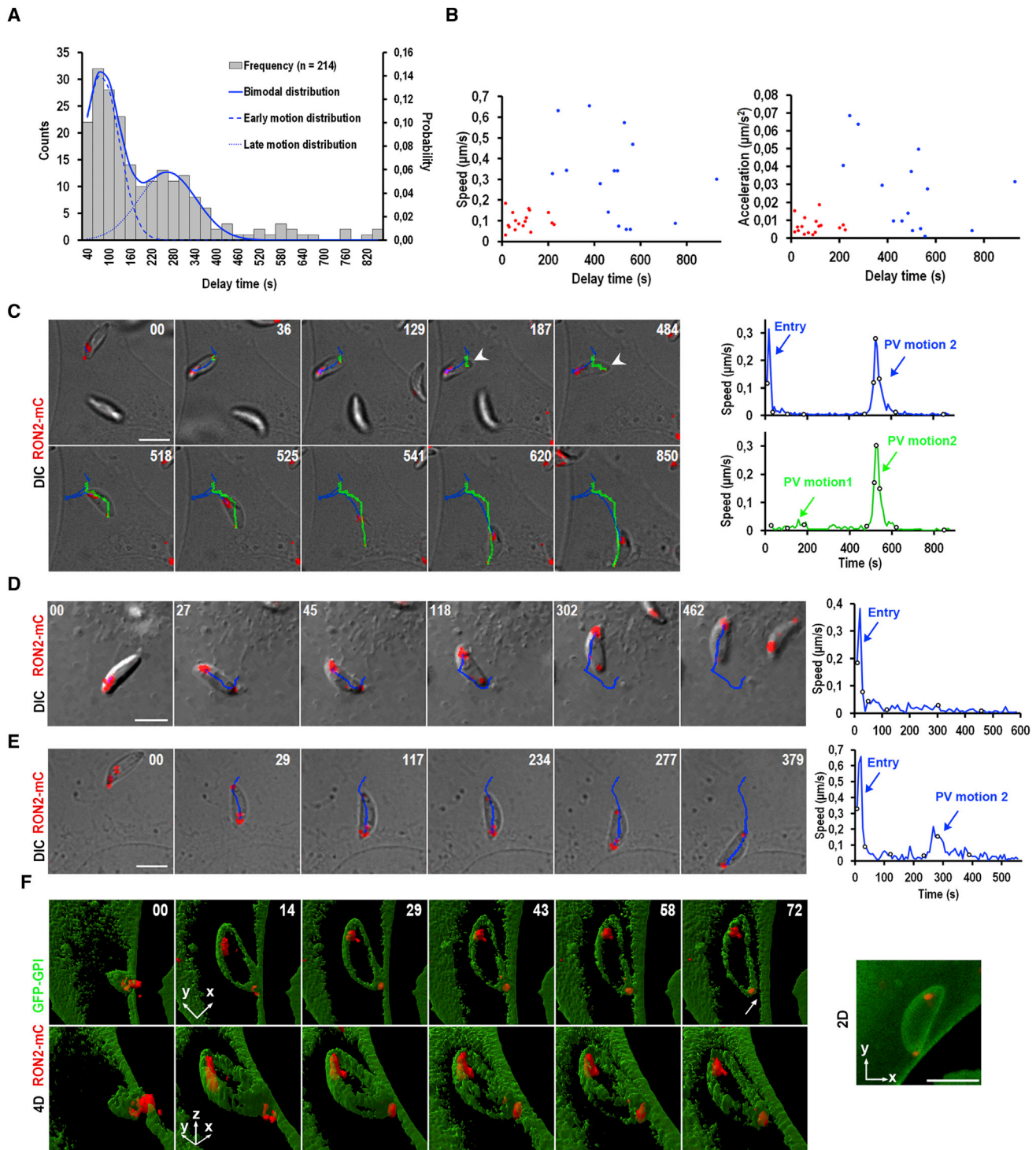


**Figure 6. Two Types of PV Movements Are Characterized by Distinct Kinematical Parameters**

(A) Delay time between torus closure and first PV movement is measured over  $n = 214$  samples and reveals a bimodal distribution, delineated with dashed blue and dotted blue lines, respectively.

(B) Speed of PV and its acceleration are measured over  $n = 32$ , uncovering that for early post-closure motion the determined parameters are low (red) while for the late motion they are comparatively higher and more dispersed (blue).

(C–E) Time lapses of DIC-mC overlays show during entry the tracking of the RON2-mC from the rhoptries (blue trajectories) and from the closed torus (E, green trajectory) while corresponding graphs document the speed of the tracked objects. The three typical situations are presented: (C) first early PV motion, where only the RON2-mC torus moves, thus accounting for PV scission (green trajectory pointed with arrowhead and first peak in the graph, blue arrow), and second PV

(legend continued on next page)

see also Mendeley Movie S21). Redistribution of the GFP-TM PDGFR and GFP-GPI markers were precisely monitored in 4D (Figures 7B and 7D; see also Mendeley Movies S22 and S23) and confirmed dynamic clustering over the whole PV volume. In addition to these high-frequency patterns (Figure 7I), we also noticed more subtle, apical, and dynamic membrane deformations on the PVM (Figure 7C). When the GFP was fused to either the CAAX or MyrPalm PM targeting motifs, the protein faced the cytoplasmic side of the PVM and fluorescence selectively vanished (Figures 7E and 7G; see also Mendeley Movies S24 and S25), as indicated by the fluorescence signal intensity profile along a transect overlapping both PVM and host cell cytoplasm (lines in Figures 7E and 7G, and graphs in Figures 7F and 7H). Moreover, these reorganizations correlated with an increased in the length of the parasite anterior-posterior axis, consistent with a whole parasite body relaxation, seen for each PM marker studied (Figure 7J). Collectively these analyses uncover significant early membrane dynamics in the PVM, likely to involve the delivery of material to the PVM post-torus closure rather than before, therefore at a time when extracellular tachyzoites shifted to an intracellular replicative status.

## DISCUSSION

In this study, we report that the release, in the host cell cytoplasm, of the *T. gondii*-hosting functional PV is mechanically driven by the parasite that closes the nanodevice it first inserts in the host cell PM to allow active invasion. Remarkably, we found no involvement of the host cell master membrane fission dynamin in the process.

### A Parasite Mechanical Twist Imposes Spiral Motion on the Tachyzoite Basal End and Guarantees PV Tightness and Functionality

High-speed live imaging of the invading RON2-mC tachyzoite allowed capturing the torus geometry of the RON nanodevice from the time it inserted and stretched into the target PM to the time it shrunk and capped the rear of the ellipsoid zoite, along with its progression into the host cell cytoplasm, within a budding entry vesicle. To reach this key developmental transition phase, the tachyzoite executed a specific twist along its major axis which amplitude varied between  $\sim 90^\circ$  to several continuous  $360^\circ$  rotations. This twisting motion analyzed by automatic tracking and quantification of two distinct fluorescent internal markers was also detected during invasion of Matrigel-embedded host cell spheroids. Importantly the twist imposed a spiral motion on the parasite rear end, and was synchronous with torus closure. We next provided independent evidence for the twisting motion as part of the torus closure mechanism. First, by pulling a piece of host cell PM material firmly attached at the posterior pole prior to and during cell entry, the tachyzoite induced elongation of a PM filopodium-like projection that retracted upon the tachyzoite twist. Secondly, when submicron-sized beads were weakly

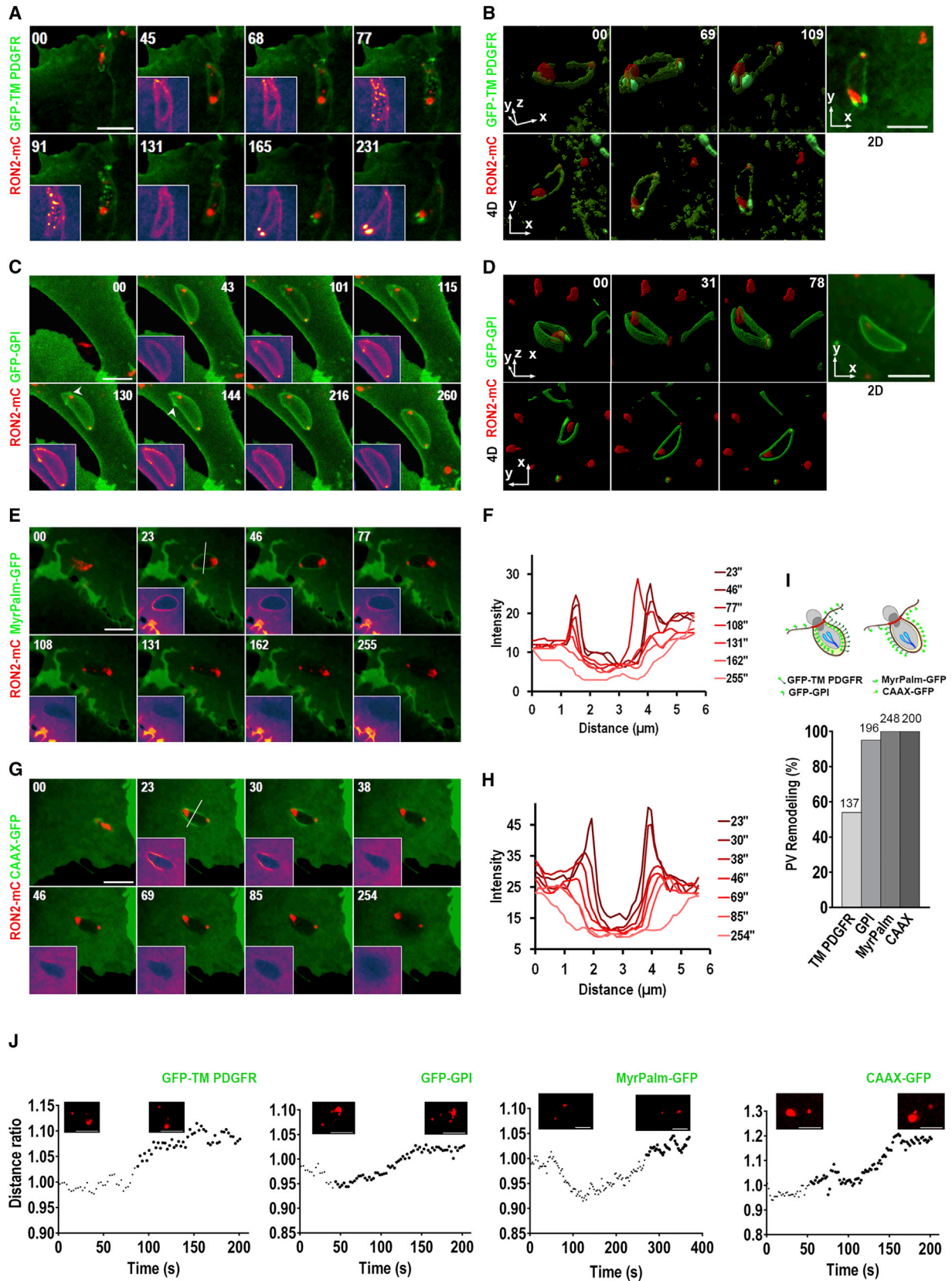
bound to the rear pole of invading zoites, they neither prevented twist nor vesicle sealing and pinch-off. Finally, invading tachyzoites could be mechanically withdrawn from the open but not closed torus by a posteriorly conjoined partner. Of note, the simultaneous retraction of the budding entry vesicle membrane and the parasite suggests a physical coupling between the two membranes, although the features of the interactions have still to be defined.

Moreover, image data-driven mathematical modeling of the torus behavior allowed describing an irregular closure, which would conform well to the twist motion directing the closure event. Future experiments should test whether the specific myosins (Frénel et al., 2017) and actin filaments (F-actin) (Periz et al., 2017) that populate the parasite basal pole, or/and the host cell F-actin anchoring the TJ (Gonzalez et al., 2009) could contribute to the force(s) driving torus closure. The transgenic tachyzoites in which the myosin A encoding gene is deleted ( $\Delta MyoA$ ) are known to assemble a TJ but to be driven into the entry vesicle by an alternative host cell-driven force (Egarter et al., 2014; Bichet et al., 2016). These mutant parasites were able to perform the typical  $90^\circ$  to  $180^\circ$  final twist prior to the release of their PV, suggesting that other motor(s) than MyoA might be involved during this step ( $n = 22$ , Figure S2F; see also Mendeley Movie S26). Definitive evidence for the role of twisting motion during torus closure and PV birth came with parasites arrested just prior closure. Invading tachyzoites that carried covalently bound microbeads at their rear, remained blocked in the budding entry vesicle while being connected to the PM through the RON2-mC torus. This caused the bud to transform into a balloon-like inclusion, therefore indicating a defect in closure with two main consequences. First, the vacuolar space became accessible to the extracellular fluid, as evidenced by sodium influx, which led to osmotic water flow from the cytoplasm followed by ballooning and tachyzoite death. It is worth mentioning the amazing amount of PM material, mostly lipids, that infolded as a huge bud and filled up the cell which likely impacted the whole host cell surface properties and mechanics. As balloons that contained fluid and dead tachyzoite material continued to develop, they eventually ruptured from the connecting PM and immediately underwent fragmentation known as an invariable consequence of acute swelling during cell injury.

### To the PM Severing, Reflected by the Partition of RON2-mC in the Budding PV Membrane, Succeeds the Centripetal Displacement of the Tachyzoite-Hosting Functional PV

Given that the mechanical twist of the zoite guarantees torus closure independently of host cell fission machineries, we propose that the RON torus acts as a mechanical device with analogous properties of the GTPase dynamins. Similarly to the twist of dynamin helical spirals that generate torsion forces on the neck of an endocytic vesicle, the parasite twist would draw together the PM bilayers at the boundary with the torus site,

motion, where both tracked points move simultaneously (green and blue trajectories, peaks in the two graphs labeled with color arrows); (D) PV late motion; (E) short delay between the two PV motions post-TJ closure, which does not allow discrimination between them. (F) 4D reconstruction of the entry sequence shows a top view (top) and side view (bottom) of a RON2-mC tachyzoite entering a GFP-GPI expressing U2OS cell. Note that the delay between torus closure and PVM fission (arrow) is less than a minute. A 2D view frame indicates the scale bar. All scale bars,  $5 \mu\text{m}$ ; time is shown in seconds.



(legend on next page)

hence favoring membrane severing upstream from the torus. In support of this scheme was the typical partition of RON2-mC into the membrane of the newly born PV (i.e., the PVM). To figure out the kinetics of membrane severing and PV release with respect to torus closure, we first identified a bimodal distribution of the dataset reporting the time interval between torus closure and PV intracellular displacement. This distribution fits with two distinct motile events post-torus closure, which were then revealed by dual tracking of the rhoptry/torus and 4D image reconstruction. The PV first executed a space-limited displacement of low speed and acceleration that proceeded with a change of the angle or a forward-backward spring-like movement, and could occur within only tens of seconds. Next, the PV traveled at significantly higher speed and acceleration. Whether the increased amplitude of the tachyzoite final twist to several full rotations reflected less favorable conditions for membrane fission is not yet clear. Interestingly, tachyzoite rotation systematically stopped when the PV had separated from the PM (i.e., fission has occurred). Taking into account that *in vitro* membrane tension influences the kinetics, but not the rate of membrane fission (Dar et al., 2015), exploring a role of membrane tension *in situ* should be informative. Finally, the distinct kinematical features of the second PV motion argue for another force mechanism to control the cytoplasmic PV traveling, such as those supported by microtubule and microfilament motors.

#### A Significant Burst of PVM Remodeling Occurs upon Torus Closure and Coincides with the Transition to Intracellular Lifestyle in a Functional PV

While the fluorescent signal of the budding entry vesicle was detected as quasi-uniform until the torus closed, it became uneven after closure was achieved, giving rise to specific patterns for given PVM markers. The discharge of the ROP2 family members (i.e., ROP2, 4, 5, and 7), as well as of the GRA proteins (i.e., GRA2 as first released GRAs) that insert in or associate with the PVM is expected to promote PVM component, lipid and protein included, redistribution. Numerous factors including proteolytic activities released in the vacuolar space by the parasite, changes in luminal pH or ionic composition of the PV or changes in physical constraints could also contribute to PVM remodeling. Finally, we cannot exclude that the rhoptry-derived e-vacuoles secreted into the cell (Håkansson et al., 2001) could modify the early PVM composition. While future investigation will require characterizing the distinct players along with PVM fluorescent pattern formation, we propose that the torus closure may act as a signal for the tachyzoite to start secreting a pool of proteins and shape a

functional intracellular niche. Such gain of PVM material would also explain the usual relaxation of the tachyzoite body observed upon PVM remodeling by causing an increase in PV volume or/and PVM elasticity. Of note, when the torus was arrested before it closed, as with conjoined parasites or microbeads, we never observed membrane patterning of the budding vesicle including before and during osmotic damages. These observations are consistent with the view of a parasite-derived signal (possibly a combination signals) to regulate the early remodeling of the newly formed PV.

In conclusion, this study highlights the multifunctional properties of a device evolved by the *T. gondii* tachyzoite: once inserted in a limited domain of the host cell PM, thus initiating the invasive process, this parasite device displays mechanical functions that mimic the ones driven by dynamin mechano-enzymes. The outputs of these mechanical functions culminate in the pinching off of the tachyzoite-loaded budding vesicle. Upon the closure of the latter and its transient membrane remodeling, not only emerges a functional PV but also rapidly proceeds the unfolding of the tachyzoite developmental program.

#### STAR★METHODS

Detailed methods are provided in the online version of this paper and include the following:

- KEY RESOURCES TABLE
- CONTACT FOR REAGENT AND RESOURCE SHARING
- EXPERIMENTAL MODELS AND SUBJECT DETAILS
  - Cell Culture
- METHOD DETAILS
  - Cell Lines Engineered to Stably and Ectopically Express Fluorescent Reporters
  - Western blots
  - Immunofluorescence Labeling
  - Image Processing, Kinematic and Mathematical Modeling
  - Manual Tracking with ImageJ Software
  - Automatic Tracking with Icy Software
  - Automatic Tracking and Mathematical Modeling with MATLAB
  - Videomicroscopy
  - 3D/4D Reconstruction
  - 3D Matrigel Co-culture Assays
  - Microbead Assays
  - Large-Scale Invasion Assay

#### Figure 7. A Burst of Membrane Remodeling and Deformation of the Unborn and Newly Born PVs Is Revealed by Different Host Cell PM Reporters

(A–H) Time lapses of fluorescent channel overlays showing RON2-mC expressing zoites entering U2OS cells that express (A) GFP-TM PDGFR, (C) GFP-GPI, (E) MyrPalm-GFP, and (G) CAAX-GFP. Dual-color inlays of GFP channel are shown in the lower left corner of selected frames. Note the dynamic clustering of the GFP (A) and the PVM deformation sites marked with arrowheads (C). 4D reconstruction is shown (B and D) of deconvolved images from (A) and (C), respectively. Both side (top) and top (bottom) orientations are shown as indicated with coordinates. The 2D view shows the scale bar. Dispersion of the PVM signal (E and G) is observed post-torus closure as verified by the GFP signal intensity profiles over time of dissections (F and H) marked by white lines (E and G).

(I) Top shows cartoons of the GFP fusion position in the PM and the entry vesicle, bottom shows histogram of the frequency of characteristic PVM patterns; the number of samples scored is indicated. Note that only clearly detectable patterns were considered positive.

(J) Graphs of representative examples for each PM marker, showing the evolution in parasite length post-torus closure. Length is automatically measured by tracking the RON2-mC at the rhoptry and the torus. The parasite length values prior to and after PVM remodeling are presented as black squares and circles respectively. The data are normalized relative to the parasite length at the time of torus closure.

All scale bars, 5  $\mu$ m.

- **QUANTIFICATION AND STATISTICAL ANALYSIS**
  - Dataset Distribution
  - Quantitative Invasion Assay
- **DATA AND SOFTWARE AVAILABILITY**

### SUPPLEMENTAL INFORMATION

Supplemental Information includes 4 figures and 10 videos and can be found with this article online at <https://doi.org/10.1016/j.chom.2018.06.003>.

### ACKNOWLEDGMENTS

We thank Prof. P. De Camilli (Yale University, New Haven, CT) for the TKO dynamin MEFs, Prof. R. Sadoul (GIN, Grenoble, France) for the KO *Alix* MEFs, Prof. G. Charras (UCL, London, UK) for the CAAX-GFP and MyrPalm-GFP-encoding plasmids, and Dr. H. Ewers (Freie Universität, Berlin, Germany) for the GFP-GPI plasmid. We thank the Foundation for Innovation in Infectiology (FINOVI) for funding this research program, the University Grenoble-Alpes for the AGIR PhD fellowship support to G.P., and Prof. P. Hainaut (IAB, Grenoble, France) for internship support to M. Biesaga. This work was supported by the European Research Council (ERC Consolidator Grant no. 614880 Hosting TOXO to M.-a.H.). V.L. performed the work in the team of I.T. when appointed at the Institut Cochin (Paris, France).

### AUTHOR CONTRIBUTIONS

Conceptualization, I.T.; Software, M. Biesaga, A.D.; Formal Analysis, G.P., M. Biesaga, B.T., I.T., A.D.; Investigation, G.P., B.T., M. Biesaga, I.T., M. Balland; Resources, B.T., V.L., M. Balland, I.T.; Writing – Original Draft, I.T.; Writing – Review & Editing, I.T., G.P.; Visualization, G.P., M. Biesaga, B.T.; Supervision, I.T.; Funding Acquisition, M.-a.H., I.T., M. Balland.

### DECLARATION OF INTERESTS

The authors declare no competing of interests.

Received: January 12, 2018

Revised: March 27, 2018

Accepted: June 5, 2018

Published: June 28, 2018

### REFERENCES

Amiar, S., MacRae, J.I., Callahan, D.L., Dubois, D., van Dooren, G.G., Shears, M.J., Cesbron-Delauw, M.-F., Maréchal, E., McConville, M.J., McFadden, G.I., et al. (2016). Apicomplast-localized lysophosphatidic acid precursor assembly is required for bulk phospholipid synthesis in *Toxoplasma gondii* and relies on an algal/plant-like glycerol 3-phosphate acyltransferase. *PLoS Pathog.* **12**, e1005765.

Antony, B., Burd, C., De Camilli, P., Chen, E., Daumke, O., Faelber, K., Ford, M., Frolov, V.A., Frost, A., Hinshaw, J.E., et al. (2016). Membrane fission by dynamin: what we know and what we need to know. *EMBO J.* **35**, 2270–2284.

Besteiro, S., Michelin, A., Poncet, J., Dubremetz, J.-F., and Lebrun, M. (2009). Export of a *Toxoplasma gondii* rhoptry neck protein complex at the host cell membrane to form the moving junction during invasion. *PLoS Pathog.* **5**, e1000309.

Bichet, M., Joly, C., Henni, A.H., Guilbert, T., Xémard, M., Tafani, V., Lagal, V., Charras, G., and Tardieux, I. (2014). The *Toxoplasma*-host cell junction is anchored to the cell cortex to sustain parasite invasive force. *BMC Biol.* **12**, 773.

Bichet, M., Touquet, B., Gonzalez, V., Florent, I., Meissner, M., and Tardieux, I. (2016). Genetic impairment of parasite myosin motors uncovers the contribution of host cell membrane dynamics to *Toxoplasma* invasion forces. *BMC Biol.* **14**, 97.

Caldas, L.A., Attias, M., and de Souza, W. (2009). Dynamin inhibitor impairs *Toxoplasma gondii* invasion. *FEMS Microbiol. Lett.* **301**, 103–108.

Cesarz, Z., and Tamama, K. (2016). Spheroid culture of mesenchymal stem cells. *Stem Cells Int.* **2016**, 9176357.

Charron, A.J., and Sibley, L.D. (2004). Molecular partitioning during host cell penetration by *Toxoplasma gondii*. *Traffic* **5**, 855–867.

de Chaumont, F., Dallongeville, S., Chenouard, N., Hervé, N., Pop, S., Provoost, T., Meas-Yedid, V., Pankajakshan, P., Lecomte, T., Le Montagner, Y., et al. (2012). Icy: an open bioimage informatics platform for extended reproducible research. *Nat. Methods* **9**, 690–696.

Cossart, P., and Helenius, A. (2014). Endocytosis of viruses and bacteria. *Cold Spring Harb. Perspect. Biol.* **6**, <https://doi.org/10.1101/cshperspect.a016972>.

Dar, S., Kamerkar, S.C., and Pucadyil, T.J. (2015). A high-throughput platform for real-time analysis of membrane fission reactions reveals dynamin function. *Nat. Cell Biol.* **17**, 1588–1596.

Delorme-Walker, V., Abrivard, M., Lagal, V., Anderson, K., Perazzi, A., Gonzalez, V., Page, C., Chauvet, J., Ochoa, W., Volkmann, N., et al. (2012). Toxofilin upregulates the host cortical actin cytoskeleton dynamics, facilitating *Toxoplasma* invasion. *J. Cell Sci.* **125**, 4333–4342.

Egarter, S., Andenmatten, N., Jackson, A.J., Whitelaw, J.A., Pall, G., Black, J.A., Ferguson, D.J.P., Tardieux, I., Mogilner, A., and Meissner, M. (2014). The *Toxoplasma* Acto-MyoA motor complex is important but not essential for gliding motility and host cell invasion. *PLoS One* **9**, e91819.

Ferguson, S.M., and De Camilli, P. (2012). Dynamin, a membrane-remodeling GTPase. *Nat. Rev. Mol. Cell Biol.* **13**, 75–88.

Ferguson, S.M., Ferguson, S., Raimondi, A., Paradise, S., Shen, H., Mesaki, K., Ferguson, A., Destaing, O., Ko, G., Takasaki, J., et al. (2009). Coordinated actions of actin and BAR proteins upstream of dynamin at endocytic clathrin-coated pits. *Dev. Cell* **17**, 811–822.

Fischer-Friedrich, E., Hyman, A.A., Jülicher, F., Müller, D.J., and Helenius, J. (2014). Quantification of surface tension and internal pressure generated by single mitotic cells. *Sci. Rep.* **4**, 6213.

Frénal, K., Jacot, D., Hammoudi, P.-M., Graindorge, A., Maco, B., and Soldati-Favre, D. (2017). Myosin-dependent cell-cell communication controls synchronicity of division in acute and chronic stages of *Toxoplasma gondii*. *Nat. Commun.* **8**, 15710.

Goddard, T.D., Huang, C.C., Meng, E.C., Pettersen, E.F., Couch, G.S., Morris, J.H., and Ferrin, T.E. (2017). UCSF ChimeraX: meeting modern challenges in visualization and analysis. *Protein Sci.* **27**, 14–25.

Gonzalez, V., Combe, A., David, V., Malmquist, N.A., Delorme, V., Leroy, C., Blazquez, S., Ménard, R., and Tardieux, I. (2009). Host cell entry by apicomplexa parasites requires actin polymerization in the host cell. *Cell Host Microbe* **5**, 259–272.

Guérin, A., Corrales, R.M., Parker, M.L., Lamarque, M.H., Jacot, D., El Hajj, H., Soldati-Favre, D., Boulanger, M.J., and Lebrun, M. (2017). Efficient invasion by *Toxoplasma* depends on the subversion of host protein networks. *Nat. Microbiol.* **2**, 1358–1366.

Håkansson, S., Charron, A.J., and Sibley, L.D. (2001). *Toxoplasma* evacuoles: a two-step process of secretion and fusion forms the parasitophorous vacuole. *EMBO J.* **20**, 3132–3144.

Kumari, S., Mg, S., and Mayor, S. (2010). Endocytosis unplugged: multiple ways to enter the cell. *Cell Res.* **20**, 256–275.

Lee, G.Y., Kenny, P.A., Lee, E.H., and Bissell, M.J. (2007). Three-dimensional culture models of normal and malignant breast epithelial cells. *Nat. Methods* **4**, 359–365.

Lodoen, M.B., Gerke, C., and Boothroyd, J.C. (2010). A highly sensitive FRET-based approach reveals secretion of the actin-binding protein toxofilin during *Toxoplasma gondii* infection. *Cell. Microbiol.* **12**, 55–66.

Mercier, V., Laporte, M.H., Destaing, O., Blot, B., Blouin, C.M., Pernet-Gallay, K., Chatellard, C., Saoudi, Y., Albiges-Rizo, C., Lamaze, C., et al. (2016). ALG-2 interacting protein-X (Alix) is essential for clathrin-independent endocytosis and signaling. *Sci. Rep.* **6**, 26986.

Mordue, D.G., Desai, N., Dustin, M., and Sibley, L.D. (1999). Invasion by *Toxoplasma gondii* establishes a moving junction that selectively excludes

- host cell plasma membrane proteins on the basis of their membrane anchoring. *J. Exp. Med.* *190*, 1783–1792.
- Morisaki, J.H., Heuser, J.E., and Sibley, L.D. (1995). Invasion of *Toxoplasma gondii* occurs by active penetration of the host cell. *J. Cell Sci.* *108* (Pt 6), 2457–2464.
- Park, R.J., Shen, H., Liu, L., Liu, X., Ferguson, S.M., and De Camilli, P. (2013). Dynamin triple knockout cells reveal off target effects of commonly used dynamin inhibitors. *J. Cell Sci.* *126*, 5305–5312.
- Periz, J., Whitelaw, J., Harding, C., Gras, S., Del Rosario Minina, M.I., Latorre-Barragan, F., Lemgruber, L., Reimer, M.A., Insall, R., Heaslip, A., et al. (2017). *Toxoplasma gondii* F-actin forms an extensive filamentous network required for material exchange and parasite maturation. *Elife* *6*, <https://doi.org/10.7554/eLife.24119>.
- Persaud, A., Cormerais, Y., Pouyssegur, J., and Rotin, D. (2018). Dynamin inhibitors block activation of mTORC1 by amino acids independently of dynamin. *J. Cell Sci.* *131*, <https://doi.org/10.1242/jcs.211755>.
- Poupel, O., Boleti, H., Axisa, S., Couture-Tosi, E., and Tardieux, I. (2000). Toxofilin, a novel actin-binding protein from *Toxoplasma gondii*, sequesters actin monomers and caps actin filaments. *Mol. Biol. Cell* *11*, 355–368.
- Preta, G., Cronin, J.G., and Sheldon, I.M. (2015). Dynasore - not just a dynamin inhibitor. *Cell Commun. Signal.* *13*, 24.
- Sidik, S.M., Huet, D., Ganesan, S.M., Huynh, M.-H., Wang, T., Nasamu, A.S., Thiru, P., Saeij, J.P.J., Carruthers, V.B., Niles, J.C., et al. (2016). A genome-wide CRISPR screen in *Toxoplasma* identifies essential apicomplexan genes. *Cell* *166*, 1423–1435.e12.
- Straub, K.W., Peng, E.D., Hajagos, B.E., Tyler, J.S., and Bradley, P.J. (2011). The moving junction protein RON8 facilitates firm attachment and host cell invasion in *Toxoplasma gondii*. *PLoS Pathog.* *7*, e1002007.
- Suss-Toby, E., Zimmerberg, J., and Ward, G.E. (1996). *Toxoplasma* invasion: the parasitophorous vacuole is formed from host cell plasma membrane and pinches off via a fission pore. *Proc. Natl. Acad. Sci. USA* *93*, 8413–8418.

## STAR★METHODS

### KEY RESOURCES TABLE

| REAGENT or RESOURCE  | SOURCE  | IDENTIFIER  |
|--|---|---|
| <b>Antibodies</b>  |   |   |
| Mouse monoclonal Anti-P30 Novocastra Clone TP3   | Leica   | Cat#NCL-TG; RRID:AB_564038  |
| Rabbit homemade polyclonal Anti-Alix   | Covalab   | Cat#pab0204; RRID:AB_2716810  |
| Monoclonal mouse Anti-Dynamin (Clone41)  | BD Biosciences  | Cat#610245; RRID:AB_397640  |
| Rabbit polyclonal Anti-p34-Arc/ARPC2   | Millipore   | Cat#07-227; RRID:AB_310447  |
| Mouse monoclonal Anti-GAPDH  | Ambion  | Cat#AM4300; RRID:AB_437392  |
| <b>Chemicals, Peptides, and Recombinant Proteins</b>   |   |   |
| 4-Hydroxytamoxifen   | Sigma-Aldrich   | H6278   |
| <b>Deposited Data</b>  |   |   |
| Additional supplemental videos and legends   | Mendeley Data   | Tardieux, Isabelle (2018), "Pavlou et al. Cell Host Microbe Supplemental Data," Mendeley Data, v1 <a href="https://doi.org/10.17632/fmhnprp66j.1">https://doi.org/10.17632/fmhnprp66j.1</a> |
| <b>Experimental Models: Cell Lines</b>   |   |   |
| U2OS (female)  | ATCC  | Cat#HTB-96; RRID:CVCL_0042  |
| U2OS GFP-Flag-Alix (female)  | This paper  | N/A   |
| U2OS GFP-GPI (female)  | This paper  | N/A   |
| U2OS GFP-TMPDGFR (female)  | This paper  | N/A   |
| U2OS MyrPalm-GFP (female)  | This paper  | N/A   |
| U2OS CAAX-GFP (female)   | This paper  | N/A   |
| HFF (male)   | ATCC  | Cat# SCRC-1041; RRID:CVCL_3285  |
| MEFs isolated from Alix KO mice provided by R. Sadoul (who did not reveal the sex)                           | <a href="#">Mercier et al., 2016</a>  | N/A   |
| MEFs isolated from Alix KO mice provided by R. Sadoul (who did not reveal the sex) transfected with GFP-Alix | This paper  | N/A   |
| MEFs isolated from TKO mice provided by P. De Camilli (who did not reveal the sex)                           | <a href="#">Park et al., 2013</a>   | N/A   |
| MEFs isolated from parental mice provided by P. De Camilli (who did not reveal the sex)                      | <a href="#">Park et al., 2013</a>   | N/A   |
| U2OS GFP-Dynamin1(Low expression) (female)   | This paper  | N/A   |
| U2OS GFP-Dynamin1(High expression) (female)  | This paper  | N/A   |
| <b>Experimental Models: Organisms/Strains</b>  |   |   |
| <i>T.gondii</i> :RH $\Delta$ KU80 RON2-mC (DHFR)   | <a href="#">Bichet et al., 2014</a>   | N/A   |
| <i>T.gondii</i> :RH YFP  | Laboratory of David Roos  | N/A   |
| <i>T.gondii</i> :RH-TATi FNR-mRFP  | <a href="#">Amiar et al., 2016</a>  | N/A   |
| <i>T.gondii</i> :RH $\Delta$ KU80 $\Delta$ MyoA  | <a href="#">Bichet et al., 2016</a>   | N/A   |
| <b>Software and Algorithms</b>   |   |   |
| MATLAB R2016a  | Mathworks   | RRID:SCR_001622   |
| ImageJ 1.51j8  | <a href="https://imagej.nih.gov/ij/">https://imagej.nih.gov/ij/</a>                   | RRID:SCR_003070   |
| Icy 1.9.5.1  | <a href="http://icy.bioimageanalysis.org/">http://icy.bioimageanalysis.org/</a>       | RRID:SCR_010587   |
| UCSF ChimeraX 0.1  | <a href="https://www.rbvi.ucsf.edu/chimerax/">https://www.rbvi.ucsf.edu/chimerax/</a> | RRID:SCR_015872   |
| Graphpad Prism 6.01  | Graphpad  | RRID:SCR_002798   |
| MetaMorph 7.7.0.0  | Molecular devices   | RRID:SCR_002368   |
| ScanR 2.7.1  | Olympus   | N/A   |

(Continued on next page)

### Continued

| REAGENT or RESOURCE  | SOURCE                  | IDENTIFIER    |
|--|-------------------------|---------------|
| Other  |                         |               |
| FluoSpheres Carboxylate-Modified Microspheres, 0.2 $\mu\text{m}$ , dark red fluorescent (660/680), 2% solids | ThermoFisher Scientific | F8807         |
| CoroNa Green, cell impermeant  | ThermoFisher Scientific | C36675        |
| SYTOX Green Nucleic Acid Stain   | ThermoFisher Scientific | S7020         |
| BD Matrigel Matrix   | BD                      | 356234        |
| Cell Tracker CMAC blue dye   | Life Technologies       | C2110         |
| Chamlide chambers  | LCI Corp., Seoul, Korea | CM-B18-1      |
| HBSS++   | Life Technologies       | 24020117      |
| DMEM   | Life Technologies       | 10566016      |
| Penicillin/Streptomycin  | Life Technologies       | 15140122      |
| HEPES  | Life Technologies       | 15630080      |
| Protease inhibitors  | Roche                   | 11697498001   |
| Poly-L-lysine  | Sigma-Aldrich           | P8920         |
| Fibronectin  | Sigma-Aldrich           | F1141-5MG     |
| MatTek glass bottom dishes   | MatTek                  | P35G-1.5-14-C |
| MES  | Sigma-Aldrich           | M3671-1KG     |
| Lipofectamine LTX  | Invitrogen              | 15338100      |
| Neon transfection system kit   | Invitrogen              | MPK1096       |

### CONTACT FOR REAGENT AND RESOURCE SHARING

Further information and requests for reagents may be directed to and will be fulfilled by the Lead Contact, Isabelle Tardieux ([isabelle.tardieux@inserm.fr](mailto:isabelle.tardieux@inserm.fr)).

### EXPERIMENTAL MODELS AND SUBJECT DETAILS

No vertebrate animals were used in this study.

#### Cell Culture

Human cell lines expressing fluorescent reporters of interest (i.e., targeting the host cell PM and the PVM as well as membrane fission players such as dynamin and Alix proteins) were obtained from human female bone-derived U2OS cells (ATCC. no. HTB-96) or from MEF cells. The MEF TKO cell line isolated from dynamin TKO mice was given by P. De Camilli (Yale University, New Haven, CT) who did not reveal the sex. This cell line was derived in De Camilli laboratory from mice harboring floxed alleles of all Dynamin 1, 2, and 3 genes (triple KO: TKO) and transgenic for 4-hydroxytamoxifen (OHT)-inducible Cre recombinase (Park et al., 2013). Briefly, De Camilli laboratory obtained the TKO mice by interbreeding 129SV/J and C57Bl6 mice first with dynamin 1 and 2 conditional double KO with the dynamin 3 conditional KO and with mice transgenic for Cre-ER to generate tamoxifen-inducible triple conditional KO mice (Dnm1<sup>loxP/loxP</sup>; Dnm2<sup>loxP/loxP</sup>; Dnm3<sup>loxP/loxP</sup>; Cre-ER<sup>+/-</sup>).

MEFs isolated from Alix KO mice were provided by R. Sadoul (GIN, Grenoble) who did not reveal the sex. This line has been generated in R. Sadoul laboratory from 3 individual E12.5 embryos of Alix homozygous KO mouse. To obtain the Alix ko mice, exon 2 of *alix* (chromosome 9) was targeted by LoxP sites and the floxed mice was backcrossed with the CMV-Cre mouse (Mercier et al., 2016).

To silence the MEF TKO cells, we adapted the protocol from (Ferguson et al., 2009) such as cells were incubated with 4  $\mu\text{M}$  4-hydroxytamoxifen for 3 days and left on 0.4  $\mu\text{M}$  OHT until use, resulting in dynamin depletion at 5-6 days from the start of the treatment period. For all assays, silenced cells were not used after 9 days post start of OHT exposure and they were systematically checked for dynamin depletion by western blot prior to video-recording sessions.

Both U2OS and MEF cell lines were certified as *Mycoplasma* free and grown in high glucose Dulbecco's Modified Eagle's Medium Glutamax (DMEM) supplemented with 10% fetal bovine serum (FBS), 10 mM 4-(2-HydroxyEthyl)-1-PiperazineEthaneSulfonic acid (HEPES), 100 units/mL penicillin, and 100 mg/mL streptomycin (i.e., complete medium) at 37°C with 95% air and 5% CO<sub>2</sub>.

#### *Toxoplasma Gondii*

The type 1 *T. gondii* strains (RH- $\Delta\text{KU}80$ -RON2-mCherry, and RH-YFP (Bichet et al., 2014, 2016) (RH-FNR-mRFP; (Amiar et al., 2016) were propagated *in vitro* by serial passages on human foreskin fibroblasts (HFF-1, ATCC. no. SCRC-1041) monolayers grown in complete medium at 37°C with 95% air and 5% CO<sub>2</sub>. HFF cells were certified as *Mycoplasma* free. Invasive parasites were prepared in

Motility Buffer (HBSS<sup>++</sup> supplemented with 0.2 to 1% FCS) for immediate live imaging of invasion sequences of human cells previously plated on poly-L-Lysine (50  $\mu$ g/mL) or fibronectin (50  $\mu$ g/mL) coated glass coverslips.

## METHOD DETAILS

### Cell Lines Engineered to Stably and Ectopically Express Fluorescent Reporters

To engineer stable cells line expressing chimeric GFP-PM reporters that include the transmembrane domain of the PDGFR, GPI, CAAX and MyrPalm domain or chimeric GFP-dynamin1 or chimeric GFP-Alix, lipofectamin LTX was used for U2OS cell DNA transfection and the Neon transfection system was preferred for MEFs. Lipofectamin-mediated transfection was conducted with a combination of plasmids encoding the chimeric protein of interest (1  $\mu$ g) and a puromycin resistance cassette (0.16  $\mu$ g). MEFs were electroporated, ([www.thermofisher.com](http://www.thermofisher.com)). Puromycin was added  $\sim$  68 hr following DNA transfection at 1  $\mu$ g/mL final dilution and fresh medium containing antibiotic was changed every 3 days. Once GFP fluorescent cell colonies were detected they were isolated and expanded. Alternatively independent stable transfectant clones were obtained by serial dilution in 96-well plates.

### Western blots

Cultures of Alix KO and rescued Alix KO GFP-Alix MEF cells as well as U2OS WT and U2OS expressing GFP-dynamin1 or GFP-Alix were harvested using trypsin-EDTA followed by addition of complete medium. Cell suspensions were collected by centrifuged in a large volume of PBS and were lysed in 10 mM Tris-HCl, pH 7.4, 100 mM NaCl, 1 mM EDTA, 1mM EGTA, 1% Triton X-100, 0.1 SDS, 0.5% deoxycholate, 10% glycerol-containing buffer supplemented with a cocktail of protease inhibitors (30 min, 4°C). After clarification (13.000g, 10 min, 4°C), the protein extracts from  $2 \times 10^5$  cells were separated on 4-12% gradient pre-cast SDS-PAGE gels and transferred onto a polyvinylidene fluoride membrane by liquid transfer. Membranes were probed using appropriate primary antibodies - mouse anti-dynamin (clone 41, 1:2500) or rabbit anti-Alix (1:3000) - followed by phosphatase-conjugated goat appropriate secondary antibodies (1:7000). Signals were detected using NBT-BCIP. The same membranes were also probed with rabbit anti-GAPDH antibodies (1:7000), to control for protein loads.

### Immunofluorescence Labeling

Immunofluorescence labeling of MEF TKO dynamin cells before and after OHT treatment was performed following cell fixation in 3.7% paraformaldehyde (PFA) in PBS, pH 7.5 (20 min, 23°C) and the quenching of residual PFA with  $\text{NH}_4^+\text{Cl}$  (50 mM) in PBS (10 min). Fixed cells were permeabilized with 0.2% Triton X-100 in PBS for 10 min and incubated in 2% BSA as a saturating buffer (30 min) and all reagents subsequently used were diluted in this buffer. Polyclonal anti-p34-Arc/ARPC2 antibodies (1:150) were used (2 hr, 23°C) followed by Alexa Fluor 488 anti-rabbit cross-adsorbed IgG [ $\text{H}^+\text{L}$ ] antibodies (1:1000). Samples were mounted in Mowiol 14-88 and analyzed by laser scanning confocal microscopy. For the invasion assays (see below), immunolabeling was performed without cell permeabilization to allow discriminating between the extracellular and intracellular parasites. Extracellular tachyzoites were selectively stained using antibodies raised against the surface exposed TgP30 protein (1:800) followed by Alexa-594-coupled anti-mouse cross-adsorbed IgG (H+L) (1:1000) antibodies while SYBR Green-i-nucleic acid (1:20,000) was added to detect all cell nuclei. The 96-well plates were then scanned as detailed in the invasion assay section.

### Image Processing, Kinematic and Mathematical Modeling

All samples processed were randomly selected by researchers that were not blinded during the study. Images from x,y,z,t stacks for every event of interest were prepared and annotated with time, bar scale and sometimes, graphic labels, using MetaMorph ([www.moleculardevices.com](http://www.moleculardevices.com)) software from the raw image data file. Image processing methods along with kinematic and mathematical modelling was subsequently applied using ImageJ (<https://imagej.nih.gov/ij/>), Icy (<http://Icy.bioimageanalysis.org>), MATLAB ([www.mathworks.com](http://www.mathworks.com)), and ChimeraX (<https://www.cgl.ucsf.edu/chimerax/docs/credits.html>) software.

### Manual Tracking with ImageJ Software

Manual tracking plugin was applied on DIC-mC channel overlay images obtained with MetaMorph software to describe in time the spatial xy positions of both the parasite RON2-mC rhoptries and closed torus as a way to monitor the PV motion in the cytoplasm and examine fission delay time.

### Automatic Tracking with Icy Software

Automatic tracking was applied on the images retrieved from the mC channel of the video-recording assays to describe the tachyzoite twisting motion. We first used the “Median filter” to remove noise, and the tool “Spot detector” for selecting-filtering size and intensity values and for automatic detection of the RON2-mC spots. Next, the tool “Track Manager” allowed tracking of the detected mC spots, while the “Track Painter” allowed painting of the tracks and “Track Processor Time Clip” the editing of the timing of the track visualization. Finally, the speed values were provided with the “Track Processor Instant Speed.” Automatic tracking combined with “Track Processor intensity profile” was also used to analyze signal intensity of the tracked object during parasite rotation. To measure the change in parasite length once intracellular and enclosed in the newly formed PV, both the front and back RON2-

mC spots were tracked and the “Distance Profiler” plugin was used to calculate the distance between the two spots overtime. Data obtained either by manual or automatic tracking were exported in Excel files and then visualized using Prism ([www.graphpad.com](http://www.graphpad.com)) and Excel software.

### Automatic Tracking and Mathematical Modeling with MATLAB

In order to track and model the torus shrinkage, images were preprocessed in MATLAB by applying *medfilt2* function and binarized over a manually chosen threshold. For the two-point model, the *bwareafilt* function was used to extract two biggest objects. Consequently, two most-distanced pixels were selected for each timeframe and tracked over time. Speed was calculated on the basis of displacement in relation to first point. For the ellipse model, *fit\_ellipse* function was used to fit the ellipse equation. For the ellipse model, the ellipse Equation 1 was fit with the least squares method.

$$ax^2 + bxy + cy^2 + dx + ey + f = 0 \quad (\text{Equation 1})$$

### Videomicroscopy

Time-lapse video microscopy was conducted in chamlide chambers (LCI Corp., Seoul, Korea) installed on an Eclipse Ti inverted confocal microscope (Nikon France Instruments, Champigny sur Marne, France) with a temperature and CO<sub>2</sub>-controlled stage and chamber (LCI Corp., Seoul, Korea), equipped with a coolsnap HQ2 camera and a CSU X1 spinning disk (Yokogawa, Roper Scientific, Lisses, France). The microscope was piloted using MetaMorph software (Universal Imaging Corporation, Roper Scientific, Lisses, France). Similar parameters for image acquisition (i.e., exposure time, gain, laser power, etc) and image processing (i.e., with ScanR, deconvolution, etc, see below) were used throughout each independent experiment.

### 3D/4D Reconstruction

For 3D reconstruction, the raw data (i.e., xyz files) obtained with MetaMorph software were processed with Icy to crop the sequence and region of interest and of z stack from each channel were deconvoluted using the “Iterative Deconvolve 3D” plugin (ImageJ software). For 4D reconstruction, the x,y,z,t raw data were similarly processed with Icy to extract each fluorescent channel separately and to save it as multiple files. We then used the TIF converter (MATLAB, M. Biesaga) to create one file for all the z stacks in the specific time point and then used the plugin “DeconvolutionBatchProcessing” (ImageJ, M. Biesaga) to deconvolute the z stacks over time. Except for the Matrigel assays (see next section), z step was 0.3 μm. The UCSF ChimeraX software (Goddard et al., 2017) was used for both 3D and 4D reconstruction of processed images.

### 3D Matrigel Co-culture Assays

HFF cells infected by 1 to 2 Ron2-mC tachyzoites and GFP-GPI U2OS cells were harvested with trypsin-EDTA, further diluted in excess of complete medium and numerated.  $\sim 2 \times 10^5$  cells of each cell line were combined and centrifuged (5 min, 500g) before being collected in 200 μL of a pre-chilled solution containing EHS (BD Matrigel Basement Membrane Matrix Growth Factor Reduced Source: Engelbreth-Holm-Swarm (EHS) Mouse Tumor) and complete DMEM (ratio = 1/3.6). The mixture of cells and EHS/DMEM was gently deposited with cold prechilled pipettes on a MatTek glass bottom surface pre-coated with a thin layer of EHS/DMEM mixture (15-30 min at 37°C, 5% CO<sub>2</sub>). The whole setting was incubated 1 hr at 37°C, 5% CO<sub>2</sub> to allow EHS to gel before addition of 2 mL of complete medium which was replaced every 48 hr. The 3D cultures were monitored over a 96 hr time period to control for egress (starting  $\sim$  40-48 hr post embedding) and U2OS cell spheroid development. Z-image stacks (n= 50-100, z step = 0,5 μm) and time-lapse acquisition of sequences showing the progeny egress from HFF cells and the invasion of U2OS cells were captured using the spinning disk confocal Eclipse microscope as mentioned above. Iterative deconvolution followed by 3D reconstruction was applied to image stacks as explained in a previous section. This 3D culture protocol is adapted from (Lee et al., 2007) but the EHS/DMEM ratio used appeared as a critical parameter to allow tachyzoite egress from HFFs.

### Microbead Assays

0.2 μm diameter carboxylate-modified dark-red fluospheres were activated using the “Microsphere Coupling – Two-step EDC/Sulfo NHS Covalent Coupling Procedure for Estapor Carboxyl-modified Dyed Microspheres” protocol ([www.merckmillipore.com](http://www.merckmillipore.com)). 50 μL of stock suspension were diluted in 150 μL MES buffer (50 mM, pH 6.0) following activation. Then 5 μL beads solution were mixed with  $\sim 10^5$  tachyzoites in 150 μL of MB 0.2% FCS. 40 μL of the mix were added to the chamber containing the U2OS adherent cells plated on coverslips in 100 μL of MB. In specific assays, ETBR (2 mM stock solution in DMSO), SYTOX green (5 mM stock solution in DMSO), and CoroNa green (1 mM stock solution in DMSO) were perfused in the chamber setting to reach 0.5 to 1 μM final concentration of each reagent.

### Large-Scale Invasion Assay

U2OS (WT, GFP-Alix, GFP-dynamin1) and MEF (WT, TKO, KO *Alix* and KO *Alix* GFP-Alix i.e., “Rescue KO *Alix*”) were seeded at a density of 10<sup>4</sup> or 2 × 10<sup>4</sup> cells per well, respectively, into 96-well plates and cultivated for 24 hr at 37°C and 5% CO<sub>2</sub> to allow cell reaching sub-confluency. Cells from wells that serve as controls were stained with the nuclear dye Hoechst 33342 (1 μg/mL) and automatically scanned under microscope to quantify the average number of cells per well prior the invasion assay.  $\sim 5 \times 10^6$

to  $10^7$  parasites were collected upon spontaneous egress from synchronously infected HFF monolayers and next loaded with the Cell Tracker CMAC blue dye (15  $\mu$ M final dilution, stock solution 10 mM in DMSO) in 10 mL of complete medium (20 min at 37°C). Dye-loaded tachyzoites were dispersed in large amount of complete medium before centrifugation (900g, 7 min) to remove non-internalized excess dye. The parasites were gently resuspended in 10 mL of complete medium and enumerated. The amount of tachyzoites to add to each well was carefully adjusted such as the 20:1 MOI was maintained similar among the human cell types under study taking into consideration their respective density per well (see above). To optimize invasion, tachyzoites were gently centrifuged (1 min, 100 g) and immediately incubated for 45 min at 37°C and 5% CO<sub>2</sub> until invasion was stopped by PFA addition. After immunofluorescence labeling (see above), samples were automatically scanned at a magnification of  $\times 20$  under an Olympus ScanR automated inverted microscope. Images were acquired for 3 (MEF TKO dynamins) and 4 (U2OS GFP-dynamain, KO MEF *Alix* and U2OS GFP-*Alix*) wells per condition for each invasion assay, with 20 randomly scanned fields for each well and further processed with ScanR software. ScanRAnalysis includes successive algorithms to provide automated cell nuclei segmentation following signal-to-noise ratio optimization and accurate cell surface mask definition. To identify intracellular (blue cytoplasm, P30 negative) over extracellular (blue cytoplasm + surface P30 positive, red) parasites, image subtraction from each channel was automatically obtained. Data collected allowed determining the total number of intracellular tachyzoites over the total number of host cells for each well.

## QUANTIFICATION AND STATISTICAL ANALYSIS

### Dataset Distribution

Bimodality: Bin width was chosen arbitrarily as 30 s to emphasise the distribution features and to correspond to the timescale of observed events. A Gaussian function, sum of two and three of them was fitted using MATLAB command *fit* with *fitType* argument set to '*gauss1*', '*gauss2*' and '*gauss3*' respectively.

| Number of Gaussians | 1      | 2      | 3      |
|---------------------|--------|--------|--------|
| R-square            | 0.9214 | 0.9836 | 0.9867 |
| RMSE                | 2.4216 | 1.1583 | 1.0928 |

With increasing number of Gaussian functions the fit was better as assessed by comparing R-square error. However, for the fit characterized by the smallest error (sum of three Gaussians) one component was significantly smaller as its amplitude constituted 29.2% of the biggest component amplitude and was considered as a subpopulation. Hence, the data were assessed as bimodal and fitted with sum of two Gaussian functions.

### Quantitative Invasion Assay

3 independent assays were conducted for analyzing the effect of conditional silencing of dynamins in MEFs, and on the overexpression of dynamin1 in U2OS. With the same protocol, 3 independent invasion assays were carried out on both KO *Alix* and "rescued" *Alix* (i.e., expressing GFP-*Alix*) MEFs as well as on U2OS WT and U2OS ectopically expressing GFP-*Alix*. Following image processing, data from triplicates or quadruplicate (see section above) were statistically analyzed using GraphPad *Prism* software. Where appropriate, figure legends define the statistical test and associated parameters used to analyze data are displayed in the corresponding Figure. For Figures 1C and 1F, statistical analyses were performed using a Student's t test (*Prism*), with significance being represented as a p value <0.05". For Figure 2G, the n indicated represents the total number of parasites, which were checked for the twisting motion. For Figures 6A and 6B, n values represent the number of parasites while for Figure 7I the number indicated on the top of each bar represents the parasite samples tested for remodeling of the PVM post-twisting motion.

## DATA AND SOFTWARE AVAILABILITY

Additional supplemental videos and legend files are available on Mendeley Data: Tardieux, Isabelle (2018), "Pavlou et al. *Cell Host & Microbe* Supplemental Data," Mendeley Data, v1 <https://doi.org/10.17632/fmhnprp66j.1>.

# The *Toxoplasma* Tour de Force to Unfold its Intravacuolar Developmental Program

Georgios Pavlou, Isabelle Tardieux\*

Institute for Advanced Biosciences (IAB), Team Membrane dynamics of parasite-host cell interactions, CNRS UMR5309, INSERM U1209, Université Grenoble Alpes, Grenoble, France

## Article Info

### Article Notes

Received: September 10, 2018

Accepted: October 20, 2018

### \*Correspondence:

Dr. Isabelle Tardieux, Institute for Advanced Biosciences (IAB), Team Membrane dynamics of parasite-host cell interactions, CNRS UMR5309, INSERM U1209, Université Grenoble Alpes, Grenoble, France;  
Email: isabelle.tardieux@inserm.fr

© 2018 Tardieux I. This article is distributed under the terms of the Creative Commons Attribution 4.0 International License.

### Keywords:

*Toxoplasma gondii*  
Invasive nano-device  
Host cell Invasion  
Membrane fission  
Dynamins  
Vacuole biogenesis

**Original Article Citation:** Pavlou G, Biesaga M, Touquet B, Lagal V, Balland M, Dufour A, Hakimi MA, Tardieux I. *Toxoplasma* Parasite Twisting Motion Mechanically Induces Host Cell Membrane Fission to Complete Invasion within a Protective Vacuole. Cell Host Microbe. 2018 Jul 11;24(1):81-96.e5. doi: 10.1016/j.chom.2018.06.003. Epub 2018 Jun 28. PMID:30008293

## Abstract

*Toxoplasma gondii* is an obligate intracellular single-celled eukaryotic parasite with an impressive ability to invade virtually all nucleated cells from all warm-blooded animals, within a second time-scale. The invasive *T. gondii* tachyzoite achieves this feat by injecting a multi-unit nanodevice in the plasma membrane and underlying cortical cytoskeleton of the targeted cell that serves as an anchor point to withstand the parasite invasive force. Whether this nanodevice could also contribute at the latest step of invasion when the budding entry vesicle pinches off of the plasma membrane as a parasitophorous vacuole had not been yet addressed. Using fluorescent versions of both a parasite nanodevice component and a reporter for the target plasma membrane in conjunction with quantitative high-resolution live imaging, Pavlou *et al.* characterized the nanodevice toroidal shape once inserted in the membrane as well as its stretching and shrinking when accommodating the passage of the several micron-sized ellipsoid shaped tachyzoite. Tracking in real time the motion of internal eccentric markers allowed defining the tachyzoite final rotation along the long axis which imposes a twisting motion on its basal pole and directs closure of the torus hence promoting both sealing and release of the entry vesicle. Monitoring distinct host cell plasma markers allowed Pavlou *et al.* to propose that the twisting motion could also act as an initial mechanical trigger for the transition to the intracellular lifestyle. Their publication therefore brings evidence for a key new contribution of the nanodevice to end the high-speed multi-step invasion process.

## Introduction

The protozoan *Toxoplasma gondii* belongs to the phylum of Apicomplexa that exceeds 6000 members, most of which depend on hosting cells to achieve their life cycle<sup>1,2</sup>. *T. gondii* is considered as one of the most successful Apicomplexa because of its worldwide distribution, its host spectrum that comprises most warm-blooded vertebrates, human included, and its amazing ability to colonize virtually any type of nucleated cells in only a few tens of seconds. The *T. gondii* developmental stage called tachyzoite is a model of choice for investigating the mechanisms of cell invasion because this polarized cell has high invasive and replicative skills and is tractable to genetic modifications owing to recent conceptual and technological advances in molecular genetics<sup>3,4,5</sup>. About a decade ago, the discovery of a protein complex stored in the neck of apical secretory organelles typifying the phylum, namely the rhoptries, has been a major breakthrough in the *Toxoplasma*-cell invasion field of investigation. This protein complex is first released at the tachyzoite apical tip and injected into the target cell surface - Plasma Membrane (PM) and cortex - after a still molecularly undefined interaction. Made of four RhOptry Neck proteins - RON2, 4, 5, 8 -

and defined as the RON complex<sup>6,7</sup>, this complex is seen as the main component of the Zoite-Cell circular Junction (ZCJ) often named Tight Junction (TJ) that bridges the two cells during the invasion process<sup>8,9,10</sup>. While in the 1980-1990s, the ZCJ was described as an electron dense close contact or a moving junction for several species of zoites invading their respective host cells, recent live imaging on *T. gondii* (strain RH type 1) tachyzoites that express a fluorescent tagged version of RON2 - which spans the target cell PM - allowed demonstrating the anchor point function of the ZCJ. This platform was indeed shown to be anchored to the target cell cortex<sup>11</sup> and withstand a tachyzoite actin myosin (myosinA-myosinA)-based traction force<sup>12,13</sup> driving the parasite into a budding Entry Vesicle (EV). At about the same time genetic evidence raised the possibility that the traction force model does not fully explain the motile and invasive potential of tachyzoites. Motor-independent mechanisms, in particular relying on viscoelastic properties of the tachyzoite cell were first proposed<sup>14,15</sup>. Then a compensatory function by myoC for the genetic loss of myoA has been claimed<sup>16</sup>, but real time imaging of  $\Delta$ myoA parasites argues rather for an alternative mode of entry depending on the host cell actin when the parasite is unable to apply its own traction force on the ZCJ<sup>17</sup>.

During uptake by non-phagocytic and phagocytic host cells, a majority of intracellular microbes subvert the endocytosis pathway<sup>18,19</sup>. The process that promotes scission of endocytic buds (or pits) from the cell PM accounts for the endosome birth and involves the activity of ubiquitous mechano-enzymes that belong to the dynamin family. Dynamins assemble as helical oligomers wrapping around the neck of budding vesicles and applying torsional and contractile forces on the two membranes apposed at the neck region hence directing membrane fission<sup>20,21</sup>. Interestingly, early electrophysiology studies on tachyzoite entry into cells highlighted shared features with the endocytic fusion pore during endosome formation<sup>22</sup> while pharmacological and *in situ* imaging assays suggested the functional contribution of host cell dynamins during the release of the tachyzoite-loaded EV<sup>23,24</sup>. However, in absence of direct proof for such contribution and because of the recent identification of off target effects for dynamin inhibitors, Pavlou *et al.* decided to examine the features of the RON complex at the time of closure and immediately post-closure. Their working hypothesis was that the RON complex positioned at the interface between the host cell PM and the budding EV could influence the process leading to the pinch off of the vacuole-containing tachyzoite, namely the Parasitophorous Vacuole (PV). Their main findings are discussed below.

### **The twisting motion of the *T. gondii* tachyzoite from the ZCJ platform, coincides with the RON torus closure**

An important limitation in dissecting the multi-step

sequence that defines a successful entry event relates to the second-scale dynamics of the process, hence difficult to accurately characterize. To provide the best framework for assessing the invasive skills of the parasite, the Tardieux laboratory has in the recent past engineered a *T. gondii* line (RH type I strain) in which the gene encoding RON2 is replaced by a chimeric sequence encoding a fluorescent RON2-mCherry (RON2-mC) as well as human cell lines expressing a set of constructs to target the GFP protein at the cell PM<sup>13</sup>. Using spinning-disk laser scanning live microscopy with high spatio-temporal resolution, Pavlou *et al.* could resolve the early secretion of the RON2-mC-containing complex that organizes a toroidal ZCJ platform, which progressively stretches and shrinks as the ellipsoidal zoite passes through and forces the budding of an EV. More excitingly, they observed that once the tachyzoite basal end is about to reach the torus, the parasite executes an anticlockwise rotation that coincides with closure of the torus (Figure 1). The closed status of the torus was convincingly assessed by the disconnection of any extra material tightly bound posteriorly on the invading tachyzoite occurring concomitantly with the zoite twisting motion. Next, the definition of a long axis with the two RON-mC signals from the rhoptries at the apex and the closed torus at the basal pole respectively, together with the detection of a set of internal eccentric fluorescent spherical markers, allowed automatic “xyt” tracking of the three particles. This unambiguously identified a rotation of the internal marker around the long axis, a rotation imposed by the twisting motion of the tachyzoite. In addition, when the tracking was coupled with the analysis of the signal intensity of the internal particle, it was possible to detect periodic fluctuations in pixel intensity which agrees with a continuous rotation of the internal marker, hence of the parasite. Moreover, several lines of evidence suggest that the host cell cortical tension and contractibility underneath the torus could significantly determine the number of 360° rotation of the internal particle around the axis, and therefore the number of parasite twists “required” prior to PV release.

### **PV release requires the parasite twisting motion but not the major host cell membrane fission players namely dynamins and Alix**

The authors interrogated whether the key host cell membrane fission players, namely dynamins, could assist the process of PV release. Quantifying and monitoring invasion in MEF cells genetically silenced for the three dynamin encoding-genes<sup>25</sup> they found that dynamins are not required for full invasiveness of tachyzoites unlike previously thought. Importantly in the mutant cells lacking dynamins, the invasion scenario is identical with those in dynamin-expressing cells and includes the typical twisting motion prior to the pinch off of the PM that terminates

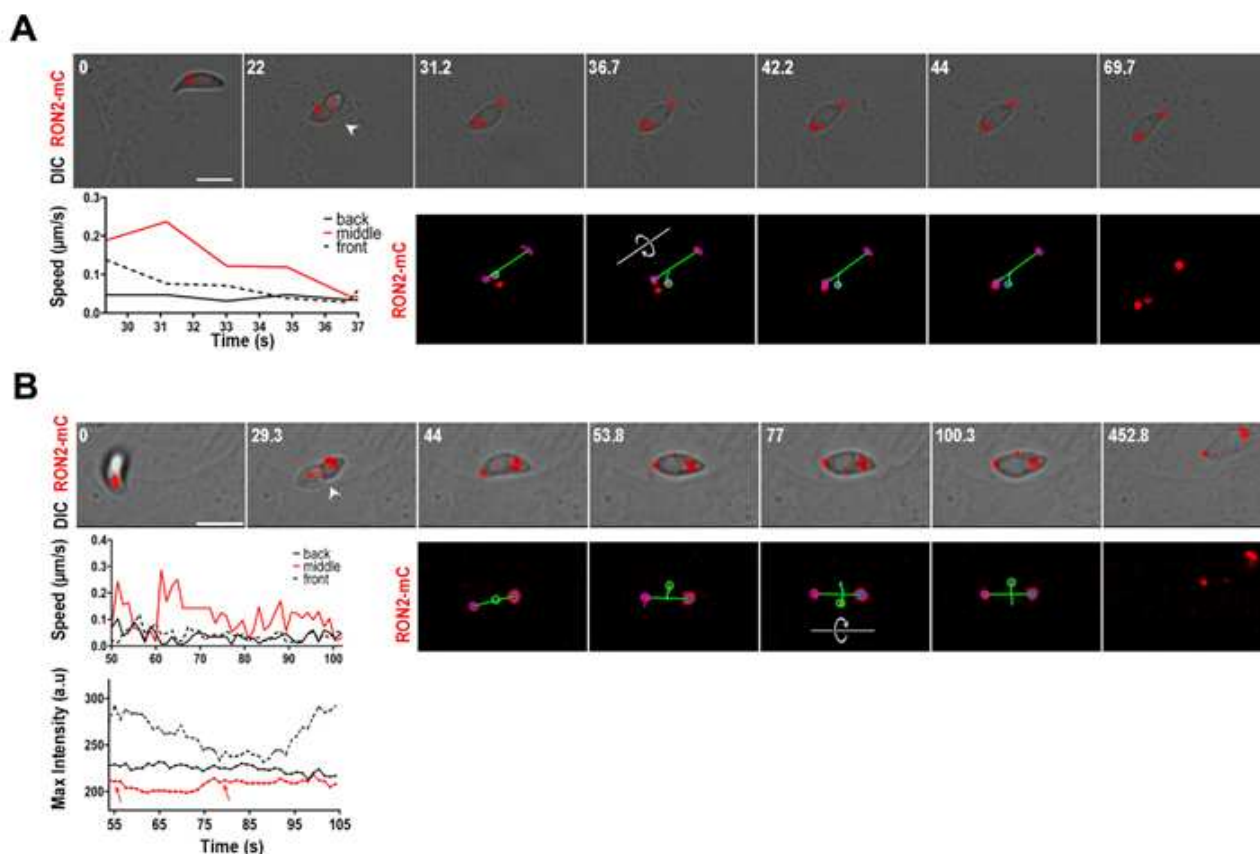


**Figure 1: The twisting motion of the *T. gondii* tachyzoite from the ZCJ platform, coincides with the RON torus closure**

(A, B) Time lapses of DIC (top) and fluorescent channel overlays (bottom) show the parasites prior to RON2-mC release and halfway inside a U2OS (b) or a MEF(c) cell (see the torus marked by arrowheads). Upon torus closure, automatic tracking of the RON2-mC pools at the parasite poles is reported by blue circles and short blue trajectories while the cytoplasmic RON2-mC circular object (middle, green circle) tracking identifies the twisting motion ( $\sim 180^\circ$  for b,  $\sim 540^\circ$  for c) of the parasite along its main axis (green bar between the two poles, see the circular arrows). Graphs (A, top B) indicate the speed of the three objects tracked and bottom B shows the signal intensity profile of the tracked objects. Note (i) the higher speed of the internal reference and (ii) the periodic fluctuations in signal intensity that correlates with the position with regard to focal point (full focus is indicated by red arrows).

the process. Besides the dynamin machinery, the Endosomal Sorting Complexes Required for Transport (ESCRT) family of proteins has also been characterized as driving membrane scission. The ESCRTs, in particular the ESCRT-III known to form helical polymers and their cofactors, control the release of enveloped viral particles in the extracellular milieu, the cytokinetic abscission of mammalian cells as well as the biogenesis of multivesicular bodies<sup>26,27</sup>. Since the ESCRT-III cofactor Alix has been detected at the ZCJ during cell invasion<sup>28</sup>, the authors directly assessed whether the lack of Alix in cells derived from  $\Delta\text{Alix}$  mice could impact the PV scission process. In disagreement with this study, they found no quantitative or qualitative difference of the whole tachyzoite cell invasion process in Alix-positive or -deficient cells. Importantly while the tachyzoite applies torque on the RON torus independently of host cell dynamins, Pavlou *et al.* do not exclude that dynamin partners in particular actin or other host cell component could collaborate with the twisting motion to drive membrane fission upstream the torus.

### Closure of the torus is required for PV biogenesis and could serve as an initiating mechanical signal for transition to unfold and complete *T. gondii* developmental program

To functionally correlate the tachyzoite twisting motion with the mechanism of torus closure, Pavlou *et al.* designed an innovative assay in which the invading tachyzoite carries microbeads at the basal pole, which makes it unable to properly close the torus at the ZCJ. Under this “artificial” situation, while they did not observe twisting motion, they monitored the unusual inflow of extracellular sodium ions that progressively filled the budding EV space. The osmotic unbalance between the bud and the host cell led to a balloon-like expansion of the former and the death of the tachyzoite, presumably due to an increased pressure in the balloon (Figure 2). Interestingly, based on the fluorescence stability of the balloon membrane, the authors concluded that despite the ZCJ site showed leakiness, the ZCJ preserved

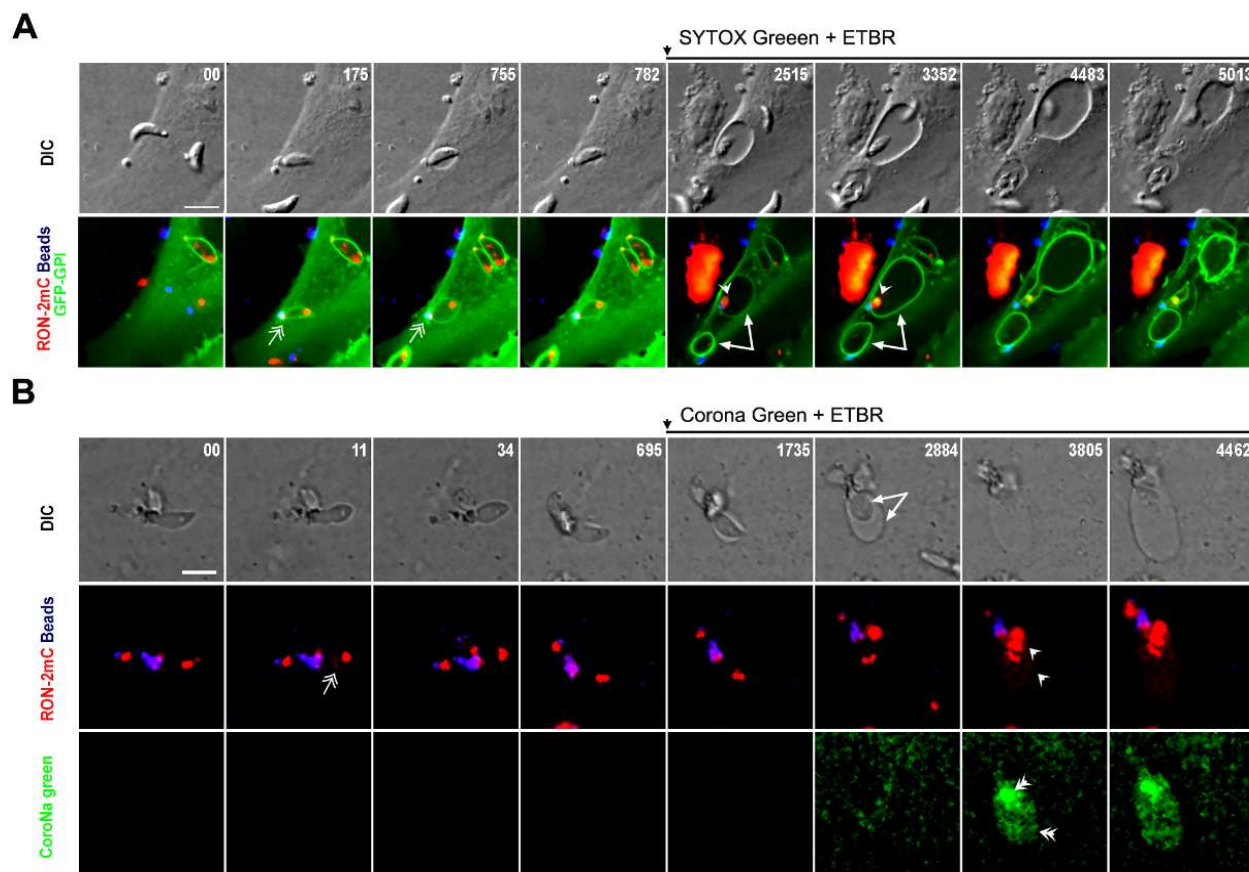


**Figure 2: Closure of the torus is required for PV biogenesis and mechanical impairment of the process causes parasite death due to osmotic damages**

(A, B) Time lapses show DIC (top) and fluorescent channel overlays (lower). Tachyzoites attached to microbeads (blue) and to both a bead and a partner (B). (A) At about 40 min post-block, SYTOX green and ETBR added to the extracellular milieu (as indicated with an arrow above the frame) are readily incorporated in the cell debris in the medium and are detected in the tachyzoite nucleus indicating loss of membrane integrity (arrowheads). Note that the extracellular beads are surrounded by PM protrusions and with time the huge balloon (arrows) can separate from the parasite to undergo vesiculation. (B) At about 45-60 min post-block, ETBR (arrowheads) and Corona green reagents (double arrowheads) are detected in the PV and the parasite, attesting torus leakiness and subsequent tachyzoite death.

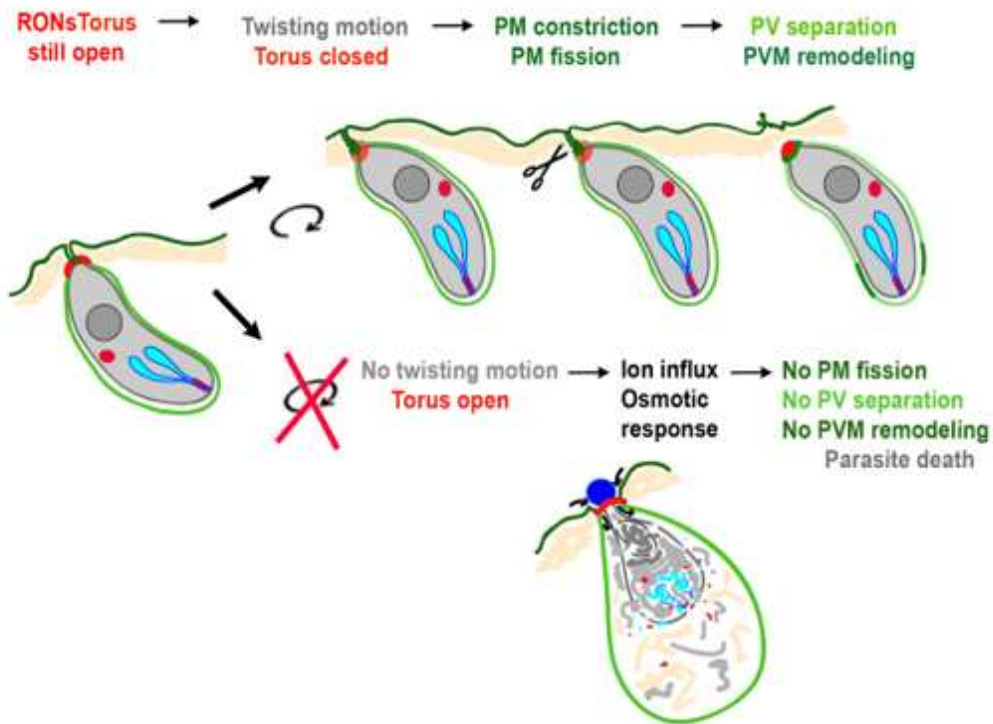
its ability to sieve the molecular components of the PM entering into the composition of the enlarging bud. Indeed, if the balloon had resulted from the stretching of the initial bud membrane, a proportional loss of fluorescence would have characterized the balloon membrane. In contrast changes in the membrane fluorescence can be visualized in the unborn PV immediately post twisting motion and post torus closure. These changes reveal that when the parasite has lost contact with the extracellular milieu - i.e., the EV is sealed - lipids and proteins composing the membrane of the EV ready to pinch already reassemble as new microdomains. This dynamic feature of the PVM suggests import or/and removal of material signaling for the early maturation of the PV niche.

## Conclusion

Benefiting from recent advances in both live imaging that provide significant gain in spatio-temporal resolution

and *T.gondii* molecular genetics that eases the introduction of fluorescent markers in the genome, Pavlou *et al.* have collected highly informative images on the invasion process. More specifically, image processing with open source and home made algorithms provided an accurate qualitative and quantitative description of the tachyzoite behavior at the end of the process (see Graphical abstract, Figure 3). Data analysis led the authors uncovering a mechanism by which the extracellular parasite actively accesses the intracellular environment within a cell PM-derived bud. While the nano-scale architecture of the RON torus within the recipient PM in the course of entry remains puzzling and deserves to be investigated in depth, this work unveiled a new functional contribution of the RON complex. Qualifying this complex as invasive nanodevice, these authors document that a parasite-derived torque applied on the nanodevice can indeed account for proper sealing and subsequent release of a membrane-bound PV

**Birth of *T. gondii* tachyzoite intracellular vacuole**



**Birth of endosome during CME**

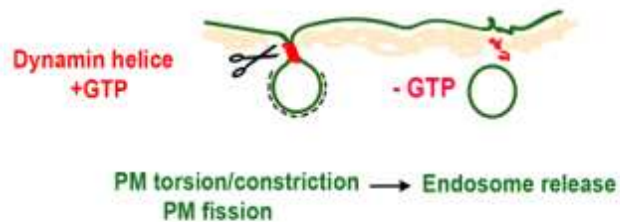


**Figure 3: Schematic representation of the host cell invasion process by *T. gondii*.**

The invasive tachyzoite stage injects an invasive nanodevice into the Plasma Membrane (PM) of the target cell that organises as a torus and promotes the formation of a tight Zoite-Cell Junction (ZCJ). The nanodevice successively stretches and shrinks while the parasite enters within a budding entry vesicle derived from the PM. Closure of the nanodevice and vesicle sealing behind the parasite are critical for the release of the parasite protective vacuole in the host cell cytoplasm. This study unveils a twisting motion of the tachyzoite imposing rotation on its basal end and likely constriction/torsion of the entry vesicle neck that facilitates membrane fusion and fission upstream the torus to release a Parasitophorous Vacuole (PV) whose membrane (PVM) is rapidly remodelled. When closure is mechanically prevented by microbeads that stay tightly bound to the posterior end of the tachyzoite, the leaky ZCJ causes an osmotic response from the host cell leading to parasite lysis. This work suggests a functional similarity between the mode of action of (i) the GTPase dynamins that form helices around the neck of vesicles (endocytic buds) at the PM to apply torsion and constriction forces that mediate fission (i.e. release of endosomes) and (ii) the torque applied by the tachyzoite on the toroidal nanodevice to ensure PV birth and intracellular development.

while preserving the host cell PM integrity. In addition, the authors monitored for the first time how dynamic is the PV compartment: whether the early remodeling contributes to protect the PV from host cell endocytic processing and build a niche where to expand a replicating-prone tachyzoite progeny is the next question to address. This study also

leads to ask fascinating follow-up questions on the forces underlying the torque and the identity of host cell factors other than dynamins that could possibly assist the process. Of note, a common requirement for membrane fission under different topologies is the need for a contractile ring and spiral around adjacent membranes which is provided

by helical polymers of proteins such as dynamins or ESCRT-III<sup>21,29</sup>. Intriguingly the protozoan *Toxoplasma* has evolved a torus positioned at the interface between the bud neck and the donor PM, which is twisted and constricted immediately prior to membrane rupture upstream.

## References

1. Gubbels MJ, Duraisingh MT. Evolution of apicomplexan secretory organelles. *Int J Parasitol*. 2012; 42: 1071–1081.
2. Seeber F, Steinfeld S. Recent advances in understanding apicomplexan parasites. *F1000Res*. 2016; 5.
3. Huynh MH, Carruthers VB. Tagging of endogenous genes in a *Toxoplasma gondii* strain lacking Ku80. *Eukaryotic Cell*. 2009; 8: 530–539.
4. Fox BA, Ristuccia JG, Gigley JP, et al. Efficient gene replacements in *Toxoplasma gondii* strains deficient for nonhomologous end joining. *Eukaryotic Cell*. 2009; 8: 520–529.
5. Sidik SM, Huet D, Lourido S. CRISPR-Cas9-based genome-wide screening of *Toxoplasma gondii*. *Nat Protoc*. 2018; 13: 307–323.
6. Besteiro S, Michelin A, Poncet J, et al. Export of a *Toxoplasma gondii* rhoptry neck protein complex at the host cell membrane to form the moving junction during invasion. *PLoS Pathog*. 2009; 5: e1000309.
7. Straub KW, Peng ED, Hajagos BE, et al. The moving junction protein RON8 facilitates firm attachment and host cell invasion in *Toxoplasma gondii*. *PLoS Pathog*. 2011; 7: e1002007.
8. Bannister LH, Butcher GA, Dennis ED, et al. Structure and invasive behaviour of *Plasmodium knowlesi* merozoites in vitro. *Parasitology*. 1975; 71: 483–491.
9. Aikawa M, Miller LH, Johnson J, et al. Erythrocyte entry by malarial parasites. A moving junction between erythrocyte and parasite. *J Cell Biol*. 1978; 77: 72–82.
10. Dubey JP, Lindsay DS, Speer CA. Structures of *Toxoplasma gondii* tachyzoites, bradyzoites, and sporozoites and biology and development of tissue cysts. *Clin Microbiol Rev*. 1998; 11: 267–299.
11. Gonzalez V, Combe A, David V, et al. Host cell entry by apicomplexa parasites requires actin polymerization in the host cell. *Cell Host Microbe*. 2009; 5: 259–272.
12. Sibley LD. How apicomplexan parasites move in and out of cells. *Curr Opin Biotechnol*. 2010; 21: 592–598.
13. Bichet M, Joly C, Henni AH, et al. The *Toxoplasma*-host cell junction is anchored to the cell cortex to sustain parasite invasive force. *BMC Biol*. 2014; 12: 773.
14. Egarter S, Andenmatten N, Jackson AJ, et al. The *Toxoplasma* Acto-MyoA motor complex is important but not essential for gliding motility and host cell invasion. *PLoS ONE*. 2014; 9: e91819.
15. Whitelaw JA, Latorre-Barragan F, Gras S, et al. Surface attachment, promoted by the actomyosin system of *Toxoplasma gondii* is important for efficient gliding motility and invasion. *BMC Biol*. 2017; 15: 1.
16. Fréchal K, Marq JB, Jacot D, . Plasticity between MyoC- and MyoA-glideosomes: an example of functional compensation in *Toxoplasma gondii* invasion. *PLoS Pathog*. 2014; 10: e1004504.
17. Bichet M, Touquet B, Gonzalez V, et al. Genetic impairment of parasite myosin motors uncovers the contribution of host cell membrane dynamics to *Toxoplasma* invasion forces. *BMC Biol*. 2016; 14: 97.
18. Cossart P, Helenius A. Endocytosis of viruses and bacteria. *Cold Spring Harb Perspect Biol*. 2014; 6.
19. Colonne PM, Winchell CG, Voth DE. Hijacking Host Cell Highways: Manipulation of the Host Actin Cytoskeleton by Obligate Intracellular Bacterial Pathogens. *Front Cell Infect Microbiol*. 2016; 6: 107.
20. Antonny B, Burd C, De Camilli P, et al. Membrane fission by dynamin: what we know and what we need to know. *EMBO J*. 2016; 35: 2270–2284.
21. Colom A, Redondo-Morata L, Chiaruttini N, et al. Dynamic remodeling of the dynamin helix during membrane constriction. *Proc Natl Acad Sci USA*. 2017; 114: 5449–5454.
22. Suss-Toby E, Zimmerberg J, Ward GE. *Toxoplasma* invasion: the parasitophorous vacuole is formed from host cell plasma membrane and pinches off via a fission pore. *Proc Natl Acad Sci USA*. 1996; 93: 8413–8418.
23. Caldas LA, Attias M, de Souza W. Dynamin inhibitor impairs *Toxoplasma gondii* invasion. *FEMS Microbiol Lett*. 2009; 301: 103–108.
24. Caldas LA, Soares LL, Henrique Seabra S, et al. Monitoring of dynamin during the *Toxoplasma gondii* cell cycle. *Pathog Dis*. 2016; 74.
25. Park RJ, Shen H, Liu L, et al. Dynamin triple knockout cells reveal off target effects of commonly used dynamin inhibitors. *J Cell Sci*. 2013; 126: 5305–5312.
26. Chiaruttini N, Redondo-Morata L, Colom A, et al. Relaxation of Loaded ESCRT-III Spiral Springs Drives Membrane Deformation. *Cell*. 2015; 163: 866–879.
27. Votteler J, Sundquist WI. Virus Budding and the ESCRT Pathway. *Cell Host Microbe*. 2013; 14.
28. Guérin A, Corrales RM, Parker ML, et al. Efficient invasion by *Toxoplasma* depends on the subversion of host protein networks. *Nat Microbiol*. 2017; 2: 1358–1366.
29. Lafaurie-Janvore J, Maiuri P, Wang I, et al. ESCRT-III assembly and cytokinetic abscission are induced by tension release in the intercellular bridge. *Science*. 2013; 339: 1625–1629.

# Intracellular protozoan parasites: living probes of the host cell surface molecular repertoire

Georgios Pavlou<sup>1</sup>, Geneviève Milon<sup>2</sup> and Isabelle Tardieux<sup>1</sup>



Intracellular protozoans co-evolved with their mammalian host cells a range of strategies to cope with the composite and dynamic cell surface features they encounter during migration and infection. Therefore, these single-celled eukaryotic parasites represent a fascinating source of living probes for precisely capturing the dynamic coupling between the membrane and contractile cortex components of the cell surface. Such biomechanical changes drive a constant re-sculpting of the host cell surface, enabling rapid adjustments that contribute to cellular homeostasis. As emphasized in this review, through the design of specific molecular devices and stratagems to interfere with the biomechanics of the mammalian cell surface these parasitic microbes escape from dangerous or unfavourable microenvironments by breaching host cell membranes, directing the membrane repair machinery to wounded membrane areas, or minimizing membrane assault using discretion and speed when invading host cells for sustained residence.

## Addresses

<sup>1</sup>Institute for Advanced Biosciences (IAB), Team Membrane Dynamics of Parasite-Host Cell Interactions, CNRS UMR5309, INSERM U1209, Université Grenoble Alpes, Grenoble 38700, France

<sup>2</sup>Institut Pasteur, Paris 75015, France

Corresponding author: Tardieux, Isabelle ([isabelle.tardieux@inserm.fr](mailto:isabelle.tardieux@inserm.fr))

Current Opinion in Microbiology 2019, 52:116–123

This review comes from a themed issue on **Host–microbe interactions: parasites**

Edited by **Norma Andrews** and **Dario Zamboni**

<https://doi.org/10.1016/j.mib.2019.06.007>

1369-5274/© 2019 Elsevier Ltd. All rights reserved.

## Introduction

Over the last few decades, researchers have shed light on how micron-size single-celled eukaryotes – that is, protozoan microbes – utilize diverse tactics to overcome the challenge of invading cells from a range of mammalian hosts. In close partnership with either ectotherm or warm-blooded mammalian hosts, those protozoan microbes sculpt the dynamic protective and feeding niches to sustain transient to prolonged-time intracellular residence. Regardless of the ‘manoeuvres’ co-evolved by

each pair of invasive protozoan–host cell to build heterotypic associations of distinct life-time and fate, the parasites must inevitably cope with the structural and functional complexity of the host cell surface. This complexity is dictated by the host cell identity alongside a micro-environment that usually consists of scaffolding bioactive matrices and, in the context of barrier tissues, of connecting neighbouring cells. In this short review only a few examples have been selected to illustrate how Trypanosomatid and Apicomplexan intracellular protozoan parasites make use of their target cell properties to generate selective paths towards the intracellular world, where they unfold developmental programs responsible for further producing transmissible populations.

## What invasive protozoan microbes face/ perceive when meeting the surface of targeted mammalian cells

When confronted with the surface of the mammalian permissive host cell, pre-invading protozoan parasites encounter a continuous, non-uniform interface that behaves as a dual-active composite [1]. While a fluid bilayer predominantly composed of phospholipids and loaded with hundreds of proteins and protein modules is positioned at the extracellular interface – namely the Plasma Membrane (PM) –, underneath is tethered a thin ActoMyosin Contractile Meshwork (AMCM) known as cortex [2]. The dynamic coupling that operates between the two composite entities over a range of spatiotemporal scales is key for ensuring vital contributions and adjustments of the PM, which concurrently maintain cellular homeostasis. Through the control of nano-domain to micro-domain assembly, PM-AMCM active coupling allows ‘out-in’ signals to be sensed, amplified and conveyed before promoting a choreography of events that reshape the cell surface architecture. Recently, *in vitro* minimal composite models revealed how cortex contractile myosins [1] (including mammalian myosin 2 isoforms, myosin 1 and myosin 17) [3] can drive mini-filament assembly alongside the actin architecture to precisely regulate cortical tension gradients, thus sculpting the cell surface into distinct shapes [2].

In this context, when protozoans and host cells come into contact with each other, signals emitted by the single-celled eukaryotic parasite – either through surface-exposed or secreted ligands – are expected to be captured by host cell surface through lectin-carbohydrate, protein–protein or protein–lipid molecular interactions and processed to regulate PM-AMCM dynamics in a way compatible with

the safe intracellular installation of the parasitic microbes. However, to reach the selected residence cell/tissue alive, some protozoans need first to take tough measures to deal with barriers/hurdles impeding their intruding progression.

### **The extreme case: the protozoan parasite disrupts the mammalian cell surface, *en route* to safer residence in *bona fide* hosting cells**

A somehow ‘drastic’ strategy was reported for parasites encountering a continuous host cell layer before reaching a growth-permissive cell/tissue. Such layers called endothelia or epithelia are composed of type-specific cells that collectively develop robust apico-basal polarity through engagement with specialized cell–cell and cell–substratum molecular anchors, forming a physical barrier to the progression of non-parasitic intruders [4]. As a way to circumvent this obstacle, some parasitic intruders such as protozoan parasites can literally cross cells by causing the PM-AMCM to irreversibly breach, imposing a rapid exit of the invader from the sacrificed host cell. This cell traversal (CT) scheme seems to be a quasi-obligate path for the malaria-causing *Plasmodium* spp. Sporozoites, which are delivered into the dermis of warm-blooded mammals by blood-feeding anopheline mosquitoes. A fraction of these sporozoites eventually initiate the intra-hepatocyte phase of the *Plasmodium* spp. intracellular development, provided that the parasites first achieve traversal of endothelial cells of the dermal blood microvascular bed, of the liver sinusoid endothelial cells, as well as resident K upffer macrophages [5–7]. Relying on *Plasmodium* gene disruption, the latter teams provided insights on a required discharge of stage-specific pore-forming or putative pore-forming proteins by sporozoites (e.g. sporozoite-restricted SPECT1 and SPECT2/PLP1, sporozoite/oocinete-restricted CelTOS) that enable cell traversal. Upon exocytosis from a calcium-responsive secretory organelle called microneme, the SPECT1 and SPECT2 plasmodial proteins were proposed to promote destabilization of the PM by forming trans-membrane channels in K upffer macrophages and fenestrated sinusoidal endothelial cells, ultimately promoting PM rupture and parasite translocation across the cell layer adjacent to hepatocytes. Tandem cooperation between the PM-inserted channels and yet undefined sporozoite effectors has also been speculated as a way to impact the cell cortex integrity, contributing to the extent of PM wounds and facilitating CT. However, *in vivo* live imaging of pore formation in endothelial cells and macrophages targeted by sporozoites in experimentally relevant <hosts – mice or humanized mice – remains a challenge. These limitations preclude definitive conclusions on which membrane domains, apical versus basal, are targeted by the plasmodial molecules, and how the sporozoite intracellular gliding behavior contributes to achieve CT. To add complexity to the CT issue, it was recently reported that CT can occur without detectable lesions at the site of entry,

whereas the SPECT2/PLP1-triggered membrane disruption actually accounts only for exit out of entry vesicles and host cells to complete rapid CT [8]. Of note, this study interrogated CT of rodent-associated *Plasmodium* spp. in human – possibly not fully polarized – hepatocytes, mammalian cells that typically support both rapid parasite CT and progeny production. Thus, this scenario might not be valid for CT of macrophages and endothelial cells. Interestingly, comparative analysis of CT and productive invasion processes using hepatoma cell lines [8] established a link with a large body of work performed in several Apicomplexa underscoring the crucial post-entry role of a large family of canonical pore-forming proteins [excellently reviewed in Ref. [9]]. Finally, an intriguing structure depicting a 4-helix bundle connected to a helical hook was identified between the rodent-associated *Plasmodium berghei* SPECT1 and the mammalian sperm protein Izumo, the latter being proposed as a critical member of an egg-sperm fusogenic complex in mice [10]. This finding raised even more perplexity about the mechanisms by which SPECT 1 could perhaps cooperate with the pore-forming SPECT2 [5] and other partners to orchestrate CT [11,9].

### **Do invasive protozoan microbes design selective paths within permissive mammalian host cells by benefiting from PM-AMCM dynamic features?**

In contrast to *Plasmodium* sporozoites that cause crude, deadly cell surface attack when confronted with a non-growth permissive cellular barrier, a large number of protozoan parasites from different lineages have evolved developmental stages that tackle the cell surface in a more subtle way to ensconce the parasite intracellularly. They have elaborated an array of unrelated procedures that all (i) serve the same goal – that is, preserve cell viability for longer pairing – and (ii) obey a common principle – that is, benefit from PM-AMCM dynamic features for designing selective paths of entry. Depending on the mode of entry, the intracellular microbe subsequently either escapes from or reconfigures the PM-derived entry compartment to satisfy its metabolic needs and to perceive and counteract any endogenous cell defences. Because these crucial determinants for successful parasitism operate post-cell invasion, they are beyond the scope of this review and have been discussed elsewhere [12,13].

### **Taking advantage of PM-AMCM dynamics driving multiple types of endocytosis to gain intracellular residence**

Among the predominant strategies elaborated to preserve PM integrity are those relying on (i) parasite surface-exposed ligands – such as glycoproteins, proteins and lipids – that recognize surface-exposed receptor molecule(s) of the target cell or (ii) specific molecular sets of parasite delivery systems and effectors, the first directing the second

to differentially target host cell elements. Both designs modulate signalling pathways, most commonly PIP3 phosphoinositide-centred pathways, that in turn promote the formation of PM outward protrusions through processes derived from the ancestral feeding mode of free phagotrophic predators and broadly dedicated to nutrient uptake in mammalian cells (for recent reviews see Refs. [14,15]). While these processes typify a large set of closely related endocytic events, they invariably proceed at the expense of PM regions that shape ruffles, filopodia and blebs or pseudopods during macropinocytosis and phagocytosis, respectively. Driven by a variety of stimuli that promote the activation of cortical F-actin assembly, these PM folds emerge and expand to engulf micrometer sized droplets of medium or/solid materials within a PM-derived bud that is subsequently removed from the cell surface through the action of a multi-component and multistep fission force machinery [16]. The PM-AMCM dynamic coupling driving macropinocytosis is so robust that it allows tissue-patrolling immune cells to both overcome hydraulic resistance and clear undesired materials [17]. As an efficient way to safely access the cytoplasm of mammalian cells, a range of medically relevant parasitic protozoans – among them the Trypanosomatids and Apicomplexans discussed in Ref. [18] – but mostly non-protozoan invasive microbes – including viruses, bacteria and fungi – have exploited facets of the endocytic potential of their hosts [19,20]. Likewise, functional reprogramming of macrophages from receptor-mediated phagocytosis to macropinocytosis has been observed upon activation by non-protozoan microbes, leading to increased bacterial killing in the case of *Mycobacterium* [21]. In the case of the protozoan *Leishmania amazonensis* (Trypanosomatids), amastigotes in the progeny released from reprogrammed macrophages display phosphatidylserine lipid on their outer leaflet, which serves as a signal to promote uptake via macropinocytosis and subsequent rapid amastigote cycling [22]. These examples underline that alternative uptake modes may be used by a parasite developmental stage population that is not as homogeneous as often perceived, considering the inflammatory/counter-inflammatory milieu operating in the hosting tissue(s). Future investigation should continue documenting the contrasting immune-metabolic features of two clinically silent tissues – the dermis and skin-draining lymph nodes – populated with (i) a large number of reprogrammed macrophages hosting rapidly cycling *Leishmania* amastigotes and (ii) a small number of the following reprogrammed populations: monocyte-derived macrophages, monocyte-derived dendritic cells and fibroblasts hosting persistent *Leishmania* amastigotes.

### Promoting cooperation between PM-AMCM dynamics and endo-exocytic organelle functions of mammalian cells to shape a hybrid entry compartment

Invasive stratagems that mitigate the cell surface composite contribution have been evolutionary retained by

some protozoan developmental stages. For instance, *Leishmania* spp. and *Trypanosoma* spp. have evolved slender, flagellated invasive parasite stages of up to a few tenths of a micron in length that do not exclusively rely on macropinocytic or phagocytotic routes to access their host cells. Indeed, when targeting non-professional vertebrate phagocytic cells, these ‘actively swimming stages’ are endowed with the capacity to subvert intracellular membrane pools from the host cell endo-exocytic pathway as a way to assist the PM in generating a nascent entry compartment while alleviating the risk of irreversible damage to the PM. First uncovered for fibroblast or epithelial cell invasion by the trypomastigote stage of the Chagas disease-causing *Trypanosoma cruzi* and recently demonstrated for fibroblast invasion by the metacyclic promastigote stage of *L. amazonensis* [23], this path of entry is proposed to rely at least in part on parasite mechanical forces to actually inflict local PM injury to the target cell. In response to such microbe-induced cell surface lesions and initiated by the resulting calcium influx, a local disruption of the cortex promotes exocytosis of a specific subset of PM-associated (*T. cruzi*) or PM-redistributed (*T. cruzi* and *L. amazonensis*) lysosomes at the mammalian cell surface. Explored in the *T. cruzi* model and still to be investigated for *L. amazonensis*, the concomitant release of acid sphingomyelinase to the PM outer leaflet was identified as the trigger for massive caveolae endocytosis [24]. This PM remodelling event drives removal of the wounded cell surface area, hence heading off any threats of prolonged PM leakage. To achieve efficient PM lesion mending, a contribution of the Exocyst complex to direct cytoplasmic vesicles – lysosomes and/or endosomes – to the cell surface was also observed during *T. cruzi* trypomastigote entry [25] and it awaits confirmation in the case of invading *Leishmania* promastigotes. In addition to protecting the PM integrity, this ordered sequence of events provides the required extra membrane to enable host cell entry by both parasites in a PM-endosome-lysosome hybrid/mosaic compartment, and independently of any target cell AMCM-generated force. In this peculiar invasive scenario that unifies two groups of Trypanosomatidae, the early event(s) responsible for PM rupture of the target cells are not yet fully characterized. How the parasites mechanically assault the cell surface and how the interplay between parasite-mammalian cell surface molecules [26] could act as additive mechanisms for ensuring calcium-mediated effector functions to ensure parasite entry are issues to be addressed.

### Designing a protozoan molecular device to target the PM-AMCM and to allow traction into a non-fusogenic entry compartment with minimal disturbance

In contrast to the aforementioned parasites, some invading Apicomplexa parasites can perform discreet space and time minimally imposing, although not silent,

remodelling of the PM-AMCM. Achieved in only a few tens of seconds, this entry process is not associated with (i) large membrane ruffling; hence it does not co-opt with any of the 'uptaking' cortical forces driven by the mammalian cell PM-AMCM, nor with (ii) significant surface damage, not relying on endocytic/exocytic sources of membrane to support formation of an entry compartment. Falling in this category are the well-studied *Plasmodium* merozoite and *Toxoplasma gondii* tachyzoite developmental stages. Lacking motile appendages these parasites show a robust polarized architecture, primarily featured by an apical complex whose functions govern the parasite invasive skills. Indeed, within the club-shaped rhoptry organelles that populate the zoite apex, is stored a very unique invasive nanodevice designed to timely direct both the development of actomyosin-based invasive forces and the formation of a PM bud containing the invading zoites. The discovery of the RhOptry Neck (RON) multi-subunit complex and its regulated discharge once the zoite is apically positioned on the cell surface [27–29] were key clues for solving these parasites' invasive stratagem.

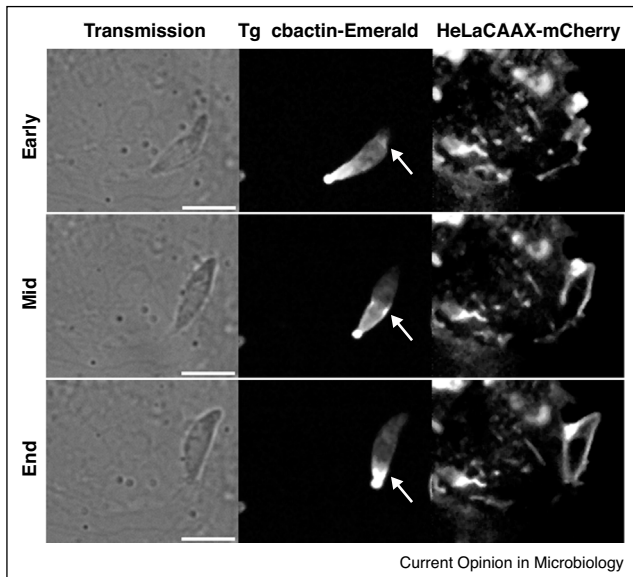
Despite notorious differences between the molecular composition and biomechanical properties of the PM-AMCM in the a-nucleated and organelle-free erythrocyte – the only cell targeted by the *Plasmodium* ovoid merozoite – and the wide repertoire of non-erythrocyte nucleated cells targeted by the *Toxoplasma* ellipsoidal tachyzoite, the two zoites still initiate invasion *per se* by releasing the rhoptry-derived RON complex into the mammalian cell surface. Likewise, while several specific duos of merozoite ligand-erythrocyte receptor molecules have been characterized and their timely interaction shown to initiate specific changes in architecture of the very peculiar erythrocyte PM-AMCM before RONs' discharge [30], the upstream molecular events directing the latter event remain less defined for the invasive tachyzoite. However, a first clue on the identity of a molecular trigger for RONs' delivery was provided by the recent discovery of Ferlin2, a calcium sensor strictly required for this step. This was an important finding that also provided insights into the mode of RON delivery into the target PM [31].

### Visualizing the *Toxoplasma* nanodevice functions after assembly in the mammalian cell surface

Genetically transformed *T. gondii* tachyzoites engineered to express a fluorescent version of RON2, a member of the complex that spans the mammalian cell PM, combined to genetically transformed mammalian cells expressing chimeric fluorescent proteins of interest and high speed live cell imaging allowed assessment in real time the 'one shot process' of RON material release, and its assembly as a toroidal platform in the recipient PM-AMCM composite [32,33]. Such approaches have

proven particularly fruitful to dissect salient features of the tachyzoite invasive stratagem, taking advantage of the 5–7  $\mu\text{m}$  size of the tachyzoite, its wide host cell repertoire and its genetic tractability. The toroidal nanodevice can – within a few seconds – stretch and shrink in coordination with forces applied by the tachyzoite, which rapidly moves its body through the device into a budding portion of the PM [32]. Such a force, which is sensed by the nanodevice, is generally thought to arise from a divergent parasite actomyosin motor housed in the space between the parasite PM and the Internal Membrane Complex (IMC) underneath the PM [34]. Transmission of this force across the torus occurs through an evolutionary conserved structural interaction between the ectodomain of RON2 and the surface-exposed AMA1 protein [35,36], a surface-exposed protein that is secreted from the cigar-shaped, apically positioned microneme organelles. Although the intrinsic dynamic properties of *Plasmodium* and *Toxoplasma* actin have been extensively debated – and are not discussed here –, let us mention that the original model for motion implies that the myosin motor is fixed in place on the IMC and pulls actin filaments toward the basal end of the zoite [37]. Alternative, related [38] or more divergent [39] models assign force generation or force anchorage to the parasite actomyosinA system during both gliding and invasive motions. Overall it is clear that the actomyosinA motor drives tachyzoite gliding in 2D and 3D conditions [39] as well as during cell invasion [40]: the visualization of F-actin dynamics using a *T. gondii* tachyzoite line expressing a fluorescent chromobody actin chimera [41] confirmed that a F-actin ring is co-aligned with the nanodevice site in most invading parasites (Figure 1). Recent biophysical approaches have allowed detecting and measuring of gliding force at the PM for *Plasmodium* sporozoites [42] while laser trap-devices revealed a typical reorganization of the motor machinery along the main axis only under conditions promoting tachyzoite directional motility [43]. However, directly observing the invasive force, which might not be simply overlaid to the motile force of the free gliding tachyzoite, remains a challenge considering the second-scale time frame of interest. The most convincing datasets in support of a tachyzoite traction force applied on the torus during invasion was brought on by tracking the xyt trajectory of the apex of the parasite and the nanodevice, while the former experienced resistance to forward progression by hitting an obstacle ahead from it [32]. In this setting, the torus together with the PM into which it is inserted were seen to translocate backward. Even stronger evidence is now available thanks to a peculiar situation where invading conjoined parasites are simultaneously pulled back by each other, resulting in both being impeded in their forward motion (Figure 2). As recently attributed to force application on the nanodevice, this peculiar parasite arrangement allowed visualization of the mechanism, by which the budding entry vesicle actually separates from the PM it is derived from, to give birth to a

Figure 1



*T. gondii* tachyzoite F-actin re-localizes nearby the RON nanodevice insertion site in the metazoan target cell surface during the entry process.

Evidence has accumulated that the tachyzoite relies on its actomyosin motor to propel itself into a unique nascent parasitophorous vacuole, but the parasite F-actin has remained difficult to visualize in the parasite. The recent availability of a tachyzoite line expressing a chimeric F-actin chromobody-Emerald GFP has allowed visualization of F-actin dynamics during invasion in real time. The movie stills show the tachyzoite at early (top panel), mid (middle panel) and end (bottom panel) stages of the invasion event. The columns show the two cells by transmission light (left), the actin-chromobody-Emerald GFP in the tachyzoite (middle) and the CAAX-mCherry construct expressed in HeLa cells and targeted to the plasma membrane (right). White arrows point to the enrichment of F-actin aligning with the site where the nanodevice is inserted, and from where emerges the plasma membrane-derived bud that allows parasite entry. Scale bar: 5  $\mu$ m.

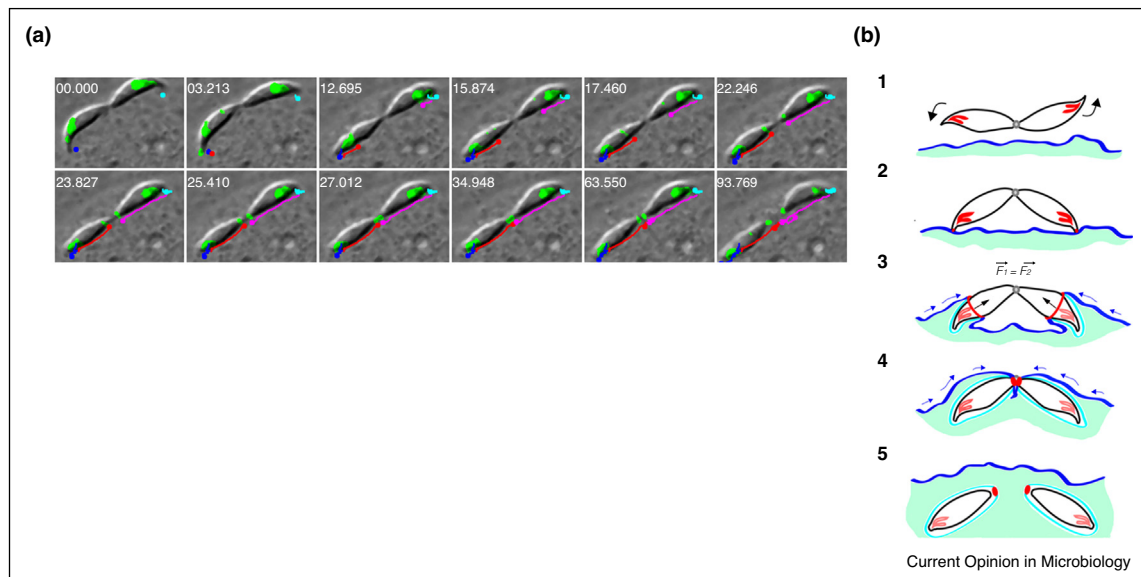
Parasitophorous Vacuole (PV) enclosing the tachyzoite in the mammalian cell cytoplasm. Unlike previously thought, this fission step does not require PM fission specialized mechanoenzymes, namely dynamins, but instead relies on a parasite twisting motion that imposes a spiral motion of the tachyzoite basal end. The compressive forces applied on the nanodevice co-drive mechanical closure of the torus and tight sealing of the bud [33]. The authors of this study proposed that torsion and constriction during torque achieve PM fission upstream of the nanodevice, similar to what is commonly performed in concert by dynamins, actin and associated proteins to complete fission of endocytic vesicles [16]. As a result, the nanodevice incorporates in the cytoplasmic PV, thereby being removed from the cell surface. Whether the host cell PM is left totally unscathed during the torus functions has not been formerly investigated (see below), but it already became clear that unusual PM-AMCM reorganizations including PM defects are

associated with the minute-range persistence of the nanodevice in the cell surface in the case of impaired invasion events [40,33].

### Optimal function of the nanodevice requires PM specificities and AMCM anchoring points: can these requirements be associated with cell surface damage, hence activating membrane repair mechanisms?

To sustain insertion of the nanodevice and the resulting tensile stress force application while avoiding excessive alterations in local PM tension, proper anchoring of the RON nanodevice on the host cell is expected. RON2 partners (RON4, 8) that are retained in the cortex through interactions with the RON2 N terminal region were reported to selectively interact with the F-actin [44] and microtubule cytoskeletons [45], suggesting how the torus might acquire the ability to handle the mechanical load imposed by AMA1–RON2 during invasion. Although details on molecular links between specific RON proteins and the cytoskeleton await confirmation, anchoring reinforcement through local assembly of cortical actin is supported by the transient recruitment of the ARP2/3 actin nucleator complex and its regulatory partner cortactin to the site of parasite entry [46]. Two novel mammalian proteins that bind directly to different regions of RON4 were recently identified: ALIX, an accessory member of the endosomal sorting complex required for transport (ESCRT), and the adaptor protein CIN85 (Cbl-interacting protein of 85 kDa) which acts as a scaffold for a variety of endocytic accessory proteins, including ALIX [47]. However, ALIX-associated ESCRT components required for membrane fission and repair were not detected at the nanodevice site [47] and the invasion process remains unaltered in ALIX null fibroblasts [33]. Interestingly, Poupel *et al.* proposed that ALIX and CIN85 might assist the actin cytoskeleton for cortical anchoring of the nanodevice through their ability to bind cortactin, an activator of the ARP2/3 actin nucleator complex. In addition, the rhoGTP effector toxofilin protein was shown to directly impact the AMCM actin dynamics [48]. Delivered by the tachyzoite upon apical contact with the host cell surface [49], toxofilin promotes severing of actin filaments, causing local release of actin monomers [50]. Therefore, the actin monomer pool could potentially fuel the ARP2/3 complex-driven actin assembly seen at the nanodevice site. It is still unclear if toxofilin-mediated loosening of the cortex, known to facilitate formation of the tachyzoite entry compartment, can also facilitate attachment of the RON nanodevice to the F-actin cortex. Major challenges to be overcome include deciphering the spatial organization of the RON members within an active torus, and better understanding the torus capacity to withstand the parasite invasive force when bridged to specific components of both parasite and mammalian cells. Similarly, there is a need to clarify the unique sieving properties of the invasive nanodevice, which allows selection of PM components that

Figure 2



The tachyzoite applies an invasive force on the RONs nanodevice to propel itself into the metazoan host cell.

Evidence has accumulated that the nanodevice acts as a traction point for tachyzoite invasion of the host cell. A unique demonstration of this is shown with two *Toxoplasma* tachyzoites attached at their posterior ends through the maternal residual body. Both parasites simultaneously assemble a nanodevice and start to invade the same cell, thereby pulling on each other and imposing reciprocal resistance. Because the two invasion events are precisely synchronized, both parasites attempt to apply traction force that translates into a symmetrical rearward displacement and closure of their junctions, eventually isolating each in a distinct vacuole (*unpublished data*). Movie stills are shown in (a) schematic is shown in (b).

- 1\_ Constrained extracellular motility: posteriorly connected tachyzoites extrude their conoids and attempt to move forward in opposite directions on top of a Ptk cell monolayer; by applying similar force this results in almost no net displacement of the parasites, which remain attached to each other.
- 2\_ Torus assembly: both tachyzoites simultaneously release RONs (visualized by RON2-mCherry) that assemble a torus in the host cell surface.
- 3\_ Force engagement on the torus: both tachyzoites pull simultaneously on the torus inserted in the PM and impose resistance to forward movement on each other. This situation leads to a symmetrical rearward displacement of the torus, suggesting that the forces applied by both zoites are of similar intensity.
- 4\_ Membrane sealing: complete translocation of the torus to the posterior pole coincides in both tachyzoites, leading to concomitant closure of the PM at the torus site.
- 5\_ Intracellular vacuole: each tachyzoite ends up in their respective vacuoles.

incorporate into the parasite-driven PM bud. By retaining most PM-associated proteins outside from this bud, the nanodevice controls the emergence of a lipid-enriched and fluid membrane around the invading tachyzoite, probably easing the invasion process. In addition, the PVM is rapidly remodeled post PV fission [33] and remains excluded from the endocytic pathway thereby provide a safe growth-permissive residence to the parasite [51].

## Conclusions

The diversity of invasive stratagems evolved by intracellular protozoans to access mammalian cells are obviously not restricted to the situations depicted in this review. For instance, some medically important Apicomplexa including *Cryptosporidium* spp. in humans or *Theileria* spp. in non-human animals do not rely on the RON nanodevice to remodel the PM-AMCM when they infect target cells. Here we have highlighted recent advances in molecular and imaging technologies that have brought insights on the fascinating 'molecular language' repertoire unfolding

at the cell surface composite of a range of mammalian cells, as they interact with Apicomplexan and Trypanosomatidae protozoans. Yet, the distinct mammalian cell lineages operating as either host cells or parasite-shuttling cells are durably or transiently anchored to basement membranes or the extracellular matrix (ECM), so how the dynamic ECM features contribute to the molecular language repertoire remains understudied. We foresee that these gaps may be approached by (i) implementing biomechanics and mechanotransduction analysis to determine how bilateral force generation and cellular responses are integrated during microbe-induced PM-AMCM coupling, and (ii) engineering organoids of metazoan host cells where single-celled eukaryotic parasites can deploy the complex stepwise developmental programs on which their fitness relies.

## Conflict of interest

Nothing declared.

## Appendix A. Supplementary data

Supplementary material related to this article can be found, in the online version, at doi:<https://doi.org/10.1016/j.mib.2019.06.007>.

## Acknowledgements

We thank the Foundation for Innovation in Infectiology (FINOVI) for funding our research program (France), the University Grenoble-Alpes for the AGIR PhD fellowship support to Georgios Pavlou, and Prof. P. Hainaut (IAB, Grenoble, France) for internship support to the IT team. We thank Dr MA. Hakimi for sharing discussions along the writing of this review.

## References

- Köster DV, Husain K, Iljazi E, Bhat A, Bieling P, Mullins RD, Rao M, Mayor S: **Actomyosin dynamics drive local membrane component organization in an in vitro active composite layer.** *Proc Natl Acad Sci U S A* 2016, **113**:E1645-E1654.
- Chugh P, Clark AG, Smith MB, Cassani DAD, Dierkes K, Ragab A, Roux PP, Charras G, Salbreux G, Paluch EK: **Actin cortex architecture regulates cell surface tension.** *Nat Cell Biol* 2017, **19**:689-697.
- Chugh P, Paluch EK: **The actin cortex at a glance.** *J Cell Sci* 2018, **131** jcs186254.
- Luscinskas FW, Leick M, Newton G, Nusrat A: **Introduction for the special issue on "Tissue Barriers in Inflammation."** *Tissue Barriers* 2015, **3**:e1015825.
- Ishino T, Chinzei Y, Yuda M: **A plasmodium sporozoite protein with a membrane attack complex domain is required for breaching the liver sinusoidal cell layer prior to hepatocyte infection: role of a MACPF-related protein in the malarial life cycle.** *Cell Microbiol* 2004, **7**:199-208.
- Tavares J, Formaglio P, Thiberge S, Mordelet E, Van Rooijen N, Medvinsky A, Ménard R, Amino R: **Role of host cell traversal by the malaria sporozoite during liver infection.** *J Exp Med* 2013, **210**:905-915.
- Yang ASP, O'Neill MT, Jennison C, Lopatnicki S, Allison CC, Armistead JS, Erickson SM, Rogers KL, Ellisdon AM, Whisstock JC *et al.*: **Cell traversal activity is important for plasmodium falciparum liver infection in humanized mice.** *Cell Rep* 2017, **18**:3105-3116.
- Risco-Castillo V, Topçu S, Marinach C, Manzoni G, Bigorgne AE, Briquet S, Baudin X, Lebrun M, Dubremetz J-F, Silvie O: **Malaria sporozoites traverse host cells within transient vacuoles.** *Cell Host Microbe* 2015, **18**:593-603.
- Guerra Alfredo, Carruthers Vern: **Structural features of apicomplexan pore-forming proteins and their roles in parasite cell traversal and egress.** *Toxins* 2017, **9**:265.
- Inoue N, Hagihara Y, Wright D, Suzuki T, Wada I: **Oocyte-triggered dimerization of sperm IZUMO1 promotes sperm-egg fusion in mice.** *Nat Commun* 2015, **6**.
- Nishimura K, Han L, Bianchi E, Wright GJ, de Sanctis D, Jovine L: **The structure of sperm izumo1 reveals unexpected similarities with Plasmodium invasion proteins.** *Curr Biol* 2016, **26**:R661-R662.
- David Sibley L: **Invasion and intracellular survival by protozoan parasites: parasite invasion strategies.** *Immunol Rev* 2011, **240**:72-91.
- Walker DM, Oghumu S, Gupta G, McGwire BS, Drew ME, Satoskar AR: **Mechanisms of cellular invasion by intracellular parasites.** *Cell Mol Life Sci* 2014, **71**:1245-1263.
- King JS, Kay RR: **The origins and evolution of macropinocytosis.** *Philos Trans R Soc B Biol Sci* 2019, **374** 20180158.
- Bloomfield G, Kay RR: **Uses and abuses of macropinocytosis.** *J Cell Sci* 2016, **129**:2697-2705.
- Antony B, Burd C, De Camilli P, Chen E, Daumke O, Faelber K, Ford M, Frolov VA, Frost A, Hinshaw JE *et al.*: **Membrane fission by dynamin: what we know and what we need to know.** *EMBO J* 2016, **35**:2270-2284.
- Moreau HD, Blanch-Mercader C, Attia R, Maurin M, Alraies Z, Sanséau D, Malbec O, Delgado M-G, Bousso P, Joanny J-F *et al.*: **Macropinocytosis overcomes directional bias in dendritic cells due to hydraulic resistance and facilitates space exploration.** *Dev Cell* 2019, **49**:171-188.e5.
- de Carvalho TMU, Barrias ES, de Souza W: **Macropinocytosis: a pathway to protozoan infection.** *Front Physiol* 2015, **6**.
- Fernandes MC, Flannery AR, Andrews N, Mortara RA: **Extracellular amastigotes of Trypanosoma cruzi are potent inducers of phagocytosis in mammalian cells: T. cruzi amastigotes induce phagocytosis.** *Cell Microbiol* 2013, **15**:977-991.
- Mercer J, Helenius A: **Virus entry by macropinocytosis.** *Nat Cell Biol* 2009, **11**:510-520.
- BoseDasgupta S, Pieters J: **Inflammatory stimuli reprogram macrophage phagocytosis to macropinocytosis for the rapid elimination of pathogens.** *PLoS Pathog* 2014, **10**:e1003879.
- Wanderley JLM, Deolindo P, Carlsen E, Portugal AB, DaMatta RA, Barcinski MA, Soong L: **CD4+ T cell-dependent macrophage activation modulates sustained PS exposure on intracellular amastigotes of Leishmania amazonensis.** *Front Cell Infect Microbiol* 2019, **9**.
- Cavalcante-Costa VS, Costa-Reginaldo M, Queiroz-Oliveira T, Oliveira ACS, Couto NF, dos Anjos DO, Lima-Santos J, Andrade LO, Horta MF, Castro-Gomes T: **Leishmania amazonensis hijacks host cell lysosomes involved in plasma membrane repair to induce invasion in fibroblasts.** *J Cell Sci* 2019, **132** jcs226183.
- Fernandes MC, Cortez M, Flannery AR, Tam C, Mortara RA, Andrews NW: **Trypanosoma cruzi subverts the sphingomyelinase-mediated plasma membrane repair pathway for cell invasion.** *J Exp Med* 2011, **208**:909-921.
- Fernandes MC, Corrotte M, Miguel DC, Tam C, Andrews NW: **The exocyst is required for trypanosome invasion and the repair of mechanical plasma membrane wounds.** *J Cell Sci* 2015, **128**:27-32.
- Maeda FY, Cortez C, Yoshida N: **Cell signaling during Trypanosoma cruzi invasion.** *Front Immunol* 2012, **3**.
- Lebrun M, Michelin A, El Hajj H, Poncet J, Bradley PJ, Vial H, Dubremetz JF: **The rhopty neck protein RON4 re-localizes at the moving junction during Toxoplasma gondii invasion.** *Cell Microbiol* 2005, **7**:1823-1833.
- Alexander DL, Mital J, Ward GE, Bradley P, Boothroyd JC: **Identification of the moving junction complex of Toxoplasma gondii: a collaboration between distinct secretory organelles.** *PLoS Pathog* 2005, **1**:e17.
- Besteiro S, Michelin A, Poncet J, Dubremetz J-F, Lebrun M: **Export of a Toxoplasma gondii rhopty neck protein complex at the host cell membrane to form the moving junction during invasion.** *PLoS Pathog* 2009, **5**:e1000309.
- Weiss GE, Gilson PR, Taechalerpaisarn T, Tham W-H, de Jong NWM, Harvey KL, Fowkes FJI, Barlow PN, Rayner JC, Wright GJ *et al.*: **Revealing the sequence and resulting cellular morphology of receptor-ligand interactions during Plasmodium falciparum invasion of erythrocytes.** *PLOS Pathog* 2015, **11**:e1004670.
- Coleman BI, Saha S, Sato S, Engelberg K, Ferguson DJP, Coppens I, Lodoen MB, Gubbels M-J: **A member of the ferlin calcium sensor family is essential for Toxoplasma gondii rhopty secretion.** *mBio* 2018, **9**:14.
- Bichet M, Joly C, Henni AH, Guilbert T, Xémard M, Tafani V, Lagal V, Charras G, Tardieux I: **The toxoplasma-host cell junction is anchored to the cell cortex to sustain parasite invasive force.** *BMC Biol* 2014, **12**:773.
- Pavlou G, Biesaga M, Touquet B, Lagal V, Balland M, Dufour A, Hakimi M-A, Tardieux I: **Toxoplasma parasite twisting motion**

- mechanically induces host cell membrane fission to complete invasion within a protective vacuole.** *Cell Host Microbe* 2018, **24**:81-96.e5.
34. Meissner M, Schlüter D, Soldati D: **Role of *Toxoplasma gondii* myosin A in powering parasite gliding and host cell invasion.** *Science* 2002, **298**:837-840.
  35. Tonkin ML, Roques M, Lamarque MH, Pugniere M, Douquet D, Crawford J, Lebrun M, Boulanger MJ: **Host cell invasion by apicomplexan parasites: insights from the co-structure of AMA1 with a RON2 peptide.** *Science* 2011, **333**:463-467.
  36. Vulliez-Le Normand B, Tonkin ML, Lamarque MH, Langer S, Hoos S, Roques M, Saul FA, Faber BW, Bentley GA, Boulanger MJ *et al.*: **Structural and functional insights into the malaria parasite moving junction complex.** *PLoS Pathog* 2012, **8**:e1002755.
  37. Heintzelman MB: **Gliding motility in apicomplexan parasites.** *Semin Cell Dev Biol* 2015, **46**:135-142.
  38. Tardieux I, Baum J: **Reassessing the mechanics of parasite motility and host-cell invasion.** *J Cell Biol* 2016, **214**:507-515.
  39. Whitelaw JA, Latorre-Barragan F, Gras S, Pall GS, Leung JM, Heaslip A, Egarter S, Andenmatten N, Nelson SR, Warshaw DM *et al.*: **Surface attachment, promoted by the actomyosin system of *Toxoplasma gondii* is important for efficient gliding motility and invasion.** *BMC Biol* 2017, **15**:1.
  40. Bichet M, Touquet B, Gonzalez V, Florent I, Meissner M, Tardieux I: **Genetic impairment of parasite myosin motors uncovers the contribution of host cell membrane dynamics to *Toxoplasma* invasion forces.** *BMC Biol* 2016, **14**:97.
  41. Periz J, Whitelaw J, Harding C, Gras S, Del Rosario Minina MI, Latorre-Barragan F, Lemgruber L, Reimer MA, Insall R, Heaslip A *et al.*: ***Toxoplasma gondii* F-actin forms an extensive filamentous network required for material exchange and parasite maturation.** *eLife* 2017, **6**.
  42. Quadt KA, Streichfuss M, Moreau CA, Spatz JP, Frischknecht F: **Coupling of retrograde flow to force production during malaria parasite migration.** *ACS Nano* 2016, **10**:2091-2102.
  43. Stadler RV, White LA, Hu K, Helmke BP, Guilford WH: **Direct measurement of cortical force generation and polarization in a living parasite.** *Mol Biol Cell* 2017, **28**:1912-1923.
  44. Straub KW, Peng ED, Hajagos BE, Tyler JS, Bradley PJ: **The moving junction protein RON8 facilitates firm attachment and host cell invasion in *Toxoplasma gondii*.** *PLoS Pathog* 2011, **7**: e1002007.
  45. Takemae H, Sugi T, Kobayashi K, Gong H, Ishiwa A, Recuenco FC, Murakoshi F, Iwanaga T, Inomata A, Horimoto T *et al.*: **Characterization of the interaction between *Toxoplasma gondii* rhoptyr neck protein 4 and host cellular  $\beta$ -tubulin.** *Sci Rep* 2013, **3**.
  46. Gonzalez V, Combe A, David V, Malmquist NA, Delorme V, Leroy C, Blazquez S, Ménard R, Tardieux I: **Host cell entry by apicomplexa parasites requires actin polymerization in the host cell.** *Cell Host Microbe* 2009, **5**:259-272.
  47. Guérin A, Corrales RM, Parker ML, Lamarque MH, Jacot D, El Hajj H, Soldati-Favre D, Boulanger MJ, Lebrun M: **Efficient invasion by *Toxoplasma* depends on the subversion of host protein networks.** *Nat Microbiol* 2017, **2**:1358-1366.
  48. Poupel O, Boleti H, Axisa S, Couture-Tosi E, Tardieux I: **Toxofilin, a novel actin-binding protein from *Toxoplasma gondii*, sequesters actin monomers and caps actin filaments.** *Mol Biol Cell* 2000, **11**:355-368.
  49. Lodoen MB, Gerke C, Boothroyd JC: **A highly sensitive FRET-based approach reveals secretion of the actin-binding protein toxofilin during *Toxoplasma gondii* infection.** *Cell Microbiol* 2010, **12**:55-66.
  50. Delorme-Walker V, Abrivard M, Lagal V, Anderson K, Perazzi A, Gonzalez V, Page C, Chauvet J, Ochoa W, Volkmann N *et al.*: **Toxofilin upregulates the host cortical actin cytoskeleton dynamics, facilitating *Toxoplasma* invasion.** *J Cell Sci* 2012, **125**:4333-4342.
  51. Charron AJ, Sibley LD: **Molecular partitioning during host cell penetration by *Toxoplasma gondii*.** *Traffic* 2004, **5**:855-867.



## Phenotyping *Toxoplasma* Invasive Skills by Fast Live Cell Imaging

Georgios Pavlou and Isabelle Tardieux

### Abstract

Host cell invasion by *Toxoplasma gondii*/*T. gondii* tachyzoites is an obligate but complex multistep process occurring in second-scale. To capture the dynamic nature of the whole entry process requires fast and high-resolution live cell imaging. Recent advances in *T. gondii*/host cell genome editing and in quantitative live cell imaging—image acquisition and processing included—provide a systematic way to accurately phenotype *T. gondii* tachyzoite invasive behaviour and to highlight any variation or default from a standard scenario. Therefore, applying these combined strategies allows gaining deeper insights into the complex mechanisms underlying host cell invasion.

**Key words** *T. gondii* tachyzoite, Host cell invasion, Live cell microscopy, Image processing

---

### 1 Introduction

Once it reaches warm-blooded metazoan tissues, the tachyzoite developmental stage of *Toxoplasma gondii*/*T. gondii* strictly depends on nutrients supplied by hosting cells where to either expand a replicating-prone progeny or where to differentiate as slow replicating bradyzoite developmental stage. This condition imposes to first achieve entry of the target cell by a mechanism that allows rapid biogenesis of an intracellular niche in which the tachyzoite further multiplies. Once the mature progeny fills up the hosting cell, it actively moves out to undergo a transient extracellular phase prior to new successive phases of cell invasion and intracellular multiplication. In this context, the invasive skills of *T. gondii* determine to which extent the parasite population expands, and accordingly the amount of tissue damages which impacts on clinical outcomes. Therefore, a comprehensive and molecular understanding of how tachyzoites access the intracellular niche remains actively investigated with the perspective of designing anti-invasive strategies to combat or prevent the disease.

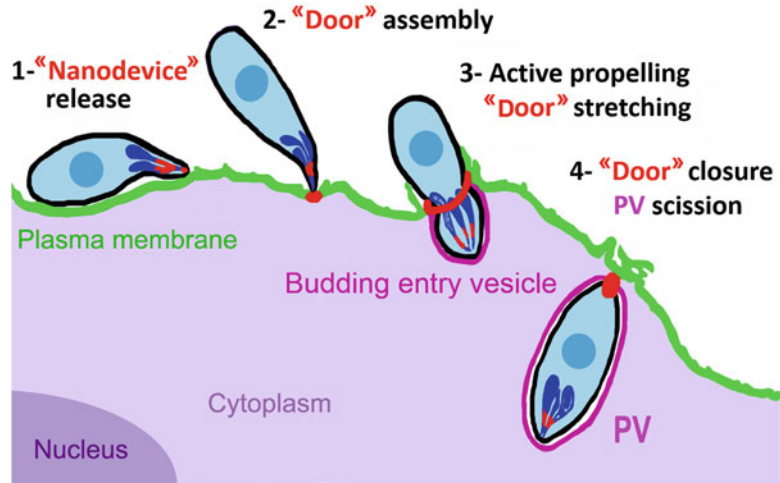


**Fig. 1** Schematic depicting the four main steps of the invasion process defined by the RON complex fate. RON stands for *T. gondii* RhOptr1 Neck complex

Since decades, such **productive invasion** event is described as a short lasting but also as a well-coordinated multistep sequence (Fig. 1) [1]. Despite recent advances in the identification of key molecules of both *T. gondii*—a single-celled eukaryotic parasite—and the metazoan host cell, the whole set of players and the mechanisms that control the transition from an extracellular motile to an no more motile intracellular immotile/replicative tachyzoite, remain unresolved in large part. A major limitation clearly relates to the second-scale dynamic of the entry process, hence difficult to capture and accurately characterize. Indeed, although recent advances in molecular genetics have provided unprecedented tools with the design of genetic screens from which have been generated—and will continue to be—several *T. gondii* mutants potentially disabled in invasive skills [2, 3], the optimal assessment of these is still difficult. However conclusive evidence for any invasion-defective trait that would translate into a specific phenotype can greatly benefit from **fast live microscopy settings** in particular when combined with multiple markers for the *T. gondii* tachyzoite or/and the targeted cell.

Here we provide basic guidelines to set up an optimized experimental framework enabling to collect high-content image datasets from which accurate information can be retrieved using commercial and open source software. By tracking defined objects of interest in time and space, key parameters of the invasion process have been/can be identified and quantified, and have proven/prove to bring informative mechanistic insights. Importantly, as exemplified below, introducing new variables and upgrading the settings allow automatic analysis of successive steps of the whole invasion event and provide unbiased high-resolution analysis of the invasive

capabilities of tachyzoites. Accordingly, any differences with a **standard entry process** including when associated with entry failure can be reliably **qualitatively and quantitatively** assessed and in turn provide information towards a comprehensive mechanistic model of cell invasion.

Recent imaging studies have allowed clarifying or uncovering key events that define successful invasion and can therefore serve as **reference features** for analysing the invasive skills of tachyzoites. They first execute a specific short movement we have described as “impulse” [4], which in association or not with movement production—circular or helical gliding—is characterized by the extrusion of the tubulin-based appendage termed conoid [5]. Conoid extrusion and zoite motility are both controlled by calcium signalling [6–8], but their functional link has been pharmacologically invalidated [9]. Interestingly, entry into the host cell is systematically initiated by zoites with extruded conoids but whether and why this is essential for the process to start has not been solved yet. Cell penetration per se proceeds with the regulated secretion of cargoes prestored in the apical pear-shaped secretory organelles called rhoptries. The identity of molecular triggers for early cargo release is earnestly investigated and these might operate only when conoid is elongated. Several cargoes have been identified and include compounds with distinct final destination such as the host cell (a) Plasma Membrane (hPM) (b) CytoPlasm (hCP), (c) nucleus [10], yet how these are routed and delivered is not known. Delivery of cargoes has indeed rarely been monitored in real time but the visualization of the RhOptry Neck complex—the RON complex—that travels in the rhoptry canal to the tip of the conoidal channel, allowing invasion to begin, appears as a **key early reference feature**. Once the RON material contacts the hPM, it assembles a tight circular interface called a Tight Junction (TJ) between the zoite and the metazoan cell. At this early stage of invasion, local changes in hPM curvature can already be detected with a tightly curved fold surrounding the apex of the tachyzoite while discrete outward projections emerge at the TJ site lining the extracellular part of the *T. gondii* tachyzoite body. Forward progression of the tachyzoite occurs owing to the zoite traction force applied on the TJ with the actin-myosin H activity [11], which is then rapidly relayed by the actin-myosin A motor [4]. Traction force concurs with the stretching of the TJ and the enlargement of the intracellular curved fold that shapes a unique type of entry vesicle. Although deriving from the hPM, the budding entry vesicle selectively incorporates components by virtue of the TJ-associated sieving properties [12, 13]. Invasion is achieved when the hPM-derived bud ultimately pinches off of the hPM [14] leading to a tachyzoite-loaded free vesicle. Rapid and sustained remodelling of this vesicle defined as a bona fide parasite-protective niche named the Parasitophorous Vacuole (PV) allows the tachyzoite to shift to an

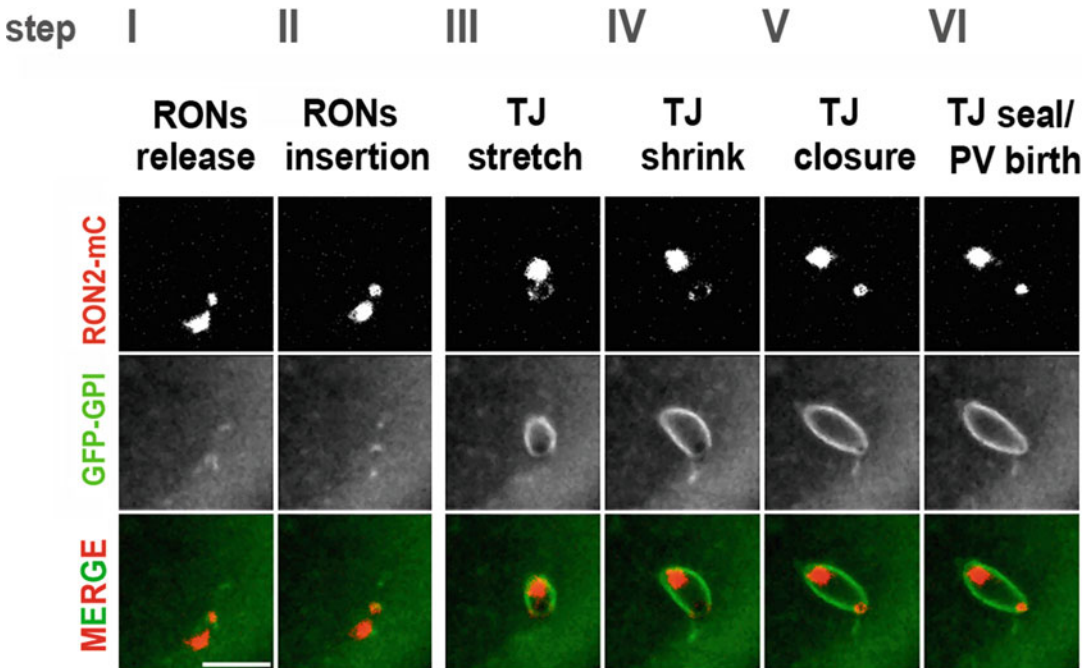


**Fig. 2** Host cell invasion is a multistep process that can be decomposed in six steps (I–VI) using key markers from the invading parasite (RON2-mC, red) and the host cell plasma membrane (GFP-GPI, green). Scale bar: 5  $\mu$ m

intracellular lifestyle [15]. Each of these events—that is, (1) **conoid extrusion/RON secretion**, (2) **RON insertion/TJ assembly** into the hPM, (3) **TJ stretching**, (4) **TJ shrinking**, (5) **TJ closure**, and (6) **PV biogenesis**—constitute six steps that can now serve as **reference features** for scoring tachyzoite invasive skills in the context of any mutation or drug effect under study (Fig. 2).

## 2 Material

### 2.1 *T. gondii* Cells

The parasite lines ideally carry one or more fluorescent markers that could include a RON TJ marker to accurately assess the dynamics of invasion and/or any other marker of interest (<http://toxodb.org/toxo/>). Multiple genetic endogenous tagging can now be easily obtained in both type I and II *T. gondii* strains engineered to lack the gene encoding the DNA double-strand break repair Ku80 protein hence showing drastic increase in the rate of homologous recombination [16, 17]. In conjunction with these breakthroughs in molecular genetics, LIC-mediated and CRISPR/Cas9 knock-in strategies [2, 3] have undoubtedly eased the introduction of a variety of fluorescent markers thus allowing any laboratory members to image parasites for specific investigation. While care must then be taken to verify expression and functionality of the fusion

constructs, a number of these have allowed precise description of preinvasive and invasive *T. gondii* tachyzoite behaviors. As such, we have generated RH (i.e., type 1)  $\Delta Ku80$  *T. gondii* strains that express a functional chimeric fluorescent version of the rhoptry-stored RON2 protein which enable visualizing in real time the whole multistep invasion event from the early RON complex release to the TJ closure and the subsequent birth of the PV [4]. Of note the CRISPR/Cas9 knock-in procedure has proved useful for genome editing—gene deletion and point mutations [18, 19]—while conditional silencing systems have allowed analysing loss of function mutants for the so-called “essential” genes [20] and the impact of all those modifications for *T. gondii* invasion-related gene candidates can now be accurately examined in the RON2-mC-expressing tachyzoite lines. Indeed, dynamic imaging of mutants deleted for the *MyoA* gene revealed an alternative mode of entry into host cells that relies on hPM actin-rich protrusions forcing the parasite into a hPM-derived bud [21].

## 2.2 Metazoan Cells

The human foreskin fibroblasts (HFF-1, ATCC no. SCRC-1041, certified mycoplasma free) have been used to propagate the *T. gondii* tachyzoites in vitro by serial passages in high glucose Dulbecco’s Modified Eagle’s Medium GlutaMAX (DMEM) supplemented with 10% fetal bovine serum (FBS), 100 units/ml penicillin, and 100 mg/ml streptomycin (i.e., complete medium) at 37 °C with 95% air and 5% CO<sub>2</sub>.

The host cell lines used for analyzing invasive skills are diverse due to the particularly broad spectrum of warm-blooded metazoan adherent cells permissive to *T. gondii* tachyzoites. We recommend choosing cells that are easy to transfect for transient or stable transgene expression and that preferentially spread thin and large lamellipodium/lamella area to ease the recording. However invasion of polarized epithelial or endothelial cell monolayers—which display rather columnar architectures—can also be used. In our hands the human U2OS sarcoma cell line (ATCC, Cat#HTB-96; RRID: CVCL\_0042) has been convenient for assessing—therefore comparing—invasive behaviors. We can derive from the U2OS cell line a large number of transgenic sublines expressing GFP, mCherry, or any other fluorescent tags in fusion with a variety of constructs targeting the hcPM [4] (i.e., using a transmembrane domain of PM-exposed receptors such as the PDGF receptor or a lipid covalent anchor/tether such as glycosyl-phosphatidylinositol, myristate, and palmitate) or/and the hc cortical cytoskeleton (using lifactin, etc.) (For details, see [4]) [15, 21, 22]. During the procedure to obtain the U2OS (or other) cell line of interest, we usually select clones that express low amounts of the fusion construct to limit the risk of mis-localisation or physiological impairment due to transgene overexpression.

### 2.3 *Microscope Platform*

We are working with a spinning disk (Yokogawa CSU-X) laser confocal microscope (Nikon Eclipse), a platform that fulfills the speed, sensitivity and resolution requirements for imaging (1) release of the RON material, (2) TJ assembly and function along with (3) parasite penetration. To achieve efficient resolution, we also use the X63 oil objective with a numerical aperture of 1.4. Because of the need to capture emitted signals from distinct fluorophores—excited with distinct laser beams—within only few seconds, fast frame rate video-recording is compulsory. In addition because we also want to capture as many events as possible in the same session to further perform quantitative analysis and apply statistics (i.e., on the same field of view for the appropriate objective), we usually extend the recording periods over two tens of minutes. Therefore, particular care must be taken to limit (1) phototoxicity due to ROS generated from high/long excitation of the fluorophore and (2) photobleaching (*see Note 1*). Although phototoxicity might not be apparent for short-imaging time windows as during invasion assay, and clearly depends on the fluorophore and the subcellular localization of the marker of interest. For each marker we therefore optimize the emission filter for a maximal signal and test the best illumination conditions aiming to limit excitation to the level that provides both satisfying signal to noise ratio and spatiotemporal resolution.

Several alternatives to counteract both the phototoxicity and photobleaching exist, including the use of other illumination techniques (Total internal reflection fluorescence—TIRF—light sheet illumination), but increasing the quantum efficiency of the emitted light detector—that is, improving the sensitivity of the camera—is certainly a good start. With these concerns, we use either the EM-CCD (Photometrics CoolSNAP HQ2, Andor iXon) or the sCMOS (Photometrics Prism BSI) cameras having a preference for the second one.

### 2.4 *Additional Microscope Settings*

To keep the physiological conditions required for long term live imaging of the *T. gondii* invasion in metazoan cells, a 37 °C temperature and 5% CO<sub>2</sub> gas as well as humidity need to be provided throughout the video session. Homemade and commercial microscope environmental chambers as well as heat and CO<sub>2</sub> flow rate controllers need to be used. As regards the heat, because the immersion objectives act as heat sink thereby creating a decrease of temperature at the interface between the objective and the sample, it is important to use an objective heater in the environmental top stage chamber while a stage heater is also good. We had also positive experience using the compact Chamlyde incubator top stage system from Live Cell Instrument, which accommodates a range of magnetic or nonmagnetic holder settings (i.e., glass bottom dishes, chambers holding glass coverslips or well plates of

various dimensions) compatible or not with liquid perfusion at controlled flow rates.

## 2.5 Software

MetaMorph 7.7.0.0 Molecular devices.

Icy 1.9.5.1 <http://icy.bioimageanalysis.org/>

ImageJ 1.51j8 <https://imagej.nih.gov/ij/>.

UCSF ChimeraX 0.1 <https://www.rbvi.ucsf.edu/chimerax/>

---

## 3 Methods

### 3.1 Plating Cells on Coated Glass-Coverslips

Twenty-four to forty-eight hours prior to recording invasion events, adherent cells are plated by default on poly-L-Lysine (100 µg/ml dH<sub>2</sub>O) -coated glass coverslips or MatTek glass bottom dishes or any other systems fitting the cell chamber holders (overnight 4 °C). For specific needs, collagen (rat tail collagen 1, 50–100 µg/ml 0.02 M acetic acid), fibronectin (50 µg/ml PBS), gelatin (0.2% dH<sub>2</sub>O) or specific extracellular matrix components can be used with adapted coating protocols. At the time of the invasion assay, cells must have reached ~80% confluence. Cells are washed with HBSS<sup>++</sup> supplemented with 0.2–1% FCS (i.e., low amounts of FCS can help to limit autofluorescence) and calcium to 1.6 mM final concentration immediately prior transfer into the cell holder setting within the microscope chamber. The so-called Motility Buffer (MB), which allows maintaining proper osmolarity, is our reference buffer used for all comparative preinvasive and invasive behaviors. However if we extend the period of live recording post-invasion—to monitor tachyzoite replication for instances—we then replace the MB by complete medium but lacking phenol red to avoid nonspecific fluorescence in particular in the blue-yellow spectrum.

### 3.2 Collecting *T. gondii* Tachyzoites for Invasion Recording

The quality of the parasite preparation is essential to sample enough events in a short amount of time, thereby limiting the photosensitivity problems (*see Note 1*). To this end, we synchronize the parasite culture and recover the progeny within 2–4 h post-spontaneous egress in the culture medium. In the case of tachyzoite mutants impaired in their egress potential (i.e., actin knockout, [23]), we scrap the cells from the flask and mechanically disrupt them by a few passages through a 26 gauge syringe needle. The amount of parasites needed for each session is washed in the MB by gentle centrifugation, resuspended in a small volume of MB and rapidly added to the target cells under the microscope. Because we limit the volume in the cell chamber, parasite sedimentation is fast allowing to rapidly proceed for image acquisition. For the 20 min regular video sessions, we do not need to add more volume but for longer imaging periods care is taken to prevent evaporation that would change the osmolarity by filling the cell chamber with

medium and keeping saturated humidity in the vicinity of the cell culture setting (i.e., in the compact or wide top-stage chambers). Importantly our priority is to maintain parasites “healthy” by limiting CO<sub>2</sub> and temperature fluctuations to obtain reliable phenotype analysis.

### **3.3 Image Acquisition and Analysis**

Images are usually acquired in DIC and two fluorescent channels at optimal speeds to achieve the efficient spatiotemporal resolution. Using MetaMorph, we systematically go below 1 s per frame and to this end, for reasons mentioned earlier, we select low laser power and low time exposure while in case the camera has a “denoise” setting, we switch off the option. Once sequences have been captured over routine 20 min video-recording sessions, the sequences of interest are cropped using MetaMorph and ImageJ software. Then using the open software Icy, the researcher can access a variety of parameters of static or moving defined “fluorescent” object(s) using tools such as (*see* **Notes 2 and 3**):

- Tracking of object(s):
  - Simultaneous tracking of multiple moving and static objects.
  - Combination of different fluorescent markers’ tracking.
  - Extraction of values depending on the tracking object(s) such as:
    - Speed.
    - Displacement.
    - Surface area.
    - Size measurement (perimeter, etc.).
    - Circularity.
    - Distance tracking between two different objects.
    - Fluorescence intensity, etc.
  - Wide variety of visualization options for the tracks.
- Deformability of static object(s) overtime:
  - Size measurement (perimeter, etc.).
  - Fluorescence intensity.
  - Circularity.
  - Surface area, etc.
- 3D/4D reconstruction:
  - Volume area.
  - Fluorescence Intensity, etc.

All the data are exported in either the .xls or the .csv file which allows easy import and processing by all common software for data

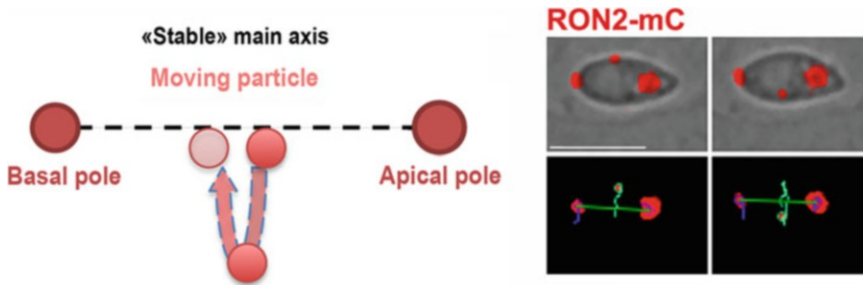


**Fig. 3** Schematic representation of the object tracking that allows quantifying the twisting motion accounting for TJ closure. Right top panel shows the overlay image (DIC-RON2-mC, red) and right bottom panel shows the three objects (rhoptry, TJ, and internal vesicle) tracked using Icy software, scale bar: 5  $\mu\text{m}$

analysis. Moreover, Icy can create graphical plots of your data of interest (*see Note 2*).

To finalize the 3D and 4D reconstruction, we use the open source software ChimeraX.

**Example:** A tachyzoite that expresses RON2 fused to the mCherry tag (red) invades a host cell which expresses the hPM reporter fused to GFP (green). This **dual fluorescence** allows detecting and monitoring the (1) release of the RON complex precisely defining the t0 point of entry, (2) stretching and shrinking of the circular TJ that accommodates parasite progression into an inward hPM-derived bud that forms concomitantly, (3) the closure of the TJ ring, and (4) the birth of the PV when the bud has separated from the hPM therefore precisely defining the final time (ft). Image processing reveals that the parasite executes a rotation around its long axis which imposes a twisting motion on its basal pole, hence ensuring TJ closure and bud sealing while promoting membrane fission upstream the TJ. Interestingly, we observe after twisting the formation of micropatterns in the PV membrane (PVM), while after fission we measure a relaxation phase of the parasite body coupled with the stretching of the tightly adjusted PVM. We focus here on how image processing of the invading RON2-mC tachyzoite has allowed analyzing the final twisting motion (Fig. 3, for details, *see* [15]).

Rotation can be defined by the movement of one object around the axis that connects two objects.

In our case, we assess the rotation using the following protocol:

1. Detection of the objects in the red fluorescent channel using the *Spot detector* plugin overtime. The RON2-mC pools correspond to the rhoptry and the closing/close TJ at each pole of the parasite respectively and define the main axis of the *T. gondii* tachyzoite.
2. Tracking of these objects overtime using the *Spot tracking* plugin.

3. After **step 2**, the *Track manager* plugin window opens automatically providing the possibility to activate different subplugins (*track processors*) that can export values for speed, displacement, etc. of all the tracked objects. In our case we use the *track processor Instant speed* which shows that the reference objects at each pole of the tachyzoite have almost zero speed and the intermediate object moves with a significant speed around the main axis. *Track processor Intensity speed* is used to assess whether the object rotates around the axis (i.e., continuous 360° rotation) (left panel Fig. 3) rather than a flip-flop like movement (i.e., 180 °C back and forward rotations). In more details, the intensity of the tracked object over time decreases when the object gets out of focus and reincreases when back in focus, thereby demonstrating the continuous rotation process.

By applying filters and threshold on the images in the fluorescent channel of interest, we clearly observe the dynamics of the hPM-derived bud that tightly surrounds the invading parasite. Icy has by default the widely used filters such as *Median filter* and the interface of the intensity brightness control panel is quite useful. By using the *Intensity profile* plugin we can access the intensity distribution of the forming and newly formed PV and therefore detect any abnormal process of PV biogenesis.

We describe the relaxation of the parasite body as follows:

1. Using the same “stable” spots that have been tracked in the rotation protocol.
2. Using the *track processor Distance profiler*, the distance between the two stable spots could be recorded over time. Results showed that there was an increase in the length of the axis that connects these two spots.

---

## 4 Notes

1. *T. gondii* tachyzoites have been found sensitive to phototoxic damages when they express high amounts of soluble protein in fusion with GFP or YFP. Mammalian cells also show differential sensitivity to illumination-induced ROS. Overall, we advise to reduce the peak intensity of the laser beam even if that means extending the exposure time provided it is compatible with the temporal resolution needed to capture the multistep sequence of cell invasion. Ideally fluorescent markers should be carefully tested and compared with available alternatives. On the same line, caution is necessary to ensure that cells are maintained in good condition and are functional while on the microscope

stage with illumination in the presence of synthetic fluorophores or fluorescent proteins.

2. Icy is an open source software that gives the ability to the user to search for similar tasks or solutions to possible problems through an online interactive forum. For example, the user can create a new thread with his/her problem and then other users or the Icy software engineers can provide advice/help.
3. Not only the best phenotypic description of a parasite preinvasive and invasive skills clearly gains from a careful comparative analysis of the dynamic behavior with the current reference scheme (i.e., as described earlier), but it can also improve the model itself by highlighting specific steps within “normal” or “abnormal” sequences. It is important to be aware of continual advances in live imaging techniques/platforms, in the design of fluorescent probes and computationally efficient algorithms to increase the accuracy of the image information content we can capture and process.

## References

1. Tardieux I, Baum J (2016) Reassessing the mechanics of parasite motility and host-cell invasion. *J Cell Biol* 214:507–515. <https://doi.org/10.1083/jcb.201605100>
2. Sidik SM, Huet D, Ganesan SM, Huynh M-H, Wang T, Nasamu AS, Thiru P, Saeij JPJ, Caruthers VB, Niles JC, Lourido S (2016) A genome-wide CRISPR screen in *Toxoplasma* identifies essential apicomplexan genes. *Cell* 166:1423–1435.e12. <https://doi.org/10.1016/j.cell.2016.08.019>
3. Sidik SM, Huet D, Lourido S (2018) CRISPR-Cas9-based genome-wide screening of *Toxoplasma gondii*. *Nat Protoc* 13:307–323. <https://doi.org/10.1038/nprot.2017.131>
4. Bichet M, Joly C, Henni AH, Guilbert T, Xémard M, Tafani V, Lagal V, Charras G, Tardieux I (2014) The *Toxoplasma*-host cell junction is anchored to the cell cortex to sustain parasite invasive force. *BMC Biol* 12:773. <https://doi.org/10.1186/s12915-014-0108-y>
5. Hu K, Johnson J, Florens L, Fraunholz M, Suravajjala S, DiLullo C, Yates J, Roos DS, Murray JM (2006) Cytoskeletal components of an invasion machine--the apical complex of *Toxoplasma gondii*. *PLoS Pathog* 2:e13. <https://doi.org/10.1371/journal.ppat.0020013>
6. Mondragon R, Frixione E (1996) Ca(2+)-dependence of conoid extrusion in *Toxoplasma gondii* tachyzoites. *J Eukaryot Microbiol* 43:120–127
7. Lourido S, Tang K, Sibley LD (2012) Distinct signalling pathways control *Toxoplasma* egress and host-cell invasion. *EMBO J* 31:4524–4534. <https://doi.org/10.1038/emboj.2012.299>
8. Lourido S, Moreno SNJ (2015) The calcium signaling toolkit of the apicomplexan parasites *Toxoplasma gondii* and *Plasmodium* spp. *Cell Calcium* 57:186–193. <https://doi.org/10.1016/j.ceca.2014.12.010>
9. Carey KL, Westwood NJ, Mitchison TJ, Ward GE (2004) A small-molecule approach to studying invasive mechanisms of *Toxoplasma gondii*. *Proc Natl Acad Sci U S A* 101:7433–7438. <https://doi.org/10.1073/pnas.0307769101>
10. Hakimi M-A, Olias P, Sibley LD (2017) *Toxoplasma* effectors targeting host signaling and transcription. *Clin Microbiol Rev* 30:615–645. <https://doi.org/10.1128/CMR.00005-17>
11. Graindorge A, Fréchal K, Jacot D, Salamun J, Marq JB, Soldati-Favre D (2016) The conoid associated motor MyoH is indispensable for *Toxoplasma gondii* entry and exit from host cells. *PLoS Pathog* 12:e1005388. <https://doi.org/10.1371/journal.ppat.1005388>
12. Mordue DG, Desai N, Dustin M, Sibley LD (1999) Invasion by *Toxoplasma gondii* establishes a moving junction that selectively excludes host cell plasma membrane proteins on the basis of their membrane anchoring. *J Exp Med* 190:1783–1792

13. Charron AJ, Sibley LD (2004) Molecular partitioning during host cell penetration by *Toxoplasma gondii*. *Traffic* 5:855–867. <https://doi.org/10.1111/j.1600-0854.2004.00228.x>
14. Suss-Toby E, Zimmerberg J, Ward GE (1996) *Toxoplasma* invasion: the parasitophorous vacuole is formed from host cell plasma membrane and pinches off via a fission pore. *Proc Natl Acad Sci U S A* 93:8413–8418
15. Pavlou G, Biesaga M, Touquet B, Lagal V, Balland M, Dufour A, Hakimi M-A, Tardieux I (2018) *Toxoplasma* parasite twisting motion mechanically induces host cell membrane fission to complete invasion within a protective vacuole. *Cell Host Microbe* 24:81–96.e5. <https://doi.org/10.1016/j.chom.2018.06.003>
16. Fox BA, Ristuccia JG, Gigley JP, Bzik DJ (2009) Efficient gene replacements in *Toxoplasma gondii* strains deficient for nonhomologous end joining. *Eukaryot Cell* 8:520–529. <https://doi.org/10.1128/EC.00357-08>
17. Huynh M-H, Carruthers VB (2009) Tagging of endogenous genes in a *Toxoplasma gondii* strain lacking Ku80. *Eukaryot Cell* 8:530–539. <https://doi.org/10.1128/EC.00358-08>
18. Sidik SM, Hackett CG, Tran F, Westwood NJ, Lourido S (2014) Efficient genome engineering of *Toxoplasma gondii* using CRISPR/Cas9. *PLoS One* 9:e100450. <https://doi.org/10.1371/journal.pone.0100450>
19. Shen B, Brown KM, Lee TD, Sibley LD (2014) Efficient gene disruption in diverse strains of *Toxoplasma gondii* using CRISPR/CAS9. *MBio* 5:e01114–e01114. <https://doi.org/10.1128/mBio.01114-14>
20. Andenmatten N, Egarter S, Jackson AJ, Jullien N, Herman J-P, Meissner M (2013) Conditional genome engineering in *Toxoplasma gondii* uncovers alternative invasion mechanisms. *Nat Methods* 10:125–127. <https://doi.org/10.1038/nmeth.2301>
21. Bichet M, Touquet B, Gonzalez V, Florent I, Meissner M, Tardieux I (2016) Genetic impairment of parasite myosin motors uncovers the contribution of host cell membrane dynamics to *Toxoplasma* invasion forces. *BMC Biol* 14:97. <https://doi.org/10.1186/s12915-016-0316-8>
22. Rhee JM, Purity MK, Lackan CS, Long JZ, Kondoh G, Takeda J, Hadjantonakis A-K (2006) In vivo imaging and differential localization of lipid-modified GFP-variant fusions in embryonic stem cells and mice. *Genesis* 44:202–218. <https://doi.org/10.1002/dvg.20203>
23. Egarter S, Andenmatten N, Jackson AJ, Whitelaw JA, Pall G, Black JA, Ferguson DJP, Tardieux I, Mogilner A, Meissner M (2014) The *Toxoplasma* Acto-MyoA motor complex is important but not essential for gliding motility and host cell invasion. *PLoS One* 9:e91819. <https://doi.org/10.1371/journal.pone.0091819>

## 2.2.5 Discussion and perspectives

In this study, we report the importance of mechanical forces generated by the *T. gondii* tachyzoite to end the invasion sequence in mammalian host cells and initiate the modeling of an intracellular niche compatible with the production of progeny. When compared to what we knew about the early steps of cell invasion, the mechanisms underlying the birth of a subcellular compartment in which the tachyzoite could safely adopt an intracellular lifestyle were quite elusive. While the functions of the RON invasive nanodevice as a traction force platform and a molecular sieve were already established and shown to support the subversion of a component-selective piece of PM during tachyzoite entry, we were curious to investigate if the presence of this nanodevice could also dictate the way the budding entry vesicle actually pinches off of the PM it derives from. To this end, we combined quantitative live imaging, *T. gondii* and mammalian cell molecular genetics and nanotools. We were able to detect a final twisting motion of the parasite that imposes rotation on the basal pole and therefore on the ZCJ and appears critical for finalizing the safe entry of the parasite while preserving the hosting cell from membrane damages. Another fascinating observation came when we imaged simultaneously the fluorescent invasive RON-nanodevice and the fluorescence associated with the host cell PM membrane. We were able not only to detect a homogeneous signal in the budding membrane when the tachyzoite entered but also the changes in the bud fluorescence that occurred only post twisting motion and led to a specific fluorescent patchy pattern in the membrane of the PV. Given the fact that when the PV emerges post-pinching off, the tachyzoite next must rapidly adjust to its new microenvironment and organize a niche appropriate for growth. These requirements are satisfied thanks to a number of proteins and lipids the tachyzoite secretes, in particular from the heterogeneous population of dense granules, which promote the assembly of an intricate network of tubular structures that ensure the import and the export of material beyond the PV membrane. Apart from dense granule products, the rhoptries also secrete components into the vacuolar space and it would be interesting to verify if the clustering of PV-derived fluorescent material can reflect the integration of known transmembrane proteins such as the ROP2 superfamily members, but also for instances MYR2 and 3 that are thought to be essential part of a translocon system underpinning the export of GRA proteins across the PVM (Arrizabalaga, 2019). Many more proteins have been identified and shown to associate with either side of the PVM and they could theoretically contribute even without spanning the elusive PVM at applying force to the PVM and trigger some redistribution of molecules in the PVM. Indeed, mechanical forces on the PVM could be expected with the rapid recruitment of ER and mitochondria that interact with the young PV.

As regard to the twisting motion, we hypothesized that the torque applied onto the the nanodevice forces the two upstream membranes facing each other to follow

the same movement and this is in line with the observation that the RON2-mC signal actually partitions into the PV. Therefore this implies that any expected fusion/fission event(s) must take place immediately upstream the nanodevice. It is tempting to compare the pinch off process with a topologically similar event occurring for the release of endocytic vesicle from the coated pits during clathrin-mediated endocytosis. In this case, the dynamins play a major role by directing the constriction and the torsion of the two membranes forming the neck of the nascent endocytic vesicle. Thanks to cells engineered to tamoxifen induce triple knockout of dynamins 1,2 and 3, we proved that the tachyzoite achieves invasion similarly in cells expressing or lacking dynamins. With the same approach, we disproved the functional involvement of ALIX during cell invasion, a protein partner of the ESCRT-I machinery which was recently reported but using indirect assays and based on (i) the *in situ* localization of a pool of ALIX at the ZCJ and (ii) the physical interaction established between ALIX and RON4 (Gu erin *et al*, 2017).

However, we do not exclude that other molecules from the host cell could assist the torus closure and membrane fission processes. An important candidate to investigate is actin, which is known to team with dynamins for force production during endosome formation. F-actin is clearly present at the ZCJ site, which led our team to propose a role of a *de novo* assembled F-actin pool in the anchorage of the nanodevice-made platform. The same situation holds for the actin ARP2/3 nucleating factor (Gonzalez *et al*, 2009), therefore positioning in space and time the actin and actin polymerization machinery to the ZCJ over the process of invasion. Finally, other host cell molecules could deserve attention to molecularly understand the fission process among which lipids that are known to determine the fusogenic capacities of membranes and that could facilitate fusion upstream the torus upon twisting motion. In terms of the fission process itself, the remarkable preservation of cell membrane integrity is a fascinating aspect of the process and it still might be important to delve deeper in the potential contribution of membrane repair mechanism.

Overall, this study highlights the cleverness of the tachyzoite to engineer a multi-functional unique “invasive nanodevice” to achieve amazing high-speed invasion of many different cell types. It allows suggesting that, with this nanodevice and the ability to apply force, the tachyzoite has evolved a dynamin like machinery to force constriction and torsion of the two facing membrane segments at the “neck” of the budding entry vesicle. With this strategy, the tachyzoite actively closes the entry door made by the toroidal invasive nanodevice and mechanically induces separation from the plasma membrane of the hosting cell to eventually reside in the intracellular niche and adopt the intracellular lifestyle.

# Conclusion

## Conclusion



During this thesis period, we wished to create a map of the forces that contribute to *Toxoplasma* motility and host cell invasion. By highlighting the key role of mechanical forces that drive cell movement in a 3D matrix or into a cell, this work opens a new era of investigation with the objective of an in-depth understanding of the peculiar forces, including torque and contraction over these processes. It is quite clear how unique is this cell by using a variety of mechanisms not only to migrate but also to invade and parasitize a host cell to fill their metabolic needs. We could make use of its “secret weapons” beyond the field

of parasitology starting with the ever-increasing range of applications for nanotechnologies including in medicine, and reaching even the macrotechnologies as for example in architecture. We could take inspiration from the invasive nanodevice and the invasion mechanisms to engineer new generation of carriers with specific surface-exposed molecules favoring their capture by given cells, such as cancer cells, and then delivery of specific cargo including pharmacological drugs or other compounds to promote destruction for tumor cells or in some other cases to eliminate the microbial threats with the minimum damage during the delivery process. As for the field of architecture and in particular the subfield of biomimicry in architecture design of which I am a big fan, one can imagine that architects could use mechanical properties of the rigid and flexible *Toxoplasma* to build objects or even buildings! Coming from a mathematics background where I love geometry, I would be very inspired by the unique cytoskeleton of the tachyzoite and especially the network of twisted microtubules and the elastic properties that this network seems to have, but also the amazing construction of connections bridging the membranous elements of the pellicle to the cytoskeleton. But it seems that a famous architect named Norman Foster had already been inspired by nature to build the Toxo-like Gherkin building in London... He was inspired from a different organism but why not from *Toxoplasma* in the future.

# Other publications

## Other publications

Del Rosario M, Periz J, Pavlou G, Lyth O, Latorre-Barragan F, Das S, Pall GS, Stortz JF, Lemgruber L, Whitelaw JA, Baum J, Tardieux I & Meissner M (2019) Apicomplexan F-actin is required for efficient nuclear entry during host cell invasion. *EMBO Rep* **20**: Available at: <https://onlinelibrary.wiley.com/doi/abs/10.15252/embr.201948896>

Siebert C, Villers C, Pavlou G, Touquet B, Yakandawala N, Tardieux I & Renesto P (2020) *Francisella novicida* and *F. philomiragia* biofilm features conditioning fitness in spring water and in presence of antibiotics. *PLoS ONE* **15**: e0228591 Available at: <https://dx.plos.org/10.1371/journal.pone.0228591>

# Apicomplexan F-actin is required for efficient nuclear entry during host cell invasion

Mario Del Rosario<sup>1</sup> , Javier Periz<sup>1</sup>, Georgios Pavlou<sup>2</sup>, Oliver Lyth<sup>3</sup>, Fernanda Latorre-Barragan<sup>1,4</sup> , Sujaan Das<sup>1</sup>, Gurman S Pall<sup>1</sup>, Johannes Felix Stortz<sup>1</sup> , Leandro Lemgruber<sup>1</sup>, Jamie A Whitelaw<sup>5</sup>, Jake Baum<sup>3</sup> , Isabelle Tardieux<sup>2</sup>  & Markus Meissner<sup>1,6,\*</sup> 

## Abstract

The obligate intracellular parasites *Toxoplasma gondii* and *Plasmodium* spp. invade host cells by injecting a protein complex into the membrane of the targeted cell that bridges the two cells through the assembly of a ring-like junction. This circular junction stretches while the parasites apply a traction force to pass through, a step that typically concurs with transient constriction of the parasite body. Here we analyse F-actin dynamics during host cell invasion. Super-resolution microscopy and real-time imaging highlighted an F-actin pool at the apex of pre-invading parasite, an F-actin ring at the junction area during invasion but also networks of perinuclear and posteriorly localised F-actin. Mutant parasites with dysfunctional actomyosin showed significant decrease of junctional and perinuclear F-actin and are coincidentally affected in nuclear passage through the junction. We propose that the F-actin machinery eases nuclear passage by stabilising the junction and pushing the nucleus through the constriction. Our analysis suggests that the junction opposes resistance to the passage of the parasite's nucleus and provides the first evidence for a dual contribution of actin-forces during host cell invasion by apicomplexan parasites.

**Keywords** actin; Apicomplexa; host cell invasion; myosin; nucleus

**Subject Categories** Cell Adhesion, Polarity & Cytoskeleton; Microbiology, Virology & Host Pathogen Interaction

**DOI** 10.15252/embr.201948896 | Received 21 July 2019 | Revised 21 August 2019 | Accepted 11 September 2019

**EMBO Reports (2019) e48896**

## Introduction

The phylum Apicomplexa consists of more than 5,000 species, most of them obligate intracellular parasites, including important human

and veterinary pathogens, such as *Plasmodium* (malaria) or *Toxoplasma* (toxoplasmosis).

During their complex life cycles, apicomplexan parasites move through different environments to disseminate within and between hosts and to invade their host cell [1]. Therefore, the invasive stages, called zoites, evolved a unique invasion device, consisting of unique secretory organelles and the parasites' actomyosin system, the Glideosome, localised in the narrow space (~30 nm) between the plasma membrane and the inner membrane complex (IMC) [2]. Zoites actively enter the host cell by establishing a tight junctional ring (TJ) at the point of contact between the two cells. The TJ is assembled by the sequential secretion of unique secretory organelles (micronemes and rhoptries), leading to the insertion of rhoptry neck proteins (RONs) into the host cell plasma membrane (PM) and underneath [3]. On the extracellular side, the exposed domain of the RON2 member binds the micronemal transmembrane protein AMA1 exposed on the parasite surface, resulting in the formation of a stable, junctional complex [3]. The TJ is further anchored to the host cell cortex by *de novo* formation of F-actin through the recruitment of actin-nucleating proteins [4,5]. During host cell invasion, the parasites use their actomyosin motor to pass through the TJ. However, the exact role and orientation of the parasite's actomyosin system is still under debate [6] and intriguingly, mutants for key component of this system show residual motile and invasive capacities [7–9], the latter reflecting in large part an alternative and host cell actin-dependant mode of entry [10]. According to the Glideosome model, the force generated for motility and invasion relies exclusively on F-actin polymerised at the apical tip of the parasite by the action of Formin-1 and translocated within the narrow space (~30 nm) between the IMC and PM of the parasite [11]. However, recent studies suggest that the parasite can also use other motility systems, such as a secretory-endocytic cycle that produces retrograde membrane flow [12], similar to the fountain flow model suggested for other eukaryotes [13,14].

In support of the linear motor model, was the detection of parasite F-actin underneath the junction formed by invading parasites

1 Wellcome Centre For Integrative Parasitology, Institute of Infection, Immunity & Inflammation, Glasgow Biomedical Research Centre, University of Glasgow, Glasgow, UK

2 Institute for Advanced Biosciences, CNRS, UMR5309, INSERM U1209, Université Grenoble Alpes, Grenoble, France

3 Department of Life Sciences, Imperial College London, London, UK

4 Faculty of Science, Food Engineering and Biotechnology, Technical University of Ambato, Ambato, Ecuador

5 CRUK Beatson Institute, Glasgow, UK

6 Experimental Parasitology, Department for Veterinary Sciences, Ludwig-Maximilians-University Munich, Munich, Germany

\*Corresponding author. Tel: +49 89 21803622; E-mail: markus.meissner@lmu.de

when using an antibody preferentially recognising apicomplexan F-actin. Furthermore, the detection of cytosolic locations, predominantly around the nucleus [15], suggests additional roles of this cytoskeletal protein during invasion.

While it was assumed a major role of F-actin in driving Apicomplexa zoite gliding motility and cell invasion, recent studies demonstrated the pivotal role of F-actin in multiple other processes, such as apicoplast inheritance [16], dense granule motility [17] and likely nuclear functions through the control of expression of virulence genes in malaria parasites [18]. However, building a comprehensive model for F-actin dynamics, localisation and function in apicomplexan parasites has been hampered for decades by the lack of tools enabling reliable F-actin detection. Interestingly, several studies suggested that F-actin is interacting with subpellicular microtubules [19] and/or the subpellicular matrix of the IMC [20,21]. Furthermore, components of the Glideosome, such as GAPM proteins [22] or the invasion-critical myosin, MyoH were demonstrated to interact with microtubules [23], suggesting a coordinated action of the actin and microtubule cytoskeleton during host cell invasion.

With the adaptation of nanobodies specifically recognising F-actin, it is now possible to analyse F-actin dynamics in apicomplexan parasites [24,25] leading to the identification of distinct cytosolic networks of dynamic actin in both *T. gondii* and *P. falciparum* [11,24,25]. We originally identified two F-actin polymerisation centres from where most of the F-actin flow occurs in intracellular parasites [24], later expanded to three based on further studies [11,25]. One polymerisation centre can be found at the apical tip, corresponding well to the described location of Formin-1, and one close to the parasite's Golgi complex, corresponding to the location of Formin-2 [11,25]. In *T. gondii*, these three polymerisation centres of F-actin correlate well with the location of Formins-1, 2 and 3 in *T. gondii* [11]. Formins-2 and 3 appear to have overlapping functions during the intracellular development of the parasite for material exchange and formation of an intravacuolar network in intracellular parasites, while Formin-1 (FH-1) has been explicitly implicated in the apical polymerisation of F-actin required for gliding motility and cell invasion [11]. In this study, although not directly shown, the authors suggested that FH-1 polymerises F-actin at the apical tip of the parasite that is exclusively transported by the action of the Glideosome within the subalveolar space to the posterior pole. Interestingly, at least in intracellular parasites, the majority of F-actin dynamics appears to occur within the cytosol of the parasite close to the parasite's Golgi, forming a continuous dynamic flow from centre to the periphery of the parasite and from the apical to the basal pole [24,25]. In addition, measurement of peripheral F-actin flow demonstrated that it can occur bidirectional from the apical to the posterior pole and vice versa [25].

In good agreement with a cytosolic oriented F-actin system, previous reports demonstrated parasite F-actin to be associated with the subpellicular microtubules that are connected to and stabilise the IMC [19–21,26]. Furthermore, gliding-associated proteins identified via co-immunoprecipitation with the Glideosome were recently found to play important roles in stabilising the IMC and directly connecting it to the subpellicular microtubules [22,27], suggesting that a close connection exists between parasite F-actin, the Glideosome and the subpellicular network.

Here we compared F-actin dynamics in WT and mutant parasites for the acto-myosin system and correlated its dynamic location with

the phenotypic consequences during host cell invasion. Interestingly, in unstimulated parasites, F-actin flow in extracellular parasites appears to be bidirectional, with the majority of events occurring in a retrograde direction, which is similar to measurements performed on intracellular parasites [25]. The activation of calcium signalling results in a shift towards retrograde F-actin flow, resulting in F-actin accumulation at the posterior pole. Comparison of F-actin dynamics in parasite mutants for the acto-myosin system helped to identify the nucleus as a major obstacle for efficient host cell invasion that needs to be squeezed through the junction using F-actin dynamics to translocate and potentially deform the nucleus through this process.

Our analysis strongly suggests a push-and-pull mechanism for nuclear entry during host cell invasion, in analogy to the dynamics observed during migration of other eukaryotes through a constricted environment [28].

## Results

### Rational for selecting parasite mutants in order to analyse F-actin dynamics during host cell invasion

Over recent years, conditional mutagenesis systems have been employed to generate and characterise a whole assortment of parasite mutants affected in host cell invasion. These mutants can be affected in different, unrelated pathways, such as microneme secretion, formation of the tight junction or host cell entry. Since we were interested in analysing F-actin dynamics during the invasion process, we chose parasite mutants that were previously characterised to be significantly affected, but not blocked in host cell entry and linked to the parasites acto-myosin system. We excluded all mutants that have been described to be completely blocked in the initiation of invasion, such as MyoH [23] or the micronemal protein MIC8 [29], since no invasion event can be expected that can be analysed. Similarly, we also excluded mutants involved in actin dynamics that have not been implicated in host cell invasion, such as FH-2,3 [11] or myosins not involved in host cell invasion, such as MyoI [30].

Therefore, we chose parasite actin [7,9], the actin depolymerisation factor ADF [31] and myosin A (MyoA), which has been used previously to successfully identify the contribution of the host cell for parasite invasion [10].

### F-actin flow is mainly organised within the cytosol of extracellular parasites and is modulated by Calcium and cGMP signalling

We previously imaged F-actin flow in intracellular parasites and were able to discriminate two major polymerisation centres, one at the apical tip and one close to the apicoplast, where F-actin is formed and subsequently transported to the posterior end of the parasite [24]. Indeed, recent studies on *Toxoplasma* and *Plasmodium* demonstrated that Formin-2 is localised to the apicoplast of the parasite and required for most of the intracellular F-actin dynamic [11,25], while Formin-1 is localised at the apical tip, where it is thought to be exclusively required for parasite motility and invasion. In good agreement, in intracellular parasites, F-actin appears

to be formed at two polymerisation centres, localised at the apical tip and close to the Golgi region of the parasite, indicating that FH-1 and FH-2 are acting as nucleators during intracellular parasite development. Intriguingly, the majority of F-actin dynamics in intracellular parasites occurs within the cytosol of the parasite with F-actin flow occurring in a bidirectional manner (retrograde and anterograde) [24,25]. We were interested to determine if during the transient extracellular life and at the time of cell invasion, the patterns of actin dynamics differ from the intracellular ones and how they were impacted upon disruption of the Glideosome or factors critically involved in F-actin regulation.

Since transient transfections are typically associated with overexpression of the target protein hence with significant uncontrolled impact on a dynamic equilibrium [24], we generated *T. gondii* lines stably expressing Cb-EmeraldFP. We ensured that the expression of the chromobody was comparable between the different parasite lines and ensured that its expression does not lead to phenotypic alterations and misleading analysis. We established transgenic parasites expressing Cb-EmeraldFP in WT parasites, a null mutant for myosin A (MyoA), the core motor of the Glideosome [16] and a conditional mutant for the critical actin regulator, actin depolymerisation factor ADF, *adf*KD [31]. Using live 3D-structured illumination microscopy (3D-SIM), we compared F-actin dynamics and found two discernible F-actin polymerisation centres (Fig 1A) as previously seen in intracellular parasites [24]. Time-lapse analysis demonstrated that the majority of F-actin dynamics occurs in the cytosol of the parasite with some F-actin flow detectable at the periphery occurring in retrograde and anterograde orientation, similar to intracellular parasites (see also [25]). In good agreement with the localisation of FH-1 and FH-2, two polymerisation centres can be detected. F-actin flow starts from the apical tip (1<sup>st</sup> polymerisation centre, yellow arrow in Fig 1A) to the second polymerisation centre close to the Golgi (red arrow, Fig 1A) to the posterior pole of the parasite (Fig 1A, Movie EV1). While disruption of *myoA* did not result in significant changes of F-actin localisation or dynamics in resting parasites (Fig 1A, Movie EV1), depletion of ADF completely abrogated actin dynamics, F-actin accumulation being observed at both apical and posterior parasite poles (Fig 1A, Movie EV1).

To map the actin structures visualised with the chromobody, we employed skeletonisation processing [32], which converts F-actin signals into individual pixels, that can be traced to obtain information about the localisation and dynamics of F-actin. The resulting skeletonised movie can be projected to show where the majority of (detectable) F-actin dynamics occur during the timeline of the movie (Fig 1B, Movie EV1). This analysis confirmed that parasite F-actin formed at the apical tip (yellow arrowhead) and Golgi region (red arrowhead), converge within the cytosol of the parasite and reach the basal pole of the parasite. Interestingly, both peripheral and cytoplasmic flow appear to be connected and do not occur independently from each other (Fig 1B). Note that both WT and *myoA*KO parasites displayed similar signals, whereas the ADF—conditional mutant did not.

Next, kymograph analysis was performed to analyse individual F-actin flow events using KymographClear and KymographDirect [33] confirming the presence of a continuous dynamic F-actin network in cytosolic location that connects the apical pole, Golgi area and basal pole of the parasite, in good agreement with the location of the 3 Formins previously described in *T. gondii* [11].

KymographClear is a FIJI plugin that generates a 3 colour-coded kymograph, where each colour labels either forward movement (red), backward movement (green) or static (blue) as shown (Fig 1C and Appendix Fig S1). This kymograph can then be read into the KymographDirect software, which uses automatic detection to trace trajectories of moving particles in the image. Values are then assigned to these trajectories based on both intensity and speed [33]. The intensity can be assessed in specified tracks over time as the average intensity over time shown in Fig 1C. Both the RH and *myoA* KO presented dynamic signals connecting the apical pole (close to the point 0), Golgi region (between 2 and 3  $\mu$ m) and basal pole. In the case of the *adf* KD, only static signals could be detected at the apical and basal pole of the parasite, confirming the lack of F-actin dynamics in these mutants.

Next, we used this analysis to investigate intensity profiles of actin signal travelling in the periphery of the parasite (Appendix Fig S1B–D). Interestingly, actin dynamics along the periphery is similar between WT and *myoA* KO with bidirectional actin flow events as revealed by the kymographs, while confirming previous results with the *adf* KD mutants, which shows a lack of F-actin dynamics across the entire parasite body (first half (–), Appendix Fig S1A–C).

Together, the data presented in this work point that similarly to intracellular parasites, the F-actin is highly dynamic in extracellular parasites displaying two major polymerisation centres, one at the apical tip and another at the Golgi region of the parasite. Of note, this analysis underlines that there is actin flow coming from the cytoplasm towards the periphery and shaping a highly dynamic network that connects the apical and basal pole of the parasite, therefore independently of any F-actin network positioned between the zoite's PM and IMC.

Tosetti *et al* [11] suggested that the activation of a  $Ca^{2+}$ -signalling cascade would lead to increased retrograde transport of F-actin, eventually accumulating posteriorly. However, we found that the treatment of parasites with the calcium ionophore A23187 induced anterior accumulation of F-actin in wild-type parasites in the majority of cases (Fig 1D–F; Appendix Fig S1A; Movie EV2), while BIPPO triggered a predominantly basal F-actin accumulation (Fig 1D–F; Appendix Fig S1A; Movie EV2). BIPPO is a drug capable of inhibiting 3',5'-cyclic nucleotide phosphodiesterases (PDEs) responsible in blocking the breakdown of cyclic nucleotides such as cAMP and cGMP. This mechanism is believed to be responsible in the activation of microneme secretion and egress by modulating the signal pathway of PKG-dependent processes [34].

Once MyoA null mutants were submitted to treatments with A23187 or BIPPO, the F-actin remained rather evenly distributed within the cytoplasm albeit with some peripheral enrichment in the first half of the parasite closer to the apical end (Fig 1D–F; Movie EV2). In contrast, depletion of ADF led to the expected phenotype with F-actin accumulating at the apical and basal pole of the parasite, independently of A23187 or BIPPO addition (Fig 1D–F; Movie EV2). Together, these data suggest that calcium signalling regulates F-actin dynamics, potentially by stimulating the activity of Formin-1 followed by F-actin transport to the posterior pole of the parasite by the action of MyoA.

In conclusion, similar to intracellular parasites, extracellular parasites show impressive F-actin dynamics within the cytosol. In parasite mutants for ADF, this dynamic is abolished, and F-actin accumulates at the apical and basal pole, independent of triggering

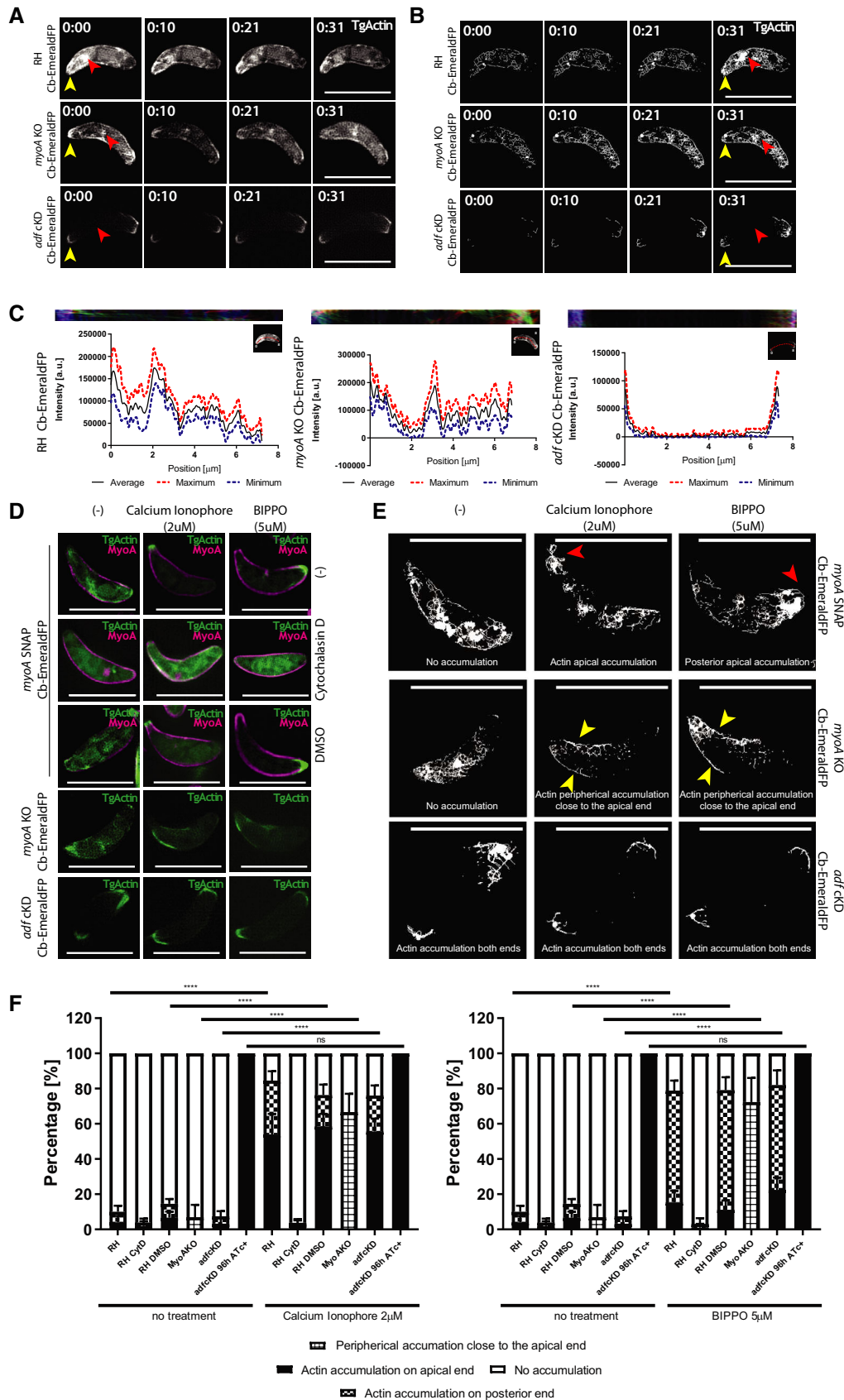


Figure 1.

### Figure 1. F-actin, formed at two major nucleation centres, forms a dynamic, continuous network within the cytosol of the parasite.

- A Stills depicting actin flow (see Movie EV1) in extracellular RH, *myoA* KO and *adf* KD parasites expressing Cb-EmeraldFP. Continuous F-actin flow can be seen from the apical tip, to the Golgi region towards the posterior pole of the parasite. No difference can be observed between RH and *myoA* KO. For *adf* KD, the flow is completely abrogated. Red arrowhead marks the Golgi region, while the yellow arrowhead marks the apical nucleation centre. The time lapse is presented in Movie EV1.
- B Skeletonisation processing of (A) depicting areas where F-actin dynamics/flow is prevalent. Individual signals for F-actin form a continuous, dynamic network that connects apical and posterior pole of the parasite. Red arrowhead marks the Golgi region nucleation centre, while the yellow arrowhead marks the apical nucleation centre. The images represent a projection of frames for each timepoint to provide a better overview of the dynamics of F-actin. The time lapse is presented in Movie EV1.
- C Kymograph analysis of (A) and (B). The kymograph was generated by tracing a line in the middle of the parasite's body (red line). The colour-coded kymograph represents forward movement (red), backward movement (green) and static F-actin (blue). The results demonstrate continuous exchange of F-actin from the apical to the posterior pole of the parasite within the cytosol of the parasite. This cytosolic exchange is similar in RH and *myoA* KO parasites, while completely abolished in the case of *adf* KD.
- D Top three rows: Parasites expressing Cb-EmeraldFP along with *myoA*-SNAP before and after  $\text{Ca}^{2+}$  ionophore (A23187) or BIPPO treatment. The parasites were also treated with 2  $\mu\text{M}$  of cytochalasin D or DMSO (as control) for 30 min. After the addition of A23187, preferential relocalisation of actin can be observed at the apical tip, while the addition of BIPPO caused F-actin accumulation at the basal end. 4<sup>th</sup> row: *myoA*KO parasites expressing Cb-EmeraldFP before and after treatment with A23187 and BIPPO. While no apical or basal accumulation of F-actin is observed, some peripheral location of F-actin occurs in the presence of A23187 or BIPPO, preferentially in the apical half of the parasite. Bottom row: *adf* cKD parasites expressing Cb-EmeraldFP before and after treatment with  $\text{Ca}^{2+}$  ionophore or BIPPO. No apparent change in F-actin localisation can be seen upon treatment. The time lapse is presented in Movie EV2.
- E Skeletonisation of movies shown in (D). Before the addition of A23187 or BIPPO, RH and *myoA* KO parasites behave similar with no accumulation of F-actin at the apical tip. After treatment with calcium ionophore A23187, preferential accumulation of F-actin at the apical tip can be observed for RH (red arrowhead), while BIPPO presented preferential accumulation in the basal end (red arrowhead). In *myoA* KO, some relocalisation of actin is observed at the periphery of the parasite (yellow arrowhead). In the case of *adf* cKD, no relocalisation occurs. The images represent a projection of frames for each timepoint to provide a better overview of the dynamics of F-actin.
- F Quantification of actin accumulation before and after treatment with  $\text{Ca}^{2+}$  ionophore or BIPPO. The parasites were counted for F-actin accumulation after adding  $\text{Ca}^{2+}$  ionophore or BIPPO. Numbers were generated by counting total number of parasites and then number of parasites with actin accumulation on the apical or basal tip. A minimum of 200 parasites were counted upon 3 biological replicates. Two-way ANOVA was used for statistical analysis and Tukey's multiple comparison test. \*\*\*\* $p < 0.0001$ . Error bars represent standard deviation.

Data information: Numbers indicate minutes:seconds, and scale bars represent 5  $\mu\text{m}$ .  
Source data are available online for this figure.

a calcium-signalling cascade. In contrast, disruption of MyoA results in normal F-actin dynamics, but upon calcium signalling, F-actin remains more diffusely localised within the cytosol of the parasite with some accumulation at the periphery.

### The acto-myosin system is required to ensure efficient invasion

To investigate whether this impressive cytoplasmic F-actin dynamics could assist the parasite over the invasion of the target cell, namely when it fits through the junction and constricts (Fig 2A and B), we first measured the average diameter of parasites prior and during invasion. We observed a significant decrease at mid-invasion, (prior: 2.5–3  $\mu\text{m}$  and mid-invasion 1.5–2  $\mu\text{m}$ ) that attests significant body deformation and compression in order to fit through the junction (Fig 2A and B). In good agreement, analysis of the average diameter of the parasite's nucleus indicated that this organelle suffers a striking deformation, up to ~50% of its normal diameter (i.e. < 1  $\mu\text{m}$ ) while passing through the junction (Fig 2A and B). Since the acto-myosin system generates traction force at the junction to account for the invasive force, we investigated if interference causes changes, that is differences in the diameter of the TJ and/or stronger deformations of the parasite. While a slight reduction in the average TJ diameter was observed during invasion of *myoA* KO parasites (Fig 2C), the junctional ring appears remarkably constant upon interference with the acto-myosin system of the parasite.

Previously, it was demonstrated that mutants for the acto-myosin system enter the host cell in a stop-and-go manner, leading to a prolonged invasion process with different features [7,9,31]. While mutant parasites could be driven through the TJ by the host cell membrane outward projections in an uncompleted micropinocytosis-like process [10], they could in some cases remain trapped in the TJ and die, probably due to compressive forces exerted on the

embedded part of the parasite by the host cell membrane protrusions [10]. We infer from these observations that the tachyzoite likely needs to counteract compressive forces at the TJ to secure entry of its bulky organelles, such as the nucleus and hypothesised that the parasite acto-myosin is critically involved in nuclear entry.

We compared the invasion process of WT and mutant parasites in detail using time-lapse analysis (Fig 2D and E, Appendix Fig S2, Movie EV3 and EV4). Interestingly, the invasion process of WT parasites proceeded with an initial rapid invasion step, followed by a short pause when ~1/3 of the body was inside the host cell, and another acceleration until the parasite was fully inside the host cell (Fig 2D and E, Movie EV3). In contrast, while initial invasion steps appeared to be comparable between WT parasites and mutants for the acto-myosin system (*act1cKO*, *mlc1cKO*, *myoAKO*), an extended period then followed, where parasites stalled (up to 8 min), before invasion continued (Fig 2D and E, Appendix Fig S2, Movie EV4). In some cases, we also observed abortive invasion events, where the invading parasites terminally stalled before being pushed out from the TJ (Fig 2F, Movie EV5). Interestingly, this stalling occurred approximately when the nucleus reached the TJ suggesting that in addition to providing the traction force that promotes entry through the TJ [30], F-actin also assists the passage of the nucleus through the TJ, akin to other eukaryotes when migrating through constricted environments [35].

### F-actin accumulates at the posterior pole and in most cases at the junction

To correlate F-actin dynamics with the invasive behaviour of parasites, we stably expressed F-actin chromobodies in fusion with Emerald FP in *T. gondii* [24] WT and mutant parasites and compared the localisation and dynamics of F-actin when they

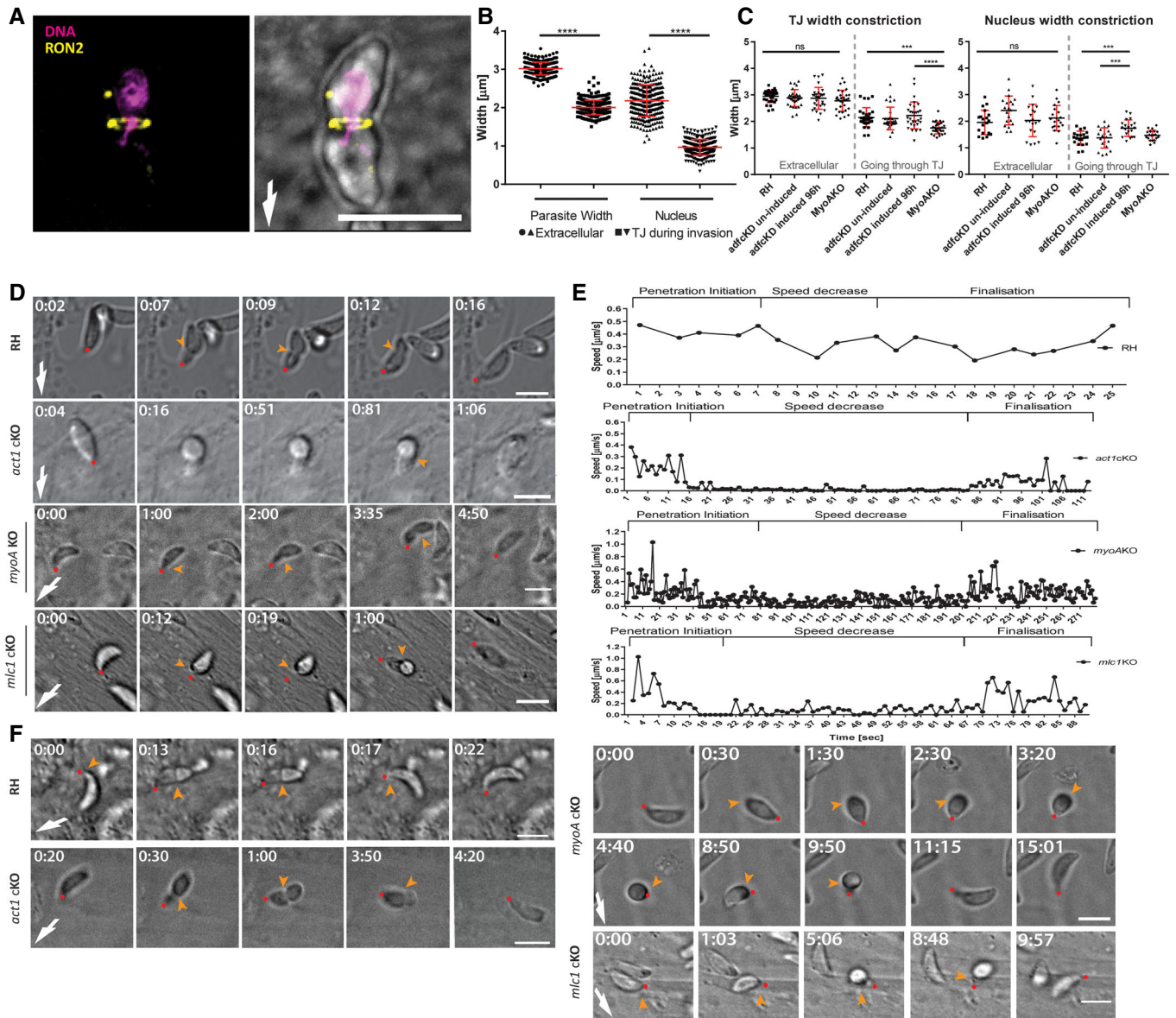


**Figure 2. The nucleus is a limiting factor for host cell invasion.**

- A** Wild-type RH parasites mid-invasion. Tight junction assay was done by allowing freshly egressed parasite to invade for 5 min, fixed with 4% PFA before labelling the TJ with anti-Ron2 (yellow) and DAPI (magenta) for nuclear staining. White arrow points at invasion direction.
- B** Graph showing deformation of the whole parasite and its nucleus between invading and non-invading parasites. 100 parasites found mid-invasion were counted in triplicate and compared to extracellular, freshly egressed parasites. One-way ANOVA was used for statistical analysis. \*\*\*\* $P < 0.0001$ .
- C** Graph showing deformation of the whole parasite and its nucleus between invading and non-invading parasites. Indicated parasites were analysed. For *adf* cKD, induced and non-induced conditions were compared, as indicated. 30 parasites were counted for each condition in triplicate. One-way ANOVA was used for statistical analysis and Tukey's multiple comparison test. \*\*\*\* $P < 0.0001$ . \*\*\* $P < 0.0009$ .
- D** Time-lapse microscopy analysis of indicated parasites invading HFFs cells. Time was determined from the onset of invasion. The time lapse is presented in Movie EV4. White arrow points at invasion direction; yellow arrow points at tight junction; red dot follows the apical pole of the parasite.
- E** Speed profiles of invading parasites shown in (D). The relative displacement of the apical tip over time allowed speed calculations. Individual stages were named in regard to the invasion step (penetration initiation, speed decrease and finalisation). Invasion was analysed with Icy Image Processing Software (Pasteur Institut) using the Manual Tracking plugin by analysing each movie 10 times and averaging the measurements (for additional speed profiles, see Appendix Fig S2).
- F** Time-lapse analysis demonstrating abortive invasion of indicated parasites. Time was determined from the onset of invasion. The time lapse is presented in Movie EV5. White arrow points at invasion direction; yellow arrow points at tight junction; red dot follows the apical pole of the parasite.

Data information: Error bars represent standard deviation. Numbers indicate minutes:seconds, and scale bars represent 5 μm.

Source data are available online for this figure.

invaded the host cells. To ensure specificity of Cb-EmeraldFP for F-actin during the invasion process, we used a previously validated antibody raised against *P. falciparum* actin that preferentially recognises F-actin [15] and compared the staining obtained with this antibody on WT parasites with the staining obtained with Cb Emerald-expressing parasites. In both cases, F-actin accumulation at the junction and the posterior pole was apparent (Appendix Fig S3). Interestingly, while posterior accumulation of F-actin could always (100% of all analysed images) be detected, it was not systematic for the F-actin localised at the junction site (Fig 3A, E and F). We also ensured that the expression of Cb Emerald did not cause any significant differences in the behaviour of parasites during invasion (Appendix Fig S3, see also [24]). Combining live cell and super-resolution microscopy, we were able to identify two situations in WT parasites: in the majority of cases (76%), we detected F-actin forming a ring coinciding with the TJ, while in ~24% of all cases, no significant accumulation was detectable, as confirmed by intensity plots (Fig 3A–C, Appendix Fig S4, Movie EV6). Importantly, genetic interference with actin dynamics led to constrictions/TJ devoid of F-actin at the junction, as seen in the case of *adf* cKD (Fig 3A and B, Movie EV6), demonstrating that F-actin accumulation at the junction requires correctly regulated F-actin dynamics, as suggested previously [31]. Previously, it was shown that WT parasites can enter the host cell through static or capped TJ depending on whether the TJ is respectively firmly or loosely anchored [4]. Analysis of parasites entering the host cell via capping shows F-actin at the TJ (Fig 3A and B, Appendix Fig S4, Movie EV6), confirming the finding that both invasion scenarios rely on the parasite F-actin-based traction force [4].

Although we were unable to accurately quantify F-actin accumulation at the junction, we consistently observed that it increased during the invasion event (Fig 3A, Movie EV6). At the onset of invasion, only a relatively faint F-actin signal could be detected at the apical tip of the parasite, its intensity increasing during invasion, culminating when the parasite invaded to ~2/3. Collectively, while these observations fit well with the contribution of F-actin to the traction force applied at the TJ, the amount of invasion for which we could not detect F-actin at the TJ (25% show no F-actin ring) is close to the fraction of residual invasiveness detected for mutants for the acto-myosin system, such as shown in independent studies for mutants for *act1*, *mlc1*, *myoA*, *myoH*, *GAP45* and *adf* [11,36–38]. Together, these observations suggest that interference with either MyoA or actin dynamics results in a reduction of parasite invasion in line with the absence of an F-actin ring at the entry point.

While time-lapse analysis of invasion events allowed documenting the dynamics of F-actin at the junction and posterior pole of the parasite, this analysis remained limited by insufficient resolution. Therefore, we decided to obtain higher resolution images using fixed assays to confirm the observed variability in F-actin accumulation at the junction. We quantified F-actin at the junction and the posterior pole using a modified red-green assay based on differential immunolabelling [39]. Invading parasites expressing Cb-EmeraldFP were labelled with SAG1 (non-invaded part of the parasite) and Ron2 (TJ-marker). We confirmed that in all cases, parasites entered the host cell via a TJ, as indicated by positive Ron2 staining (Fig 3D).

In good correlation with live imaging analysis, we detected a F-actin ring at the TJ in ~80% of RH parasites, leaving ~20% of the events where the presence of an F-actin ring remained

questionable in fixed samples (Fig 3D and E). In contrast, in all invading parasites, a posterior accumulation of F-actin was apparent (orange arrow, Fig 3D and F). In the case of *adf* cKD, which showed a reduced invasion rate of ~20% compared to WT parasites, no F-actin ring at the junction was obvious in any invasion event (red arrowhead, *adf* cKD panel, Fig 3D and E), while the posterior accumulation was still maintained (orange arrow, Fig 3D and F). As expected, no F-actin at the junction or at the posterior pole of the parasite was detectable in *act1* cKO parasites and only a cytosolic signal for Cb-EmeraldFP was apparent (Fig 3A, D, E and F). Similar to *adf*cKD, an overall invasion rate of ~20% compared to WT parasites was detected for *act1*cKO parasites, as described previously [9], despite the posterior, aberrant morphology described previously [7,9] (green arrow, Fig 3D). Interestingly, in the case of *myo*AKO parasites, we found (similar to *adf*cKD and *act1*cKO) an invasion rate of ~20% compared to WT parasites, confirming previous results [9,16,40]. However, disruption of *myoA* resulted in loss of F-actin accumulation at both the junction site and the posterior pole, demonstrating that MyoA is the main motor required for retrograde F-actin flow during host cell invasion. Interestingly detectable F-actin appears to be equally distributed within the cytosol of the parasite and at the periphery of the parasite (Fig 3D–F), confirming the data obtained for extracellular parasites (Fig 1).

Together, these data confirm that an intact acto-myosin system is required for efficient host cell invasion and that the accumulation of F-actin at the posterior pole can occur independently of its accumulation at the junction, suggesting two independent processes, both dependent on MyoA-motor activity and F-actin dynamics. At this point, our analysis does not allow to pinpoint how F-actin dynamics driven by a Glideosome localised between the IMC and PM is coordinated and connected with the changes in F-actin dynamics observed within the cytosol of the parasite. One potential explanation could be that both processes are regulated by the same signalling cascades, which is supported by the actin flow analysis shown above (Fig 1).

In analogy to other eukaryotes migrating through a constricted space, where the nucleus represents a major obstacle that needs to be deformed, squeezed and pushed through the constriction [35], we speculated that the nucleus of the parasite represents a major limitation for invasion that needs to be forced through the junction.

### Posterior localised F-actin assists nuclear entry

We next simultaneously visualised F-actin dynamics and the position and shape of the nucleus using time-lapse imaging (Fig 4). We confirmed that the accumulation of F-actin at the junction became most prominent, once the nucleus reached the junction (orange arrow, Fig 4A, Movie EV7). Interestingly, in the vicinity of F-actin located at the parasite posterior pole, we observed a cup-like meshwork around the nucleus close to the junctional F-actin ring (blue arrow, Fig 4A, Movie EV7). Once the nucleus reached the junction, it became constricted and deformed when the F-actin ring is visible, (see red arrowhead 0:15–0:21, Fig 4A and B). When no F-actin ring was detectable (Fig 4B), the shape of the nucleus remained relatively constant (red arrows, Fig 4D and E). However, independently of F-actin ring formation, the posterior pole of the parasite contracted (blue arrows in Fig 4A and D; Movie EV7) prior or coinciding with nuclear entry, which was also confirmed by measuring

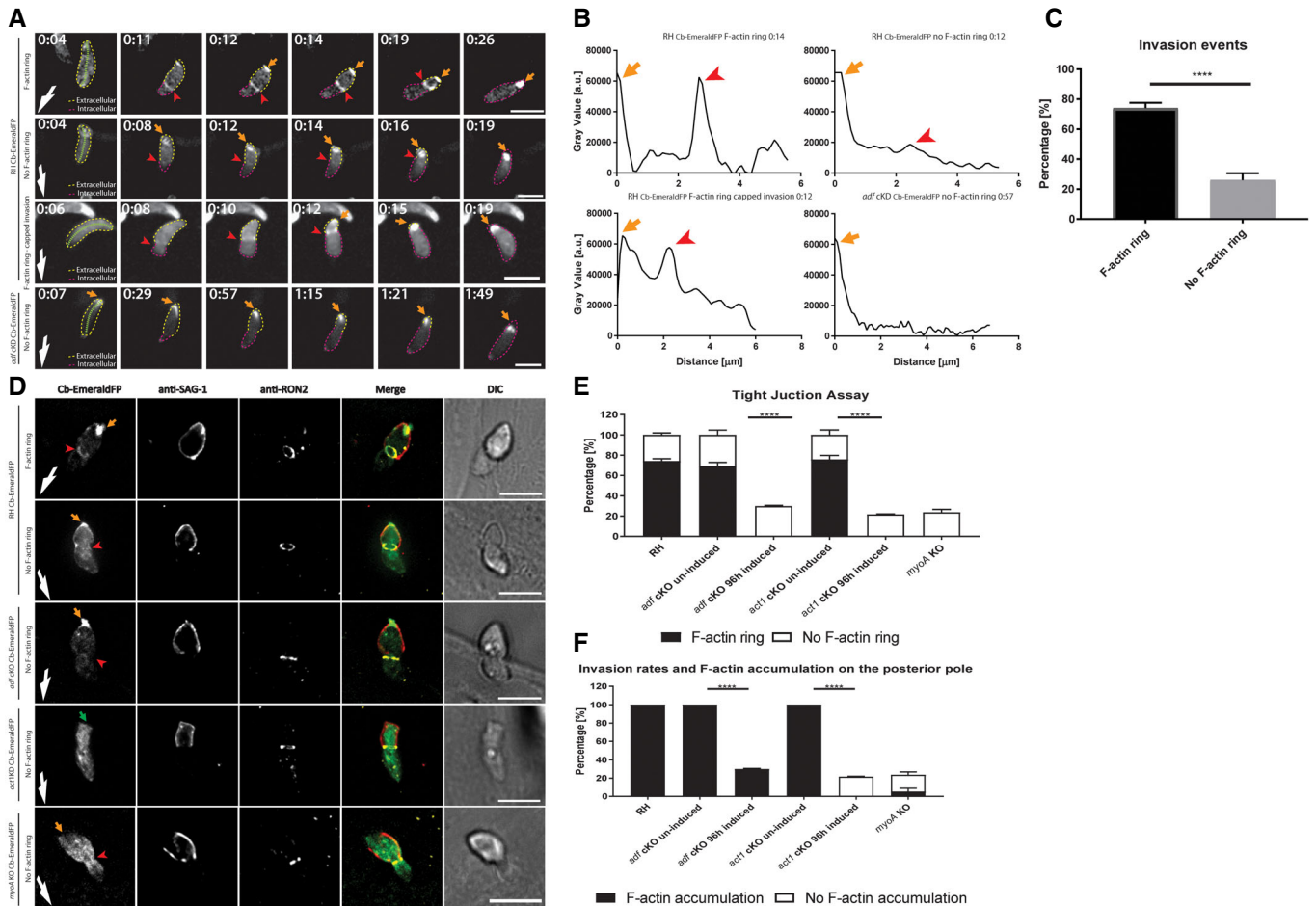


**Figure 3. F-actin dynamics during *Toxoplasma gondii* invasion during fixed and live imaging.**

- A** Time-lapse analysis depicting invading RH *adf cKD* parasites expressing Cb-EmeraldFP. A F-actin ring can be observed at the TJ in the majority of cases (red arrowheads, first panel). Invasion can also occur without formation of an F-actin ring (second panel). During capped invasion, an F-actin ring is formed (third panel). Invasion of *adf cKD* parasites occurs without formation of an F-actin ring (fourth panel). F-actin accumulation is observed at the posterior pole of the parasite in all cases (orange arrows). Green segmented lines depict the area that was measured for generation of intensity plot profiles shown in (B). Yellow and purple dotted lines indicate the extra- and intracellular part of the parasite, respectively. The time lapse is presented in Movie EV6.
- B** Intensity plot profiles of the movies shown in (A). Depicted plots correlate to half-invaded parasites. In the case of F-actin ring formation, two distinct peaks are detected, correlating to the F-actin ring at the TJ (red arrowhead) and the posterior pole of the parasite (orange arrow). In the case of no F-actin ring, no accumulation at the TJ can be observed; only the peak correlating to posterior F-actin can be detected. For *adf cKD*, only one peak can be seen corresponding to the posterior pole of the parasite.
- C** Quantification of F-actin accumulation at the TJ for RH Cb-EmeraldFP parasites as detected in time-lapse analysis. The values are expressed as percentage. 28 total parasite invasion events were captured across three different biological replicates. Two-tailed unpaired *t*-test analysis was performed. \*\*\*\* $P < 0.0001$ .
- D** Representative immunofluorescence assays on indicated parasite strains during host cell penetration. Parasites were labelled with indicated antibodies. SAG1 staining was performed prior to permeabilisation to stain only the extracellular portion of the parasite. Antibodies against Ron2 were used to stain the TJ. Red arrowhead: position of the TJ. Orange arrow: posterior pole of the parasite.
- E** Tight junction assay on fixed samples (as shown in (D)) depicting invasion rates of indicated parasites. While in the majority of control parasites, F-actin can be detected at the junction (~80%), no junctional ring can be detected in ~20% of all invasion events. In contrast, *adf cKD*, *act1 cKD* or *myoA KO* only shows an overall invasion rate of ~20% compared to controls. In these cases, junctional F-actin accumulation could never be detected. Note that the number of total invasion events for *adf cKD*, *act1 cKD* and *myoA KO* correlates to the number of invasion events, seen for RH without F-actin ring formation.
- F** Quantification of posterior F-actin accumulation during invasion of indicated parasite lines.

Data information: Error bars represent standard deviation. White arrows point to direction of invasion. Scale bars represent 5  $\mu\text{m}$ . One-way ANOVA was performed for each graph in (E, F). \*\*\*\* $P < 0.0001$ .

Source data are available online for this figure.

the diameter of the posterior pole of the parasite during the invasion process (Fig 4C and F).

We then imaged the nucleus of *myoA KO* parasites over their residual host cell invasion (Fig 4G). Since the MyoA-motor-complex

is known to generate the required traction force at the TJ [10], we interpret these data as if optimal entry by WT parasites results from a coordinated mechanism, requiring the Glideosome, acting below the surface of the parasite [6], together with

cytosolic localised F-actin accumulating at the posterior pole and surrounding the nucleus. In good support, when no F-actin was detectable at the junction, indicating independence of traction

force generated at the junction, posterior accumulation of F-actin adjacent to the nucleus was still seen during invasion (Fig 4D–F, Movie EV7).

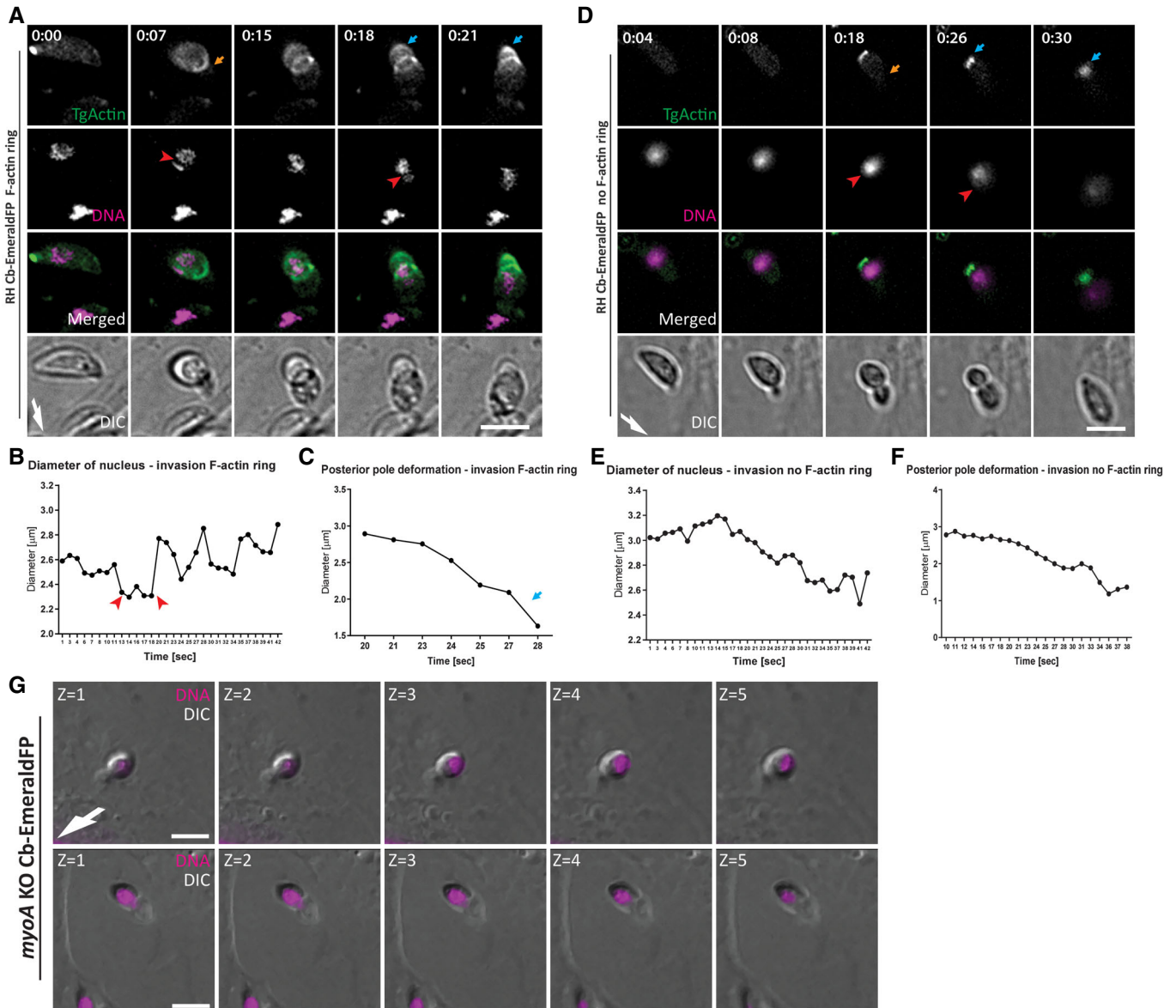


**Figure 4. Time-lapse analysis of F-actin and nuclear dynamics during host cell invasion.**

- A Time-lapse analysis of invading RH Cb-EmeraldFP parasites. During penetration, an F-actin ring is formed at the TJ (orange arrow). The nucleus (purple) is squeezed through the TJ (red arrowhead), and posterior F-actin appears to be directly connected to the nucleus and TJ (blue arrow). The time lapse is presented in Movie EV7.
- B Analysis of nucleus deformation during live imaging shown in (A). The nucleus constricts while it is passing through the TJ (red arrowheads).
- C The posterior end of the parasite deforms during the invasion process. F-actin is accumulated during invasion, with the posterior end contracting (blue arrow).
- D Time lapse stills depicting RH Cb-EmeraldFP parasites invading in the absence of detectable F-actin at the junction (orange arrow). The nucleus (purple) is squeezed through the TJ (red arrowhead) during invasion. Actin accumulation at the posterior pole of the parasite is strongly detected in all cases (blue arrow). The time lapse is presented in Movie EV7.
- E Analysis of nucleus deformation during live imaging shown in (D). The nucleus appears to not show constriction once it is passing through the TJ when the F-actin ring is not present.
- F The posterior end of the parasite also deforms during the invasion process.
- G Z-stack gallery depicting mid-invading *myoA* KO parasites. Note that the nucleus is located at the back during invasion events.

Data information: Numbers indicate minutes:seconds. Scale bar represents 5 μm. White arrow points to direction of invasion. Source data are available online for this figure.

### F-actin forms a continuous network between the junction and the posterior accumulation that surrounds the nucleus

We applied super-resolution structured illumination microscopy (SR-SIM) to analyse the distribution of F-actin in WT parasites that were at the mid of invasion and found consistently that the nucleus of the parasite is surrounded by F-actin that formed a continuous meshwork connected to the posterior pole of the parasite (Fig 5A–D). Importantly, this meshwork could be observed independently of F-actin accumulation at the junction but broke down upon disruption of *adf* and was significantly reduced in the case of *myoAKO* parasites (Fig 5A and D Movie EV8). The perinuclear F-actin meshwork formed a continuum with the posterior accumulation (Fig 5B). Finally, 3D models demonstrated that F-actin is perinuclear and can be observed in ~60% of all cases in WT parasites, while it is significantly reduced in *myoAKO* (~20%) and absent in *adfKD* parasites (Fig 5D).

In most migrating cells, the nucleus is positioned in the back, which requires the coordinated action of posterior F-actin as well as anterior microtubules, resulting in positioning of the nucleus by a pull-and-push mechanism driven by the interplay of an acto-myosin complex, actin-nucleus interface proteins and other cytoskeletal structures [28]. In the case of *T. gondii*, the subpellicular microtubules are polymerised from microtubule organising centres at the apical tip, aligned on the cytosolic side of the IMC, where they directly interact with gliding-associated membrane proteins, which are components of the Glideosome (GAPMs [22]). This subpellicular microtubules form a basket that covers ~2/3 of the parasite length. Furthermore, it was previously suggested that parasite F-actin can interact with the subpellicular microtubules [19,21], leading to the question if the basally localised meshwork consisting of F-actin might interact with the apically localised subpellicular microtubules during invasion. Therefore, we assessed the location of microtubules (MTs) during invasion by the use of SiR-tubulin [41]. The MTs cover 2/3 of the parasite body creating a rigid structure starting from the apical tip (Fig 5E–M; Movie EV9). During invasion, this MT structure appears to be significantly deformed, with several examples detected, where MTs seem to colocalise in a positive correlation with junctional F-actin (white arrows in Fig 5; Pearson's coefficient and white marker in 3D rendering Appendix Fig S5). Furthermore, MTs appear frequently bent and distorted at the junction. Interestingly, this polarisation with F-actin at the posterior end and microtubules at the leading edge is maintained throughout the invasion process, from early to late stage (Fig 5). In some cases, the MTs extended far beyond the 2/3 parasite body, aligning the nucleus (white arrow, Fig 5). The microtubules closely align to the part of the nucleus that enters through the TJ (orange arrowheads), while F-actin closely aligns to the posterior part of the nucleus (green arrowheads), resulting in a highly polarised cytoskeletal organisation around the nucleus (Appendix Fig S5; Movie EV9). It is plausible that akin to other eukaryotes, a coordinated action of microtubule and F-actin-based mechanisms supports nuclear entry and deformation through the TJ (Appendix Fig S6A and B). In good agreement with this hypothesis, a positive correlation between microtubules and actin colocalisation during the invasion process is observed for WT parasites, but not *myoAKO* or *adfKO* (Figs 5 and Appendix Fig S6A). This basic organisation is also maintained in those cases, where no F-actin accumulation is detectable at the junction (Fig 5G).

Upon interference with actin dynamics (*adfKO*) or the Glideosome (*myoAKO*), this organisation is disrupted (Appendix Fig S6B). In case of ADF depletion, posterior accumulation of F-actin is still apparent (green arrowheads, Fig 5K–M), but no F-actin meshwork around the nucleus, connecting to subpellicular microtubules, is detectable (orange arrowheads, Fig 5K–M), while microtubules and actin colocalise at the apical tip of the parasite (Appendix Fig S6B). In contrast, disruption of MyoA results in a dominant arrangement of F-actin throughout the cytosol with no accumulation at the posterior pole of the parasite or formation of perinuclear F-actin (Fig 5H–J), again suggesting that there is a tight coordination of Glideosome function in between the PM and IMC and the formation of the cytosolic localised meshwork around the nucleus. It is also noteworthy that F-actin accumulates in the region of the TJ (green arrowheads) when compared to the rest of the cell, where it shows a good colocalisation with microtubules (Appendix Fig S6B).

In summary, the combined data from fixed invasion assays and SR-SIM imaging allow documenting that the parasite's nucleus is surrounded by a F-actin meshwork and that its formation and coordination might depend on subpellicular microtubules. Here, F-actin appears to adapt a cytoskeletal conformation designed to protect, deform and push the nucleus inside the host cell and we propose that during invasion, the Glideosome provides the traction force for general movement of the parasite through the TJ, while perinuclear actin is important in order to facilitate nuclear entry.

### Perinuclear F-actin is detected during invasion of Plasmodium merozoites

While *T. gondii* is a relevant model to address general questions in apicomplexan biology, we previously observed differences in the role of F-actin during the asexual life cycles of *T. gondii* and *P. falciparum*, the causative agent of human malaria. For instance, in case of *P. falciparum*, invasion is dependent on parasite F-actin [42], while in the case of *T. gondii*, residual invasion can be observed. To analyse the role of F-actin during merozoite invasion, we expressed CB-Halo and Cb-EmeraldFP in *P. falciparum* and validated their efficiency to analyse F-actin localisation and dynamics in this parasite (see also [25]). Invasion assays and localisation analysis of F-actin during merozoite invasion showed a similar distribution of F-actin at the junction, around the nucleus and at the posterior pole of the parasite in 100% of all analysed images ( $n > 100$ ) (Fig 6A and C). We also analysed F-actin localisation during the invasion of *P. knowlesi* merozoites using a previously described antibody [15] that preferentially recognises *P. falciparum* F-actin and obtained identical results (Fig 6B). Fixed immunofluorescence imaging of merozoites in the process of invasion was analysed for the distribution of F-actin. As with *T. gondii*, F-actin can be detected at the junction, at the onset of invasion (Fig 6) pointing to a similar strategy between apicomplexan parasites. Importantly, super-resolution imaging of F-actin in merozoites in different stages of invasion clearly highlights the accumulation of F-actin at the posterior pole and in direct contact with the nucleus (Fig 6C). Quantification of invasion events demonstrated that in over 80% of cases, a close actin–nucleus association can be detected (Fig 6D) and, in over 90% of cases, actin was accumulated at the TJ (Fig 6D).

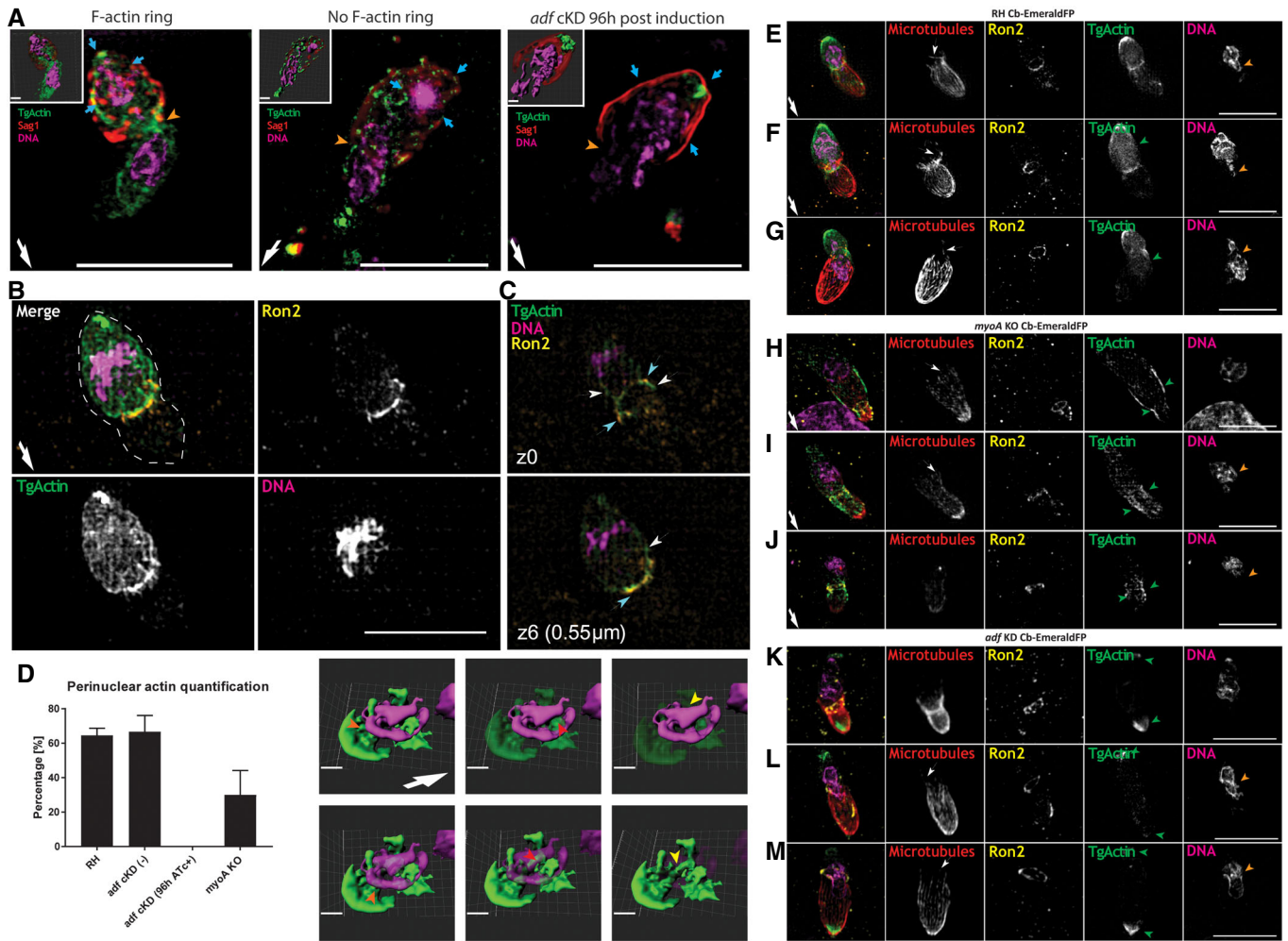


**Figure 5. Super-resolution microscopy demonstrates formation of a F-actin cage around the nucleus during invasion.**

**A** SR-SIM images depicting invading parasites with and without the presence of the F-actin ring at the tight junction and invading *adfcKD* Cb-EmeraldFP parasites. SAG1 staining (in red) was performed prior to permeabilisation to specifically label extracellular part of the parasite. Note the accumulation of actin (blue arrow) around the nucleus and the posterior pole of the parasite, irrespective of F-actin ring formation at the TJ (orange arrowhead). 3D rendering is shown for each presented case (inlet). 3D rendering is presented in Movie EV8.

**B** SR image of an invading parasite before nuclear entry. F-actin forms a continuous meshwork around the nucleus that appears connected to the posterior pole.

**C** F-actin localisation in relation to the TJ during invasion. F-actin (white arrow) is in close vicinity to the Ron2 ring (light blue arrow) during invasion.

**D** Quantification of perinuclear actin in indicated parasites. Parasites were counted by assessing Cb-EmeraldFP signal as an actin marker around or in the vicinity of the nucleus. Still images to the right represent what was considered as F-actin–nucleus association. The orange arrowhead points to F-actin surrounding the nucleus in the posterior end of the parasite, and the red and yellow arrowhead shows F-actin in the vicinity of the nucleus, hinting at a close interaction between the two. Three biological replicates were analysed with a minimum of 25 parasites per replicate.

**E–G** SR-SIM images showing three stages of invading wt parasites. SiR-tubulin staining for microtubules (in red) was performed prior to fixation to specifically label microtubules in the parasite. During invasion, the microtubules (MT) are deformed at the TJ area (white arrowhead). The accumulation of actin (green arrow) at the posterior forms a F-actin meshwork. The nucleus is deformed when it enters the TJ area (orange arrowhead). These images are expanded with additional panels in Appendix Fig S5. 3D rendering is presented in Movie EV9.

**H–J** In the case of the *myoA* KO strain, the MTs also deform when passing through the TJ (white arrowhead). However, F-actin is not concentrated at the posterior pole or the TJ, but evenly distributed within the cytosol of the parasite, with some peripheral location.

**K–M** In case of *adfcKD*, MTs are deformed at the TJ area (white arrowhead). F-actin is accumulated at both ends of the parasite (green arrowheads), with no accumulation at the TJ.

Data information: Error bars represent standard deviation. Scale bar represents 5  $\mu$ m for SR-SIM images and 1  $\mu$ m for 3D models. White arrow points to direction of invasion.

Source data are available online for this figure.

## Discussion

Host cell invasion by apicomplexan parasites occurs through a tight junctional ring (TJ), established by the parasite upon secretion of its

rhoptry content [3]. Previous studies demonstrated that the TJ is anchored to the host cell cortex via its interaction with host cell factors [5,43] thereby acting as an anchor for traction force exerted by the parasites acto-myosin system [10]. In addition, compressive

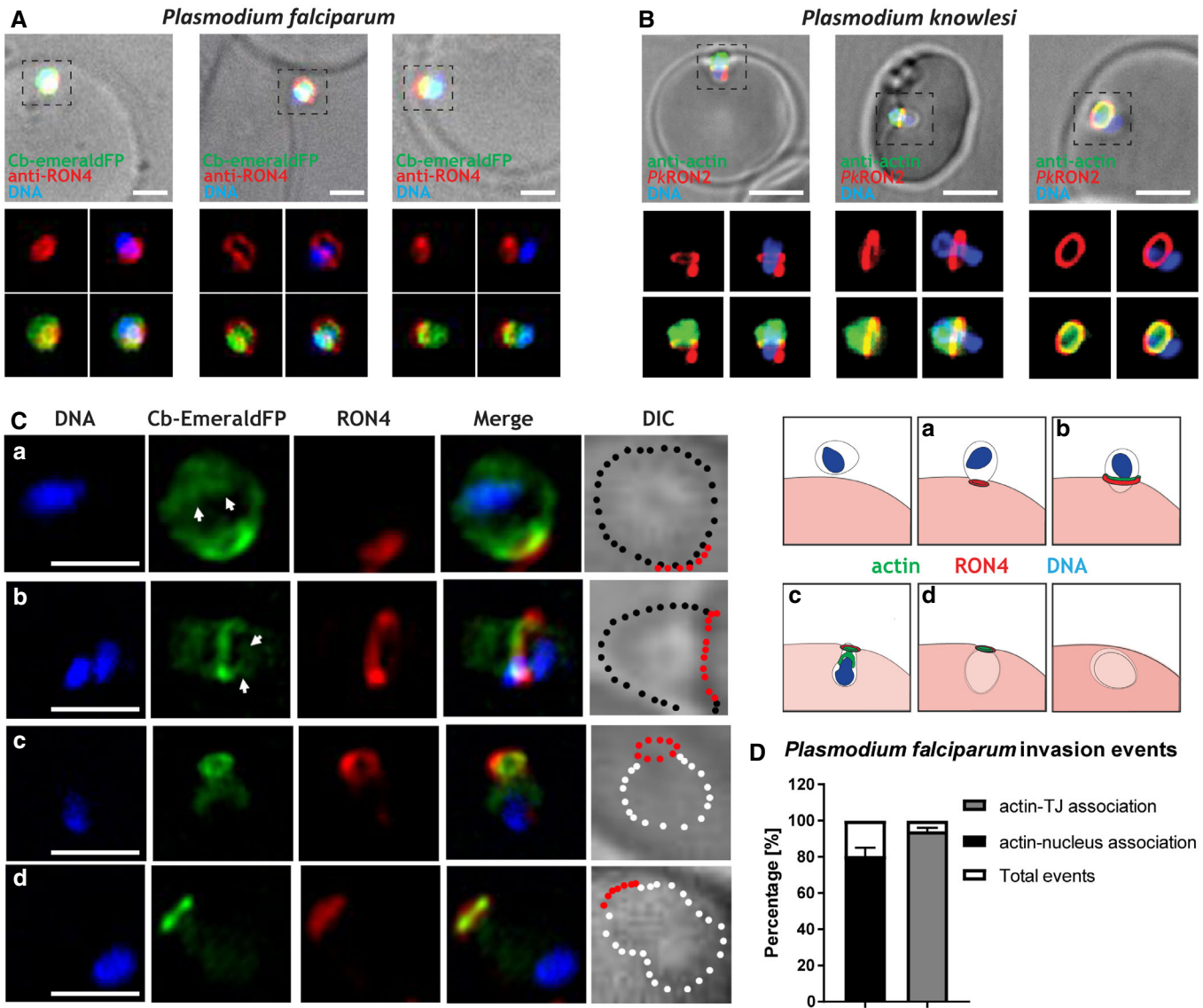


**Figure 6.** *Plasmodium* F-actin localisation during invasion.

- A** Different invasion stages of *P. falciparum* merozoites expressing Cb-EmeraldFP. DAPI labels the nucleus (DNA), Cb-EmeraldFP labels actin filaments (CB-EME, green), and anti-RON4 labels the junction (red). Left panel: onset of invasion. Middle panel: a merozoite in the middle of invasion; note the constriction of the nucleus (blue) as it passes through the RON4 junction and F-actin colocalising with it (green). Right panel: a merozoite completing invasion; note the F-actin ring beyond the RON4-junction and actin filaments surrounding the nucleus.
- B** IFA showing various stages of invasion of erythrocytes by *P. knowlesi* merozoites. DAPI labels the nucleus (DNA), anti-actin antibody labels actin filaments (anti-actin, green), and the invasion junction is marked with a C-terminally tagged *PkRON2* mCherry-HA (red). Left panel: a merozoite beginning invasion; note the formation of an F-actin ring (green) behind the *PkRON2* junction (red). Middle panel: a merozoite in the middle of the invasion event; note the constriction of the nucleus (blue) as it passes through the *PkRON2* junction and F-actin colocalising with it (green). Right panel: a merozoite completing the process of invasion; note the F-actin ring beyond the *PkRON2*-junction and actin filaments colocalising with the nucleus.
- C** Super-resolution images showing various stages of invasion of erythrocytes by *P. falciparum* merozoites expressing Cb-EmeraldFP. Left panel: DAPI labels the nucleus (blue), Cb-EmeraldFP labels actin filaments (CB-EME, green), and the invasion junction is marked with an anti-RON4 antibody (red). Brightfield images have been marked with red dots depicting the junction, black dots depicting merozoite boundary still outside the erythrocyte and white dots depicting a merozoite that has penetrated the host cell. Top panel shows an attached merozoite beginning the process of invasion, the second panel during the process of invasion, and the bottom two panels show merozoites completing the process of invasion. Right panel: schematic depicting merozoite invasion into red blood cells. Letters depict the corresponding event in the model (left) and microscopy pictures (right). White arrows depict actin filaments that colocalise with the nucleus.
- D** Quantification of *Plasmodium falciparum* invasion events categorising actin-TJ and actin-nucleus association events. 121 events were counted in total.

Data information: Error bars represent standard deviation. Scale bar represents 1  $\mu\text{m}$  for *Plasmodium falciparum* and 3  $\mu\text{m}$  for *Plasmodium knowlesi*.

Source data are available online for this figure.

forces, caused by the host cell at the TJ, require the deformation of the parasite during invasion, which appears to be counterbalanced to ensure integrity of the parasite [10]. In fact, the invasion of host cells through the TJ appears in many aspects very similar to the migration of eukaryotic cells through a constricted environment, with impressive morphological changes observed at the point of constriction [44]. Here, the nucleus represents a physical barrier for migration that requires to be modulated, deformed and protected in order to be squeezed through the constriction [35]. During migration through a constricted space, rapid actin nucleation around the nucleus facilitates nuclear deformation and protection. Furthermore, proteins that interface actin and the nucleus such as the family of LINC (Linker of Nucleoskeleton and Cytoskeleton) proteins allow the formation of intricate perinuclear F-actin structures connected to microtubules and other cytoskeletal elements that support nucleus translocation, mechanotransduction and protection [45,46].

In apicomplexan parasites, a similar function of F-actin was initially ruled out based on the assumption that F-actin acts exclusively within the narrow space between the PM and IMC, where the Glideosome is localised [2]. However, the finding that the majority of F-actin dynamics appears to occur within the cytosol of the parasite in extracellular parasites, and the fact that host cell invasion is significantly slowed down once the parasite's nucleus reaches the TJ and is usually blocked at this stage in the case of mutants for the acto-myosin system, led us to the hypothesis that parasite F-actin serves a second role during invasion, namely the facilitation of nuclear entry, akin to other eukaryotes, where a squish and squeeze model has been proposed [28].

To test this hypothesis, we performed a careful analysis of WT parasites and mutants for core components of the acto-myosin system and correlated their phenotypes with the observed changes in F-actin dynamics in extracellular and invading parasites, using quantitative imaging approaches allowing us to describe the dynamics of F-actin during host cell invasion. We used a combination of real-time and super-resolution microscopy to demonstrate that the nucleus is indeed a major obstacle that needs to be overcome for successful invasion. In good agreement, mutants of the acto-myosin system demonstrate an extended pause during invasion, as soon as the nucleus reaches the junction. In all cases, parasites accumulate F-actin at the posterior pole during invasion, which forms a continuous meshwork with perinuclear F-actin. In contrast, F-actin accumulation at the junction is not always observed during the invasion process, suggesting that the Glideosome activity is fine-tuned, depending on the force required for host cell penetration. Importantly, F-actin accumulation at the posterior pole can occur independently from F-actin accumulation at the junction, suggesting the action of two independent pools of F-actin that contribute to invasion and nuclear entry. Finally, we demonstrate that parasite F-actin and subpellicular microtubules form a highly polarised cell during invasion, with the subpellicular microtubules at the leading edge and F-actin at the posterior pole, raising the question if a tight and controlled coordination of these two cytoskeletal elements facilitates host cell invasion.

While the interplay between the F-actin and microtubule cytoskeleton of the parasite needs to be further analysed, it is interesting to note that deletion of *myoA*, the core motor of the Glideosome [40], results in complete loss of F-actin polarity and an even distribution of F-actin in the cytosol of the parasite, with some peripheral accumulation during motility and invasion. This indicates

a tight interlinkage of F-actin dynamics occurring in between the PM and IMC and controlled by the action of the Glideosome with the F-actin dynamics observed within the cytosol of the parasite. This is also reflected, by the fact that F-actin dynamics originating from the apical tip of the parasite, potentially by Formin-1 and translocated via MyoH [11] and close to the Golgi by Formin-2 [11,25] forms a continuous network that appears to be interlinked and demonstrates bidirectional F-actin flow. Interestingly, stimulation of calcium signalling with either A23187 or BIPPO resulted in preferential F-actin flow towards the basal end of the parasite. Surprisingly, F-actin dynamics in unstimulated *myoAKO* parasites is identical to WT parasites, but upon stimulation, F-actin relocation to the basal pole appears to be blocked and remains “stuck” in the first half of the parasite, demonstrating that the Glideosome is required for efficient relocation of the whole F-actin pool and that both processes are tightly interlinked. Although a more in depth analysis of the myosin machinery could provide more evidence of the interplay of actin dynamics, only MyoA and MyoH have been implicated in invasion. However, MyoH mutants were shown to be unable to initiate invasion [23], making it impossible to study the role of this myosin for parasite and nuclear entry.

Analysis of host cell invasion demonstrated that F-actin can be found at the TJ in most cases and—as expected—disruption of MyoA, ADF or Act1 results in highly reduced invasion rates, where no F-actin can be detected at the TJ. It remains to be seen, if the F-actin ring is formed in order to stabilise the junction to counteract pressure exerted by the host cell [10] or if the activity of the Glideosome can be modulated, depending on the necessity to provide the traction force to facilitate entry of the parasite. Collectively, while these observations fit well with the contribution of F-actin to traction force applied at the TJ, the amount of invasion for which we could not detect F-actin at the TJ (25% show no F-actin ring) equalled the fraction of residual invasiveness detected for mutants for the acto-myosin system, such as shown in independent studies for mutants for *act1*, *mcl1*, *myoA*, *myoH*, *GAP45* and *adf* [7,9,11,31,36–38,40].

A similar situation is seen for the formation of filamentous actin structures in close proximity to the nucleus during host cell invasion, with most parasites demonstrating the formation of an F-actin meshwork around the nucleus appearing as perinuclear actin structures. Again, disruption of the acto-myosin system causes disruption of this meshwork, demonstrating a tight interplay between Glideosome function and formation of perinuclear actin. In contrast, in all cases, F-actin is seen to accumulate at the basal pole of the parasite during invasion, which is connected to the perinuclear meshwork (if formed during invasion). Finally, live imaging analysis indicates that the basal end of the parasite contracts during host cell entry, potentially forcing the nucleus through the junction.

In most migrating cells, the nucleus is positioned in the back, which requires the coordinated action of posterior F-actin as well as anterior microtubules, resulting in positioning of the nucleus by a pull-and-push mechanism driven by the interplay of an acto-myosin complex, actin-nucleus interface proteins and other cytoskeletal structures such as intermediate filaments and microtubules [28]. In the case of *T. gondii*, the subpellicular microtubules are polymerised from microtubule organising centres at the apical tip, aligned on the cytosolic side of the IMC, where they directly interact with components of the Glideosome, such as the gliding-associated membrane

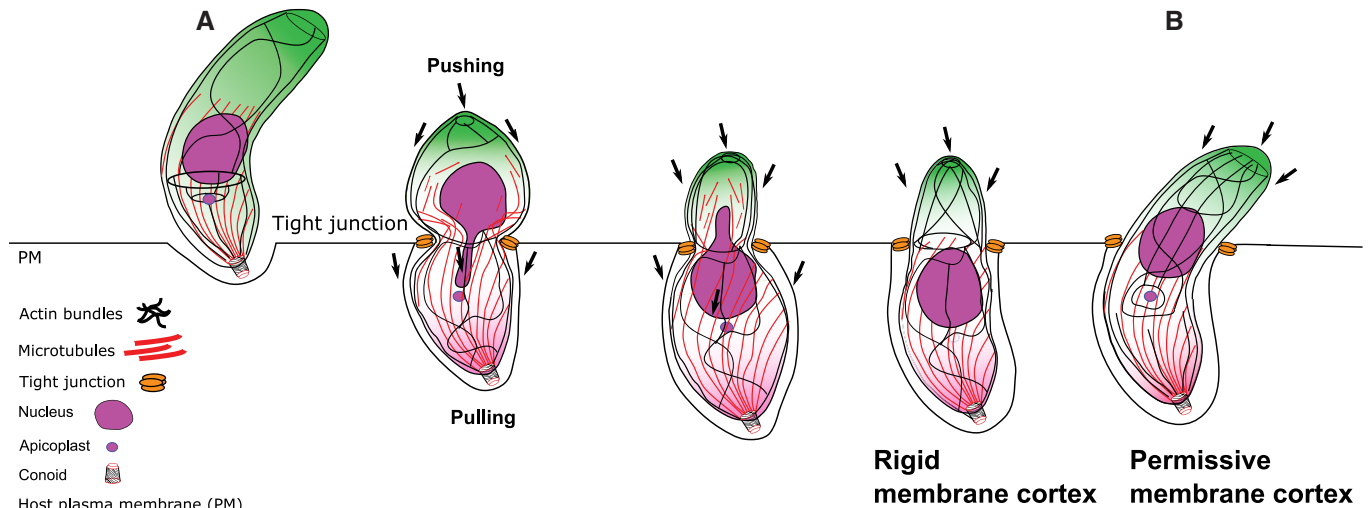


**Figure 7. Model of the proposed nuclear squeeze mechanism during apicomplexan invasion.**

- A Once the parasite attaches to the surface of a host cell, F-actin strongly accumulates at the posterior pole and at the apical end. During penetration, the junctional complex is formed that contributes to the attachment and stabilisation of the parasite to the host cell in the TJ. F-actin at the TJ provides traction force and stability for nuclear entry, while posterior F-actin provides contraction force to allow nuclear entry. At the same time, microtubules might facilitate nuclear entry by pulling. We propose that the nucleus is squeezed through the TJ by a pushing–pulling mechanism controlled by actin and potentially microtubules.
- B In some cases (e.g. due to more permissive host cells or upon modulation of F-actin dynamics), a F-actin ring at the junction is not required/formed and the nucleus can enter the host cell by the action of posterior accumulated F-actin.

proteins (GAPMs [22]). Indeed, it was previously suggested that parasite F-actin can interact with the subpellicular microtubules [19,21], leading to the question if the posterior localised meshwork consisting of F-actin might interact with the apically localised subpellicular microtubules during invasion to form a highly polarised cellular network, as seen in Figs 5 and Appendix Fig S5. Further studies are required to analyse the linkage of these two cytoskeletal elements as subpellicular microtubules could function as stabilisers of cell shape but could be also involved in force generation during invasion.

Together, these results permit us, for the first time, to reconcile discrepancies in the phenotypic invasion characteristics of apicomplexan parasites with F-actin imaging data and to propose a new model for actin's contribution during host cell invasion, in particular nuclear entry through the TJ when F-actin accumulation is present in the TJ (Fig 7A). In other cases where F-actin was not detected, we hypothesise a more permissive host cell membrane cortex is encountered upon invasion that facilitates parasite's entry, thus reducing the force required for entry (Fig 7B). While the IMC-localised acto-myosin motor complex provides traction force at the TJ to initiate and facilitate rapid cell invasion, the entry of the parasite nucleus into the host cell appears to be a major limiting step that requires direct action of a cytosolic acto-myosin system, possibly also involving the subpellicular microtubules in order to be deformed, protected and pushed into the host cell (Fig 7A).

## Materials and Methods

### Plasmid construction

The same procedure was carried out as described previously [24]. The Cb-EmeraldFP plasmid consists of a sequence encoding actin

chromobody (Cb) from Chromotek followed downstream by an in-frame sequence encoding EmeraldFP. The vector backbone contains a *DHFR* promoter for protein expression without drug resistance genes. To create Cb-EmeraldFP, the EmeraldFP coding sequence was amplified using primers (EmeraldFP-F: atgcaccggtatgggactcgt-gagcaaggg and EmeraldFP-R: atgccttaagtactgtacagctcgtcca). The EmeraldFP PCR product plasmid was subcloned using traditional restriction digestion/ligation protocols.

### Culturing of parasites and host cells

Human foreskin fibroblasts (HFFs) (RRID: CVCL\_3285, ATCC) were grown on tissue culture-treated plastics and maintained in Dulbecco's modified Eagle's medium (DMEM) supplemented with 10% foetal bovine serum, 2 mM L-glutamine and 25 mg/ml gentamicin. Parasites were cultured on HFFs and maintained at 37°C and 5% CO<sub>2</sub>. Cultured cells and parasites were regularly screened against mycoplasma contamination using the LookOut Mycoplasma detection kit (Sigma) and cured with Mycoplasma Removal Agent (Bio-Rad) if necessary.

### *Toxoplasma gondii* transfection and selection

To generate stable Cb-EmeraldFP expressing parasites,  $1 \times 10^7$  of freshly released RH  $\Delta$ *hxgprt* parasites and *adf* cKO were transfected with 20 µg DNA by AMAXA electroporation. Transfected parasites were then sorted using flow cytometry with a S3 Cell Sorter (Bio-Rad, Hercules, CA, USA).

To create Myo-SNAP vector, PMyoA-Ty-MyoA [9] was used as a template backbone and the Ty sequence replaced in frame with a sequence encoding SNAP from plasmid template SNAP (NEB) amplified with primers FWSNAP 5'TAATGAATTCCGACAAAA

TGGACAAAGACTGCGAAATGA3' and RVSNA5' TAATATGCATAC CCAGCCAGGCTTGCCAG3'.

### Merozoite isolation

PkRON2\*mCherry-HA A1-H.1 merozoites were isolated as described [47]. In brief, ring-stage parasites were tightly synchronised to a 3.5 h and allowed to develop to schizont stage. Schizonts were separated from uninfected erythrocytes by MACS magnet separation (CS column, Miltenyi Biotec). Parasites were returned to complete media at 37°C and incubated with 10 µM E64 (Sigma-Aldrich) for < 4 h. Schizonts were pelleted (850 g, 5 min) and resuspended in incomplete media and merozoites purified by 3 µm filtration (Whatman) immediately followed by 2 µm filtration (Whatman).

### Inducing the conditional *LoxPact1* cKO

The inducible *act1* cKO was obtained by the addition of 50 nM rapamycin to the parental *LoxPact1* strain for 4 h at 37°C, 5% CO<sub>2</sub> and cultured as described previously [9].

### Inducing the conditional *Cas9act1* cKO

The *act1* cKO parasite strain was obtained by addition of 50 nM of rapamycin to the parental lines. The strain was incubated for 1 h at 37°C and 5% CO<sub>2</sub> and cultured as described previously [9]. To decrease the population of un-induced parasites, the culture media was replaced by DMEM complete supplemented with 2.5% dextran sulphate after 24 h to inhibit re-invasion of WT parasites.

### MyoA-SNAP staining

Parasites expressing MyoA-SNAP were incubated with a TMR ligand for the SNAP tag [48] (1:10,000) for 30 min. The cells were then washed three times with PBS prior analysis.

### SiR-tubulin staining

Prior invasion, parasites were incubated with 1,000 nM SiR-tubulin [41] (1:1,000) for 1 h. The cells were then washed three times with PBS prior analysis.

### Light microscopy

Widefield images were acquired in z-stacks of 2 µm increments and were collected using an Olympus UPLSAPO 100× oil (1.40NA) objective on a Delta Vision Core microscope (Applied Precision, GE) attached to a CoolSNAP HQ2 CCD camera. Deconvolution was performed using SoftWoRx Suite 2.0 (Applied Precision, GE). Video microscopy was conducted with the Delta Vision Core microscope as above. Normal growth conditions were maintained throughout the experiment (37°C; 5% CO<sub>2</sub>). Further image processing was performed using FIJI [49] and Icy Image Processing Software (Institut Pasteur) [50].

Super-resolution microscopy (SR-SIM) was carried out using an ELYRA PS.1 microscope (Zeiss) as described previously [24]. 3D rendering and model views were generated using Imaris

software (Bitplane, Oxford Instruments) using the acquired SR-SIM files.

### Flow analysis time-lapse microscopy

To discriminate parasite orientation, 500 nm of SiR-tubulin was added to parasite cultures 1 h before the experiment. To prepare tachyzoites for the assay, 1 × 10<sup>6</sup> mechanically freshly released parasites per live dish were washed three times with PBS and incubated a minimum of 10 min in serum-free DMEM media. Cytochalasin D was added 30 min before imaging in a concentration of 2 µM. The samples were then imaged by widefield microscopy using a Delta Vision Core microscope or super-resolution microscopy (SR-SIM) using an ELYRA PS.1 microscope.

### Parasite treatment with A23187 and BIPPO

Calcium ionophore A23187 was added to parasite live dishes using with a final concentration of 2 µM. BIPPO was similarly used with a final concentration of 5 µM. The parasites were imaged by light microscopy immediately after adding A23187 or BIPPO.

### Tight Junction assay

For the assay 3 × 10<sup>6</sup>, mechanically freshly released parasites per well were incubated in 200 µl Endo buffer (44.7 mM K<sub>2</sub>SO<sub>4</sub>, 10 mM MgSO<sub>4</sub>, 106 mM sucrose, 5 mM glucose, 20 mM Tris-H<sub>2</sub>SO<sub>4</sub>, 3.5 mg/ml BSA, pH 8.2) for 10 min at 37°C. The parasites were then allowed to settle into confluent layer of HFFs for 3 min at room temperature. This step was followed by 20-min incubation at 37°C. The supernatant was carefully removed and replaced by pre-warmed culture media. The samples were further incubated for 5 min to allow invasion.

This was followed by fixing the samples using two different buffers: cytoskeleton buffer (CB1) (MES pH 6.1 10 mM, KCL 138 mM, MgCl 3 mM, EGTA 2 mM, 5% PFA) and cytoskeleton buffer (CB2) (MES pH6.1 10 mM, KCL 163.53 mM, MgCl 3.555 mM, EGTA 2.37 mM, sucrose 292 mM). These buffers were mixed in a 4:1 ratio, respectively, and subsequently used for fixation for 10 min. The samples were then treated with a PFA quenching solution (NH<sub>4</sub>CL 50 mM) for 10 min followed by PBS washing for three times. A minimum total of 40 parasites were counted for each sample in three biological replicates. The tight junction assay involving several mutants and wt in Fig 3E and F employed a multiple comparison 2-way ANOVA using Tukey's multiple comparison test with a *P*-value of < 0.0001.

### Cell deformation analysis

Samples were captured using SR-SIM and widefield microscopy as previously described [24]. The deformation was then analysed with Zen blue software (Zeiss) by measuring the size of the parasite body and nucleus when going through a tight junction. A total of 100 parasites per biological replicate were measured for each condition for RH in Fig 1B, and a total of 30 parasites per biological replicate were measured for the mutant in Appendix Fig S1A. Statistical analysis was carried out by ordinary one-way ANOVA, using Tukey's multiple comparison test with a *P*-value of < 0.0001.

### Colour-coded kymogram generation for particle dynamics analysis

Fourier-filtered colour-coded kymograms were generated using the KymographClear plugin on ImageJ and published in Mangeol *et al* [33]. This plugin allows to trace a path of interest on a collapse t-stack to follow particle movement. The plugin is able to generate a three colour-coded kymogram using Fourier transformation to filter different populations of particles by the orientation of the trajectory. The colour coding is represented by forward movement as red, backward movement as green and no movement as blue. These data are then exported to the stand-alone software KymographDirect to establish time-average intensity profiles. A more detailed protocol can be found on the author's website: <https://sites.google.com/site/kymographanalysis/>.

### Skeletonisation analysis

The skeletonisation process was done in FIJI using the Skeletonisation processing plugin [51]. The sample was binarised by thresholding. A skeletonisation algorithm is then employed which converts the thresholded signal into pixels, reducing the total width but not the length. The time-lapse profile was collapsed (Z-Project) to define the F-actin structures and their dynamics over the course of the time lapse. The plugin can be accessed by: <https://imagej.net/AnalyzeSkeleton>.

### Live cell invasion

Parasites were mechanically released using 23 G needle and filtered prior to inoculation on a confluent layer of HFFs, grown on glass bottom dishes (MaTek). The dish was then transferred to the DV Core microscope (Applied Precision, GE) and maintained under standard culturing conditions. Images were captured at 1.4 frames per second in DIC using an Olympus apochromat 60× oil objective. Images were analysed using the Icy Image Processing software (Institut Pasteur) [50]. Penetration speed profiles were obtained for 18 independent invasion events for RH Cb-EmeraldFP and Cb-EmeraldFP parasites. The statistical analysis of RH wt Invasion events in Fig 2C was done by unpaired two-tailed *t*-test in 28 total parasite invasion events that were captured across three different biological replicates.

### Penetration speed profile analysis

Movies obtained were analysed using Icy Image Processing software (Institut Pasteur) [50] with the Manual Tracking plugin. The methodology used consists on tracking the apical end of the parasite through the duration of penetration. The resulting data were then exported to GraphPad PRISM7 Software for posterior analysis.

### Plasmodium assays

The Cb-EmeraldFP sequence was cloned and transfected into *P. falciparum* 3D7 parasites, and parasites were cultured in RPMI 1640 supplemented with Albumax (Invitrogen). Schizonts were collected on a bed of 70% Percoll as previously described [42]. The schizonts were allowed to egress in a medium containing blood at 1% haematocrit and merozoites at various stages of invasion were

fixed in 4% paraformaldehyde with 0.0075% glutaraldehyde as previously described [42]. The junction was stained with a RON4 antibody and the nucleus stained by DAPI. Cb-EmeraldFP-labelled actin filaments were fluorescent in the green range. For image acquisition, z-stacks were collected using a UPLSAPO 100× oil (1.40 NA) objective on a Delta Vision Core microscope (Applied Precision, GE) attached to a CoolSNAP HQ2 CCD camera. Deconvolution was performed using SoftWoRx Suite 2.0 (Applied Precision, GE). An Elyra S1 microscope with super-resolution structured illumination microscopy (SR-SIM) (Zeiss) was used for super-resolution dissection of RON4 staining on the merozoite surface.

*Plasmodium knowlesi* A1-H.1 parasites were cultured as described previously [47] in human O+ RBCs in RPMI-HEPES media supplemented with 2.3 g/l sodium bicarbonate, 2 g/l dextrose, 0.05 g/l hypoxanthine, 0.025 g/l gentamicin, 0.292 g/l L-glutamine, 5 g/l Albumax II (Gibco) and 10% (v/v) equine serum (Gibco). Parasites were cultured at 37°C with a gas mixture of 90% N<sub>2</sub>, 5% O<sub>2</sub> and 5% CO<sub>2</sub>.

PkRON2\*mCherry-HA A1-H.1 merozoites were incubated with fresh erythrocytes, shaken at 1,000 rpm, 37°C for 90 s and samples fixed by addition of an equal volume of 2× fixative (8% paraformaldehyde/0.015% glutaraldehyde, Sigma-Aldrich). Cells were permeabilised with 0.1% Triton X-100/PBS for 10 min and blocked with 3% BSA/PBS. Cells were incubated with 1:500 mouse anti-actin [47] and 1:1,000 rat anti-HA (3F10, Roche) followed by 1:1,000 anti-mouse Alexa 488 (Invitrogen) and 1:1,000 anti-rat Alexa 594 (Invitrogen) secondary antibodies. Cells were smeared on slides and mounted in VectaShield (Vector Laboratories) with 0.1 ng/ml DAPI to label the parasite nucleus. Widefield fluorescent microscopy images were acquired with a Nikon plan apo 100×/1.45 oil immersion lens on a Nikon eclipse Ti microscope and images processed with NIS Elements (Nikon).

## Data availability

All imaging data and genetic material used for this paper are available from the authors on reasonable request.

**Expanded View** for this article is available online.

### Acknowledgments

We acknowledge the assistance of the Institute of Infection, Immunity and Inflammation Imaging Platform at the University of Glasgow. We also want to thank Dr. Philip Thompson for providing us with the reagent BIPPO and Dr. Maryse Lebrun for anti-RON2 antibodies. This work was supported by an ERC-Starting grant (ERC-2012-StG 309255-EndoTox), a Wellcome 087582/Z/08/Z Senior Fellowship to MM, Wellcome 100993/Z/13/Z Investigator Award to JB and a National Secretariat for Higher Education, Sciences, Technology and Innovation of Ecuador (SENESCYT) PhD scholarship (IFTH-GBE-2015-0475-M) to MD. The Wellcome Centre for Molecular Parasitology is supported by core funding from the Wellcome (085349). The funders had no role in study design, data collection and analysis, decision to publish, or preparation of the manuscript.

### Author contributions

MDR, JB, IT and MM conceived, designed or planned the study. MDR, JP, JAW, GP, OL, SD, GSP, JFS, LL and FL-B contributed to the acquisition, analysis or interpretation of the data. MM drafted the manuscript. All authors critically

reviewed or revised the manuscript for intellectual content and approved the final version.

### Conflict of interest

The authors declare that they have no conflict of interest.

## References

- Meissner M, Ferguson DJP, Frischknecht F (2013) Invasion factors of apicomplexan parasites: essential or redundant? *Curr Opin Microbiol* 16: 438–444
- Fréchal K, Dubremetz JF, Lebrun M, Soldati-Favre D (2017) Gliding motility powers invasion and egress in Apicomplexa. *Nat Rev Microbiol* 15: 645–660
- Besteiro S, Dubremetz JF, Lebrun M (2011) The moving junction of apicomplexan parasites: a key structure for invasion. *Cell Microbiol* 13: 797–805
- Bichet M, Joly C, Hadj Henni A, Guilbert T, Xémard M, Tafani V, Lagal V, Charas G, Tardieux I (2014) The toxoplasma-host cell junction is anchored to the cell cortex to sustain parasite invasive force. *BMC Biol* 12: 773
- Guérin A, Corrales RM, Parker ML, Lamarque MH, Jacot D, El Hajj H, Soldati-Favre D, Boulanger MJ, Lebrun M (2017) Efficient invasion by *Toxoplasma* depends on the subversion of host protein networks. *Nat Microbiol* 2: 1358–1366
- Tardieux I, Baum J (2016) Reassessing the mechanics of parasite motility and host-cell invasion. *J Cell Biol* 214: 507–515
- Egarter S, Andenmatten N, Jackson AJ, Whitelaw JA, Pall G, Black JA, Ferguson DJP, Tardieux I, Mogilner A, Meissner M (2014) The toxoplasma acto-myosin motor complex is important but not essential for gliding motility and host cell invasion. *PLoS One* 9: e91819
- Gras S, Jackson A, Woods S, Pall G, Whitelaw J, Leung JM, Ward GE, Roberts CW, Meissner M (2017) Parasites lacking the micronemal protein MIC2 are deficient in surface attachment and host cell egress, but remain virulent *in vivo*. *Wellcome Open Res* 2: 32
- Whitelaw JA, Latorre-Barragan F, Gras S, Pall GS, Leung JM, Heaslip A, Egarter S, Andenmatten N, Nelson SR, Warshaw DM et al (2017) Surface attachment, promoted by the actomyosin system of *Toxoplasma gondii* is important for efficient gliding motility and invasion. *BMC Biol* 15: 1
- Bichet M, Touquet B, Gonzalez V, Florent I, Meissner M, Tardieux I (2016) Genetic impairment of parasite myosin motors uncovers the contribution of host cell membrane dynamics to *Toxoplasma* invasion forces. *BMC Biol* 14: 97
- Tosetti N, Dos N, Pacheco S, Soldati-favre D, Jacot D (2019) Three F-actin assembly centers regulate organelle inheritance, cell-cell communication and motility in *Toxoplasma gondii*. *Elife* 8: e42669
- Gras S, Jimenez-Ruiz E, Klinger CM, Schneider K, Klingl A, Lemgruber L, Meissner M (2019) An endocytic-secretory cycle participates in *Toxoplasma gondii* in motility. *PLoS Biol* 17: e3000060
- O'Neill PR, Castillo-Badillo JA, Meshik X, Kalyanaraman V, Melgarejo K, Gautam N (2018) Membrane flow drives an adhesion-independent amoeboid cell migration mode. *Dev Cell* 46: 9–22
- Tanaka M, Kikuchi T, Uno H, Okita K, Kitanishi-Yumura T, Yumura S (2017) Turnover and flow of the cell membrane for cell migration. *Sci Rep* 7: 12970
- Angrisano F, Riglar DT, Sturm A, Volz JC, Delves MJ, Zuccala ES, Turnbull L, Dekiwadia C, Olshina MA, Marapana DS et al (2012) Spatial localisation of actin filaments across developmental stages of the malaria parasite. *PLoS One* 7: e32188
- Andenmatten N, Egarter S, Jackson AJ, Jullien N, Herman J-P, Meissner M (2013) Conditional genome engineering in *Toxoplasma gondii* uncovers alternative invasion mechanisms. *Nat Methods* 10: 125–127
- Heaslip AT, Nelson SR, Warshaw DM (2016) Dense granule trafficking in *Toxoplasma gondii* requires a unique class 27 myosin and actin filaments. *Mol Biol Cell* 27: 2080–2089
- Zhang Q, Huang Y, Zhang Y, Fang X, Claes A, Duchateau M, Namane A, Lopez-Rubio JJ, Pan W, Scherf A (2011) A critical role of perinuclear filamentous actin in spatial repositioning and mutually exclusive expression of virulence genes in malaria parasites. *Cell Host Microbe* 10: 451–463
- Patrón SA, Mondragón M, González S, Ambrosio JR, Guerrero BAL, Mondragón R (2005) Identification and purification of actin from the subpellicular network of *Toxoplasma gondii* tachyzoites. *Int J Parasitol* 35: 883–894
- Hliscs M, Millet C, Dixon MW, Siden-Kiamos I, Mcmillan P, Tilley L (2015) Organization and function of an actin cytoskeleton in *Plasmodium falciparum* gametocytes. *Cell Microbiol* 17: 207–225
- Yasuda T, Yagita K, Nakamura T, Endo T (1988) Immunocytochemical localization of actin in *Toxoplasma gondii*. *Parasitol Res* 75: 107–113
- Harding CR, Gow M, Kang JH, Shortt E, Manalis SR, Meissner M, Lourido S (2019) Alveolar proteins stabilize cortical microtubules in *Toxoplasma gondii*. *Nat Commun* 10: 401
- Graindorge A, Fréchal K, Jacot D, Salamun J, Marq JB, Soldati-Favre D (2016) The conoid associated motor myosin is indispensable for *Toxoplasma gondii* entry and exit from host cells. *PLoS Pathog* 12: e1005388
- Periz J, Whitelaw J, Harding C, Gras S, Minina MIDR, Latorre-Barragan F, Lemgruber L, Reimer MA, Insall R, Heaslip A et al (2017) *Toxoplasma gondii* F-actin forms an extensive filamentous network required for material exchange and parasite maturation. *Elife* 6: e24119
- Stortz JF, Del Rosario M, Singer M, Wilkes JM, Meissner M, Das S (2019) Formin-2 drives polymerisation of actin filaments enabling segregation of apicoplasts and cytokinesis in *Plasmodium falciparum*. *eLife* 8: e49030
- Shaw MK, Compton HL, Roos DS, Tilney LG (2000) Microtubules, but not actin filaments, drive daughter cell budding and cell division in *Toxoplasma gondii*. *J Cell Sci* 113(Pt. 7): 1241–1254
- Harding CR, Egarter S, Gow M, Jiménez-Ruiz E, Ferguson DJP, Meissner M (2016) Gliding associated proteins play essential roles during the formation of the inner membrane complex of *Toxoplasma gondii*. *PLoS Pathog* 12: e1005403
- McGregor AL, Hsia C-R, Lammerding J (2016) Squish and squeeze — the nucleus as a physical barrier during migration in confined environments. *Curr Opin Cell Biol* 40: 32–40
- Kessler H, Herm-Gotz A, Hegge S, Rauch M, Soldati-Favre D, Frischknecht F, Meissner M (2008) Microneme protein 8 — a new essential invasion factor in *Toxoplasma gondii*. *J Cell Sci* 121(Pt. 7): 947–956
- Fréchal K, Jacot D, Hammoudi PM, Graindorge A, Maco B, Soldati-Favre D (2017) Myosin-dependent cell-cell communication controls synchronicity of division in acute and chronic stages of *Toxoplasma gondii*. *Nat Commun* 8: 15710
- Mehta S, Sibley LD (2011) Actin depolymerizing factor controls actin turnover and gliding motility in *Toxoplasma gondii*. *Mol Biol Cell* 22: 1290–1299
- Arganda-Carreras I, Fernández-González R, Muñoz-Barrutia A, Ortiz-De-Solorzano C (2010) 3D reconstruction of histological sections: application to mammary gland tissue. *Microsc Res Tech* 73: 1019–1029

33. Mangeol P, Prevo B, Peterman EJG (2016) KymographClear and KymographDirect: two tools for the automated quantitative analysis of molecular and cellular dynamics using kymographs. *Mol Biol Cell* 27: 1948–1957
34. Howard BL, Harvey KL, Stewart RJ, Azevedo MF, Crabb BS, Jennings IG, Sanders PR, Manallack DT, Thompson PE, Tonkin CJ et al (2015) Identification of potent phosphodiesterase inhibitors that demonstrate cyclic nucleotide-dependent functions in apicomplexan parasites. *ACS Chem Biol* 10: 1145–1154
35. Thiam HR, Vargas P, Carpi N, Crespo CL, Raab M, Terriac E, King MC, Jacobelli J, Alberts AS, Stradal T et al (2016) Perinuclear Arp2/3-driven actin polymerization enables nuclear deformation to facilitate cell migration through complex environments. *Nat Commun* 7: 10997
36. Frénel K, Polonais V, Marq JB, Stratmann R, Limenitakis J, Soldati-Favre D (2010) Functional dissection of the apicomplexan glideosome molecular architecture. *Cell Host Microbe* 8: 343–357
37. Frénel K, Soldati-Favre D (2015) Plasticity and redundancy in proteins important for toxoplasma invasion. *PLoS Pathog* 11: e1005069
38. Plattner F, Yarovinsky F, Romero S, Didry D, Carlier M-F, Sher A, Soldati-Favre D (2008) Toxoplasma profilin is essential for host cell invasion and TLR11-dependent induction of an interleukin-12 response. *Cell Host Microbe* 3: 77–87
39. Huynh MH, Carruthers VB (2006) Toxoplasma MIC2 is a major determinant of invasion and virulence. *PLoS Pathog* 2: e84
40. Meissner M, Schlüter D, Soldati D (2002) Role of *Toxoplasma gondii* myosin a in powering parasite gliding and host cell invasion. *Science* 298: 837–840
41. Lukinavičius G, Reymond L, D'Este E, Masharina A, Göttfert F, Ta H, Güther A, Fournier M, Rizzo S, Waldmann H et al (2014) Fluorogenic probes for live-cell imaging of the cytoskeleton. *Nat Methods* 11: 731–733
42. Das S, Lemgruber L, Tay CL, Baum J, Meissner M (2017) Multiple essential functions of *Plasmodium falciparum* actin-1 during malaria blood-stage development. *BMC Biol* 15: 70
43. Gonzalez V, Combe A, David V, Malmquist NA, Delorme V, Leroy C, Blazquez S, Ménard R, Tardieux I (2009) Host cell entry by Apicomplexa parasites requires actin polymerization in the host cell. *Cell Host Microbe* 5: 259–272
44. Petrie RJ, Yamada KM (2016) Multiple mechanisms of 3D migration: the origins of plasticity. *Curr Opin Cell Biol* 42: 7–12
45. Guilluy C, Burrridge K (2015) Nuclear mechanotransduction: forcing the nucleus to respond. *Nucleus* 6: 19–22
46. Guilluy C, Osborne LD, Van Landeghem L, Sharek L, Superfine R, Garcia-Mata R, Burrridge K (2014) Isolated nuclei adapt to force and reveal a mechanotransduction pathway in the nucleus. *Nat Cell Biol* 16: 376–381
47. Lyth O, Vizcay-Barrena G, Wright KE, Haase S, Mohring F, Najer A, Henshall IG, Ashdown GW, Bannister LH, Drew DR et al (2018) Cellular dissection of malaria parasite invasion of human erythrocytes using viable *Plasmodium knowlesi* merozoites. *Sci Rep* 8: 10165
48. Keppler A, Gendreizig S, Gronemeyer T, Pick H, Vogel H, Johnsson K (2003) A general method for the covalent labeling of fusion proteins with small molecules *in vivo*. *Nat Biotechnol* 21: 86–89
49. Schindelin J, Arganda-Carreras I, Frise E, Kaynig V, Longair M, Pietzsch T, Preibisch S, Rueden C, Saalfeld S, Schmid B et al (2012) Fiji: an open-source platform for biological-image analysis. *Nat Methods* 9: 676–682
50. De Chaumont F, Dallongeville S, Chenouard N, Hervé N, Pop S, Provoost T, Meas-Yedid V, Pankajakshan P, Lecomte T, Le Montagner Y et al (2012) Icy: an open bioimage informatics platform for extended reproducible research. *Nat Methods* 9: 690–696
51. Doube M, Klosowski MM, Arganda-Carreras I, Cordelières FP, Dougherty RP, Jackson JS, Schmid B, Hutchinson JR, Shefelbine SJ (2010) BoneJ: free and extensible bone image analysis in ImageJ. *Bone* 47: 1076–1079



**License:** This is an open access article under the terms of the Creative Commons Attribution 4.0 License, which permits use, distribution and reproduction in any medium, provided the original work is properly cited.

## RESEARCH ARTICLE

# *Francisella novicida* and *F. philomiragia* biofilm features conditioning fitness in spring water and in presence of antibiotics

Claire Siebert<sup>1</sup>, Corinne Villers<sup>1,2</sup>, Georgios Pavlou<sup>3</sup>, Bastien Touquet<sup>3</sup>, Nandadeva Yakandawala<sup>4</sup>, Isabelle Tardieux<sup>3</sup>, Patricia Renesto<sup>1\*</sup>

**1** TIMC-IMAG UMR 5525—UGA CNRS, Grenoble Cedex 9, France, **2** Université de Caen Normandie, EA4655 U2RM, Caen, France, **3** Institute for Advanced Biosciences (IAB), Team Membrane Dynamics of Parasite-Host Cell Interactions, CNRS UMR 5309, INSERM U1209, Université Grenoble Alpes, Grenoble, France, **4** Kane Biotech, Inc., Winnipeg, Canada

\* [patricia.renesto@univ-grenoble-alpes.fr](mailto:patricia.renesto@univ-grenoble-alpes.fr)



## OPEN ACCESS

**Citation:** Siebert C, Villers C, Pavlou G, Touquet B, Yakandawala N, Tardieux I, et al. (2020) *Francisella novicida* and *F. philomiragia* biofilm features conditioning fitness in spring water and in presence of antibiotics. PLoS ONE 15(2): e0228591. <https://doi.org/10.1371/journal.pone.0228591>

**Editor:** Mohamed Ali Hakimi, Centre National de la Recherche Scientifique, FRANCE

**Received:** December 4, 2019

**Accepted:** January 17, 2020

**Published:** February 5, 2020

**Copyright:** © 2020 Siebert et al. This is an open access article distributed under the terms of the [Creative Commons Attribution License](https://creativecommons.org/licenses/by/4.0/), which permits unrestricted use, distribution, and reproduction in any medium, provided the original author and source are credited.

**Data Availability Statement:** All relevant data are within the manuscript and its Supporting Information files.

**Funding:** This work was supported by the FINOVI Foundation (Grant AO12-02) and by the ANR ASTRID (grant ANR-17-ASTR-0024). NY Yakandawala was employed by the company Kane Biotech, Inc. (Winnipeg, Canada). The authors declare that the research was conducted in the absence of any commercial or financial

## Abstract

Biofilms are currently considered as a predominant lifestyle of many bacteria in nature. While they promote survival of microbes, biofilms also potentially increase the threats to animal and public health in case of pathogenic species. They not only facilitate bacteria transmission and persistence, but also promote spreading of antibiotic resistance leading to chronic infections. In the case of *Francisella tularensis*, the causative agent of tularemia, biofilms have remained largely enigmatic. Here, applying live and static confocal microscopy, we report growth and ultrastructural organization of the biofilms formed *in vitro* by these microorganisms over the early transition from coccobacillary into coccoid shape during biofilm assembly. Using selective dispersing agents, we provided evidence for extracellular DNA (eDNA) being a major and conserved structural component of mature biofilms formed by both *F. subsp. novicida* and a human clinical isolate of *F. philomiragia*. We also observed a higher physical robustness of *F. novicida* biofilm as compared to *F. philomiragia* one, a feature likely promoted by specific polysaccharides. Further, *F. novicida* biofilms resisted significantly better to ciprofloxacin than their planktonic counterparts. Importantly, when grown in biofilms, both *Francisella* species survived longer in cold water as compared to free-living bacteria, a trait possibly associated with a gain in fitness in the natural aquatic environment. Overall, this study provides information on survival of *Francisella* when embedded with biofilms that should improve both the future management of biofilm-related infections and the design of effective strategies to tackle down the problematic issue of bacteria persistence in aquatic ecosystems.

## Introduction

*Francisella tularensis* is a non-motile Gram-negative coccobacillus and the causative agent of zoonotic tularemia disease. Due to a remarkable infectivity (< 10 bacteria) which is associated with high mortality and morbidity and a good genetic tractability, the US Centers for Disease

relationships that could be construed as a potential conflict of interest. The funders had no role in study design, data collection and analysis, decision to publish, or preparation of the manuscript.

**Competing interests:** The authors have declared that no competing interests exist.

Control and Prevention (CDC) has classified *F. tularensis* as category A bioterrorism agent [1]. The ability of *Francisella* strains to form biofilms *in vitro* was first reported in 2009 with *F. novicida* [2] and later observed with other *Francisella* species including highly virulent [3] and environmental strains [4]. Given the importance of biofilms in infectious diseases [5–10], the regulation of *Francisella* biofilm assembly was investigated and led to identifying the Sec secretion system [3] as well as of the transcription factor *qseB* [11] as main players of the biofilm regulatory cascade [12]. Although not demonstrated experimentally, and considering the role of *Francisella* chitinases in biofilm formation, it has been hypothesized that biofilms would significantly contribute to *Francisella* persistence in both aquatic habitats and mosquito hosting vectors [3, 13, 14]. The correlation between *Francisella* biofilm dispersion and an increased bacterial susceptibility towards biocides has been reported [14, 15] and we have recently brought first genetic evidence that the biofilm growth mode provides *F. tularensis* with a reduced susceptibility towards fluoroquinolones [16].

Tularemia is associated with several clinical forms whose severity depends not only on the *Francisella* subspecies, but also on the route of infection [17]. The more severe disease in human is caused by inhalation of *F. tularensis* subsp. *tularensis* (Type A) leading to a pneumonic form of tularemia [18]. Although the epidemiology of this disease is still not fully understood, risk factors include exposure to arthropods, especially ticks which are the most important vectors of the terrestrial life cycle of Type A *Francisella* [1, 19]. The two unusual outbreaks of pneumonic tularemia reported from the island of Martha's Vineyard [20, 21] together with the observed prolonged survival of Type A *F. tularensis* in brackish-water collected on this island [22] allowed hypothesizing that the aquatic environment could serve as a reservoir for *F. tularensis* [13, 23]. *F. tularensis* subsp. *holarctica* (Type B) being widespread in the Northern hemisphere is the other subspecies of major clinical importance although the disease is rarely fatal in humans [24]. Clinical and epidemiological data have highlighted a close relationship between outbreaks of *F. tularensis* subsp. *holarctica* with water sources while infected mosquitoes were described as major vectors of these bacteria, in particular in Scandinavia [1, 25–27]. *F. tularensis* subsp. *novicida* (herein *F. novicida*) is described as a rare opportunistic human pathogen despite being responsible for severe pathologies in either immuno- or medically weakened patients [28]. In healthy individuals, the consumption of contaminated water was identified as a major source of acute *F. novicida* infection following near-drowning events and ingestion of icy water [29–31]. Being the most genetically tractable *Francisella* subspecies, *F. novicida* has largely been used as an experimental relevant model to study *F. tularensis* pathogenesis [28, 32, 33]. *F. philomiragia* (previously *Yersinia philomiragia*) is another *Francisella* species which is commonly found in soil, water and aerosol samples [34]. While only a few cases of human infection with *F. philomiragia* have been described, they correlated with pneumonia in healthy individuals undergoing near-drowning accidents or in immunocompromised people. Overall, water appears as an important reservoir for some human pathogenic *Francisella* strains [23].

To gain insights on the development and composition of *Francisella* biofilms, a prerequisite for designing anti-biofilm efficient strategies to target the bacteria biofilms, we compared the main features of the biofilm dynamics and composition for both *F. novicida* and *F. philomiragia*. *F. novicida* strain U112 was used as relevant model for the highly pathogenic *Francisella* subsp. *tularensis* [28] and the *F. philomiragia* strain CHUGA-FP47 isolated from a patient [35] was used as a clinically relevant isolate. We visualized in real time the biofilm formation and analyzed the extracellular polymeric substances (EPS) of mature biofilms using selective dispersing agents. Further, the behavior of both planktonic and biofilm forms of *Francisella* was assessed both under antibiotics and cold water exposure.

## Materials and methods

### Bacterial strains and growth conditions

*F. novicida* (U112) CIP56.12 (Centre de Ressources Biologiques de l'Institut Pasteur, Paris, France) and *F. philomiragia* (CHUGA-FP47) were grown either on solid or in liquid media, as indicated. The solid medium corresponds to pre-made Polyvitex-enriched chocolate agar (PVX-CHA) plates (Ref#43109 BioMérieux, France) incubated at 37°C in a 5% CO<sub>2</sub> incubator with humidified atmosphere and used both to revive glycerol stocks and for CFU counting. Liquid cultures were carried out in Modified Mueller-Hinton broth (MMH) at 37°C under shaking. MMH corresponds to Mueller Hinton Broth (Ref#275730 Grosseron) supplemented with NaCl (Sigma; 5 g/L), BactoProteose peptone (Ref#211693 BD Biosciences; 5 g/L), Bacto-Tryptone (Ref#211705 BD Biosciences 5 g/L) and L-cysteine (Ref#C7477 Sigma; 1 g/L).

### Biofilm quantification

The static biofilm was grown in 96-well plates and detected by crystal violet staining [36]. Briefly, liquid bacterial cultures (absorbance around 0.8 at OD<sub>600 nm</sub>) were diluted in 37°C pre-warmed MMH and 200 µL of bacterial suspensions were dispensed per well of flat-bottom polystyrene 96-well plates (Falcon®). To avoid the edge effect resulting from evaporation, the peripheral wells were filled with 200 µL PBS. Plates were incubated for 24 h to 72 h at 37°C in a humidified atmosphere containing 5% CO<sub>2</sub>. The OD<sub>600 nm</sub> was measured using Tecan Plate reader to normalize bacterial growth and planktonic bacteria were gently aspirated. *F. novicida* biofilms were washed twice with sterile PBS while *F. philomiragia* biofilms were washed only once to ensure minimum to negligible amount of loss of bacteria as assessed by count of the colony forming unit (CFU) from washings. Microtiter plates were then incubated for 1 h at 70°C, stained with 200 µL of 0.1% (w/v) crystal violet/well (Merck) for 15 min and washed twice with 200 µL H<sub>2</sub>O. Biofilms were solubilized in 200 µL 30% acetic acid per well and quantified by measuring optical density at 595 nm.

### Fluorescence microscopy

For imaging, 1 mL of bacteria in MMH (1x10<sup>7</sup>/mL for *F. novicida* and 5x10<sup>7</sup>/mL *F. philomiragia*) were distributed in 24-well plates containing poly-L-lysine-coated glass coverslips. Samples were fixed at different time points with freshly made 4% paraformaldehyde in PBS for 20 minutes at room temperature. The supernatant containing planktonic cells was gently removed allowing the biofilm at the air-liquid interface to adhere to the coverslip. The wells were washed twice with PBS to remove residual planktonic cells and incubated in 50 mM NH<sub>4</sub>Cl in PBS for 5 min to quench auto-fluorescence caused by free aldehydes. Samples were stored in PBS supplemented with 0.02% (w/v) sodium azide at 4°C until staining. For staining of both bacterial membranes and biofilm glycoproteins, fixed samples were incubated in 5 µg/mL FM<sup>®</sup>1-43FX membrane probe (Life Technologies) and 200 µg/mL concanavalin (ConA)-FITC (Life Technologies) for 30 min at RT and washed 3 times with PBS. Nucleic acids were then stained with 0.5 µg/mL DAPI fluorescent dye for 5 min and the coverslips were mounted in Mowiol mounting medium. In some experiments, the presence of eDNA was visualized on unfixed biofilms and using the cell-impermeant DITO™-1 (2 µM; AAT Bioquest), a chemical analog to TOTO® together with Hoechst 33342 (1:5,000). The viability of bacteria within biofilms was also assessed from unfixed samples stained for 30 min at room temperature with the membrane impermeant dye propidium iodide (PI) (3 µM, Molecular Probes) that does not penetrate intact cells. Slides were imaged under Zeiss Apo Tome microscope with 63x/1.4 oil-immersion objective using Zeiss Zen software. Images were further processed using ImageJ

[37] and Adobe Photoshop software. 3D reconstruction of images was achieved by processing raw data (i.e., xyz files) using ImageJ software to crop the sequence and region of interest. When needed, z stack from each channel was deconvoluted using the “Iterative Deconvolve 3D” plugin with a z-step of 0.3  $\mu\text{m}$ . Zen software was used for 3D reconstruction and to produce movies from processed images.

### Time-lapse microscopy and image processing

Time-lapse video microscopy was performed with bacteria diluted in MMH and placed in ChamSlide™ chambers (LCI Corp., Seoul, Korea) installed on an Eclipse Ti inverted confocal microscope (Nikon France Instruments, Champigny sur Marne, France) with a temperature (37°C) and CO<sub>2</sub> (5%)-controlled stage. Images were collected every 15 minutes with a z-step of 0.3  $\mu\text{m}$  using a CMOS camera (Photometrics, Tucson, AZ, USA) and a CSU X1 spinning disk (Yokogawa, Roper Scientific, Lisses, France). Analysis was performed using MetaMorph software (<http://www.moleculardevices.com>) from the raw image data files.

### Dispersion of *Francisella* biofilms

The effect of dispersants was evaluated by using 24 h and 48 h-old biofilms of *F. novicida* and *F. philomiragia* biofilms, respectively. *F. novicida* biofilms were grown in 96-well polystyrene plates (Falcon®) starting from an inoculum of  $1 \times 10^7$  CFU/mL ( $2 \times 10^6$  bacteria/well), while for *F. philomiragia*  $5 \times 10^7$  CFU/mL ( $10^7$  bacteria/well) were used. After one (*F. philomiragia*) or two (*F. novicida*) gentle PBS washes, the MMH was replaced with 200  $\mu\text{L}$  fresh medium supplemented with increasing concentrations of dispersing agents including DNase I (Roche), EDTA (Sigma-Aldrich), chitinase from *Streptomyces griseus* (E.C. 3.2.1.14) (Sigma-Aldrich), cellulase (Sigma-Aldrich), proteinase K (Invitrogen) or Dispersin B (Kane Biotech Inc. Canada). Microtiter plates were incubated at 37°C for 24 h under 5% CO<sub>2</sub> and biofilm was quantified as described elsewhere. Data were expressed as percentage of remaining biofilm calculated in comparison to untreated biofilm under the same experimental conditions.

### Evaluation of antimicrobial resistance of planktonic and biofilm bacteria

The antibiotic resistance of *F. novicida* and *F. philomiragia* was evaluated under the same conditions as the dispersion assays but using MMH supplemented with increasing concentrations of antibiotics. Following 24 h incubation at 37°C the bacterial viability was evaluated using both the resazurin assay detailed above and the CFU method, as previously described and detailed below [16]. The antibiotic susceptibility of planktonic bacteria was assessed in parallel using the same culture medium and starting from a bacterial suspension containing an equal amount of bacteria as those present in biofilms. The growth of planktonic bacteria was evaluated by OD<sub>600nm</sub> measurement and their viability was tested by the metabolic resazurin test (see below). The minimal inhibitory concentrations (MICs) of gentamicin (Panpharma) and ciprofloxacin (Sigma-Aldrich) used as reference values were obtained using the broth-dilution method and in line with the CLSI guidelines [38]. For *F. novicida*, they were of 1 mg/L and 0.064 mg/L, respectively, these values being of 0.5 mg/L and 0.032 mg/L for *F. philomiragia*,

### Survival of planktonic or biofilm bacteria in water

*F. novicida* and *F. philomiragia* biofilms were grown and washed as described for dispersal experiments. After washings, the wells were filled with 200  $\mu\text{L}$  of water collected from a spring around Grenoble and sterilized by filtration using 0.45  $\mu\text{m}$  then 0.22  $\mu\text{m}$  filters. The microtiter plates were stored at 4°C, and bacteria survival was assessed by CFU assay at each time point.

In parallel, the viability of planktonic bacteria was determined starting from exponential growth phase bacteria. The bacterial suspension was centrifuged and washed with PBS and the resulting pellet was resuspended in a volume of spring water such as the bacterial density was close to that found within biofilms ( $5 \times 10^7$  bacteria/200  $\mu$ L).

### CFU counting

Biofilms previously disrupted to release cells by vigorous pipetting with PBS and planktonic cell suspensions were serially diluted in PBS. For each sample 100  $\mu$ L of at least four different dilutions were plated on PVX-CHA plates, incubated for 24–48 h at 37°C under 5% CO<sub>2</sub>, and CFU were counted.

### Measurement of bacterial viability by resazurin assay

This assays was done with resazurin (Sigma-Aldrich), a fluorescent indicator of mitochondrial function conveniently used for the evaluation of cell viability in of several bacterial species [39, 40] including *Neisseria gonorrhoeae* [41] and *Francisella* LVS strains [16]. In this metabolic assay, the incubation time was significantly lower (1–2 h vs 24h) than the conditions for which this compound was depicted as being an antimicrobial agent towards *Francisella* and *Neisseria* species [42]. Viable bacteria reduce blue non-fluorescent resazurin dye ( $\lambda_{\max} = 600$  nm) to the pink fluorescent compound resorufin (max absorbance  $\lambda_{\max} = 570$  nm). Antibiotic treated or untreated biofilms were washed with PBS to remove planktonic cells, supplemented with 200  $\mu$ L/well of a 0.02 mg/mL resazurin (Sigma-Aldrich) solution in MMH, and incubated for 2 h at 37°C under static conditions. Cell viability was estimated by using absorbance was measured at (OD<sub>570nm</sub>-OD<sub>600nm</sub>). Planktonic cells (200  $\mu$ L) were supplemented with 20  $\mu$ L of resazurin (0.2 mg/mL), incubated for 1 h at 37°C, and cell viability was evaluated and expressed as percent viability in comparison to untreated cells.

### Statistical analysis

Statistical analysis was performed using the GraphPad PRISM software and Student's t- tests. Data correspond to means  $\pm$  standard errors of the means (SEM) of at least three independent replicates from independent experiments, as depicted. *P* values less than 0.05 were considered statistically significant.

## Results

### Quantification of biofilm formation by *F. novicida* and *F. philomiragia*

The ability of *F. novicida* U112 and *F. philomiragia* strain CHUGA-FP47 to produce biofilm was first compared starting from increasing concentrations of the bacterial inoculum incubated under static conditions in MMH broth at 37°C. The biofilm biomass was quantified by crystal violet staining, a basic dye that binds non-specifically to negatively charged surface including polysaccharides and eDNA present into the extracellular matrix. As shown Fig 1A, increasing *F. novicida* inoculum size translated in a higher bacterial density in the wells after a 24 h incubation time, while the biofilm biomass remained unchanged (Fig 1B). The largest amount of biofilm was observed for an inoculum of  $10^6$ – $10^7$  bacteria/mL while its production estimated by the ratio biofilm biomass/bacteria number was seen to significantly drop beyond  $10^8$  bacteria/mL ( $P < 0.05$ ;  $n = 12$ ). The recovery of viable bacteria evaluated by CFU counting from a 24 h biofilm formed with  $10^7$  bacteria/mL in the starting starting inoculum was of  $4.95 \times 10^7 \pm 0.7 \times 10^7$  bacteria/well ( $n = 13$ ). While the *F. novicida* biofilm biomass measured after 48 h incubation was close to that observed at 24 h (not shown), the number of recovered bacteria

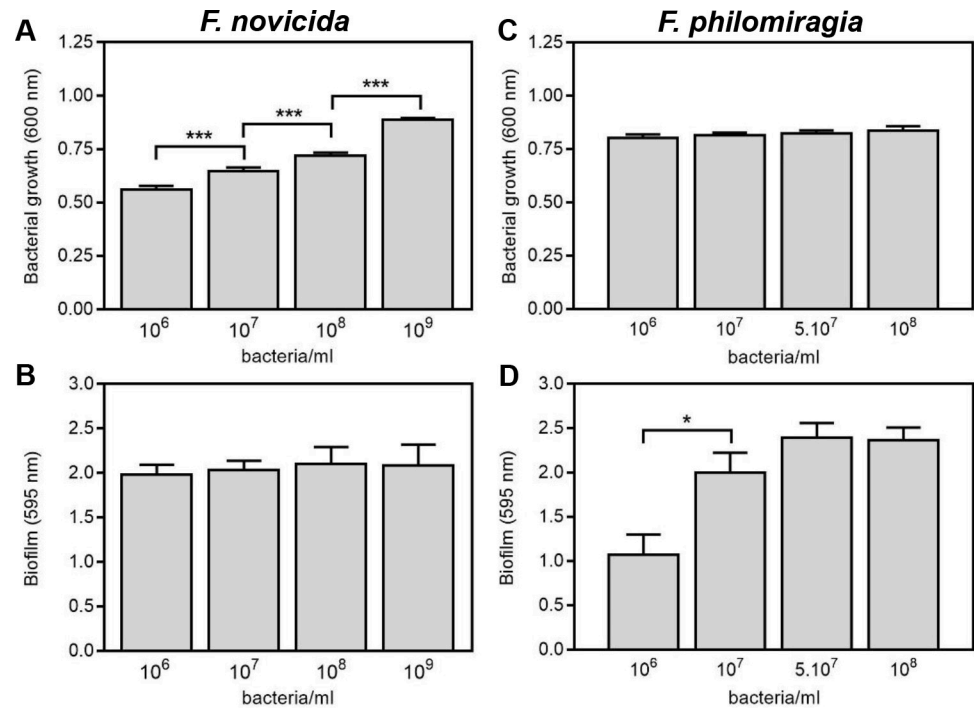


**Fig 1. Quantitative measurement of biofilm formation by *F. novicida* and *F. philomiragia*.** Biofilm formation was quantified in 96-well plates inoculated with increasing concentrations of bacteria and incubated under static conditions. Following 24 h (*F. novicida*) or 48 h (*F. philomiragia*) incubation at 37°C the bacterial growth (A, C) was quantified by OD<sub>600nm</sub> and biofilm biomass (B, D) was estimated by crystal violet staining. The data correspond to the mean ± SEM of three or more independent experiments with  $n = 6$  replicates for each. \* $P < 0.05$  and \*\*\* $P < 0.0005$ .

<https://doi.org/10.1371/journal.pone.0228591.g001>

was significantly increased  $8.15 \times 10^7 \pm 2.4 \times 10^7$  bacteria/well ( $n = 4$ ). In contrast to *F. novicida*, the *F. philomiragia* 24 h-old biofilm was found particularly fragile since it detached easily from the bottom of the microtiter plate and sheared despite gentle washing procedures (not shown). The quantification of *F. philomiragia* biofilm formation was thus analyzed over a 48 h incubation period. Under such conditions, the optimal inoculum for the *F. philomiragia* CHU-GA-FP47 strain was of  $5 \times 10^7$  bacteria/mL (Fig 1C and 1D) leading to a recovery of  $5.49 \times 10^7 \pm 1.38 \times 10^7$  viable bacteria from a 96 well-biofilm ( $n = 12$ ).

### Visualization and microscopic analysis of *Francisella* biofilm growth

The formation of both *F. novicida* and *F. philomiragia* biofilms was then monitored during several hours by real time confocal laser scanning microscopy (CLSM) at 37°C (Fig 2 and S1 Movie). These observations confirmed the greater capacity of *F. novicida* to replicate and to spatially organize as biofilms. The biofilm evolution over time was also imaged using Structured Illumination Microscopy SIM (Figs 3 and 4). Over the 15 min post-inoculation period, no bacteria were observed on the coverslips used to retain the floating biofilm formed at the air-liquid interface after gentle aspiration of planktonic cells. To have a reference point prior to biofilm formation, we examined the bacterial suspension from the inoculum. For both strains, bacteria displayed an uniform coccobacillary shape visualized by the dual labeling of membrane and surface-exposed carbohydrates using the styryl fluorescent dye and the ConA lectin, respectively (Figs 3A and 4A). Over the few following hours, confocal images attest from cell-to-cell juxtaposition of bacteria secreting large amounts of glycoconjugates (Fig 3B–3E and Fig 4B–4D). The floating colonies progressively developed in a more robust biofilm

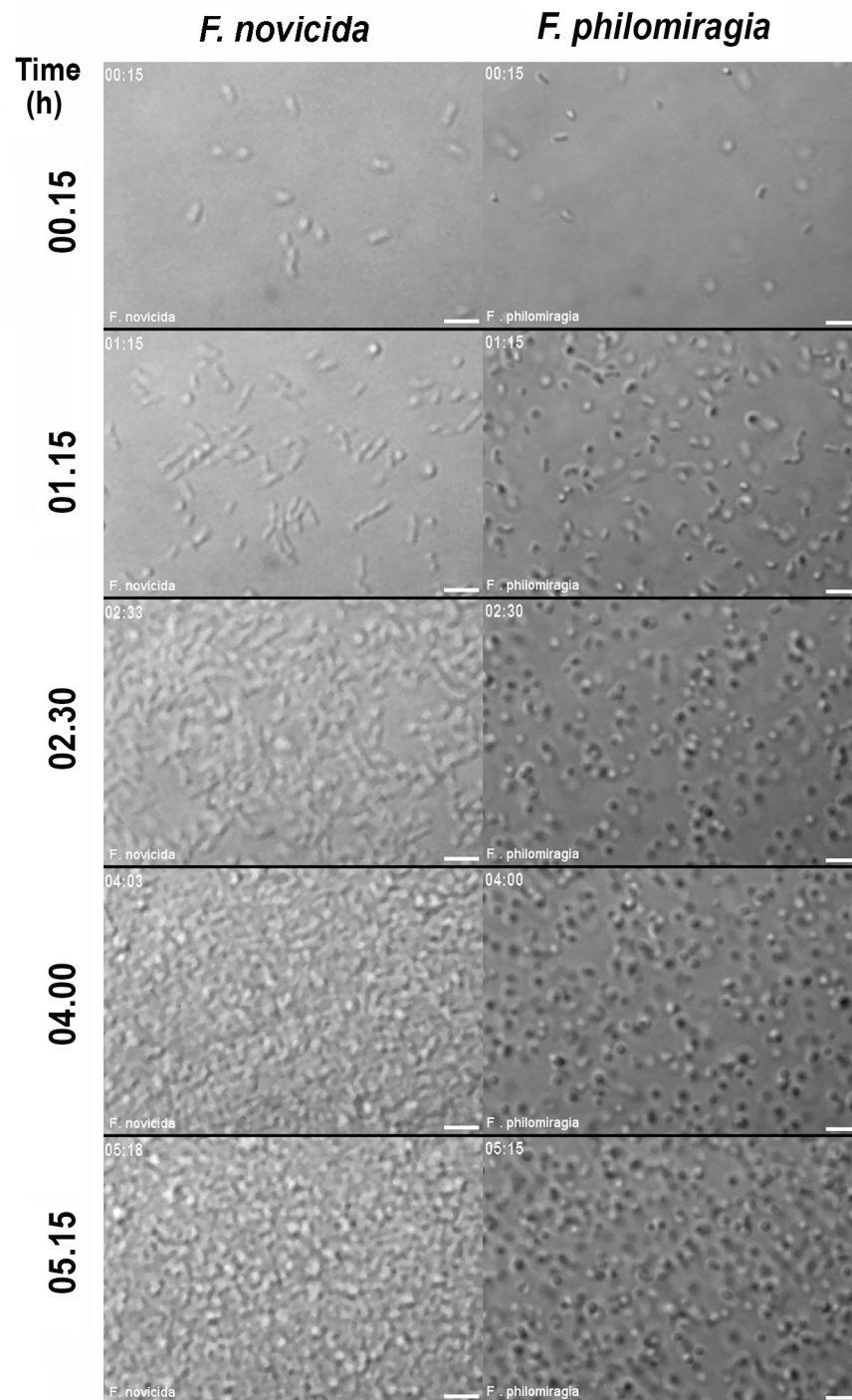


**Fig 2. Kinetics of biofilm formation by *F. novicida* and *F. philomiragia*.** Confocal images were taken at each of indicated time points from bacterial suspension grown at 37°C without agitation in Chamlyde™ chambers installed on an Eclipse Ti inverted confocal microscope as detailed in Materials and Methods. The scale bar indicates 5μM.

<https://doi.org/10.1371/journal.pone.0228591.g002>

with bacteria embedded in EPS. A striking morphological feature of both strains was the spherical shape they adopted in course of the biofilm formation, an effect observed as early as

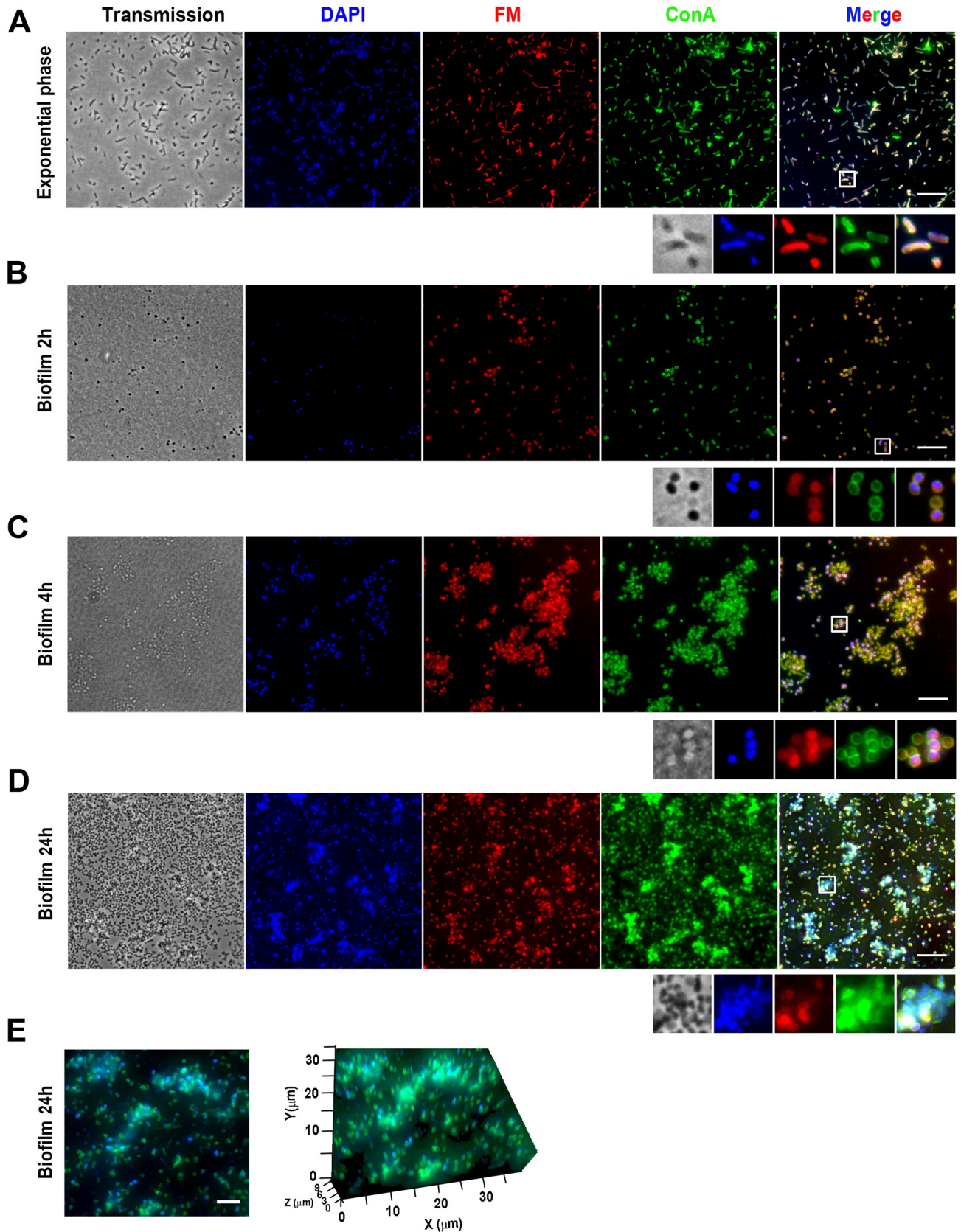


**Fig 3. Fluorescence microscopy analysis of *F. novicida* biofilm formation.** (A) Planktonic exponential phase bacteria and (B-D) biofilms formed upon incubation of bacteria for different time intervals were fixed and stained with DAPI (nucleic acids—blue), FM<sup>®</sup>1-43FX (FM; bacterial membranes

—red), ConA-FITC (ConA; EPS sugar residues—green). The scale bar represents 10  $\mu\text{m}$ . (E) Z maximal projection of the 24 h biofilm. The zoomed panels show the volume of the region of interest under two different orientations; note that the thickness of the biofilm reaches approximately 9  $\mu\text{m}$ .

<https://doi.org/10.1371/journal.pone.0228591.g003>

the 2 first hours for *F. novicida* (Fig 3B). During the 24 h of biofilm assembly, these bacteria continued to proliferate within the matrix and the thickness was estimated around 9  $\mu\text{m}$  (Fig 3E). In agreement with the biomass quantification data, a delayed biofilm assembly was observed for *F. philomiragia*, with packed bacteria communities that clustered within a ~ 4.5  $\mu\text{m}$ -thick EPS after 48 h (Fig 4D).

### Treatment of mature *Francisella* biofilms with potential dispersing agents

Given that main components of the bacterial biofilm EPS include eDNA, proteins and polysaccharides which adhere to each other and maintain microbial cells together [6], the capacity of enzymes or reagents targeting these specific compounds to induce biofilm dispersal was investigated. Taking in consideration biofilm biomass, thickness and the number of biofilm embedded bacteria, these assays were carried out using 24 h and 48 h-old biofilms of *F. novicida* and *F. philomiragia*, respectively. Results obtained showed that, following 24 h exposure, the DNase I induced a concentration-dependent dispersion of *F. novicida* biofilm with a maximum level of around 70% reached at 50  $\mu\text{g}/\text{mL}$  (Fig 5A). The role of eDNA in *F. novicida* biofilm stabilization was further suggested using the chelating agent EDTA (Fig 5B) that similarly affected the structural integrity of the EPS matrix but by impacting the electrostatic interactions between divalent cations and negatively charged DNA [43]. Biofilm dispersion was almost complete ( $87.93\% \pm 0.8\%$ ;  $n = 12$ ) following treatment with 0.5  $\mu\text{g}/\text{mL}$  proteinase K, indicating that proteinaceous structures largely contribute to *F. novicida* biofilm structure and integrity (Fig 5C). This biofilm also contains polysaccharides and more specifically poly- $\beta$ (1,4)-N-acetylglucosamine hydrolyzed by chitinase, leading to more than 80% dispersion when used at 300  $\mu\text{g}/\text{ml}$  (Fig 5D). Another polysaccharide identified as a key component of *F. novicida* biofilm is the  $\beta$ (1,4)-linked D glucose homopolymer cellulose (Fig 5E) which displays the same coupling as the acetylamine group with chitin. In contrast, dispersin B which targets poly- $\beta$ -(1,6)-linked N-acetylglucosaminoglycans [44, 45] rather induced a moderate decrease of the biofilm biomass (Fig 5F). The capacity of DNase I, proteinase K and cellulase to dissociate *F. novicida* biofilms has been reported but under incubation time and concentration conditions different from our assays [14].

Interestingly, the composition of the biofilm matrix appeared strikingly different for *F. philomiragia* (Table 1). Importantly, proteinase K did not impact the *F. philomiragia* biofilm biomass, even used at a concentration as high as 200  $\mu\text{g}/\text{mL}$ , whereas dispersin B treatment led to a greater biofilm detachment than observed toward *F. novicida*. Taking into account these data together with the chitinase and cellulase inefficiency seen on *F. philomiragia* biofilm underscores the differences in EPS-secreted polysaccharides between both bacterial species. In contrast, and as observed with *F. novicida*, both DNase I and EDTA treatment significantly affected the biofilm formed by *F. philomiragia*, albeit at a lesser extent. Accordingly, eDNA seems to be a common and essential constituent of *Francisella* EPS, a point further confirmed from biofilms treated or not with DNase I prior staining and imaging using the selective DITO™-1 eDNA marker (Fig 6).

### Antimicrobial susceptibility of planktonic and biofilm-embedded *Francisella*

Because bacteria embedded within biofilm matrix were often described extremely resistant to antibiotics [7, 8], we then compared the antibiotic susceptibility of *F. novicida* and *F.*

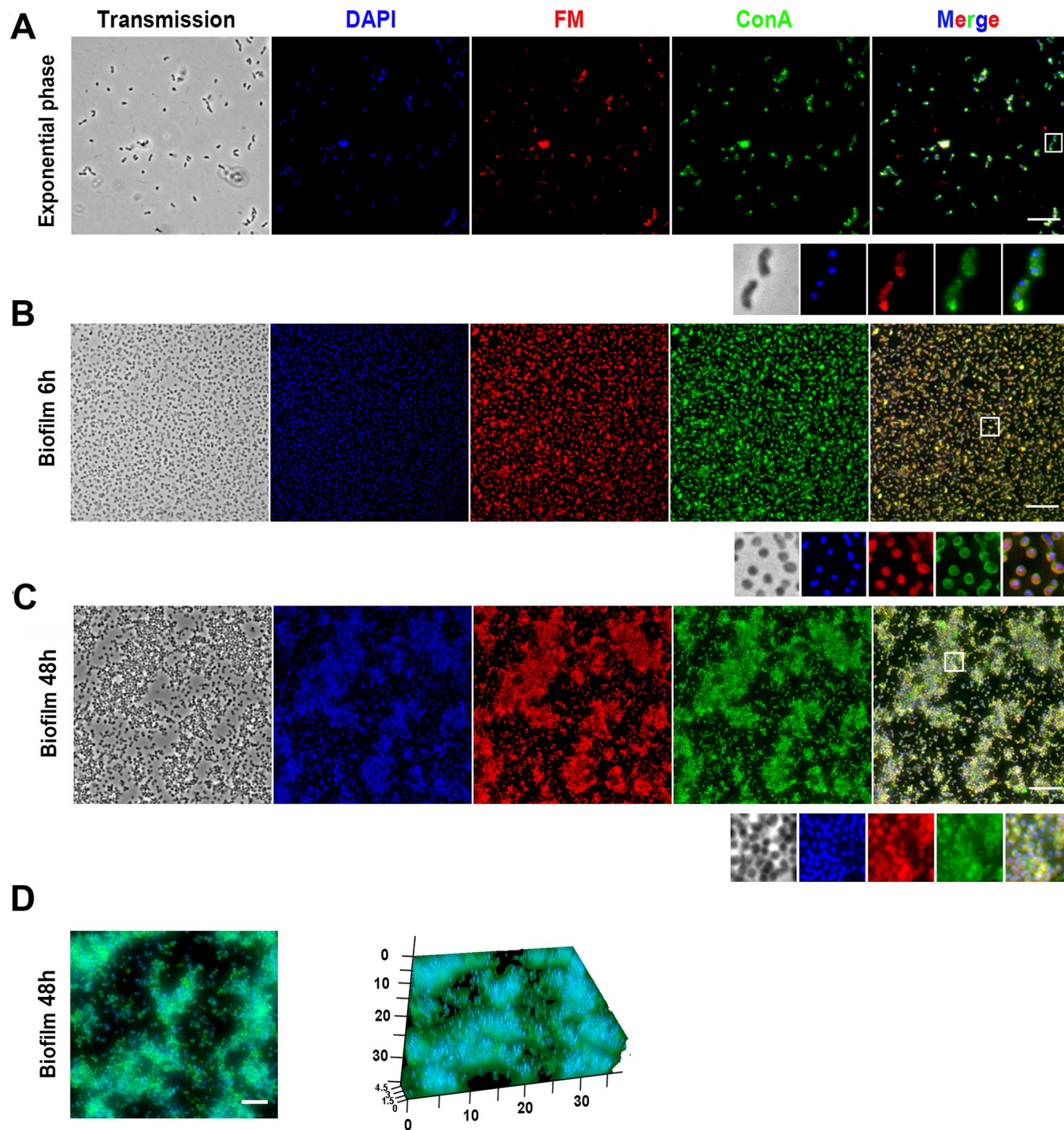


**Fig 4. Fluorescence microscopy analysis of *F. philomiragia* biofilm formation.** Same legend as in Fig 3 with a biofilm thickness at 48 h around 4.5  $\mu$ m.

<https://doi.org/10.1371/journal.pone.0228591.g004>

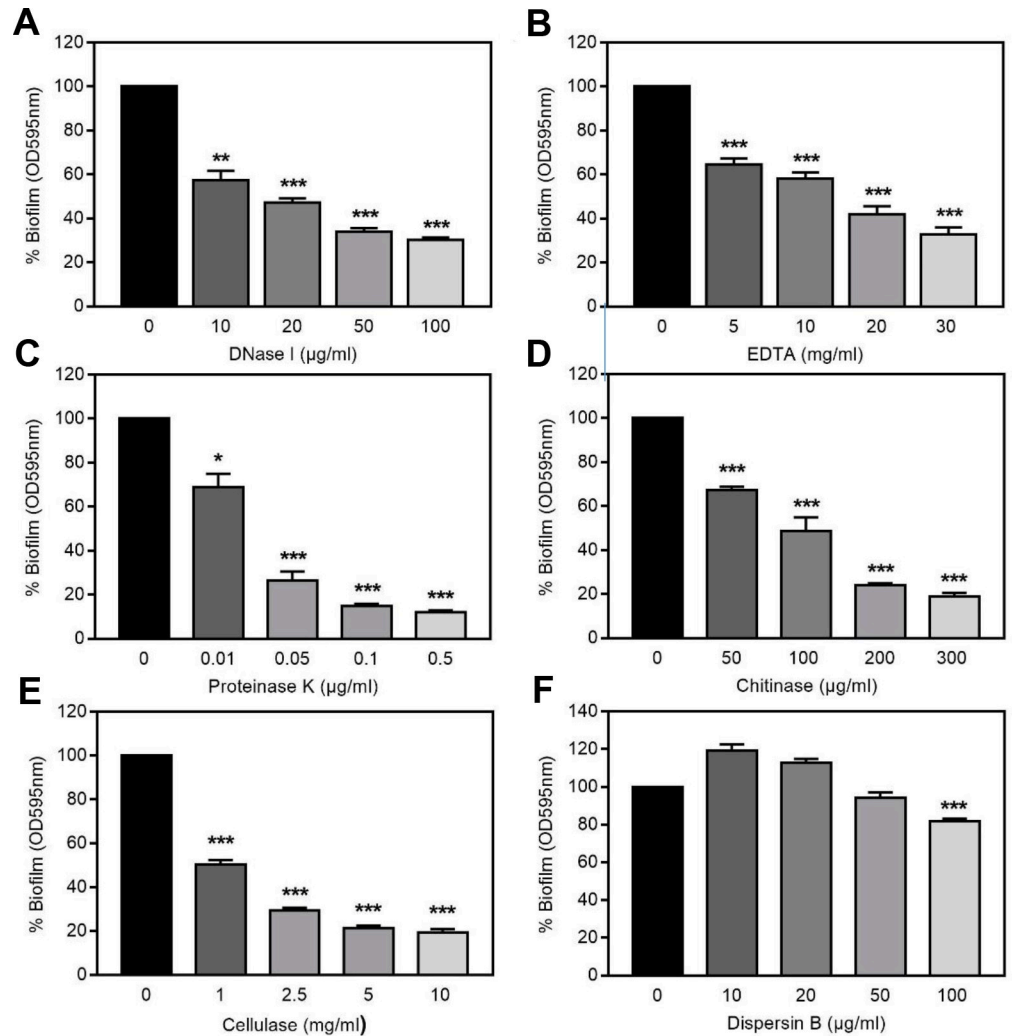


**Fig 5. Disruption of *F. novicida* biofilms.** *F. novicida* biofilms (24 h-old) were incubated with different concentrations of (A) DNase I, (B) EDTA, (C) proteinase K, (D) chitinase, (E) cellulase and (F) dispersin B. After 24 h incubation at 37 °C, biofilm biomass was estimated by crystal violet staining. Values were expressed as percentage of data obtained in absence of dispersing agents and correspond to mean ± SEM from at least three different experiments with four replicates for each. \*  $P < 0.05$ , \*\*  $P < 0.005$  and \*\*\*  $P < 0.0005$ .

<https://doi.org/10.1371/journal.pone.0228591.g005>

**Table 1. Effect of various components on *F. novicida* and *F. philomiragia* biofilms.**

| Dispersant   | Concentration | % of remaining biomass after treatment |                        | P value |
|--------------|---------------|--|------------------------|---------|
|              |               | <i>F. novicida</i>                     | <i>F. philomiragia</i> |         |
| DNase I      | 100 µg/mL     | 30.2 ± 1.1                             | 60.8 ± 4.4             | 0.0001  |
| EDTA         | 30 mg/mL      | 32.8 ± 3.3                             | 50.7 ± 3.3             | 0.0005  |
| Proteinase K | 200 µg/mL     | 12.2 ± 2.1                             | 116.3 ± 6.9            | 0.0001  |
| Chitinase    | 300 µg/mL     | 18.9 ± 1.7                             | 104.2 ± 5.7            | 0.0001  |
| Cellulase    | 50 mg/mL      | 19.9 ± 0.9                             | 121.1 ± 10.7           | 0.0001  |
| Dispersin B  | 100 µg/mL     | 81.7 ± 1.4                             | 49,02 ± 3.6            | 0.0005  |

Same legend as in Fig 5 using 24 h and 48 h-old biofilms for *F. novicida* and *F. philomiragia*, respectively.

<https://doi.org/10.1371/journal.pone.0228591.t001>

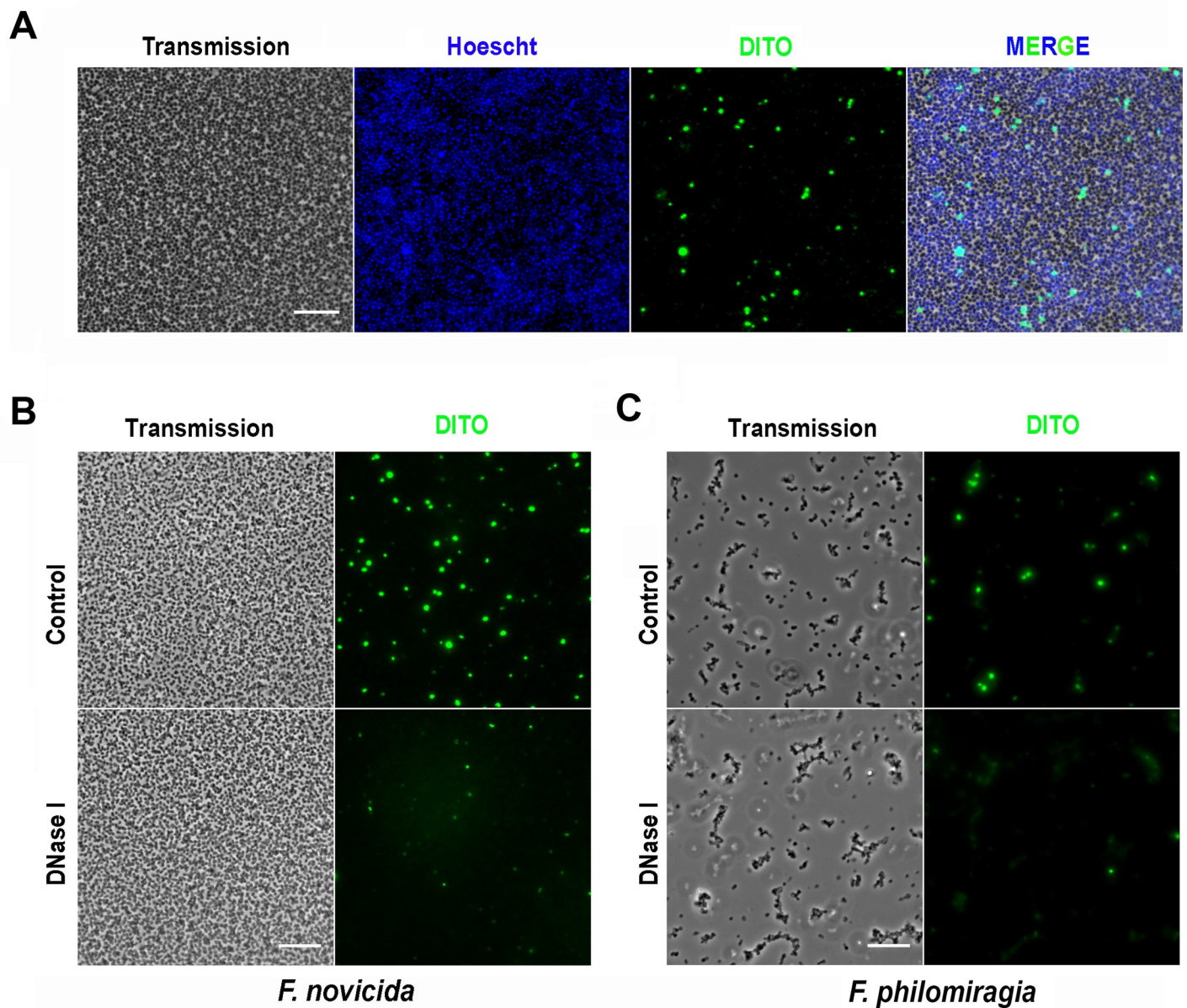


**Fig 6. Evidence of eDNA in *Francisella* biofilms.** (A) Brightfield and fluorescence images showing typical biofilm of *F. novicida* after 24 h growth. Whole bacterial population was stained with Hoescht (blue) and eDNA was visualized using DITO<sup>TM</sup>-1, a cell-impermeant, high-affinity nucleic acid stain (green). (B) Staining of 24 h-old *F. novicida* and (C) 48 h-old *F. philomiragia* biofilms following 1 h incubation with 100 μg/mL DNase 1 (lower panels) which efficiently reduced the amount of detected eDNA. The scale bars correspond to 10 μm.

<https://doi.org/10.1371/journal.pone.0228591.g006>

*philomiragia* embedded in biofilms with that of planktonic cells. Two bactericidal antimicrobials commonly approved for the treatment of tularemia were used, i.e. ciprofloxacin and gentamicin [46]. The growth of planktonic cells exposed to antibiotics was determined from OD<sub>600nm</sub> while their metabolic activity was estimated through the reduction of resazurin [39, 40]. This approach also conveniently enabled assessing the viability of biofilm bacteria whose survival was evaluated in parallel by CFU counting, as recently described for *F. tularensis* [16]. The results obtained demonstrated that *F. novicida* became significantly less susceptible to

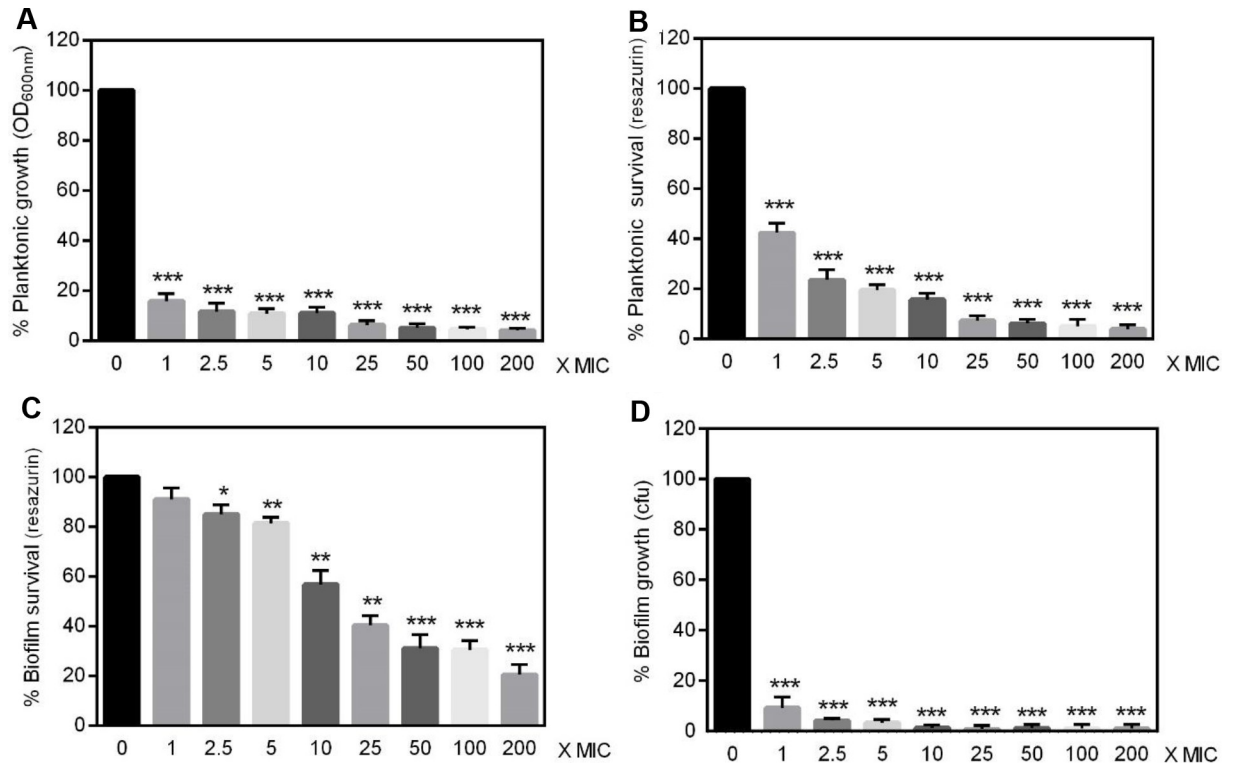


**Fig 7. Ciprofloxacin susceptibility of *F. novicida* U112.** (A, B) Planktonic or (C, D) 24 h-old biofilm bacteria were incubated for 24 h with concentrations of ciprofloxacin ranging from 1-time to 200-times the MIC (0.064 mg/L). (A) Bacterial replication in liquid media calculated from the OD<sub>600nm</sub> (B, C) metabolic activity estimated using the resazurin reduction assay (D) amount of viable bacteria present in biofilms as determined by CFU counting. Values were expressed as percentage of data obtained without antibiotics and correspond to mean ± SEM of 6 replicates. Similar data were obtained in four to six experimental repeats. \* $P < 0.05$  \*\* $P < 0.005$  \*\*\* $P < 0.0005$ .

<https://doi.org/10.1371/journal.pone.0228591.g007>

ciprofloxacin when growing within biofilms (Fig 7). Thus, approximately 40-times more ciprofloxacin was required to induce 80% reduction of the metabolic activity in biofilms relative to planktonic cultures (from 5x to 200x MIC) (Fig 7B and 7C). Strikingly, as few as 9.2% ± 2.4% bacteria ( $n = 3$ ) were recovered from biofilms treated with the ciprofloxacin MIC (Fig 7D), whereas the bacterial viability evaluated in parallel through metabolic activity measurement was of 91.1% ± 2.7% ( $n = 3$ ;  $P < 0.0005$ ) (Fig 7C).

These data suggested that, in addition to the increased biofilm-specific antibiotic resistance, ciprofloxacin treatment induced a viable but non culturable (VBNC) state in *F. novicida* when organized as biofilm, similarly to what was reported for *F. tularensis* LVS [16]. The assumption that *F. novicida* enter a VBNC state in biofilm exposed to ciprofloxacin was further confirmed using the cell non-permeant DNA intercalating dye propidium iodide (Fig 8).

This protective effect of *F. novicida* biofilm toward antibiotic was found specific for ciprofloxacin since gentamicin killed biofilm bacteria almost as efficiently as planktonic ones (Fig 9). Moreover, a significant correlation between the metabolic activity and CFU counting recovered from *F. novicida* biofilms exposed to gentamicin was observed (80.06% ± 3.2% vs 68.33% ± 9.8% respectively for 2.5x MIC;  $n = 3$ ;  $P > 0.05$ ), therefore confirming the reliability of resazurin fluorescence signal to quantitatively assess bacteria viability (Fig 9C and 9D). Interestingly, when embedded in biofilms, *F. philomiragia* did not acquire higher resistance than planktonic cells toward neither ciprofloxacin nor gentamicin (Figs 10 and 11).

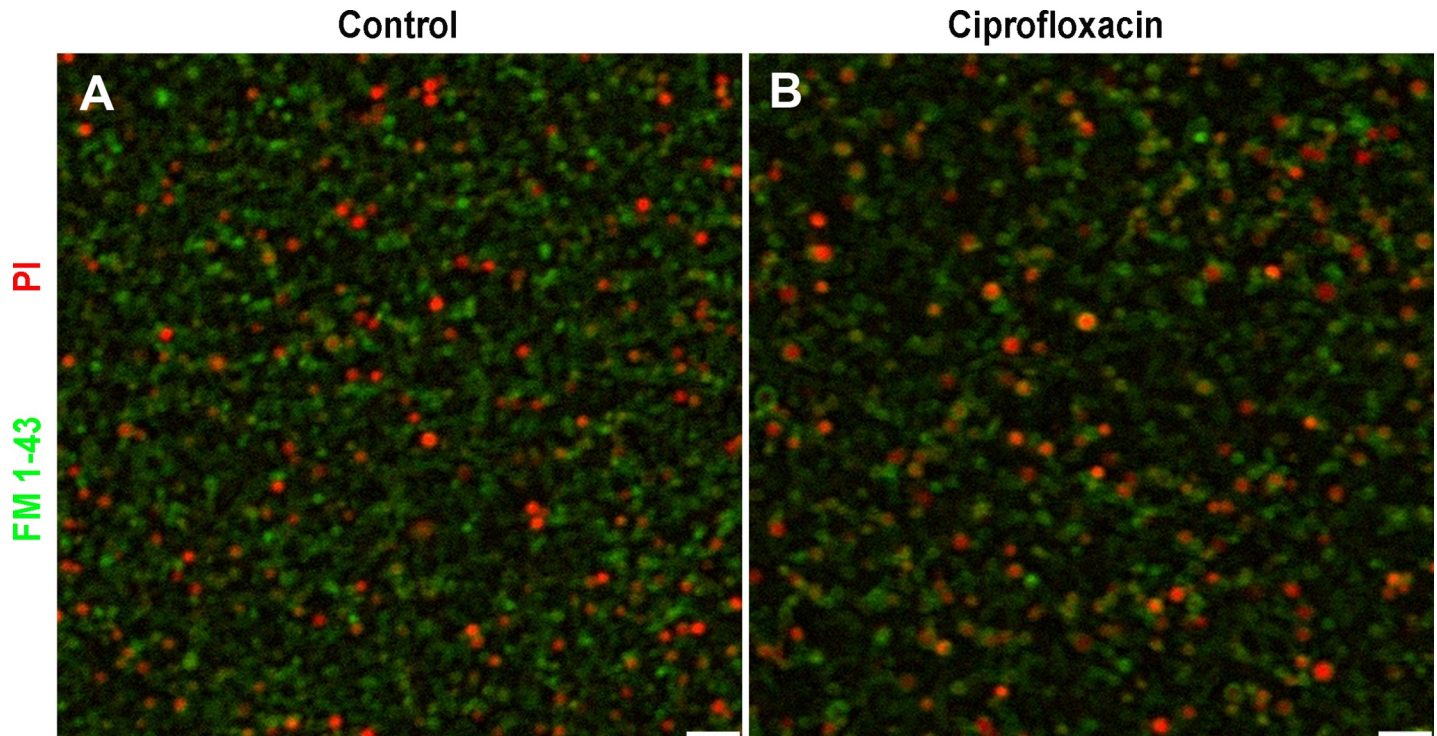


**Fig 8. *F. novicida* in biofilms acquire a VBNC state after exposure to ciprofloxacin.** Viability of *F. novicida* was analyzed in 24 h-old biofilms washed and incubated (A) in fresh MMH or (B) in presence of ciprofloxacin (0.32 mg/L; MIC 5x). Live and dead cells were visualized following 24 h incubation at 37°C by staining with the FilmTracer™ FM® 1–43 green biofilm cell stain (Molecular probes) and PI. The proportion of dead bacteria with damaged membranes exhibiting red fluorescence is similar in both conditions.

<https://doi.org/10.1371/journal.pone.0228591.g008>

### Survival of planktonic and biofilm-embedded *Francisella* in water

By providing the capacity of bacteria to survive in nutrient-limited aquatic environment, the biofilms could also contribute to the environmental persistence and thus indirectly promote the transmission of *Francisella* to hosts [13, 23]. To address this question, *Francisella* biofilms formed in microtiter plates were incubated in water at 4°C and survival of bacterial was evaluated over time by CFU counting until no bacteria were recovered. These viability scores were compared with those of exponential growth phase (planktonic) bacteria at similar density in water and thus exposed to the same conditions. Interestingly, the obtained CFU decay curve of planktonic *F. novicida* in spring water (Fig 12A) was found comparable to that observed by Berrada and Telford when incubating the same strain in brackish-water [22]. Importantly, our results showed that both strains survived longer to cold water exposure when embedded in biofilms. Thus, while planktonic *F. novicida* persisted no more than nine weeks, at this stage  $1.18 \times 10^4 \pm 0.5 \times 10^4$  ( $n = 6$ ) colonies were still enumerated from the biofilm. Actually, *F. novicida* survived two times longer in biofilm than their planktonic counterparts (52 vs 98 days) (Fig 12A). Importantly, the biofilm was found to extend even more significantly the survival of the clinical strain *F. philomiragia* CHUGA-FP47 from three to seven weeks in cold water (Fig 12B).

### Discussion

In this study, we bring new insights on *Francisella* biofilms using the strains *F. novicida* and *F. philomiragia* for which human infections have been mainly associated with environmental

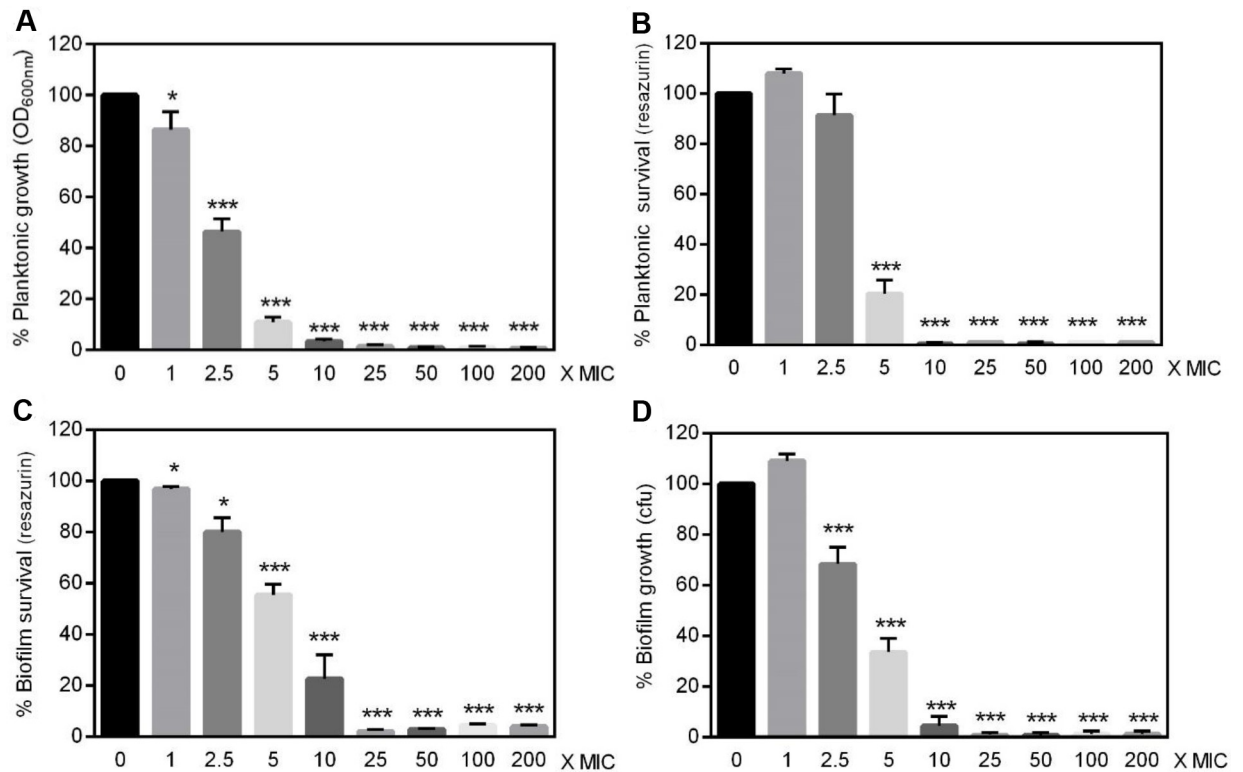


**Fig 9. Gentamicin susceptibility of *F. novicida* U112.** (A, B) Planktonic or (C, D) 24 h-old biofilm bacteria were incubated for 24 h with concentrations of gentamicin ranging from 1-time to 200-times the MIC (1 mg/L). (A) Bacterial replication in liquid media calculated from the OD<sub>600nm</sub> (B, C) metabolic activity estimated using the resazurin reduction assay (D) amount of viable bacteria present in biofilms as determined by CFU counting. Values were expressed as percentage of data obtained without antibiotics and correspond to mean ± SEM of 6 replicates. Similar data were obtained in four to six experimental repeats. \**P*<0.05 \*\**P*<0.005 \*\*\* *P*< 0.0005.

<https://doi.org/10.1371/journal.pone.0228591.g009>

contaminations including near-drowning events and use of outdoor ice machines [29–31]. In contrast to the highly virulent *F. tularensis* strains that can only be assayed under BSL-3 conditions, these strains can be handled under standard BSL-2 laboratory, being thus more tractable to live imaging. The selection of these strains in this study was also driven by their capacity to form higher biofilm biomasses than the *F. tularensis* subspecies *tularensis* (SCHU S4) [3] or *F. tularensis* subspecies *holarctica* LVS [3, 16], hence being more relevant to assess how dispersing agents impact on bacteria viability.

To ensure reproducible biofilm assays, we first evaluated the formation of the biofilm biomass relative to the initial number of bacteria. To assess the biofilm matrix composition while reducing potential bias due to heterogeneity in nutrient availability, a limitation already described for *Staphylococcus aureus* [47] and also recently for *Francisella* [48], both strains were grown in MMH at 37°C. Under such conditions, we determined that the biofilm development by *F. novicida* was optimal starting from a bacterial inoculum of 10<sup>7</sup> CFU/mL, this value being of 5.10<sup>7</sup> bacteria/mL for *F. philomiragia*. Live and static images analyzed over time confirmed a slower kinetic of bacterial replication and assembly of *F. philomiragia* biofilm as compared to *F. novicida* as previously observed when comparing other *F. novicida* and *F. philomiragia* isolates grown at 37°C [4]. It can be hypothesized that different capacity of both strains to form biofilms could result from a differential activation of genes encoding two-components system or of quorum sensing involved in the maturation and disassembly of biofilms [49, 50]. Immunofluorescence confocal microscopy also provided structural insights of the

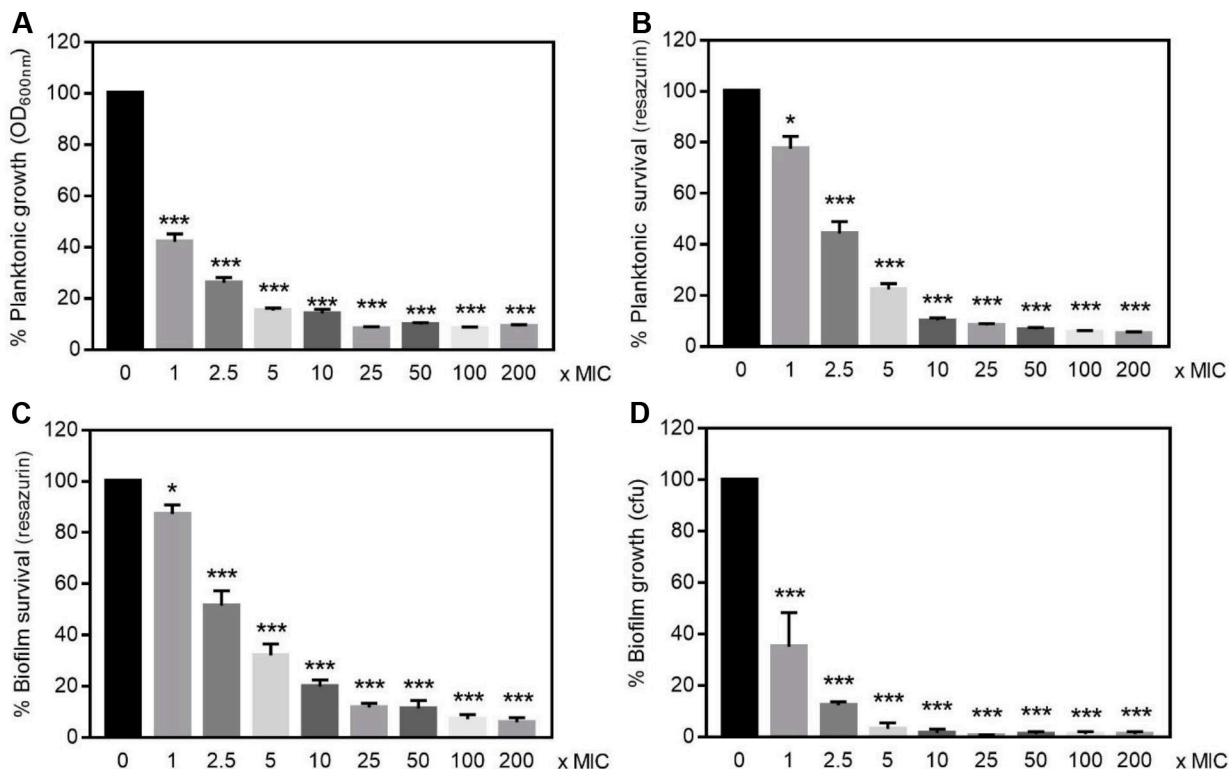


**Fig 10. Ciprofloxacin susceptibility of *F. philomiragia* CHUGA-FP47.** Same legend as in Fig 7 using 48h-old biofilm with a ciprofloxacin MIC value of 0.032 mg/L.

<https://doi.org/10.1371/journal.pone.0228591.g010>

mature biofilms. Interestingly, as early as 2 h of growth under static conditions, the cocobacillus shape typically observed for exponentially growing *F. novicida* was lost and the bacteria shifted to a coccoid form. Changes of bacterial shapes are not accidental but are rather described as biologically relevant [51]. Indeed the coccoid morphology previously observed for *F. novicida* biofilms grown on chitin surfaces [3], but never reported before for *F. philomiragia*, could reflect lower nutrient requirements and slow-growth conditions resulting from oxygen limitation under static conditions. Both strains, which secreted EPS containing glucose and mannose residues, as shown by ConA-FITC binding, later organized into a several micron-sized 3D structure. The thickness of *F. novicida* biofilm was quantified by CLSM by others [3, 14, 48], but the comparison of results obtained across different laboratories is challenging when considering differences in nutrient availability, temperature, or the flow conditions [52]. In this study, a slight discrepancy between biofilm thickness and their biomass assessed with crystal violet staining was noticed and could result from the growth devices respectively used (coated glass coverslips or polystyrene microtiter plates) [52]. Of note, the detachment or erosion of the structurally fragile *F. philomiragia* biofilm provoked by extensive washings during immunostaining procedure cannot be excluded.

Based on the resulting biofilm morphology, 24 h-old *F. novicida* and 48 h-old *F. philomiragia* biofilms were respectively used to determine their composition and to investigate their potential protective effect against chemical stresses or cold water exposure mimicking the aquatic environmental niche of these microorganisms. Results obtained highlighted marked differences in the composition of the biofilm between *F. novicida* U112 and *F. philomiragia* CHUGA-FP47. Only DNase I and EDTA significantly reduced the biofilm biomass of both

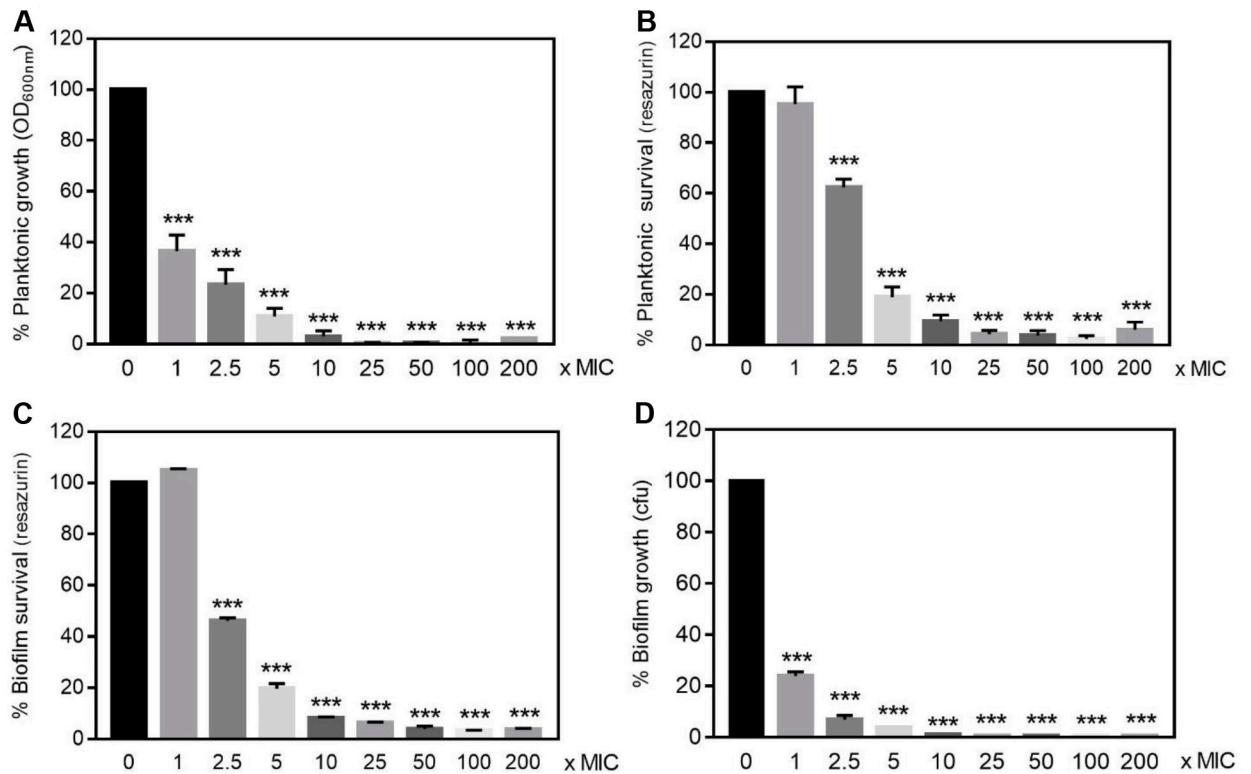


**Fig 11. Gentamicin susceptibility of *F. philomiragia* CHUGA-FP47.** Same legend as in Fig 8 using 48h-old biofilm with a gentamicin MIC value of 0.5 mg/mL.

<https://doi.org/10.1371/journal.pone.0228591.g011>

strains, suggesting that eDNA is a major common structural component of *Francisella* biofilms, similarly to several species of bacteria [53]. Surprisingly, the biofilm produced by *F. novicida* was found more susceptible than the *F. philomiragia* biofilm to almost all the dispersing agents tested despite a much higher mechanical resistance to fluids during washing procedures. Even more striking was the proteinase K resistance of the *F. philomiragia*-associated EPS that exceeds about four hundred times the *F. novicida*-associated matrix. Since proteinase K is a potent and broad-spectrum serine protease, these data indicated that the stabilization of *F. philomiragia* biofilm does not require proteinaceous proteinase K-sensitive adhesins although the contribution of proteins exhibiting another proteolytic profile [54] or resistant to proteases, like amyloid fibers [55], cannot be excluded. In addition to nucleic acids and proteins, exopolysaccharides including cellulose and polymeric  $\beta$ -1,4-linked *N*-acetylglucosamine were also identified within the biofilm matrix of *F. novicida*. These EPS components appear to be missing in *F. philomiragia* biofilm, which indeed remained intact after cellulase or chitinase treatments. The observed mechanical fragility of *F. philomiragia* biofilms fits well with the absence of the rigid  $\beta$ -1,4-linked polymers, notably cellulose [56]. Such « viscous hence non rigid mass » biofilms were demonstrated to be ecologically advantageous to *Pseudomonas* strains in a static liquid microcosm [56], a point supporting water source as potential reservoir for the clinical strain CHUGA-PFP47. Another phenotypic difference between both biofilms relies on their distinct sensitivity to dispersin B. Interestingly, the negative correlation between the dispersal efficacy of proteinase K and dispersin B that characterizes *F. philomiragia* biofilm is also shared for different isolates of *S. aureus* [47, 54].

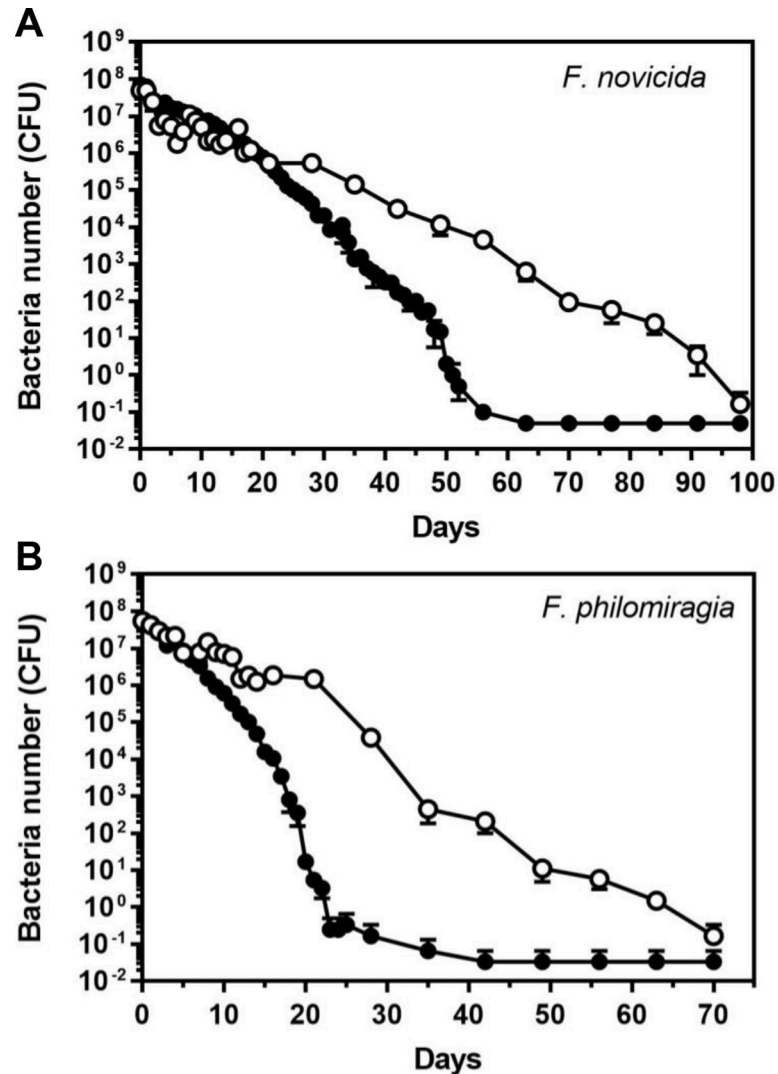


**Fig 12. Survival of planktonic and biofilm bacteria in water.** Exponential phase (black circles) or biofilm bacteria (white circles) were incubated in spring water at 4°C. Samples were taken every 24 h then every week and plated onto PVX-CHA plates to estimate the number of bacterial CFU. Data correspond to mean  $\pm$  SEM of five independent cultures.

<https://doi.org/10.1371/journal.pone.0228591.g012>

Over the last decade, it became increasingly clear that the formation of biofilm was implicated in resistance towards antimicrobials and caused persistent infections for many bacterial species [5, 7, 8, 10]. Accordingly, in recent years several biofilm-targeting approaches were developed as emerging therapeutic strategies [57]. This bacterial lifestyle usually results in a lower efficacy of antimicrobials that need to penetrate the dense biofilm matrix, coupled to a slow or even stopped bacteria growth, hence protecting microbes from the detrimental effects of both antibiotics and the host immune system. Considering the diffusion barrier limit imposed by the EPS in the biofilms, the protection provided is intrinsically linked to its biochemical composition as exemplified by the interactions between gentamicin and alginate, the major component of mucooid *P. aeruginosa* biofilms [58]. Variations in the components ensuring the structural integrity of biofilms formed by different isolates of a bacterial strain such as *S. aureus* [47, 59] or *Propionibacterium acnes* [60] were previously reported. Accordingly, the

heterogeneous composition of biofilms formed by *F. novicida* or *F. philomiragia* observed here is not surprising. This biofilm structural heterogeneity was found associated with specific and unexpected responses towards exogenous stressors including exposure to antibiotics and cold water. Indeed *F. novicida* biofilms displayed a significantly lower susceptibility towards ciprofloxacin than planktonic bacteria, hence raising important concerns about current therapies as this antibiotic belongs to the first-line agents to treat tularemia [1, 46]. Such a ciprofloxacin-protected lifestyle was also recently observed with a *F. tularensis* LVS isolate [16]. In contrast, the clinical strain *F. philomiragia* CHUGA-FP47 showed unaltered antibiotic resistance regardless of the free or biofilm-associated bacteria status.

Besides protecting bacteria against antibiotics, the biofilm formation by *Francisella* spp. was hypothesized to be key mechanism of environmental survival and persistence, specifically in aquatic habitats which constitute an important ecological niche of these microorganisms [13, 23, 61]. In line with this scheme, we now report that both strains growing in biofilms were far more resistant to harsh water-based conditions than free-living bacteria, an effect particularly pronounced for the clinical strain of *F. philomiragia* CHUGA-FP47.

In summary, our findings pave the way for further in-depth investigations to optimize the design of new therapeutic approaches against tularemia in particular with the combined use of antibiotics and dispersal agents or antibiotic adjuvants [7]. In this context, the precise role of eDNA, a common feature of *Francisella* EPS, in biofilm formation and stability should be thoroughly addressed. However, our data already indicate that treatment of these biofilms with DNase I and EDTA, two compounds already approved for human use [62, 63] may enhance the ability of antibiotics to clear infections, especially when ciprofloxacin is used. Finally, this study suggests that the functional role of biofilms could be intrinsically linked to their EPS composition with a proteinase K resistant and carbohydrate-rich matrix [54] hence more prone to promote the survival of *Francisella* spp. in aquatic environments.

## Supporting information

**S1 Movie. Formation of biofilm by *F. novicida* and *F. philomiragia*.** Videorecording of bacterial suspension grown at 37°C 5% CO<sub>2</sub> without agitation in Chamlide™ chambers installed on an Eclipse Ti inverted. DIC images were taken at 15 min interval over a 17h50 and 21h20 period for *F. novicida* and *F. philomiragia*, respectively. Scale bar: 5 μM. (AVI)

## Acknowledgments

The authors gratefully acknowledge Pr Max Maurin (CNR Francisella, CHU Grenoble-Alpes) for supplying *Francisella* strains and Salima Kamche (TIMC-IMAG UMR 5525, Grenoble) for her technical assistance.

## Author Contributions

**Conceptualization:** Isabelle Tardieux, Patricia Renesto.

**Formal analysis:** Claire Siebert, Georgios Pavlou, Bastien Touquet, Isabelle Tardieux.

**Funding acquisition:** Patricia Renesto.

**Investigation:** Claire Siebert, Corinne Villers, Georgios Pavlou, Bastien Touquet, Isabelle Tardieux, Patricia Renesto.

**Methodology:** Claire Siebert, Georgios Pavlou, Bastien Touquet, Isabelle Tardieux.

**Project administration:** Patricia Renesto.

**Resources:** Nandadeva Yakandawala.

**Supervision:** Patricia Renesto.

**Validation:** Isabelle Tardieux, Patricia Renesto.

**Writing – original draft:** Claire Siebert, Isabelle Tardieux, Patricia Renesto.

**Writing – review & editing:** Georgios Pavlou, Nandadeva Yakandawala.

## References

1. Oyston PC, Sjostedt A, Titball RW. Tularaemia: bioterrorism defence renews interest in *Francisella tularensis*. *Nat Rev Microbiol*. 2004; 2(12):967–78. <https://doi.org/10.1038/nrmicro1045> PMID: [15550942](https://pubmed.ncbi.nlm.nih.gov/15550942/).
2. Dean RE, Ireland PM, Jordan JE, Titball RW, Oyston PC. RelA regulates virulence and intracellular survival of *Francisella novicida*. *Microbiology*. 2009; 155(Pt 12):4104–13. <https://doi.org/10.1099/mic.0.031021-0> PMID: [19762448](https://pubmed.ncbi.nlm.nih.gov/19762448/).
3. Margolis JJ, El-Etr S, Joubert LM, Moore E, Robison R, Rasley A, et al. Contributions of *Francisella tularensis* subsp. *novicida* chitinases and Sec secretion system to biofilm formation on chitin. *Appl Environ Microbiol*. 2010; 76(2):596–608. <https://doi.org/10.1128/AEM.02037-09> PMID: [19948864](https://pubmed.ncbi.nlm.nih.gov/19948864/); PubMed Central PMCID: PMC2805214.
4. Verhoeven AB, Durham-Colleran MW, Pierson T, Boswell WT, Van Hoek ML. *Francisella philomiragia* biofilm formation and interaction with the aquatic protist *Acanthamoeba castellanii*. *Biol Bull*. 2010; 219(2):178–88. <https://doi.org/10.1086/BBLv219n2p178> PMID: [20972262](https://pubmed.ncbi.nlm.nih.gov/20972262/).
5. Costerton JW, Stewart PS, Greenberg EP. Bacterial biofilms: a common cause of persistent infections. *Science*. 1999; 284(5418):1318–22. <https://doi.org/10.1126/science.284.5418.1318> PMID: [10334980](https://pubmed.ncbi.nlm.nih.gov/10334980/).
6. Flemming HC. EPS-Then and Now. *Microorganisms*. 2016; 4(4). <https://doi.org/10.3390/microorganisms4040041> PMID: [27869702](https://pubmed.ncbi.nlm.nih.gov/27869702/); PubMed Central PMCID: PMC5192524.
7. Lebeaux D, Ghigo JM, Beloin C. Biofilm-related infections: bridging the gap between clinical management and fundamental aspects of recalcitrance toward antibiotics. *Microbiol Mol Biol Rev*. 2014; 78(3):510–43. <https://doi.org/10.1128/MMBR.00013-14> PMID: [25184564](https://pubmed.ncbi.nlm.nih.gov/25184564/); PubMed Central PMCID: PMC4187679.
8. Davies D. Understanding biofilm resistance to antibacterial agents. *Nat Rev Drug Discov*. 2003; 2(2):114–22. <https://doi.org/10.1038/nrd1008> PMID: [12563302](https://pubmed.ncbi.nlm.nih.gov/12563302/).
9. Balcazar JL, Subirats J, Borrego CM. The role of biofilms as environmental reservoirs of antibiotic resistance. *Frontiers in microbiology*. 2015; 6:1216. <https://doi.org/10.3389/fmicb.2015.01216> PMID: [26583011](https://pubmed.ncbi.nlm.nih.gov/26583011/); PubMed Central PMCID: PMC4628128.
10. Hall-Stoodley L, Costerton JW, Stoodley P. Bacterial biofilms: from the natural environment to infectious diseases. *Nat Rev Microbiol*. 2004; 2(2):95–108. <https://doi.org/10.1038/nrmicro821> PMID: [15040259](https://pubmed.ncbi.nlm.nih.gov/15040259/).
11. Durham-Colleran MW, Verhoeven AB, van Hoek ML. *Francisella novicida* forms in vitro biofilms mediated by an orphan response regulator. *Microb Ecol*. 2010; 59(3):457–65. <https://doi.org/10.1007/s00248-009-9586-9> PMID: [19763680](https://pubmed.ncbi.nlm.nih.gov/19763680/).
12. Zogaj X, Wyatt GC, Klose KE. Cyclic di-GMP stimulates biofilm formation and inhibits virulence of *Francisella novicida*. *Infect Immun*. 2012; 80(12):4239–47. <https://doi.org/10.1128/IAI.00702-12> PMID: [22988021](https://pubmed.ncbi.nlm.nih.gov/22988021/); PubMed Central PMCID: PMC3497427.
13. van Hoek ML. Biofilms: an advancement in our understanding of *Francisella* species. *Virulence*. 2013; 4(8):833–46. <https://doi.org/10.4161/viru.27023> PMID: [24225421](https://pubmed.ncbi.nlm.nih.gov/24225421/); PubMed Central PMCID: PMC3925715.
14. Chung MC, Dean S, Marakasova ES, Nwabueze AO, van Hoek ML. Chitinases are negative regulators of *Francisella novicida* biofilms. *PLoS One*. 2014; 9(3):e93119. <https://doi.org/10.1371/journal.pone.0093119> PMID: [24664176](https://pubmed.ncbi.nlm.nih.gov/24664176/); PubMed Central PMCID: PMC3963990.
15. Milton ME, Allen CL, Feldmann EA, Bobay BG, Jung DK, Stephens MD, et al. Structure of the *Francisella* response regulator QseB receiver domain, and characterization of QseB inhibition by antibiofilm 2-aminoimidazole-based compounds. *Mol Microbiol*. 2017; 106(2):223–35. <https://doi.org/10.1111/mmi.13759> PMID: [28755524](https://pubmed.ncbi.nlm.nih.gov/28755524/); PubMed Central PMCID: PMC5630518.
16. Siebert C, Lindgren H, Ferre S, Villers C, Boisset S, Perard J, et al. *Francisella tularensis*: FupA mutation contributes to fluoroquinolone resistance by increasing vesicle secretion and biofilm formation.

- Emerg Microbes Infect. 2019; 8(1):808–22. <https://doi.org/10.1080/22221751.2019.1615848> PMID: [31164053](https://pubmed.ncbi.nlm.nih.gov/31164053/).
17. Sjostedt A. Tularemia: history, epidemiology, pathogen physiology, and clinical manifestations. *Ann N Y Acad Sci.* 2007; 1105:1–29. <https://doi.org/10.1196/annals.1409.009> PMID: [17395726](https://pubmed.ncbi.nlm.nih.gov/17395726/).
  18. Kugeler KJ, Mead PS, Janusz AM, Staples JE, Kubota KA, Chalcraft LG, et al. Molecular Epidemiology of *Francisella tularensis* in the United States. *Clin Infect Dis.* 2009; 48(7):863–70. <https://doi.org/10.1086/597261> PMID: [19245342](https://pubmed.ncbi.nlm.nih.gov/19245342/).
  19. Akimana C, Kwaik YA. *Francisella*-arthropod vector interaction and its role in patho-adaptation to infect mammals. *Frontiers in microbiology.* 2011; 2:34. <https://doi.org/10.3389/fmicb.2011.00034> PMID: [21687425](https://pubmed.ncbi.nlm.nih.gov/21687425/); PubMed Central PMCID: PMC3109307.
  20. Teutsch SM, Martone WJ, Brink EW, Potter ME, Eliot G, Hoxsie R, et al. Pneumonic tularemia on Martha's Vineyard. *N Engl J Med.* 1979; 301(15):826–8. <https://doi.org/10.1056/NEJM197910113011507> PMID: [481515](https://pubmed.ncbi.nlm.nih.gov/481515/).
  21. Feldman KA, Ensore RE, Lathrop SL, Matyas BT, McGuill M, Schriefer ME, et al. An outbreak of primary pneumonic tularemia on Martha's Vineyard. *N Engl J Med.* 2001; 345(22):1601–6. <https://doi.org/10.1056/NEJMoa011374> PMID: [11757506](https://pubmed.ncbi.nlm.nih.gov/11757506/).
  22. Berrada ZL, Telford Iii SR. Survival of *Francisella tularensis* Type A in brackish-water. *Arch Microbiol.* 2011; 193(3):223–6. <https://doi.org/10.1007/s00203-010-0655-8> PMID: [21136042](https://pubmed.ncbi.nlm.nih.gov/21136042/); PubMed Central PMCID: PMC3962107.
  23. Hennebique A, Boisset S, Maurin M. Tularemia as a waterborne disease: a review. *Emerg Microbes Infect.* 2019; 8(1):1027–42. <https://doi.org/10.1080/22221751.2019.1638734> PMID: [31287787](https://pubmed.ncbi.nlm.nih.gov/31287787/); PubMed Central PMCID: PMC6691783.
  24. Maurin M, Gyuranecz M. Tularemia: clinical aspects in Europe. *Lancet Infect Dis.* 2016; 16(1):113–24. [https://doi.org/10.1016/S1473-3099\(15\)00355-2](https://doi.org/10.1016/S1473-3099(15)00355-2) PMID: [26738841](https://pubmed.ncbi.nlm.nih.gov/26738841/).
  25. Backman S, Naslund J, Forsman M, Thelaus J. Transmission of tularemia from a water source by transstadial maintenance in a mosquito vector. *Sci Rep.* 2015; 5:7793. <https://doi.org/10.1038/srep07793> PMID: [25609657](https://pubmed.ncbi.nlm.nih.gov/25609657/); PubMed Central PMCID: PMC4302321.
  26. Thelaus J, Andersson A, Broman T, Backman S, Granberg M, Karlsson L, et al. *Francisella tularensis* subspecies *holarctica* occurs in Swedish mosquitoes, persists through the developmental stages of laboratory-infected mosquitoes and is transmissible during blood feeding. *Microb Ecol.* 2014; 67(1):96–107. <https://doi.org/10.1007/s00248-013-0285-1> PMID: [24057273](https://pubmed.ncbi.nlm.nih.gov/24057273/); PubMed Central PMCID: PMC3907667.
  27. Broman T, Thelaus J, Andersson AC, Backman S, Wikstrom P, Larsson E, et al. Molecular Detection of Persistent *Francisella tularensis* Subspecies *holarctica* in Natural Waters. *Int J Microbiol.* 2011;2011. <https://doi.org/10.1155/2011/851946> PMID: [20885922](https://pubmed.ncbi.nlm.nih.gov/20885922/); PubMed Central PMCID: PMC2946586.
  28. Kingry LC, Petersen JM. Comparative review of *Francisella tularensis* and *Francisella novicida*. *Front Cell Infect Microbiol.* 2014; 4:35. <https://doi.org/10.3389/fcimb.2014.00035> PMID: [24660164](https://pubmed.ncbi.nlm.nih.gov/24660164/); PubMed Central PMCID: PMC3952080.
  29. Brett M, Doppalapudi A, Respicio-Kingry LB, Myers D, Husband B, Pollard K, et al. *Francisella novicida* bacteremia after a near-drowning accident. *J Clin Microbiol.* 2012; 50(8):2826–9. <https://doi.org/10.1128/JCM.00995-12> PMID: [22692740](https://pubmed.ncbi.nlm.nih.gov/22692740/); PubMed Central PMCID: PMC3421515.
  30. Whitehouse CA, Kesterson KE, Duncan DD, Eshoo MW, Wolcott M. Identification and characterization of *Francisella* species from natural warm springs in Utah, USA. *Letters in applied microbiology.* 2012; 54(4):313–24. <https://doi.org/10.1111/j.1472-765X.2012.03214.x> PMID: [22283482](https://pubmed.ncbi.nlm.nih.gov/22283482/).
  31. Brett ME, Respicio-Kingry LB, Yendell S, Ratard R, Hand J, Balsamo G, et al. Outbreak of *Francisella novicida* bacteremia among inmates at a louisiana correctional facility. *Clin Infect Dis.* 2014; 59(6):826–33. <https://doi.org/10.1093/cid/ciu430> PMID: [24944231](https://pubmed.ncbi.nlm.nih.gov/24944231/).
  32. Meunier E, Wallet P, Dreier RF, Costanzo S, Anton L, Ruhl S, et al. Guanylate-binding proteins promote activation of the AIM2 inflammasome during infection with *Francisella novicida*. *Nat Immunol.* 2015; 16(5):476–84. <https://doi.org/10.1038/ni.3119> PMID: [25774716](https://pubmed.ncbi.nlm.nih.gov/25774716/); PubMed Central PMCID: PMC4568307.
  33. Ziveri J, Tros F, Guerrero IC, Chhuon C, Audry M, Dupuis M, et al. The metabolic enzyme fructose-1,6-bisphosphate aldolase acts as a transcriptional regulator in pathogenic *Francisella*. *Nature communications.* 2017; 8(1):853. <https://doi.org/10.1038/s41467-017-00889-7> PMID: [29021545](https://pubmed.ncbi.nlm.nih.gov/29021545/); PubMed Central PMCID: PMC5636795.
  34. Petersen JM, Carlson J, Yockey B, Pillai S, Kuske C, Garbalena G, et al. Direct isolation of *Francisella* spp. from environmental samples. *Letters in applied microbiology.* 2009; 48(6):663–7. <https://doi.org/10.1111/j.1472-765X.2009.02589.x> PMID: [19413814](https://pubmed.ncbi.nlm.nih.gov/19413814/).

35. Kreitmann L, Terriou L, Launay D, Caspar Y, Courcol R, Maurin M, et al. Disseminated Infection Caused by *Francisella philomiragia*, France, 2014. *Emerg Infect Dis*. 2015; 21(12):2260–1. <https://doi.org/10.3201/eid2112.150615> PMID: 26583375; PubMed Central PMCID: PMC4672438.
36. Dean SN, Chung MC, van Hoek ML. Burkholderia Diffusible Signal Factor Signals to *Francisella novicida* To Disperse Biofilm and Increase Siderophore Production. *Appl Environ Microbiol*. 2015; 81(20):7057–66. <https://doi.org/10.1128/AEM.02165-15> PMID: 26231649; PubMed Central PMCID: PMC4579433.
37. Schneider CA, Rasband WS, Eliceiri KW. NIH Image to ImageJ: 25 years of image analysis. *Nat Methods*. 2012; 9(7):671–5. <https://doi.org/10.1038/nmeth.2089> PMID: 22930834; PubMed Central PMCID: PMC5554542.
38. Barry AL, Craig W.A., Nadler H., Reller L.B., Sanders C.C., Swenson J.M. Methods for Determining Bactericidal Activity of Antimicrobial Agents; Approved Guideline. CLSI, editor. Wayne, USA: Clinical and Laboratory Standards Institute; 1999.
39. Pettit RK, Weber CA, Kean MJ, Hoffmann H, Pettit GR, Tan R, et al. Microplate Alamar blue assay for *Staphylococcus epidermidis* biofilm susceptibility testing. *Antimicrob Agents Chemother*. 2005; 49(7):2612–7. <https://doi.org/10.1128/AAC.49.7.2612-2617.2005> PMID: 15980327; PubMed Central PMCID: PMC1168683.
40. Peeters E, Nelis HJ, Coenye T. Comparison of multiple methods for quantification of microbial biofilms grown in microtiter plates. *J Microbiol Methods*. 2008; 72(2):157–65. <https://doi.org/10.1016/j.mimet.2007.11.010> PMID: 18155789.
41. Foerster S, Desilvestro V, Hathaway LJ, Althaus CL, Unemo M. A new rapid resazurin-based microdilution assay for antimicrobial susceptibility testing of *Neisseria gonorrhoeae*. *J Antimicrob Chemother*. 2017; 72(7):1961–8. <https://doi.org/10.1093/jac/dkx113> PMID: 28431096; PubMed Central PMCID: PMC5890744.
42. Schmitt DM, O'Dee DM, Cowan BN, Birch JW, Mazzella LK, Nau GJ, et al. The use of resazurin as a novel antimicrobial agent against *Francisella tularensis*. *Front Cell Infect Microbiol*. 2013; 3:93. <https://doi.org/10.3389/fcimb.2013.00093> PMID: 24367766; PubMed Central PMCID: PMC3853850.
43. Das T, Sehar S, Koop L, Wong YK, Ahmed S, Siddiqui KS, et al. Influence of calcium in extracellular DNA mediated bacterial aggregation and biofilm formation. *PLoS One*. 2014; 9(3):e91935. <https://doi.org/10.1371/journal.pone.0091935> PMID: 24651318; PubMed Central PMCID: PMC3961253.
44. Itoh Y, Wang X, Hinnebusch BJ, Preston JF 3rd, Romeo T. Depolymerization of beta-1,6-N-acetyl-D-glucosamine disrupts the integrity of diverse bacterial biofilms. *J Bacteriol*. 2005; 187(1):382–7. <https://doi.org/10.1128/JB.187.1.382-387.2005> PMID: 15601723; PubMed Central PMCID: PMC538831.
45. Kaplan JB, Ragunath C, Ramasubbu N, Fine DH. Detachment of *Actinobacillus actinomycetemcomitans* biofilm cells by an endogenous beta-hexosaminidase activity. *J Bacteriol*. 2003; 185(16):4693–8. <https://doi.org/10.1128/JB.185.16.4693-4698.2003> PMID: 12896987; PubMed Central PMCID: PMC166467.
46. Boisset S, Caspar Y, Sutera V, Maurin M. New therapeutic approaches for treatment of tularaemia: a review. *Front Cell Infect Microbiol*. 2014; 4:40. <https://doi.org/10.3389/fcimb.2014.00040> PMID: 24734221; PubMed Central PMCID: PMC3975101.
47. Sugimoto S, Sato F, Miyakawa R, Chiba A, Onodera S, Hori S, et al. Broad impact of extracellular DNA on biofilm formation by clinically isolated Methicillin-resistant and -sensitive strains of *Staphylococcus aureus*. *Sci Rep*. 2018; 8(1):2254. <https://doi.org/10.1038/s41598-018-20485-z> PMID: 29396526; PubMed Central PMCID: PMC5797107.
48. Champion AE, Catanzaro KCF, Bandara AB, Inzana TJ. Formation of the *Francisella tularensis* Biofilm is Affected by Cell Surface Glycosylation, Growth Medium, and a Glucan Exopolysaccharide. *Sci Rep*. 2019; 9(1):12252. <https://doi.org/10.1038/s41598-019-48697-x> PMID: 31439876; PubMed Central PMCID: PMC6706388.
49. van Hoek ML, Hoang KV, Gunn JS. Two-Component Systems in *Francisella* Species. *Front Cell Infect Microbiol*. 2019; 9:198. <https://doi.org/10.3389/fcimb.2019.00198> PMID: 31263682; PubMed Central PMCID: PMC6584805.
50. Solano C, Echeverez M, Lasa I. Biofilm dispersion and quorum sensing. *Curr Opin Microbiol*. 2014; 18:96–104. <https://doi.org/10.1016/j.mib.2014.02.008> PMID: 24657330.
51. Young KD. The selective value of bacterial shape. *Microbiol Mol Biol Rev*. 2006; 70(3):660–703. <https://doi.org/10.1128/MMBR.00001-06> PMID: 16959965; PubMed Central PMCID: PMC1594593.
52. Azeredo J, Azevedo NF, Briandet R, Cerca N, Coenye T, Costa AR, et al. Critical review on biofilm methods. *Crit Rev Microbiol*. 2017; 43(3):313–51. <https://doi.org/10.1080/1040841X.2016.1208146> PMID: 27868469.

53. Gloag ES, Turnbull L, Huang A, Vallotton P, Wang H, Nolan LM, et al. Self-organization of bacterial biofilms is facilitated by extracellular DNA. *Proc Natl Acad Sci U S A*. 2013; 110(28):11541–6. <https://doi.org/10.1073/pnas.1218898110> PMID: [23798445](https://pubmed.ncbi.nlm.nih.gov/23798445/); PubMed Central PMCID: PMC3710876.
54. Chaignon P, Sadovskaya I, Ragunah C, Ramasubbu N, Kaplan JB, Jabbouri S. Susceptibility of staphylococcal biofilms to enzymatic treatments depends on their chemical composition. *Applied microbiology and biotechnology*. 2007; 75(1):125–32. <https://doi.org/10.1007/s00253-006-0790-y> PMID: [17221196](https://pubmed.ncbi.nlm.nih.gov/17221196/).
55. Larsen P, Nielsen JL, Dueholm MS, Wetzel R, Otzen D, Nielsen PH. Amyloid adhesins are abundant in natural biofilms. *Environmental microbiology*. 2007; 9(12):3077–90. <https://doi.org/10.1111/j.1462-2920.2007.01418.x> PMID: [17991035](https://pubmed.ncbi.nlm.nih.gov/17991035/).
56. Koza A, Hallett PD, Moon CD, Spiers AJ. Characterization of a novel air-liquid interface biofilm of *Pseudomonas fluorescens* SBW25. *Microbiology*. 2009; 155(Pt 5):1397–406. <https://doi.org/10.1099/mic.0.025064-0> PMID: [19383709](https://pubmed.ncbi.nlm.nih.gov/19383709/).
57. Koo H, Allan RN, Howlin RP, Stoodley P, Hall-Stoodley L. Targeting microbial biofilms: current and prospective therapeutic strategies. *Nat Rev Microbiol*. 2017; 15(12):740–55. <https://doi.org/10.1038/nrmicro.2017.99> PMID: [28944770](https://pubmed.ncbi.nlm.nih.gov/28944770/); PubMed Central PMCID: PMC5685531.
58. Heriot M, Nottelet B, Garric X, D'Este M, Richards GR, Moriarty FT, et al. Interaction of gentamicin sulfate with alginate and consequences on the physico-chemical properties of alginate-containing biofilms. *International journal of biological macromolecules*. 2019; 121:390–7. <https://doi.org/10.1016/j.ijbiomac.2018.10.025> PMID: [30304700](https://pubmed.ncbi.nlm.nih.gov/30304700/).
59. Rohde H, Burandt EC, Siemssen N, Frommelt L, Burdelski C, Wurster S, et al. Polysaccharide intercellular adhesin or protein factors in biofilm accumulation of *Staphylococcus epidermidis* and *Staphylococcus aureus* isolated from prosthetic hip and knee joint infections. *Biomaterials*. 2007; 28(9):1711–20. <https://doi.org/10.1016/j.biomaterials.2006.11.046> PMID: [17187854](https://pubmed.ncbi.nlm.nih.gov/17187854/).
60. Okuda KI, Nagahori R, Yamada S, Sugimoto S, Sato C, Sato M, et al. The Composition and Structure of Biofilms Developed by *Propionibacterium acnes* Isolated from Cardiac Pacemaker Devices. *Frontiers in microbiology*. 2018; 9:182. <https://doi.org/10.3389/fmicb.2018.00182> PMID: [29491850](https://pubmed.ncbi.nlm.nih.gov/29491850/); PubMed Central PMCID: PMC5817082.
61. Telford SR 3rd, Goethert HK. Ecology of *Francisella tularensis*. *Annu Rev Entomol*. 2020; 65:351–72. <https://doi.org/10.1146/annurev-ento-011019-025134> PMID: [31600457](https://pubmed.ncbi.nlm.nih.gov/31600457/).
62. Cavaliere R, Ball JL, Turnbull L, Whitchurch CB. The biofilm matrix destabilizers, EDTA and DNaseI, enhance the susceptibility of nontypeable *Hemophilus influenzae* biofilms to treatment with ampicillin and ciprofloxacin. *Microbiologyopen*. 2014; 3(4):557–67. <https://doi.org/10.1002/mbo3.187> PMID: [25044339](https://pubmed.ncbi.nlm.nih.gov/25044339/); PubMed Central PMCID: PMC4287182.
63. Belfield K, Bayston R, Hajduk N, Levell G, Birchall JP, Daniel M. Evaluation of combinations of putative anti-biofilm agents and antibiotics to eradicate biofilms of *Staphylococcus aureus* and *Pseudomonas aeruginosa*. *J Antimicrob Chemother*. 2017; 72(9):2531–8. <https://doi.org/10.1093/jac/dkx192> PMID: [28859444](https://pubmed.ncbi.nlm.nih.gov/28859444/).

# Acknowledgements

## **Acknowledgments**

First of all, I would like to thank my supervisor Isabelle for the super amazing interaction that we had all these years. Isabelle was not only my supervisor but also a second mother for me. Scientifically, with her teaching and research experience, she passed the researcher spirit-way of thinking to me. She showed me that with hard work, there is no limit in what you can achieve. Life speaking, she is and will be part of my family. Thank you for everything!

Then, I would like to thank my lovely parents and sister for supporting me all the years that I am far away from them since I started my studies in Greece, Scotland and then France. I have strong values inside me that because of my family I managed to follow and keep them as guidance during my PhD life!

I would like to thank Bastien for being so patient with me even if I speak a lot. You are a real friend and big brother to me!

I would like to thank also all the Bachelor and Master students that we worked together! Mateusz and Luis for being part of my first two research stories!

I would like to thank Ali and his group for all the interaction and support during my PhD. Ali you are a big brother to me. Thank you for everything!

I would like to thank all the people that I worked with, Patricia Renesto, the group of Martial Balland and his colleagues at Liphy for our collaborations!

I would like to thank also Geneviève for the lovely interaction and support during my PhD!

I would like to thank my family members and friends in Greece for supporting me during these beautiful but also difficult years. Also Tomas, Vanni, Marila, Christopher and Céline!

Dayana and Sheena I don't have to say something. You know my feelings for both of you!

I would like to thank also my "Amorgos" group of friends (Iasonas, Giannis, Dimitris, Iakovos) for all the nice summer vacations that we had during my PhD years!

A big thanks to Giannis for the friendship and support during my PhD and generally my life since I moved in France!

Last but not least, I would like to thank the University Grenoble Alpes, the Fondation Recherche Médicale and the Institute for Advanced Biosciences!

**I would like to have this manuscript in the honor of all my grandparents!  
They were so proud of me that this is the minimum that I can do for them.**

# References

## References

- Abercrombie M, Heaysman JE & Pegrum SM (1970a) The locomotion of fibroblasts in culture. I. Movements of the leading edge. *Exp. Cell Res.* **59**: 393–398
- Abercrombie M, Joan E, Heaysman M & Pegrum SM (1970b) The locomotion of fibroblasts in culture: II. “Ruffling”. *Experimental Cell Research* **60**: 437–444
- Amino R, Thiberge S, Martin B, Celli S, Shorte S, Frischknecht F & Ménard R (2006) Quantitative imaging of Plasmodium transmission from mosquito to mammal. *Nat Med* **12**: 220–224
- Antony B, Burd C, De Camilli P, Chen E, Daumke O, Faelber K, Ford M, Frolov VA, Frost A, Hinshaw JE, Kirchhausen T, Kozlov MM, Lenz M, Low HH, McMahon H, Merrifield C, Pollard TD, Robinson PJ, Roux A & Schmid S (2016) Membrane fission by dynamin: what we know and what we need to know. *EMBO J* **35**: 2270–2284
- Arrizabalaga G (2019) Neighbors Working Together: a *Toxoplasma* Rhoptry Protein That Facilitates Dense Granule Protein Translocation into the Host Cell. *mSphere* **4**: e00523-19, /msphere/4/4/mSphere523-19.atom
- Barkhuff WD, Gilk SD, Whitmarsh R, Tilley LD, Hunter C & Ward GE (2011) Targeted Disruption of TgPhIL1 in *Toxoplasma gondii* Results in Altered Parasite Morphology and Fitness. *PLOS ONE* **6**: e23977
- Besteiro S, Michelin A, Poncet J, Dubremetz J-F & Lebrun M (2009) Export of a *Toxoplasma gondii* Rhoptry Neck Protein Complex at the Host Cell Membrane to Form the Moving Junction during Invasion. *PLoS Pathog* **5**: e1000309
- Bichet M, Joly C, Henni AH, Guilbert T, Xémard M, Tafani V, Lagal V, Charras G & Tardieux I (2014) The toxoplasma-host cell junction is anchored to the cell cortex to sustain parasite invasive force. *BMC Biol* **12**: 1–21
- Bosch J, Turley S, Daly TM, Bogh SM, Villasmil ML, Roach C, Zhou N, Morrissey JM, Vaidya AB, Bergman LW & Hol WGJ (2006) Structure of the MTIP-MyoA complex, a key component of the malaria parasite invasion motor. *Proceedings of the National Academy of Sciences* **103**: 4852–4857
- Boucher LE & Bosch J (2015) The apicomplexan glideosome and adhesins – Structures and function. *Journal of Structural Biology* **190**: 93–114
- Brown KM, Lourido S & Sibley LD (2016) Serum Albumin Stimulates Protein Kinase G-dependent Microneme Secretion in *Toxoplasma gondii*. *J. Biol. Chem.* **291**: 9554–9565
- Butler KL, Ambravaneswaran V, Agrawal N, Bilodeau M, Toner M, Tompkins RG, Fagan S & Irimia D (2010) Burn injury reduces neutrophil directional migration speed in microfluidic devices. *PLoS ONE* **5**: e11921

Caldas L & de Souza W (2018) A Window to *Toxoplasma gondii* Egress. *Pathogens* **7**: 69

Caldas LA, Attias M & de Souza W (2009) Dynamin inhibitor impairs *Toxoplasma gondii* invasion. *FEMS Microbiology Letters* **301**: 103–108

Carne B, Bissuel F, Ajzenberg D, Bouyne R, Aznar C, Demar M, Bichat S, Louvel D, Bourbigot AM, Peneau C, Neron P & Dardé ML (2002) Severe acquired toxoplasmosis in immunocompetent adult patients in French Guiana. *J. Clin. Microbiol.* **40**: 4037–4044

Carmen MG del, Calvo LC & Mondragón R (2016) Induction of conoid extrusion is associated to MIC secretion in *Toxoplasma gondii* tachyzoites. In *European Microscopy Congress 2016: Proceedings* pp 242–243. American Cancer Society

Colombo FA, Vidal JE, Oliveira ACP de, Hernandez AV, Bonasser-Filho F, Nogueira RS, Focaccia R & Pereira-Chioccola VL (2005) Diagnosis of Cerebral Toxoplasmosis in AIDS Patients in Brazil: Importance of Molecular and Immunological Methods Using Peripheral Blood Samples. *J Clin Microbiol* **43**: 5044–5047

Davies HS, Baranova NS, El Amri N, Coche-Guérente L, Verdier C, Bureau L, Richter RP & Débarre D (2019) An integrated assay to probe endothelial glycocalyx-blood cell interactions under flow in mechanically and biochemically well-defined environments. *Matrix Biology* **78–79**: 47–59

Delorme-Walker V, Abrivard M, Lagal V, Anderson K, Perazzi A, Gonzalez V, Page C, Chauvet J, Ochoa W, Volkmann N, Hanein D & Tardieux I (2012) Toxofilin upregulates the host cortical actin cytoskeleton dynamics, facilitating *Toxoplasma* invasion. *J. Cell. Sci.* **125**: 4333–4342

Dubey JP (1996) *Toxoplasma Gondii*. In *Medical Microbiology*, Baron S (ed) Galveston (TX): University of Texas Medical Branch at Galveston

Dubey JP (1998) Advances in the life cycle of *Toxoplasma gondii*. *International Journal for Parasitology* **28**: 1019–1024

Dubey JP, Miller NL & Frenkel JK (1970) THE TOXOPLASMA GONDII OOCYST FROM CAT FECES. *J Exp Med* **132**: 636–662

Dubois DJ & Soldati-Favre D (2019) Biogenesis and secretion of micronemes in *Toxoplasma gondii*. *Cellular Microbiology* **21**: e13018

Ferguson DJP (2009) Identification of faecal transmission of *Toxoplasma gondii*: Small science, large characters. *Int. J. Parasitol.* **39**: 871–875

Ferguson DJP, Bowker C, Jeffery KJM, Chamberlain P & Squier W (2013) Congenital toxoplasmosis: continued parasite proliferation in the fetal brain despite maternal immunological control in other tissues. *Clin. Infect. Dis.* **56**: 204–208

- Ferguson SM & De Camilli P (2012) Dynamin, a membrane-remodelling GTPase. *Nat Rev Mol Cell Biol* **13**: 75–88
- Frénal K, Dubremetz J-F, Lebrun M & Soldati-Favre D (2017) Gliding motility powers invasion and egress in Apicomplexa. *Nat Rev Microbiol* **15**: 645–660
- Frénal K, Marq J-B, Jacot D, Polonais V & Soldati-Favre D (2014) Plasticity between MyoC- and MyoA-Glideosomes: An Example of Functional Compensation in *Toxoplasma gondii* Invasion. *PLoS Pathog* **10**: e1004504
- Frixione E, Mondragón R & Meza I (1996) Kinematic analysis of *Toxoplasma gondii* motility. *Cell Motil. Cytoskeleton* **34**: 152–163
- Gaskins E, Gilk S, DeVore N, Mann T, Ward G & Beckers C (2004) Identification of the membrane receptor of a class XIV myosin in *Toxoplasma gondii*. *The Journal of Cell Biology* **165**: 383–393
- Gonzalez V, Combe A, David V, Malmquist NA, Delorme V, Leroy C, Blazquez S, Ménard R & Tardieux I (2009) Host Cell Entry by Apicomplexa Parasites Requires Actin Polymerization in the Host Cell. *Cell Host & Microbe* **5**: 259–272
- Guérin A, Corrales RM, Parker ML, Lamarque MH, Jacot D, El Hajj H, Soldati-Favre D, Boulanger MJ & Lebrun M (2017) Efficient invasion by *Toxoplasma* depends on the subversion of host protein networks. *Nat Microbiol* **2**: 1358–1366
- Gupta M, Doss B, Lim CT, Voituriez R & Ladoux B (2016) Single cell rigidity sensing: A complex relationship between focal adhesion dynamics and large-scale actin cytoskeleton remodeling. *Cell Adhesion & Migration* **10**: 554–567
- Håkansson S, Morisaki H, Heuser J & Sibley LD (1999) Time-Lapse Video Microscopy of Gliding Motility in *Toxoplasma gondii* Reveals a Novel, Biphasic Mechanism of Cell Locomotion. *Mol Biol Cell* **10**: 3539–3547
- Halonen SK & Weiss LM (2013) TOXOPLASMOSIS. *Handb Clin Neurol* **114**: 125–145
- Harding CR, Gow M, Kang JH, Shortt E, Manalis SR, Meissner M & Lourido S (2019) Alveolar proteins stabilize cortical microtubules in *Toxoplasma gondii*. *Nature Communications* **10**: 1–14
- Heintzelman MB (2006) Cellular and Molecular Mechanics of Gliding Locomotion in Eukaryotes. In *International Review of Cytology* pp 79–129. Elsevier
- Heintzelman MB (2015) Gliding motility in apicomplexan parasites. *Seminars in Cell & Developmental Biology* **46**: 135–142
- Hellmann JK, Münter S, Kudryashev M, Schulz S, Heiss K, Müller A-K, Matuschewski K, Spatz JP, Schwarz US & Frischknecht F (2011) Environmental Constraints Guide Migration of Malaria Parasites during Transmission. *PLoS Pathog* **7**: e1002080

Herm-Gotz A (2002) Toxoplasma gondii myosin A and its light chain: a fast, single-headed, plus-end-directed motor. *The EMBO Journal* **21**: 2149–2158

Hopp CS, Chiou K, Ragheb DRT, Salman AM, Khan SM, Liu AJ & Sinnis P (2015) Longitudinal analysis of Plasmodium sporozoite motility in the dermis reveals component of blood vessel recognition. *Elife* **4**:

Hortua Triana MA, Márquez-Nogueras KM, Vella SA & Moreno SNJ (2018) Calcium signaling and the lytic cycle of the Apicomplexan parasite Toxoplasma gondii. *Biochim Biophys Acta Mol Cell Res* **1865**: 1846–1856

Hunter CA & Sibley LD (2012) Modulation of innate immunity by Toxoplasma gondii virulence effectors. *Nat Rev Microbiol* **10**: 766–778

Huynh M-H & Carruthers VB (2009) Tagging of Endogenous Genes in a Toxoplasma gondii Strain Lacking Ku80. *Eukaryotic Cell* **8**: 530–539

Jacot D, Tosetti N, Pires I, Stock J, Graindorge A, Hung Y-F, Han H, Tewari R, Kursula I & Soldati-Favre D (2016) An Apicomplexan Actin-Binding Protein Serves as a Connector and Lipid Sensor to Coordinate Motility and Invasion. *Cell Host & Microbe* **20**: 731–743

Jia Y, Marq J-B, Bisio H, Jacot D, Mueller C, Yu L, Choudhary J, Brochet M & Soldati-Favre D (2017) Crosstalk between PKA and PKG controls pH-

dependent host cell egress of Toxoplasma gondii. *EMBO J.* **36**: 3250–3267

Khalil IA, Kogure K, Akita H & Harashima H (2006) Uptake Pathways and Subsequent Intracellular Trafficking in Nonviral Gene Delivery. *Pharmacol Rev* **58**: 32–45

Kühni-Boghenbor K, Ma M, Lemgruber L, Cyrklaff M, Frischknecht F, Gaschen V, Stoffel M & Baumgartner M (2012) Actin-mediated plasma membrane plasticity of the intracellular parasite Theileria annulata: Membrane plasticity of the intracellular parasite Theileria annulata. *Cell Microbiol* **14**: 1867–1879

Lämmermann T & Sixt M (2009) Mechanical modes of ‘amoeboid’ cell migration. *Curr. Opin. Cell Biol.* **21**: 636–644

Laporte MH, Chatellard C, Vauchez V, Hemming FJ, Deloulme J-C, Vossier F, Blot B, Fraboulet S & Sadoul R (2017) Alix is required during development for normal growth of the mouse brain. *Sci Rep* **7**: 44767

Legant WR, Miller JS, Blakely BL, Cohen DM, Genin GM & Chen CS (2010) Measurement of mechanical tractions exerted by cells within three-dimensional matrices. *Nat Methods* **7**: 969–971

Leung JM, Rould MA, Konradt C, Hunter CA & Ward GE (2014) Disruption of TgPHIL1 alters specific parameters of Toxoplasma gondii motility measured in a quantitative, three-dimensional live motility assay. *PLoS ONE* **9**: e85763

- Limozin L & Sengupta K (2009) Quantitative reflection interference contrast microscopy (RICM) in soft matter and cell adhesion. *Chemphyschem* **10**: 2752–2768
- Liu J, He Y, Benmerzouga I, Sullivan WJ, Morrisette NS, Murray JM & Hu K (2016) An ensemble of specifically targeted proteins stabilizes cortical microtubules in the human parasite *Toxoplasma gondii*. *Mol Biol Cell* **27**: 549–571
- Luft BJ & Remington JS (1992) Toxoplasmic encephalitis in AIDS. *Clin. Infect. Dis.* **15**: 211–222
- Ma C, Li C, Ganesan L, Oak J, Tsai S, Sept D & Morrisette NS (2007) Mutations in  $\alpha$ -Tubulin Confer Dinitroaniline Resistance at a Cost to Microtubule Function. *Mol Biol Cell* **18**: 4711–4720
- Martiel J-L, Leal A, Kurzawa L, Balland M, Wang I, Vignaud T, Tseng Q & Théry M (2015) Measurement of cell traction forces with ImageJ. In *Methods in Cell Biology* pp 269–287
- McFadden GI & Yeh E (2017) The apicoplast: now you see it, now you don't. *Int. J. Parasitol.* **47**: 137–144
- McGovern KE & Wilson EH (2013) Dark side illuminated: imaging of *Toxoplasma gondii* through the decades. *Parasites Vectors* **6**: 334
- Mohamad NR, Marzuki NHC, Buang NA, Huyop F & Wahab RA (2015) An overview of technologies for immobilization of enzymes and surface analysis techniques for immobilized enzymes. *Biotechnology & Biotechnological Equipment* **29**: 205–220
- Moudy R, Manning TJ & Beckers CJ (2001) The Loss of Cytoplasmic Potassium upon Host Cell Breakdown Triggers Egress of *Toxoplasma gondii*. *J. Biol. Chem.* **276**: 41492–41501
- Mowat AM & Agace WW (2014) Regional specialization within the intestinal immune system. *Nat. Rev. Immunol.* **14**: 667–685
- Münter S, Sabass B, Selhuber-Unkel C, Kudryashev M, Hegge S, Engel U, Spatz JP, Matuschewski K, Schwarz US & Frischknecht F (2009) Plasmodium Sporozoite Motility Is Modulated by the Turnover of Discrete Adhesion Sites. *Cell Host & Microbe* **6**: 551–562
- Murray CJL, Vos T, Lozano R, Naghavi M, Flaxman AD, Michaud C, Ezzati M, Shibuya K, Salomon JA, Abdalla S, Aboyans V, Abraham J, Ackerman I, Aggarwal R, Ahn SY, Ali MK, Alvarado M, Anderson HR, Anderson LM, Andrews KG, et al (2012) Disability-adjusted life years (DALYs) for 291 diseases and injuries in 21 regions, 1990–2010: a systematic analysis for the Global Burden of Disease Study 2010. *Lancet* **380**: 2197–2223
- Nishi M, Hu K, Murray JM & Roos DS (2008) Organellar dynamics during the cell cycle of *Toxoplasma gondii*. *J. Cell. Sci.* **121**: 1559–1568

Okimura C, Taniguchi A, Nonaka S & Iwadate Y (2018) Rotation of stress fibers as a single wheel in migrating fish keratocytes. *Sci Rep* **8**: 10615

Opitz C & Soldati D (2002) 'The glideosome': a dynamic complex powering gliding motion and host cell invasion by *Toxoplasma gondii*. *Mol. Microbiol.* **45**: 597–604

Paluch EK & Raz E (2013) The role and regulation of blebs in cell migration. *Curr Opin Cell Biol* **25**: 582–590

Park RJ, Shen H, Liu L, Liu X, Ferguson SM & De Camilli P (2013) Dynamin triple knockout cells reveal off target effects of commonly used dynamin inhibitors. *Journal of Cell Science* **126**: 5305–5312

Parussini F, Tang Q, Moin SM, Mital J, Urban S & Ward GE (2012) Intramembrane proteolysis of *Toxoplasma* apical membrane antigen 1 facilitates host-cell invasion but is dispensable for replication. *PNAS*

Pavlou G, Biesaga M, Touquet B, Lagal V, Balland M, Dufour A, Hakimi M & Tardieux I (2018) *Toxoplasma* Parasite Twisting Motion Mechanically Induces Host Cell Membrane Fission to Complete Invasion within a Protective Vacuole. *Cell Host & Microbe* **24**: 81- 96.e5

Pavlou G, Milon G & Tardieux I (2019) Intracellular protozoan parasites: living probes of the host cell surface molecular repertoire. *Current Opinion in Microbiology* **52**: 116–123

Pavlou G & Tardieux I (2020) Phenotyping *Toxoplasma* Invasive Skills by Fast Live Cell Imaging. In *Toxoplasma gondii*, Tonkin CJ (ed) pp 209– 220. New York, NY: Springer US

Periz J, Whitelaw J, Harding C, Gras S, Del Rosario Minina MI, Latorre- Barragan F, Lemgruber L, Reimer MA, Insall R, Heaslip A & Meissner M (2017) *Toxoplasma gondii* F-actin forms an extensive filamentous network required for material exchange and parasite maturation. *eLife* **6**: e24119

Petrie RJ & Yamada KM (2012) At the leading edge of three-dimensional cell migration. *J Cell Sci* **125**: 5917–5926

Quadt KA, Streichfuss M, Moreau CA, Spatz JP & Frischknecht F (2016) Coupling of Retrograde Flow to Force Production During Malaria Parasite Migration. *ACS Nano* **10**: 2091–2102

Ridley AJ, Schwartz MA, Burridge K, Firtel RA, Ginsberg MH, Borisy G, Parsons JT & Horwitz AR (2003) Cell migration: integrating signals from front to back. *Science* **302**: 1704–1709

Roiko MS, Svezhova N & Carruthers VB (2014) Acidification Activates *Toxoplasma gondii* Motility and Egress by Enhancing Protein Secretion and Cytolytic Activity. *PLOS Pathogens* **10**: e1004488

Sahoo N, Beatty W, Heuser J, Sept D & Sibley LD (2006) Unusual Kinetic and Structural Properties Control Rapid Assembly and Turnover of Actin in the Parasite *Toxoplasma gondii*. *Mol Biol Cell* **17**: 895–906

Schmitz S, Grainger M, Howell S, Calder LJ, Gaeb M, Pinder JC, Holder AA & Veigel C (2005) Malaria Parasite Actin Filaments are Very Short. *Journal of Molecular Biology* **349**: 113–125

Schmitz S, Schaap IAT, Kleinjung J, Harder S, Grainger M, Calder L, Rosenthal PB, Holder AA & Veigel C (2010) Malaria Parasite Actin Polymerization and Filament Structure. *J. Biol. Chem.* **285**: 36577–36585

Schwarz US & Soiné JRD (2015) Traction force microscopy on soft elastic substrates: A guide to recent computational advances. *Biochimica et Biophysica Acta (BBA) - Molecular Cell Research* **1853**: 3095–3104

Senger F, Pitaval A, Ennomani H, Kurzawa L, Blanchoin L & Théry M (2019) Spatial integration of mechanical forces by  $\alpha$ -actinin establishes actin network symmetry. *J Cell Sci* **132**: jcs236604

Soldati D, Foth BJ & Cowman AF (2004) Molecular and functional aspects of parasite invasion. *Trends Parasitol.* **20**: 567–574

Spreng B, Fleckenstein H, Kübler P, Di Biagio C, Benz M, Patra P, Schwarz US, Cyrklaff M & Frischknecht F (2019) Microtubule number and length determine cellular shape and function in *Plasmodium*. *EMBO J* **38**: e100984

Stortz JF, Del Rosario M, Singer M, Wilkes JM, Meissner M & Das S (2019) Formin-2 drives polymerisation of actin filaments enabling segregation of apicoplasts and cytokinesis in *Plasmodium falciparum*. *eLife* **8**: e49030

Strale P-O, Azioune A, Bugnicourt G, Lecomte Y, Chahid M & Studer V (2016) Multiprotein Printing by Light-Induced Molecular Adsorption. *Adv. Mater.* **28**: 2024–2029

Straub KW, Peng ED, Hajagos BE, Tyler JS & Bradley PJ (2011) The moving junction protein RON8 facilitates firm attachment and host cell invasion in *Toxoplasma gondii*. *PLoS Pathog.* **7**: e1002007

Suss-Toby E, Zimmerberg J & Ward GE (1996) *Toxoplasma* invasion: the parasitophorous vacuole is formed from host cell plasma membrane and pinches off via a fission pore. *Proceedings of the National Academy of Sciences* **93**: 8413–8418

Tardieux I, Webster P, Ravesloot J, Boron W, Lunn JA, Heuser JE & Andrews NW (1992) Lysosome recruitment and fusion are early events required for trypanosome invasion of mammalian cells. *Cell* **71**: 1117–1130

Théry M (2010) Micropatterning as a tool to decipher cell morphogenesis and functions. *Journal of Cell Science* **123**: 4201–4213

Tonkin ML, Roques M, Lamarque MH, Pugnère M, Douguet D, Crawford J, Lebrun M & Boulanger MJ (2011) Host cell invasion by apicomplexan parasites: insights from the co-structure of AMA1 with a RON2 peptide. *Science* **333**: 463–467

Torgerson PR & Mastroiacovo P (2013) The global burden of congenital toxoplasmosis: a systematic review. *Bull. World Health Organ.* **91**: 501–508

Tosetti N, Dos Santos Pacheco N, Soldati-Favre D & Jacot D (2019) Three F- actin assembly centers regulate organelle inheritance, cell-cell communication and motility in *Toxoplasma gondii*. *eLife* **8**: e42669

Wang Z-D, Wang S-C, Liu H-H, Ma H-Y, Li Z-Y, Wei F, Zhu X-Q & Liu Q (2017) Prevalence and burden of *Toxoplasma gondii* infection in HIV- infected people: a systematic review and meta-analysis. *Lancet HIV* **4**: e177–e188

Weiss LM & Dubey JP (2009) Toxoplasmosis: A history of clinical observations. *Int. J. Parasitol.* **39**: 895–901

Yamada KM & Sixt M (2019) Mechanisms of 3D cell migration. *Nature Reviews Molecular Cell Biology* **20**: 738–752